(12) INTERNATIONAL APPLICATION PUBLISHED UNDER THE PATENT COOPERATION TREATY (PCT)

(19) World Intellectual Property Organization
International Bureau

(43) International Publication Date
19 October 2023 (19.10.2023)

WIPO | PCT

(10) International Publication Number
WO 2023/200688 A2

(51) International Patent Classification:
H10N 69/00 (2023.01) *H10N 70/00* (2023.01)

(21) International Application Number:
PCT/US2023/017927

(22) International Filing Date:
07 April 2023 (07.04.2023)

(25) Filing Language: English

(26) Publication Language: English

(30) Priority Data:
63/329,729 11 April 2022 (11.04.2022) US

(71) Applicant: **BOARD OF REGENTS, THE UNIVERSITY OF TEXAS SYSTEM** [US/US]; 210 West 7th Street, Austin, Texas 78701 (US).

(72) Inventors: **DEMKOV, Alexander A.**; c/o The University of Texas System, 210 West 7th Street, Austin, Texas 78701 (US). **HADAMEK, Tobias**; c/o The University of Texas System, 210 West 7th Street, Austin, Texas 78701 (US). **POSADAS, Agham**; c/o The University of Texas System, 210 West 7th Street, Austin, Texas 78701 (US).

(74) Agent: **FISCHER, William M.** et al.; Setter Roche Smith & Shellenberger LLP, 1860 Blake Street, Suite 500, Denver, Colorado 80202 (US).

(81) Designated States *(unless otherwise indicated, for every kind of national protection available)*: AE, AG, AL, AM, AO, AT, AU, AZ, BA, BB, BG, BH, BN, BR, BW, BY, BZ, CA, CH, CL, CN, CO, CR, CU, CV, CZ, DE, DJ, DK, DM, DO, DZ, EC, EE, EG, ES, FI, GB, GD, GE, GH, GM, GT, HN, HR, HU, ID, IL, IN, IQ, IR, IS, IT, JM, JO, JP, KE, KG, KH, KN, KP, KR, KW, KZ, LA, LC, LK, LR, LS, LU, LY, MA, MD, MG, MK, MN, MU, MW, MX, MY, MZ, NA, NG, NI, NO, NZ, OM, PA, PE, PG, PH, PL, PT, QA, RO, RS, RU, RW, SA, SC, SD, SE, SG, SK, SL, ST, SV, SY, TH, TJ, TM, TN, TR, TT, TZ, UA, UG, US, UZ, VC, VN, WS, ZA, ZM, ZW.

(84) Designated States *(unless otherwise indicated, for every kind of regional protection available)*: ARIPO (BW, CV, GH, GM, KE, LR, LS, MW, MZ, NA, RW, SC, SD, SL, ST, SZ, TZ, UG, ZM, ZW), Eurasian (AM, AZ, BY, KG, KZ, RU, TJ, TM), European (AL, AT, BE, BG, CH, CY, CZ, DE, DK, EE, ES, FI, FR, GB, GR, HR, HU, IE, IS, IT, LT, LU, LV, MC, ME, MK, MT, NL, NO, PL, PT, RO, RS, SE,

(54) Title: GALLIUM-OXIDE-ON-SILICON (GAOXS)

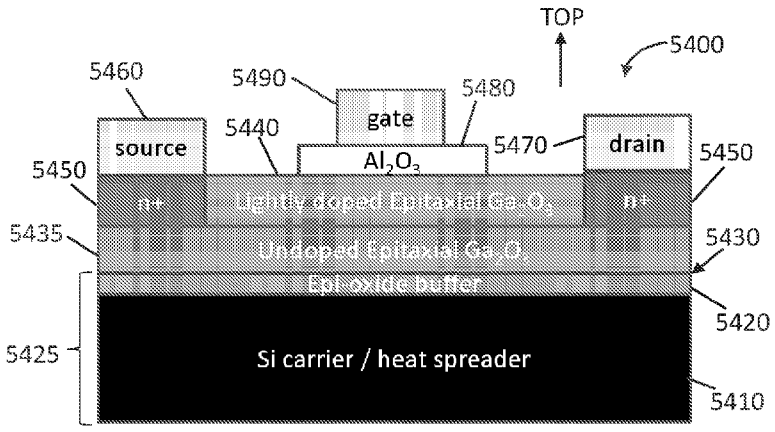

FIG. 54

(57) Abstract: Various embodiments of the present technology generally relate to silicon (Si)-based semiconductor wafer and methods of manufacturing the same. Some embodiments of the present technology relate to wafers having an epi-oxide buffer layer formed on a Si substrate and a thin film of gallia formed on the epi-oxide buffer layer. One or more additional layers of gallia may be formed on the thin film of gallia. The epi-oxide layers according to the present technology may include epitaxial alumina, strontium titanate (STO), a rare earth oxide, and combinations of the same. Further described are power electronics devices advantageously integrating the wafers and manufacturing methods of the present technology.

WO 2023/200688 A2

[Continued on next page]

SI, SK, SM, TR), OAPI (BF, BJ, CF, CG, CI, CM, GA, GN, GQ, GW, KM, ML, MR, NE, SN, TD, TG).

Published:

— *without international search report and to be republished upon receipt of that report (Rule 48.2(g))*

Attorney Docket No. 512.0035WO

Gallium-Oxide-On-Silicon (GaOxS)

FEDERALLY FUNDED RESEARCH

[0001] This invention was made with government support under Grant No. FA9550-18-1-0053 and Grant No. FA9550-12-1-0494 awarded by the Air Force Office of Scientific Research. The government has certain rights in the invention.

CROSS-REFERENCE TO RELATED APPLICATIONS

[0002] This application claims the benefit of and priority to U.S. Provisional Application No. 63/329,729, filed on April 11, 2022, which is incorporated by reference herein in its entirety.

TECHNICAL FIELD

[0003] Various embodiments of the present technology generally relate to silicon (Si)-based semiconductor manufacturing. More specifically, some embodiments of the present technology relate to systems and methods for integrating gallium oxide thin films on silicon (001) via a buffer layer.

BACKGROUND

[0004] Ga_2O_3 is a promising wide band-gap semiconductor with potential applications in high power electronics, solar-blind ultraviolet (UV) photodetectors, UV-transparent conductive films, UV detectors, electro-optical devices, and possibly microwave switching and amplification [1-3, 106, 107]. Benefits of the material are an ultra-wide band gap of ~5 eV, transparency into the deep-UV spectral range, and the availability of relatively low-cost bulk single crystals, compared to other wide band gap materials. Ga_2O_3 has a high theoretical breakdown field of about 8 MV/cm [108], higher than GaN (3.3 MV/cm) and SiC (2.5 MV/cm), which are, besides the ubiquitous Si (0.3 MV/cm), the most commonly used materials in high-power electronics [4, 5]. Larger breakdown fields can lead to the miniaturization of power electronic devices with associated reductions in cost and weight. The enhanced radiation hardness of Ga_2O_3 [6] additionally makes it suitable for space applications. Today an estimated 30 % of all electricity flows through power electronics and this is projected to reach 80 % in the future [7]. Efficient n-type doping of Ga_2O_3 can be achieved by Si, Ge, Sn and Nb incorporation [3]. Recently p-type doping with H has been demonstrated [8].

[0005] Six different polymorphs of Ga_2O_3 have been described: monoclinic (β), rhombohedral/trigonal (α), cubic defective spinel (γ), cubic bixbyite (δ), orthorhombic (κ), and hexagonal (ε) [9]. All Ga_2O_3 polymorphs are based on a close-packed arrangement of oxide ions (hexagonal close-packed (hcp) or

face-centered cubic (fcc); distorted to some degree in most cases), and Ga ions partially fill octahedral and tetrahedral voids, which show local disorder for some structures [9]. δ-Ga_2O_3 has been speculated to be a mixture of β- and ε-Ga_2O_3 [9], and hexagonal ε-Ga_2O_3 has been shown by electron microscopy to be a multi-domain structure of orthorhombic κ-Ga_2O_3 (isostructural to κ-Al_2O_3) [10]. Recently, the orthorhombic polymorph has been referred to as either as ε-Ga_2O_3 [11, 12] or as κ-Ga_2O_3 [10]; due to the analogy with κ-Al_2O_3 and to avoid ambiguity, it will be referred to herein as κ-Ga_2O_3. The crystallographic relationships between κ-, β-, and γ-polymorphs have been described [13]. In summary, there appear to be only four truly distinct polymorphs: α, β, γ and κ.

[0006] β-Ga_2O_3 is the stable polymorph under normal conditions and crystallizes in space group $C2/m$ with lattice parameters a = 12.22 Å, b = 3.04 Å, c = 5.80 Å and β = 103.75° [9]. A major advantage of β-Ga_2O_3 is that low-cost and high-quality single crystals are available: 4 inch β-Ga_2O_3 wafers are commercially available [14], and 6 inch wafers are in development [15]. The production of 6 inch β-Ga_2O_3 bulk wafers is projected to be about a 1/3 cheaper than the production of 6" SiC wafers [7]. A major disadvantage of Ga_2O_3, however, is the low thermal conductivity of 0.1-0.3 $Wcm^{-1}K^{-1}$ [5, 108], which is detrimental for high-power applications that dissipate energy in the form of Joule heating [16, 109]. Therefore, the integration of epitaxial Ga_2O_3 onto Si would be advantageous due to the 750 % higher thermal conductivity of Si compared to Ga_2O_3 [17, 110]. Currently, large-scale epitaxial films of Ga_2O_3 are unavailable commercially and bulk crystal wafers are only available up to 4 inch diameter [111]. Another benefit would be cost reduction [17], based on even larger diameter Ga_2O_3 substrates and direct process integration with Si technology. Epitaxial growth onto Si (001) wafers would open up numerous avenues for the large scale integration but, unfortunately, Ga_2O_3 cannot be directly grown on Si.

[0007] The challenge of epitaxial integration is the structural difference between silicon and gallium oxide. Si has a crystal structure with cubic symmetry, whereas β-Ga_2O_3 has monoclinic symmetry. This symmetry mismatch will unavoidably lead to a multi-orientation growth of epitaxial domains [18, 19]. Crystal grain boundaries between epitaxial domains and defects arising from the lattice mismatch to the substrate can be pernicious to the electronic properties of the epilayer.

[0008] In prior work on the integration of Ga_2O_3 with Si, a textured 1 μm β-Ga_2O_3 film was grown by HVPE on Si (111) with a ~100 nm 3C-SiC (zinc blende structure) buffer layer [24]; randomly oriented β-Ga_2O_3 rods as well as nanosheets were grown by chemical vapor deposition (CVD) on 3C-SiC/Si(001) [25, 26]; and polycrystalline β-Ga_2O_3 was grown directly on Si (001) and Si (111) without buffer layers by pulsed laser deposition (PLD) [27]. β-Ga_2O_3 of unclear structural orientation was also grown by HVPE on SiC-buffered Si (001), Si (011) and Si (111) [28, 29]. Additional prior work includes the deposition of amorphous Ga_2O_3 on Si (001) by CVD [30], and crystallization of amorphous Ga_2O_3 on Si (111) by annealing leading to grains of β-Ga_2O_3 [31]. Recently, β-Ga_2O_3 wafers have been

integrated directly, and with an alumina interlayer, onto Si and SiC wafers by wafer bonding and ion cutting [32, 33].

[0009] In many instances, Ga_2O_3 has been grown heteroepitaxially on widely available, high-structural-quality and low-cost *c*-plane sapphire substrates by a variety of physical and chemical vapor deposition methods: MBE [34-43], MOCVD [42, 44, 45], PLD [42, 46], rf-sputtering [47], CVD [11, 48, 49], HVPE [50-53], PVD [54, 55]. Depending on the growth method, growth parameters such as temperature and post-growth treatments, various phases and mixtures of phases of epitaxial Ga_2O_3 are created on *c*-plane sapphire: β-Ga_2O_3 ($\bar{2}01$), (101) and (310), α-Ga_2O_3 (00.1), γ-Ga_2O_3 (111) and κ-Ga_2O_3 (001) (wrongly assigned ε-Ga_2O_3 (00.1) [10]). The corundum crystal structure of sapphire or α-Al_2O_3 (trigonal space group $R\bar{3}c$, 167), consists of a hcp oxygen framework with two-thirds of the octahedral interstices filled with Al [56]. It has been observed by synchrotron-based x-ray diffraction (XRD) that when Ga_2O_3 is grown by oxygen plasma-assisted MBE (PAMBE) on *c*-plane α-Al_2O_3, isostructural growth of α-Ga_2O_3 is observed for the first 33 Å (for a 2.3 Å/min growth rate and 600 °C substrate temperature), which then converts to ($\bar{2}01$)-oriented β-Ga_2O_3 on top [40]. The ($\bar{2}01$) plane of β-Ga_2O_3 has a similar local oxygen arrangement as the *c*-plane of α-Al_2O_3 [54]. β-Ga_2O_3 with ($\bar{2}01$)-, (101)- and (310)-orientations has been formed after heat treatment of κ-Ga_2O_3 on sapphire [13, 57], and the (310) and (101) orientations grow as minority phases for ($\bar{2}01$) β-Ga_2O_3 on sapphire [50, 54]. For β-Ga_2O_3 grown on vicinal α-Al_2O_3, the six in-plane orientations of ($\bar{2}01$) that arise on non-vicinal substrates [54], are effectively reduced to one dominant one [49, 50], and a room temperature electron mobility of 106.6 $cm^2V^{-1}s^{-1}$ can be achieved at a doping concentration of 4.83 x 10^{17} cm^{-3} [49]. For comparison, the record value for room temperature mobility of 184 $cm^2V^{-1}s^{-1}$ in β-Ga_2O_3 was achieved with a homoepitaxial film grown by MOVPE at a doping concentration of 2.5 x 10^{16} cm^{-3} [58], and the theoretically predicted limit of the room temperature mobility of β-Ga_2O_3 is 200 $cm^2V^{-1}s^{-1}$ [59]. (111)-oriented γ-Al_2O_3 with two in-plane rotational variants can be grown on Si (001) by e-beam evaporation of Al_2O_3 at elevated temperature, with a pseudomorphic γ-Al_2O_3 (001) interlayer showing an atomically abrupt interface between Al_2O_3 and Si [60-63]. The observation of relatively large domains with average lateral extensions of more than 100 nm for γ-Al_2O_3 (111) on Si (001) was reported [60]. γ-Ga_2O_3 in (001)-orientation has been epitaxially stabilized on spinel $MgAl_2O_4$ (001) substrates [65], and on MgO (001) [66].

[0010] Previous attempts at integrating Ga_2O_3 on Si highlight the difficulty of this process. A textured 1-μm-thick β-Ga_2O_3 film was grown by hydride vapor phase epitaxy (HVPE) on Si (111) with a ~100-nm 3C-SiC (zincblende structure) buffer layer [112]; randomly oriented β-Ga_2O_3 rods as well as nanosheets were grown by chemical vapor deposition (CVD) on 3C-SiC/Si(001) [113, 114]; and polycrystalline β-Ga_2O_3 was grown directly on Si (001) and Si (111) without buffer layers using pulsed laser deposition (PLD) [115]. β-Ga_2O_3 of unspecified structural orientation was also grown by HVPE on SiC-buffered Si (001), Si (011) and Si (111) [116, 117]. Additional prior work includes the deposition

of amorphous Ga_2O_3 on Si (001) by CVD [118], and crystallization of amorphous Ga_2O_3 on Si (111) by annealing, leading to grains of β-Ga_2O_3 [119]. Recently, β-Ga_2O_3 wafers have been integrated directly onto Si and SiC wafers with an alumina interlayer using wafer bonding and ion cutting [120, 121].

[0011] Epitaxial Ga_2O_3 thin films have previously been grown on some oxide substrates. The (100)-oriented epitaxial relationship was found for Ga_2O_3 grown by MOCVD on $SrTiO_3$ (STO) (001) after annealing the sample above 1000°C [122]. Other examples of Ga_2O_3 growth on oxide surfaces include the deposition of κ-Ga_2O_3 (001) on STO (111) via tin-assisted pulsed-laser deposition [123] and by mist CVD [124]. We have also recently reported the integration of β-Ga_2O_3 by plasma-assisted molecular beam epitaxy onto a γ-Al_2O_3 (111) buffer layer grown at 840 °C by e-beam evaporation on a clean Si (001) surface [125].

[0012] Integration of β-Ga_2O_3 on Si (001) is highly challenging due to multiple fundamental differences between the sesquioxide and the semiconductor substrate.

REFERENCES

[0013] [1] S.J. Pearton, J. Yang, P.H. Cary, F. Ren, J. Kim, M.J. Tadjer, and M.A. Mastro, Appl. Phys. Rev. 5, 011301 (2018).

[0014] [2] B. Bayraktaroglu, "Assessment of Gallium Oxide Technology" - Air Force Research Laboratory Report No. AFRL-RY-WP-TR-2017-0167 (Wright-Patterson Air Force Base, OH, 2017).

[0015] [3] J. Zhang, J. Shi, D.C. Qi, L. Chen, and K.H.L. Zhang, APL Mater. 8, (2020).

[0016] [4] H. Zhang, L. Yuan, X. Tang, J. Hu, J. Sun, Y. Zhang, Y. Zhang, and R. Jia, IEEE Trans. Power Electron. 35, 5157 (2020).

[0017] [5] H. Murakami, M. Higashiwaki, Y. Kumagai, T. Masui, K. Sasaki, A. Kuramata, S. Yamakoshi, and A. Koukitu, Semicond. Sci. Technol. 31, 034001 (2016).

[0018] [6] J. Kim, S.J. Pearton, C. Fares, J. Yang, F. Ren, S. Kim, and A.Y. Polyakov, J. Mater. Chem. C 7, 10 (2019).

[0019] [7] S.B. Reese, T. Remo, J. Green, and A. Zakutayev, Joule 3, 903 (2019).

[0020] [8] M.M. Islam, M.O. Liedke, D. Winarski, M. Butterling, A. Wagner, P. Hosemann, Y. Wang, B. Uberuaga, and F.A. Selim, Sci. Rep. 10, 1 (2020).

[0021] [9] H.Y. Playford, A.C. Hannon, E.R. Barney, and R.I. Walton, Chem. - A Eur. J. 19, 2803 (2013).

[0022] [10] I. Cora, F. Mezzadri, F. Boschi, M. Bosi, M. Čaplovičová, G. Calestani, I. Dódony, B. Pécz, and R. Fornari, CrystEngComm 19, 1509 (2017).

[0023] [11] D. Oka, S. Yusa, K. Kimura, A.K.R. Ang, N. Happo, K. Hayashi, and T. Fukumura, Jpn. J. Appl. Phys. (2020).

[0024] [12] H. Nishinaka, H. Komai, D. Tahara, Y. Arata, and M. Yoshimoto, (2018).

[0025] [13] I. Cora, Z. Fogarassy, R. Fornari, M. Bosi, A. Rečnik, and B. Pécz, Acta Mater. 183, 216 (2020).

[0026] [14] 'Tamura Corp β- Ga2O3 substrate specifications sheet', accessed 2020-05-20. https://www.tamuracorp.com/file.jsp?id=13281.

[0027] [15] A.E. Romanov, S.I. Stepanov, V.I. Nikolaev, and V.E. Bougrov, Rev. Adv. Mater. Sci (2016).

[0028] [16] M. Higashiwaki, K. Sasaki, A. Kuramata, T. Masui, and S. Yamakoshi, Phys. Status Solidi Appl. Mater. Sci. 211, 21 (2014).

[0029] [17] O. Hilt, E.B. Treidel, M. Wolf, C. Kuring, K. Tetzner, H. Yazdani, A. Wentzel, and J. Würfl, IET Power Electron. 12, 3919 (2019).

[0030] [18] M. Grundmann, T. Böntgen, and M. Lorenz, Phys. Rev. Lett. 105, 1 (2010).

[0031] [19] M. Grundmann, Phys. Status Solidi Basic Res. 248, 805 (2011).

[0032] [20] D.G. Schlom, APL Mater. 3, 1 (2015).

[0033] [21] K.J. Hubbard and D.G. Schlom, J. Mater. Res. 11, 2757 (1996).

[0034] [22] H.W. Xue, Q.M. He, G.Z. Jian, S.B. Long, T. Pang, and M. Liu, Nanoscale Res. Lett. 13, 1 (2018).

[0035] [23] P. Vogt, F.V.E. Hensling, K. Azizie, C.S. Chang, D. Turner, J. Park, J.P. McCandless, H. Paik, B.J. Bocklund, G. Hoffman, and others, ArXiv Prepr. ArXiv2011.00084 (2020).

[0036] [24] S.A. Kukushkin, V.I. Nikolaev, A. V. Osipov, E. V. Osipova, A.I. Pechnikov, and N.A. Feoktistov, Phys. Solid State 58, 1876 (2016).

[0037] [25] S. Rafique, L. Han, C.A. Zorman, and H. Zhao, Cryst. Growth Des. 16, 511 (2016).

[0038] [26] S. Rafique, L. Han, J. Lee, X.-Q. Zheng, C.A. Zorman, P.X.-L. Feng, and H. Zhao, J. Vac. Sci. Technol. B, Nanotechnol. Microelectron. Mater. Process. Meas. Phenom. 35, 011208 (2017).

[0039] [27] Y. Berencén, Y. Xie, M. Wang, S. Prucnal, L. Rebohle, and S. Zhou, Semicond. Sci. Technol. 34, 0 (2019).

[0040] [28] A. V. Osipov, A.S. Grashchenko, S.A. Kukushkin, V.I. Nikolaev, E. V. Osipova, A.I. Pechnikov, and I.P. Soshnikov, Contin. Mech. Thermodyn. 30, 1059 (2018).

[0041] [29] A.S. Grashchenko, S.A. Kukushkin, V.I. Nikolaev, A. V. Osipov, E. V. Osipova, and I.P. Soshnikov, Phys. Solid State 60, 852 (2018).

[0042] [30] D.H. Kim, S.H. Yoo, T.M. Chung, K.S. An, H.S. Yoo, and Y. Kim, Bull. Korean Chem. Soc. (2002).

[0043] [31] H.W. Kim, N.H. Kim, and C. Lee, Br. Ceram. Trans. (2004).

[0044] [32] W. Xu, X. Wang, Y. Wang, T. You, X. Ou, G. Han, H. Hu, S. Zhang, F. Mu, T. Suga, Y. Zhang, and Y. Hao, in Tech. Dig. - Int. Electron Devices Meet. IEDM (2019), pp. 274–277.

[0045] [33] Y.B. Wang, W.H. Xu, T.G. You, F.W. Mu, H.D. Hu, Y. Liu, H. Huang, T. Suga, G.Q. Han, X. Ou, and Y. Hao, Sci. China Physics, Mech. Astron. 63, 1 (2020).

[0046] [34] T. Oshima, T. Okuno, and S. Fujita, Japanese J. Appl. Physics, Part 1 Regul. Pap. Short Notes Rev. Pap. 46, 7217 (2007).

[0047] [35] M.-Y. Tsai, O. Bierwagen, M.E. White, and J.S. Speck, J. Vac. Sci. Technol. A Vacuum, Surfaces, Film. 28, 354 (2010).

[0048] [36] S.J. Hao, M. Hetzl, F. Schuster, K. Danielewicz, A. Bergmaier, G. Dollinger, Q.L. Sai, C.T. Xia, T. Hoffmann, M. Wiesinger, S. Matich, W. Aigner, and M. Stutzmann, J. Appl. Phys. 125, (2019).

[0049] [37] P. Vogt, O. Brandt, H. Riechert, J. Lähnemann, and O. Bierwagen, Phys. Rev. Lett. 119, 6 (2017).

[0050] [38] M. Kracht, A. Karg, J. Schörmann, M. Weinhold, D. Zink, F. Michel, M. Rohnke, M. Schowalter, B. Gerken, A. Rosenauer, P.J. Klar, J. Janek, and M. Eickhoff, Phys. Rev. Appl. 8, 1 (2017).

[0051] [39] J. Wei, K. Kim, F. Liu, P. Wang, X. Zheng, Z. Chen, D. Wang, A. Imran, X. Rong, X. Yang, F. Xu, J. Yang, B. Shen, and X. Wang, J. Semicond. 40, (2019).

[0052] [40] Z. Cheng, M. Hanke, P. Vogt, O. Bierwagen, and A. Trampert, Appl. Phys. Lett. 111, 1 (2017).

[0053] [41] S. Ghose, M.S. Rahman, J.S. Rojas-Ramirez, M. Caro, R. Droopad, A. Arias, and N. Nedev, J. Vac. Sci. Technol. B, Nanotechnol. Microelectron. Mater. Process. Meas. Phenom. 34, 02L109 (2016).

[0054] [42] R. Schewski, G. Wagner, M. Baldini, D. Gogova, Z. Galazka, T. Schulz, T. Remmele, T. Markurt, H. Von Wenckstern, M. Grundmann, O. Bierwagen, P. Vogt, and M. Albrecht, Appl. Phys. Express 8, (2015).

[0055] [43] S. Nakagomi and Y. Kokubun, Phys. Status Solidi Basic Res. 253, 1217 (2016).

[0056] [44] F. Mezzadri, G. Calestani, F. Boschi, D. Delmonte, M. Bosi, and R. Fornari, Inorg. Chem. 55, 12079 (2016).

[0057] [45] V. Gottschalch, S. Merker, S. Blaurock, M. Kneiß, U. Teschner, M. Grundmann, and H. Krautscheid, J. Cryst. Growth 510, 76 (2019).

[0058] [46] M. Kneiß, A. Hassa, D. Splith, C. Sturm, H. Von Wenckstern, T. Schultz, N. Koch, M. Lorenz, and M. Grundmann, APL Mater. 7, (2019).

[0059] [47] H.C. Kang, Mater. Lett. 119, 123 (2014).

[0060] [48] S. Rafique, L. Han, A.T. Neal, S. Mou, M.J. Tadjer, R.H. French, and H. Zhao, Appl. Phys. Lett. 109, (2016).

[0061] [49] S. Rafique, L. Han, A.T. Neal, S. Mou, J. Boeckl, and H. Zhao, Phys. Status Solidi Appl. Mater. Sci. 215, 1 (2018).

[0062] [50] Y. Oshima, E.G. Víllora, and K. Shimamura, J. Cryst. Growth 410, 53 (2015).

[0063] [51] S. Shapenkov, O. Vyvenko, E. Ubyivovk, O. Medvedev, G. Varygin, A. Chikiryaka, A. Pechnikov, M. Scheglov, S. Stepanov, and V. Nikolaev, Phys. Status Solidi Appl. Mater. Sci. 1900892, 1 (2020).

[0064] [52] V.I. Nikolaev, A.I. Pechnikov, S.I. Stepanov, I.P. Nikitina, A.N. Smirnov, A. V. Chikiryaka, S.S. Sharofidinov, V.E. Bougrov, and A.E. Romanov, Mater. Sci. Semicond. Process. 47, 16 (2016).

[0065] [53] Y. Oshima, E.G. Víllora, and K. Shimamura, Appl. Phys. Express 8, 4 (2015).

[0066] [54] S. Nakagomi and Y. Kokubun, J. Cryst. Growth 349, 12 (2012).

[0067] [55] G. V. Chaplygin and S.A. Semiletov, Thin Solid Films 32, 321 (1976).

[0068] [56] H.P. Pinto, R.M. Nieminen, and S.D. Elliott, Phys. Rev. B 70, 125402 (2004).

[0069] [57] R. Fornari, M. Pavesi, V. Montedoro, D. Klimm, F. Mezzadri, I. Cora, B. Pécz, F. Boschi, A. Parisini, A. Baraldi, C. Ferrari, E. Gombia, and M. Bosi, Acta Mater. 140, 411 (2017).

[0070] [58] Z. Feng, A.F.M. Anhar Uddin Bhuiyan, M.R. Karim, and H. Zhao, Appl. Phys. Lett. 114, (2019).

[0071] [59] N. Ma, N. Tanen, A. Verma, Z. Guo, T. Luo, H. (Grace) Xing, and D. Jena, Appl. Phys. Lett. 109, 1 (2016).

[0072] [60] C. Merckling, M. El-Kazzi, G. Saint-Girons, G. Hollinger, L. Largeau, G. Patriarche, V. Favre-Nicolin, and O. Marty, J. Appl. Phys. 102, (2007).

[0073] [61] C. Merckling, M. El-Kazzi, G. Delhaye, M. Gendry, G. Saint-Girons, G. Hollinger, L. Largeau, and G. Patriarche, Appl. Phys. Lett. 89, 87 (2006).

[0074] [62] C. Merckling, M. El-Kazzi, V. Favre-Nicolin, M. Gendry, Y. Robach, G. Grenet, and G. Hollinger, Thin Solid Films 515, 6479 (2007).

[0075] [63] M. El Kazzi, M. Silly, F. Sirotti, C. Merckling, G. Saint-Girons, G. Grenet, and G. Holliger, Appl. Phys. Lett. 97, 1 (2010).

[0076] [64] M. Zinkevich and F. Aldinger, J. Am. Ceram. Soc. (2004).

[0077] [65] T. Oshima, Y. Kato, E. Magome, E. Kobayashi, and K. Takahashi, Jpn. J. Appl. Phys. 58, (2019).

[0078] [66] S. Nakagomi and Y. Kokubun, J. Cryst. Growth 479, 67 (2017).

[0079] [67] M. El Kazzi, C. Merckling, G. Grenet, G. Saint-Girons, M. Silly, F. Sirotti, and G. Hollinger, MRS Symp. Proc. 1155, 1 (2009).

[0080] [68] P.J. Cumpson and M.P. Seah, Surf. Interface Anal. 25, 430 (1997).

[0081] [69] T. Schoonjans, A. Brunetti, B. Golosio, M. Sanchez Del Rio, V.A. Solé, C. Ferrero, and L. Vincze, Spectrochim. Acta - Part B At. Spectrosc. 66, 776 (2011).

[0082] [70] P. Vogt and O. Bierwagen, Phys. Rev. Mater. 2, 1 (2018).

[0083] [71] T. Hahn, editor , International Tables for Crystallography. Vol. A., 5th ed. (Kluwer Academic Publishers, Dordrecht, 2002).

[0084] [72] G. Schmitz, P. Gassmann, and R. Franchy, J. Appl. Phys. 83, 2533 (1998).

[0085] [73] R. Yokoyama, K. Omote, K. Endo, and R. Matsuo, US 6,937,694 B2 (2005).

[0086] [74] M. Birkholz, Thin Film Analysis by X-Ray Scattering (John Wiley & Sons, 2006).

[0087] [75] M.-Y. Tsai, O. Bierwagen, M.E. White, and J.S. Speck, J. Vac. Sci. Technol. A Vacuum, Surfaces, Film. 28, 354 (2010).

[0088] [76] S. Ghose, M.S. Rahman, J.S. Rojas-Ramirez, M. Caro, R. Droopad, A. Arias, and N. Nedev, J. Vac. Sci. Technol. B, Nanotechnol. Microelectron. Mater. Process. Meas. Phenom. 34, 02L109 (2016).

[0089] [77] H.C. Kang, Mater. Lett. 119, 123 (2014).

[0090] [78] R. Schewski, K. Lion, A. Fiedler, C. Wouters, A. Popp, S. V. Levchenko, T. Schulz, M. Schmidbauer, S. Bin Anooz, R. Grüneberg, Z. Galazka, G. Wagner, K. Irmscher, M. Scheffler, C. Draxl, and M. Albrecht, APL Mater. 7, (2019).

[0091] [79] P. Mazzolini, A. Falkenstein, C. Wouters, R. Schewski, T. Markurt, Z. Galazka, M. Martin, M. Albrecht, and O. Bierwagen, APL Mater. 8, (2020).

[0092] [80] S. Hofmann, Auger- and X-Ray Photoelectron Spectroscopy in Materials Science (Springer Berlin Heidelberg, Berlin, Heidelberg, 2013).

[0093] [81] M.P. Seah, J. Electron Spectros. Relat. Phenomena 71, 191 (1995).

[0094] [82] Materials, A. S. for T. and. Standard practice for calibration of the electron binding-energy scale of an x-ray photoelectron spectrometer. E 2108-00 1–16 (2000) doi:10.1520/E2108-10.

[0095] [83] P.J. Cumpson and M.P. Seah, Surf. Interface Anal. 25, 430 (1997).

[0096] [84] J.H. Scofield, J. Electron Spectros. Relat. Phenomena 8, 129 (1976).

[0097] [85] Y. Wei, X. Hu, Y. Liang, D.C. Jordan, B. Craigo, R. Droopad, Z. Yu, A. Demkov, J.L. Edwards, and W.J. Ooms, J. Vac. Sci. Technol. B Microelectron. Nanom. Struct. 20, 1402 (2002).

[0098] [86] C. Merckling, M. El-Kazzi, G. Saint-Girons, G. Hollinger, L. Largeau, G. Patriarche, V. Favre-Nicolin, and O. Marty, J. Appl. Phys. 102, (2007).

[0099] [87] Villars, P. & Cenzual, K. Pearson's Crystal Data: Crystal Structure Database for Inorganic Compounds (on DVD), Release 2017/18, ASM International®. (2017).

[0100] [88] C. Merckling, M. El-Kazzi, V. Favre-Nicolin, M. Gendry, Y. Robach, G. Grenet, and G. Hollinger, Thin Solid Films 515, 6479 (2007).

[0101] [89] M. Björck and G. Andersson, J. Appl. Crystallogr. 40, 1174 (2007).

[0102] [90] C. Merckling, M. El-Kazzi, G. Delhaye, M. Gendry, G. Saint-Girons, G. Hollinger, L. Largeau, and G. Patriarche, Appl. Phys. Lett. 89, 87 (2006).

[0103] [91] M. El Kazzi, M. Silly, F. Sirotti, C. Merckling, G. Saint-Girons, G. Grenet, and G. Holliger, Appl. Phys. Lett. 97, 1 (2010).

[0104] [92] P. Vogt and O. Bierwagen, Phys. Rev. Mater. 2, 1 (2018).

[0105] [93] H. Lipson, J.I. Langford, and H.-C. Hu., in Int. Tables Crystallogr. (2006). Vol. C, edited by E. Prince, 1st ed. (International Union of Crystallography (IUCr), 2006), pp. 596–598.

[0106] [94] B.B. He, in Int. Tables Crystallogr. (2019). Vol. H, edited by C.J. Gilmore, J.A. Kaduk, and H. Schenk (International Union of Crystallography (IUCr), 2019), pp. 130–131.

[0107] [95] J. Als-Nielsen and D. McMorrow, Elements of Modern X-Ray Physics (John Wiley & Sons, 2011).

[0108] [96] K. Momma and F. Izumi, J. Appl. Crystallogr. 44, 1272 (2011).

[0109] [97] J.H. Hubbell and S.M. Seltzer, NIST Standard Reference Database 126: Tables of X-Ray Mass Attenuation Coefficients and Mass Energy-Absorption Coefficients from 1 KeV to 20 MeV for Elements Z = 1 to 92 and 48 Additional Substances of Dosimetric Interest (National Institute of Standards and Technology, 2004).

[0110] [98] J. Wei, K. Kim, F. Liu, P. Wang, X. Zheng, Z. Chen, D. Wang, A. Imran, X. Rong, X. Yang, F. Xu, J. Yang, B. Shen, and X. Wang, J. Semicond. 40, (2019).

[0111] [99] G. Kresse and J. Furthmüller, Phys. Rev. B - Condens. Matter Mater. Phys. 54, 11169 (1996).

[0112] [100] P.E. Blöchl, Phys. Rev. B 50, 17953 (1994).

[0113] [101] V.M. Bermudez, Chem. Phys. 323, 193 (2006).

[0114] [102] T. Zacherle, P.C. Schmidt, and M. Martin, Phys. Rev. B - Condens. Matter Mater. Phys. (2013).

[0115] [103] W. Sun and G. Ceder, Surf. Sci. 617, 53 (2013).

[0116] [104] J.R. Rumble, editor , in CRC Handb. Chem. Phys., 101st ed. (CRC Press/Taylor & Francis, Boca Raton, FL, 2020).

[0117] [105] R. Schewski, K. Lion, A. Fiedler, C. Wouters, A. Popp, S. V. Levchenko, T. Schulz, M. Schmidbauer, S. Bin Anooz, R. Grüneberg, Z. Galazka, G. Wagner, K. Irmscher, M. Scheffler, C. Draxl, and M. Albrecht, APL Mater. 7, (2019).

[0118] [106] S.J. Pearton, J. Yang, P.H. Cary, F. Ren, J. Kim, M.J. Tadjer, and M.A. Mastro, Appl. Phys. Rev. 5, 011301 (2018).

[0119] [107] B. Bayraktaroglu, Assessment of Gallium Oxide Technology (Wright-Patterson Air Force Base, OH, 2017).

[0120] [108] H. Murakami, M. Higashiwaki, Y. Kumagai, T. Masui, K. Sasaki, A. Kuramata, S. Yamakoshi, and A. Koukitu, Semicond. Sci. Technol. 31, 034001 (2016).

[0121] [109] M. Higashiwaki, K. Sasaki, A. Kuramata, T. Masui, and S. Yamakoshi, Phys. Status Solidi Appl. Mater. Sci. 211, 21 (2014).

[0122] [110] O. Hilt, E.B. Treidel, M. Wolf, C. Kuring, K. Tetzner, H. Yazdani, A. Wentzel, and J. Würfl, IET Power Electron. 12, 3919 (2019).

[0123] [111] Nov. Cryst. Technol. Inc. (2021).

[0124] [112] S.A. Kukushkin, V.I. Nikolaev, A. V. Osipov, E. V. Osipova, A.I. Pechnikov, and N.A. Feoktistov, Phys. Solid State 58, 1876 (2016).

[0125] [113] S. Rafique, L. Han, C.A. Zorman, and H. Zhao, Cryst. Growth Des. 16, 511 (2016).

[0126] [114] S. Rafique, L. Han, J. Lee, X.-Q. Zheng, C.A. Zorman, P.X.-L. Feng, and H. Zhao, J. Vac. Sci. Technol. B, Nanotechnol. Microelectron. Mater. Process. Meas. Phenom. 35, 011208 (2017).

[0127] [115] Y. Berencén, Y. Xie, M. Wang, S. Prucnal, L. Rebohle, and S. Zhou, Semicond. Sci. Technol. 34, 035001 (2019).

[0128] [116] A. V. Osipov, A.S. Grashchenko, S.A. Kukushkin, V.I. Nikolaev, E. V. Osipova, A.I. Pechnikov, and I.P. Soshnikov, Contin. Mech. Thermodyn. 30, 1059 (2018).

[0129] [117] A.S. Grashchenko, S.A. Kukushkin, V.I. Nikolaev, A. V. Osipov, E. V. Osipova, and I.P. Soshnikov, Phys. Solid State 60, 852 (2018).

[0130] [118] D.H. Kim, S.H. Yoo, T.M. Chung, K.S. An, H.S. Yoo, and Y. Kim, Bull. Korean Chem. Soc. 23, 225 (2002).

[0131] [119] H.W. Kim, N.H. Kim, and C. Lee, Br. Ceram. Trans. 103, 187 (2004).

[0132] [120] W. Xu, X. Wang, Y. Wang, T. You, X. Ou, G. Han, H. Hu, S. Zhang, F. Mu, T. Suga, Y. Zhang, and Y. Hao, in Tech. Dig. - Int. Electron Devices Meet. IEDM (2019), pp. 274–277.

[0133] [121] Y.B. Wang, W.H. Xu, T.G. You, F.W. Mu, H.D. Hu, Y. Liu, H. Huang, T. Suga, G.Q. Han, X. Ou, and Y. Hao, Sci. China Physics, Mech. Astron. 63, 277311 (2020).

[0134] [122] D. Wang, L. He, Y. Le, X. Feng, C. Luan, H. Xiao, and J. Ma, Ceram. Int. 46, 4568 (2020).

[0135] [123] M. Kneiß, A. Hassa, D. Splith, C. Sturm, H. Von Wenckstern, T. Schultz, N. Koch, M. Lorenz, and M. Grundmann, APL Mater. 7, 022516 (2019).

[0136] [124] H. Nishinaka, H. Komai, D. Tahara, Y. Arata, and M. Yoshimoto, Jpn. J. Appl. Phys. 57, 115601 (2018).

[0137] [125] T. Hadamek, A.B. Posadas, F. Al-Quaiti, D.J. Smith, M.R. McCartney, and A.A. Demkov, AIP Adv. 11, 045209 (2021).

[0138] [126] K.J. Hubbard and D.G. Schlom, J. Mater. Res. 11, 2757 (1996).

[0139] [127] S. Rafique, L. Han, A.T. Neal, S. Mou, J. Boeckl, and H. Zhao, Phys. Status Solidi Appl. Mater. Sci. 215, 1700467 (2018).

[0140] [128] Y. Zhang, F. Alema, A. Mauze, O.S. Koksaldi, R. Miller, A. Osinsky, and J.S. Speck, APL Mater. 7, 022506 (2019).

[0141] [129] P. Vogt, F.V.E. Hensling, K. Azizie, C.S. Chang, D. Turner, J. Park, J.P. McCandless, H. Paik, B.J. Bocklund, G. Hoffman, and others, Appl. Phys. Lett. Mater. 9, 031101 (2020).

[0142] [130] R.A. McKee, F.J. Walker, and M.F. Chisholm, Phys. Rev. Lett. 81, 3014 (1998).

[0143] [131] D. Wang, X. Ma, H. Xiao, Y. Le, and J. Ma, Mater. Sci. Semicond. Process. 128, 105749 (2021).

[0144] [132] T. Shimizu, N. Gotoh, N. Shinozaki, and H. Okushi, Appl. Surf. Sci. 117–118, 400 (1997).

[0145] [133] P. Vogt and O. Bierwagen, Appl. Phys. Lett. 108, 072101 (2016).

[0146] [134] P. Villars and K. Cenzual, "Pearson's crystal data-crystal structure database for inorganic compounds" (on DVD), ASM International (Materials Park, Ohio, USA, 2018).

[0147] [135] R.C. Hatch, K.D. Fredrickson, M. Choi, C. Lin, H. Seo, A.B. Posadas, and A.A. Demkov, J. Appl. Phys. 114, 103710 (2013).

[0148] [136] V.M. Bermudez, Chem. Phys. 323, 193 (2006).

[0149] [137] R. Schewski, K. Lion, A. Fiedler, C. Wouters, A. Popp, S. V. Levchenko, T. Schulz, M. Schmidbauer, S. Bin Anooz, R. Grüneberg, Z. Galazka, G. Wagner, K. Irmscher, M. Scheffler, C. Draxl, and M. Albrecht, APL Mater. 7, 022515 (2019).

[0150] [138] M. Grundmann, T. Böntgen, and M. Lorenz, Phys. Rev. Lett. 105, 146102 (2010).

[0151] [139] M. Grundmann, Phys. Status Solidi Basic Res. 248, 805 (2011).

[0152] [140] M. Grundmann, T. Böntgen, and M. Lorenz, Phys. Rev. Lett. 105, 146102 (2010).

[0153] [141] M. Grundmann, Phys. Status Solidi Basic Res. 248, 805 (2011).

[0154] [142] S. J. Pearton, J. Yang, P.H. Cary, F. Ren, J. Kim, M.J. Tadjer, and M.A. Mastro, Appl. Phys. Rev. 5, 011301 (2018).

[0155] [143] P.G. Staib, J. Vac. Sci. Technol. B, Nanotechnol. Microelectron. Mater. Process. Meas. Phenom. 29, 03C125 (2011).

[0156] [144] P.H. Carey, F. Ren, D.C. Hays, B.P. Gila, S.J. Pearton, S. Jang, and A. Kuramata, Jpn. J. Appl. Phys. 56, 071101 (2017).

[0157] [145] M. Hattori, T. Oshima, R. Wakabayashi, K. Yoshimatsu, K. Sasaki, T. Masui, A. Kuramata, S. Yamakoshi, K. Horiba, H. Kumigashira, and A. Ohtomo, Jpn. J. Appl. Phys. 55, 1202B6 (2016).

[0158] [146] G. Kresse and J. Furthmüller, Phys. Rev. B - Condens. Matter Mater. Phys. 54, 11169 (1996).

[0159] [147] P.E. Blöchl, Phys. Rev. B 50, 17953 (1994).

[0160] [148] V.M. Bermudez, Chem. Phys. 323, 193 (2006).

[0161] [149] T. Zacherle, P.C. Schmidt, and M. Martin, Phys. Rev. B - Condens. Matter Mater. Phys. (2013).

[0162] [150] W. Sun and G. Ceder, Surf. Sci. 617, 53 (2013).

[0163] [151] J.R. Rumble, editor , in CRC Handb. Chem. Phys., 101st ed. (CRC Press/Taylor & Francis, Boca Raton, FL, 2020).

[0164] [152] K. Eisenbeiser, J. M. Finder, Z. Yu, J. Ramdani, J. A. Curless, J. A. Hallmark, R. Droopad, W. J. Ooms, L. Salem, S. Bradshaw, and C. D. Overgaard, Appl. Phys. Lett. 76, 1324 (2000).

[0165] [153] Z. Yu, J. Ramdani, J. A. Curless, J. M. Finder, C. D. Overgaard, R. Droopad, K. W. Eisenbeiser, J. A. Hallmark, W. J. Ooms, J. R. Conner, and V. S. Kaushik, J. Vac. Sci. Technol. B Microelectron. Nanom. Struct. 18, 1653 (2002).

[0166] In this disclosure, references to the above sources, which are numbered in single bracket "[ ]", are made using the corresponding number in the single brackets, in the same manner as those sources are listed above. Each of the above listed references, along with other patents, patent applications, and non-patent literature not specifically listed above, are incorporated herein by reference in their entireties.

SUMMARY

[0167] In some embodiments, β-Ga_2O_3 was deposited in thin film form by plasma-assisted molecular beam epitaxy at 670 °C and 630 °C onto a γ-Al_2O_3 (111) buffer layer grown at 840 °C by e-beam evaporation on a clean Si (001) surface. The β-Ga_2O_3 film was 66 nm thick, stoichiometric, and strongly textured, as determined by x-ray reflectivity, x-ray photoelectron spectroscopy, reflection high-energy electron diffraction, x-ray diffraction and transmission electron microscopy, with three basal growth planes $(\bar{2}01)$, (101) and {310}, including one twin variant $\{\overline{31}0\}$. The observed basal growth planes correspond to the close-packing planes of the distorted face-centered cubic oxygen sublattice of β-Ga_2O_3. Local structural ordering can be thought to occur due to a continuation of the oxygen sublattice from the γ-alumina buffer layer into the β-gallia film. Each β-Ga_2O_3 growth plane further gives rise to 12 symmetry-derived rotational in-plane variants, resulting in a total of 48 domain variants. Atomistic models of possible gallia-alumina interfaces are presented.

[0168] In other embodiments, thin Ga_2O_3 films were deposited by plasma-assisted molecular beam epitaxy on $SrTiO_3$ (001) and $SrTiO_3$-buffered Si (001) substrates. Examination using reflection-high-energy electron diffraction, x-ray diffraction and transmission electron microscopy shows a consistent picture of (100)- and $(\bar{1}12)$-oriented β-Ga_2O_3 grains. The structural alignments are β-Ga_2O_3 [010] ‖ STO ⟨110⟩ and β-Ga_2O_3 [021] ‖ STO ⟨100⟩ respectively, each with four in-plane rotational domain variants. Successful integration of epitaxial β-Ga_2O_3 with Si could enable major opportunities for monolithically integrated Ga_2O_3 technology by serving as a high-quality seed layer for further epitaxial growth.

[0169] The observation of relatively large domains with average lateral extensions of more than 100 nm for γ-Al_2O_3 (111) on Si (001) was reported [60]. This result motivates the possible use of such a bi-domain γ-Al_2O_3 (111) layer as a buffer layer to grow Ga_2O_3 on Si. Al_2O_3 is further interesting as a buffer layer due to the isostructural polymorphs shared between Al_2O_3 and Ga_2O_3 with similar lattice constants [64], which is a useful prerequisite for successful epitaxy. In the defective spinel γ-Al_2O_3 crystal structure (space group $Fd\bar{3}m$, 227), the oxygen ions form an fcc framework with the close-packed layers stacked along ⟨111⟩. As in the case of c-plane α-Al_2O_3, previously used for the hetero-epitaxy of Ga_2O_3, the (111) plane of γ-Al_2O_3 is composed of equilateral triangles of oxygen ions [56]. Therefore, we expect to observe similar epitaxial relationships between Ga_2O_3 and γ-Al_2O_3 as have been observed with Ga_2O_3 and α-Al_2O_3. An elevated growth temperature and the method of PAMBE, without the use of a metal catalyst [37, 38], makes β-Ga_2O_3 the most likely polymorph to form, although the possible occurrence of isostructural γ-Ga_2O_3 (111) should be kept in mind. γ-Ga_2O_3 in (001)-orientation has been epitaxially stabilized on spinel $MgAl_2O_4$ (001) substrates [65], and on MgO (001) [66]. Here we report the integration of strongly textured β-Ga_2O_3 onto e-beam evaporated γ-Al_2O_3 (111) on Si (001) by PAMBE. We characterize the polymorph and its texture by reflection high-energy electron diffraction

(RHEED), x-ray diffraction (XRD), x-ray reflectivity (XRR) and transmission electron diffraction (TEM) and present a model for the local structural order in terms of a structural interface model of the oxygen sublattices of β-Ga_2O_3 and γ-Al_2O_3. Stoichiometries were confirmed by x-ray photoelectron spectroscopy (XPS).

[0170] A first aspect of the disclosure provides a wafer. The wafer may include a silicon substrate; a buffer layer including a thin film of epitaxial strontium titanate (STO) formed on the silicon substrate; and a thin film including a gallium oxide formed on the buffer layer. In a first embodiment of the first aspect of the disclosure, the buffer layer may be, or may include: a first layer including STO formed on the silicon substrate; and a second layer including an aluminum oxide formed on the first layer, where the thin film including the gallium oxide is formed on the second layer. In one example of the first embodiment of the first aspect of the disclosure, the aluminum oxide may be, or may include, gamma-aluminum oxide (γ-Al_2O_3). In another example of the first embodiment of the first aspect of the disclosure, the aluminum oxide may be, or may include, an aluminum-gallium alloy oxide.

[0171] In any of the above discussed embodiments or examples of the first aspect of the disclosure, the thin film including the gallium oxide may be, at least in part, integrated hetero-epitaxially onto the silicon substrate via the buffer layer. In any of the above discussed embodiments or examples of the first aspect of the disclosure, the wafer may include one or more additional layers of a gallium oxide formed on the thin film including the gallium oxide. In one example where the wafer includes the one or more additional layers of a gallium oxide formed on the thin film including the gallium oxide, the one or more additional layers of the gallium oxide are grown using chemical vapor deposition. In another example where the wafer includes the one or more additional layers of a gallium oxide formed on the thin film including the gallium oxide, at least a first layer of the one or more additional layers of the gallium oxide may be, or may include, a layer of an aluminum-gallium alloy oxide formed on the thin film including the gallium oxide, where at least a second layer of the one or more additional layers of the gallium oxide is formed on the layer of the aluminum-gallium alloy oxide.

[0172] In any of the above discussed embodiments or examples of the first aspect of the disclosure, the wafer may include at least one of: a microelectronic device, an optoelectronic device, a micro-electromechanical system (MEMS), a field-effect transistor, a sensor, and a semiconductor device, formed in or on: the thin film including the gallium oxide, or the one or more additional layers of the gallium oxide. In any of the above discussed embodiments or examples of the first aspect of the disclosure, the wafer may include one or more components of a power electronics device operably coupled to: the thin film including the gallium oxide, or the one or more additional layers of gallium oxide.

[0173] In one example where the wafer includes the one or more additional layers of a gallium oxide formed on the thin film including the gallium oxide, at least a portion of the one or more additional layers of gallium oxide may be at least one of: etched, polished, and annealed. In another example where the wafer includes the one or more additional layers of a gallium oxide formed on the thin film including

the gallium oxide, at least a portion of the one or more layers of gallium oxide may be, or may include, bulk-like crystals of gallium oxide.

[0174] In any of the above discussed embodiments or examples of the first aspect of the disclosure, the silicon substrate may be, or may include, silicon (001). In any of the above discussed embodiments or examples of the first aspect of the disclosure, at least a portion of the thin film including the gallium oxide is gamma-gallium oxide (γ-Ga_2O_3). In any of the above discussed embodiments or examples of the first aspect of the disclosure, at least a portion of the thin film including the gallium oxide is beta-gallium oxide (β-Ga_2O_3).

[0175] A second aspect of the disclosure provides a power electronics device. The power electronics device may include the wafer according to any of the above discussed embodiments or examples of the first aspect of the disclosure. The power electronics device may include: means for receiving a first electric current coupled to a first portion of the wafer; and means for transmitting a second electric current coupled to a second portion of the wafer. In one example of the second aspect of the disclosure, the power electronics device may include at least one of structural and functional components of: a rectifier, or a transistor.

[0176] A third aspect of the disclosure provides a method. The method may be, or may include, a method for manufacturing a wafer or a power electronics device according to any of the above discussed embodiments or examples of the first and/or second aspect(s) of the disclosure. The method may include forming, on a silicon substrate, a buffer layer including a thin film of epitaxial strontium titanate (STO); and forming a thin film including a gallium oxide on the buffer layer. In a first embodiment of the third aspect of the disclosure, forming the buffer layer may include: forming a first layer including STO on the silicon substrate; and forming a second layer including an aluminum oxide on the first layer, where forming the thin film including the gallium oxide includes forming the thin film including the gallium oxide on the second layer. In one example of the first embodiment of the third aspect of the disclosure, forming the second layer includes forming the second layer including gamma-aluminum oxide (γ-Al_2O_3).

[0177] In any of the above discussed embodiments or examples of the third aspect of the disclosure, forming the thin film including the gallium oxide may include hetero-epitaxially integrating the thin film including the gallium oxide onto the silicon substrate via the buffer layer. In any of the above discussed embodiments or examples of the third aspect of the disclosure, the method may include forming one or more additional layers of gallium oxide on the thin film including the gallium oxide. In one example where the method includes forming the one or more additional layers of gallium oxide on the thin film including the gallium oxide, forming the one or more additional layers of gallium oxide may include growing the one or more additional layers of gallium oxide on the thin film including the gallium oxide using a process including chemical vapor deposition. In another example where the method includes forming the one or more additional layers of gallium oxide on the thin film including the gallium oxide, forming the one or more additional layers of gallium oxide may include: forming at least a first layer of the one or more additional layers of gallium oxide as a layer of an aluminum-gallium alloy oxide formed

on the thin film including the gallium oxide; and forming at least a second layer of the one or more additional layers of gallium oxide on the layer of the aluminum-gallium alloy oxide.

[0178] In any of the above discussed embodiments or examples of the third aspect of the disclosure, the method may include forming at least one of: a microelectronic device, an optoelectronic device, a micro-electromechanical system (MEMS), a field-effect transistor, a sensor, and a semiconductor device, in or on: the thin film including the gallium oxide, or the one or more additional layers of gallium oxide. In any of the above discussed embodiments or examples of the third aspect of the disclosure, the method may include operably coupling one or more components of a power electronics device to: the thin film including the gallium oxide, or the one or more additional layers of gallium oxide.

[0179] In one example where the method includes forming the one or more additional layers of gallium oxide on the thin film including the gallium oxide, the method may include at least one of: etching, polishing, and annealing, at least a portion of the one or more additional layers of gallium oxide. In another example where the method includes forming the one or more additional layers of gallium oxide on the thin film including the gallium oxide, forming the one or more additional layers of gallium oxide may include forming at least a portion of the one or more layers of gallium oxide as bulk-like crystals of gallium oxide.

[0180] In any of the above discussed embodiments or examples of the third aspect of the disclosure, forming the buffer layer may include forming the buffer layer on a silicon (001) substrate. In any of the above discussed embodiments or examples of the third aspect of the disclosure, forming the thin film including the gallium oxide may include forming at least a portion of the thin film including the gallium oxide as gamma-gallium oxide (γ-Ga_2O_3). In any of the above discussed embodiments or examples of the third aspect of the disclosure, forming the thin film including the gallium oxide includes forming at least a portion of the thin film including the gallium oxide as beta-gallium oxide (β-Ga_2O_3).

[0181] A fourth aspect of the disclosure provides a wafer. The wafer may include a silicon substrate; a buffer layer formed on the silicon substrate, wherein the buffer layer includes an epitaxial thin film of an aluminum, or rare earth, oxide; and a thin film including a gallium oxide formed on the buffer layer. In a first embodiment of the fourth aspect of the disclosure, the buffer layer may be, or may include, the epitaxial thin film of aluminum oxide. In one example of the first embodiment of the fourth aspect, the aluminum oxide may be, or may include, gamma-aluminum oxide (γ-Al_2O_3). In another example of the first embodiment of the fourth aspect, the aluminum oxide may be, or may include, an aluminum-gallium oxide alloy. In yet another example of the first embodiment of the fourth aspect, the buffer layer may be, or may include: a first layer including the aluminum oxide formed on the silicon substrate; and at least a second layer of an aluminum-gallium alloy oxide formed on the first layer, where the thin film including the gallium oxide is formed on the at least a second layer.

[0182] In a second embodiment of the fourth aspect of the disclosure, the buffer layer may be, or may include, the epitaxial thin film of a rare earth oxide. In one example of the second embodiment of the fourth aspect, the rare earth oxide may be, or may include, gadolinium oxide (Gd_2O_3) and/or erbium

oxide (Er_2O_3). In another example of the second embodiment of the fourth aspect, the rare earth oxide may be, or may include, a gallium-rare earth alloy oxide. In yet another example of the second embodiment of the fourth aspect, the buffer layer may be, or may include: a first layer including the rare earth oxide formed on the silicon substrate; and at least a second layer of a gallium-rare earth alloy oxide, where the thin film including the gallium oxide is formed on the at least a second layer.

[0183] In any of the above discussed embodiments or examples of the fourth aspect of the disclosure, the buffer layer may be, at least in part, compositionally graded. In any of the above discussed embodiments or examples of the fourth aspect of the disclosure, the thin film including the gallium oxide may be, at least in part, integrated hetero-epitaxially onto the silicon substrate via the buffer layer. In any of the above discussed embodiments or examples of the fourth aspect of the disclosure, the wafer may include one or more additional layers of a gallium oxide formed on the thin film including the gallium oxide.

[0184] In one example where the wafer includes the one or more additional layers of a gallium oxide formed on the thin film including the gallium oxide, the one or more additional layers of the gallium oxide may be grown using chemical vapor deposition. In another example where the wafer includes the one or more additional layers of a gallium oxide formed on the thin film including the gallium oxide, the buffer layer may include an epitaxial film of aluminum oxide, where at least a first layer of the one or more additional layers of the gallium oxide may include a layer of an aluminum-gallium alloy oxide formed on the thin film including the gallium oxide, and where at least a second layer of the one or more additional layers of the gallium oxide may be formed on the layer of the aluminum-gallium alloy oxide. In yet another example where the wafer includes the one or more additional layers of a gallium oxide formed on the thin film including the gallium oxide, the buffer layer may include an epitaxial film of a rare earth oxide, where at least a first layer of the one or more additional layers of the gallium oxide may include a layer of a rare earth-gallium alloy oxide formed on the thin film including the gallium oxide, and where at least a second layer of the one or more additional layers of the gallium oxide may be formed on the layer of the rare earth-gallium alloy oxide.

[0185] In any of the above discussed embodiments or examples of the fourth aspect of the disclosure, the wafer may include at least one of: a microelectronic device, an optoelectronic device, a micro-electromechanical system (MEMS), a field-effect transistor, a sensor, and a semiconductor device, formed in or on: the thin film including the gallium oxide, or the one or more additional layers of the gallium oxide. In any of the above discussed embodiments or examples of the fourth aspect of the disclosure, the wafer may include one or more components of a power electronics device operably coupled to: the thin film including the gallium oxide, or the one or more additional layers of gallium oxide.

[0186] In one example where the wafer includes the one or more additional layers of a gallium oxide formed on the thin film including the gallium oxide, at least a portion of the one or more additional layers of gallium oxide may be at least one of: etched, polished, and annealed. In another example where the

wafer includes the one or more additional layers of a gallium oxide formed on the thin film including the gallium oxide, at least a portion of the one or more layers of gallium oxide includes bulk-like crystals of gallium oxide.

[0187] In any of the above discussed embodiments or examples of the fourth aspect of the disclosure, the silicon substrate includes silicon (001). In any of the above discussed embodiments or examples of the fourth aspect of the disclosure, at least a portion of the thin film including the gallium oxide is gamma-gallium oxide (γ-Ga_2O_3). In any of the above discussed embodiments or examples of the fourth aspect of the disclosure, at least a portion of the thin film including the gallium oxide is beta-gallium oxide (β-Ga_2O_3).

[0188] A fifth aspect of the disclosure provides a power electronic device. The power electronics device may include the wafer according to any of the above discussed embodiments or examples of the fourth aspect of the disclosure. The power electronics device may include: means for receiving a first electric current coupled to a first portion of the wafer; and means for transmitting a second electric current coupled to a second portion of the wafer. In one example of the second aspect of the disclosure, the power electronics device may include at least one of structural and functional components of: a rectifier, or a transistor.

[0189] A sixth aspect of the disclosure provides a method. The method may be, or may include, a method for manufacturing a wafer or a power electronics device according to any of the above discussed embodiments or examples of the fourth and/or fifth aspect(s) of the disclosure. The method may include forming, on a silicon substrate, a buffer layer including an epitaxial thin film of an aluminum, or rare earth, oxide; and forming a thin film including a gallium oxide on the buffer layer. In a first embodiment of the sixth aspect of the disclosure, forming the buffer layer may include forming the buffer layer including the epitaxial thin film of aluminum oxide.

[0190] In one example of the first embodiment of the sixth aspect, the aluminum oxide may be, or may include, gamma-aluminum oxide (γ-Al2O3). In another example of the first embodiment of the sixth aspect, the aluminum oxide may be, or may include, an aluminum-gallium oxide alloy. In yet another example of the first embodiment of the sixth aspect, forming the buffer layer may include: forming a first layer including the aluminum oxide on the silicon substrate; and forming at least a second layer of an aluminum-gallium alloy oxide on the first layer, where forming the thin film including the gallium oxide includes forming the thin film including the gallium oxide on the at least a second layer.

[0191] In a second embodiment of the sixth aspect, forming the buffer layer includes forming the buffer layer including the epitaxial thin film of the rare earth oxide. In one example of the second embodiment of the sixth aspect, the rare earth oxide may be, or may include, gadolinium oxide (Gd2O3) and/or erbium oxide (Er2O3). In another example of the second embodiment of the sixth aspect, the rare earth oxide may be, or may include, a gallium-rare earth alloy oxide. In yet another example of the second embodiment of the sixth aspect, forming the buffer layer further may include: forming a first layer including the rare earth oxide on the silicon substrate; and forming at least a second layer of a gallium-

rare earth alloy oxide on the first layer, where forming the thin film including the gallium oxide may include forming the thin film including the gallium oxide on the at least a second layer.

[0192] In any of the above discussed embodiments or examples of the sixth aspect of the disclosure, forming the buffer layer may include forming the buffer layer , at least in part, as a compositionally graded buffer layer. In any of the above discussed embodiments or examples of the sixth aspect of the disclosure, forming the thin film including the gallium oxide may include hetero-epitaxially integrating the thin film including the gallium oxide onto the silicon substrate via the buffer layer. In any of the above discussed embodiments or examples of the sixth aspect of the disclosure, the method may include forming one or more additional layers of gallium oxide on the thin film including the gallium oxide.

[0193] In one example where the method of the sixth aspect includes forming the one or more additional layers of gallium oxide on the thin film including the gallium oxide, forming the one or more additional layers of gallium oxide may include growing the one or more additional layers of gallium oxide on the thin film including the gallium oxide using a process including chemical vapor deposition. In another example where the method includes forming the one or more additional layers of gallium oxide on the thin film including the gallium oxide, the buffer layer may be, or may include, the epitaxial film of aluminum oxide, where forming the one or more additional layers of gallium oxide on the thin film including the gallium oxide may include: first forming at least one layer including an aluminum-gallium alloy oxide on the thin film including the gallium oxide; and second forming at least one additional layer including the one or more additional layers of gallium oxide on the at least one layer. In yet another example where the method includes forming the one or more additional layers of gallium oxide on the thin film including the gallium oxide, the buffer layer may include the epitaxial film of the rare earth oxide, wherein forming the one or more additional layers of gallium oxide on the thin film including the gallium oxide may include: first forming at least one layer including a rare earth-gallium alloy oxide on the thin film including the gallium oxide; and second forming at least one additional layer including the one or more additional layers of gallium oxide on the at least one layer.

[0194] In any of the above discussed embodiments or examples of the sixth aspect of the disclosure, the method may include forming at least one of: a microelectronic device, an optoelectronic device, a micro-electromechanical system (MEMS), a field-effect transistor, a sensor, and a semiconductor device, formed in or on: the thin film including the gallium oxide, or the one or more additional layers of the gallium oxide. In any of the above discussed embodiments or examples of the sixth aspect of the disclosure, the method may include operably coupling one or more components of a power electronics device to: the thin film including the gallium oxide, or the one or more additional layers of gallium oxide.

[0195] In one example where the method of the sixth aspect includes forming the one or more additional layers of gallium oxide on the thin film including the gallium oxide, the method may include at least one of: etching, polishing, and annealing, at least a portion of the one or more additional layers of gallium oxide. In one example where the method of the sixth aspect includes forming the one or more additional layers of gallium oxide on the thin film including the gallium oxide, forming the one or more additional

layers of gallium oxide may include forming at least a portion of the one or more layers of gallium oxide as bulk-like crystals of gallium oxide.

[0196] In any of the above discussed embodiments or examples of the sixth aspect of the disclosure, forming the buffer layer includes forming the buffer layer on a silicon (001) substrate. In any of the above discussed embodiments or examples of the sixth aspect of the disclosure, forming the thin film including the gallium oxide includes forming at least a portion of the thin film including the gallium oxide as gamma-gallium oxide (γ-Ga_2O_3). In any of the above discussed embodiments or examples of the sixth aspect of the disclosure, forming the thin film including the gallium oxide includes forming at least a portion of the thin film including the gallium oxide as beta-gallium oxide (β- Ga_2O_3).

BRIEF DESCRIPTION OF THE DRAWINGS

[0197] The patent or application file contains at least one drawing executed in color. Copies of this patent or patent application publication with color drawing(s) will be provided by the Office upon request and payment of the necessary fee.

[0198] Embodiments of the present technology will be described and explained through the use of the accompanying drawings.

[0199] Figures 1A-1D depict reflection high-energy electron diffraction (RHEED) patterns at different stages of growth.

[0200] Figure 2 depicts a symmetric $\theta/2\theta$ coupled x-ray diffraction (XRD) scan with sample aligned to Si (004).

[0201] Figure 3 illustrates the relationship between the *conventional* monoclinic unit cell with lattice vectors *a*, *b*, *c*, and the distorted oxygen face-centered cubic (fcc) sublattice of β-Ga_2O_3.

[0202] Figure 4 illustrates the close-packing planes of the distorted oxygen sublattice of β-Ga_2O_3.

[0203] Figures 5A-5C illustrate representative interface models between the γ-Al_2O_3 (111) substrate and locally epitaxial β-Ga_2O_3 domain variants.

[0204] Figure 6 is a pole figure at $2\theta = 31.7°$ of (002) and $(20\bar{2})$ Bragg reflections of β-Ga_2O_3.

[0205] Figure 7A is a bright-field STEM image showing cross-section of gallium oxide film grown on Si (001) substrate with thin alumina buffer layer.

[0206] Figure 7B is a high-resolution TEM image showing region of gallium oxide film adjacent to alumina buffer layer.

[0207] Figure 8 is a plot demonstrating the sample heating mechanism in the MBE consists of a silicon carbide heater that is placed above the sample backside and heats the sample backside and sample holder radiatively.

[0208] Figure 9 is a plot depicting alumina rate via e-beam evaporation measured by QCM at an e-gun voltage of 7.75 kV and an emission current of 50 mA resulting in an oxygen partial pressure of ~10^{-7} torr without supplying additional oxygen in the form of molecular O_2 gas.

[0209] Figures 10A-10D depict XPS data taken *in situ* after growth of e-beam evaporated alumina on clean Si (001) with a VG Scienta spectrometer with monochromatic Al-Kα and R3000 hemispherical analyzer at 200 eV pass energy.

[0210] Figure 11 depicts plots of XRR data and GenX [89] simulation of Al_2O_3/Si.

[0211] Figure 12 depicts results of in-plane XRD coupled $2\theta_\chi/\varphi$ scan of 5 nm thick Al_2O_3/Si conducted on the Rigaku Ultima IV with in-plane arm, using parallel beam, Ni Cu-Kβ filter and 0.5° vertical Soller slits on source and detector sides.

[0212] Figure 13 depicts the θ/2θ out-of-plane diffraction pattern of the 5 nm film of alumina on Si (001).

[0213] Figure 14A and 14B are top-views of the oxygen-terminated surface of γ-Al_2O_3 (111).

[0214] Figure 14C is a side-view of the oxygen-terminated surface of γ-Al_2O_3 (111).

[0215] Figure 15A depicts a plot of gallia rate as measured by quartz crystal microbalance (QCM) at $2x10^{-5}$ torr molecular oxygen pressure and 200 W rf-plasma power and a Ga cell temperature of 880 °C, assuming a mass density of 5.95 g cm^{-3}.

[0216] Figure 15B depicts a plot of the gallia deposition rate measured by the QCM increases with increasing Ga effusion cell temperature for fixed oxygen plasma settings of 200 W rf-plasma power and 2.0 10^{-5} torr O_2 pressure.

[0217] Figures 16A-16E depict XPS data taken *in situ* after 1st PAMBE growth of gallia at 670 °C on γ-Al_2O_3(111)(5nm)/Si(001) with a VG Scienta spectrometer with monochromatic Al-Kα and R3000 hemispherical analyzer at 200 eV pass energy.

[0218] Figure 17 depicts XRR data (dots in upper panel plot, in blue) and GenX [89] simulation of Ga_2O_3/Al_2O_3/Si according to the present technology.

[0219] Figures 18A-18E depict XPS data taken *in situ* after 2nd PAMBE growth of additional gallia at 630 °C on Ga_2O_3(21nm)/γ-Al_2O_3(111)(5nm)/Si(001) with a VG Scienta spectrometer with monochromatic Al-Kα and R3000 hemispherical analyzer at 200 eV pass energy.

[0220] Figure 19 depicts a plot of the Kiessig fringe spacing, which indicates a total Ga_2O_3 thickness of 66 nm.

[0221] Figure 20 depicts a plot of the sticking probability as a function of sample temperature in the PAMBE-growth of Ga_2O_3 after the model by Vogt and Bierwagen [92].

[0222] Figures 21A-21F depict plots of Pseudo-Voigt function fits of x-ray diffraction θ/2θ reflections from the 66 nm β-Ga_2O_3 thin film.

[0223] Figures 22A-22C illustrate ideally terminated surfaces with lattice planes marking the terminations studied.

[0224] Figures 23A-23C illustrate lowest energy terminations before and after relaxation superimposed for the (310) O-termination (Figure 23A), $(\bar{2}01)$ mixed-termination (Figure 23B), and (101) O-termination (Figure 23C).

[0225] Figures 24A and 24B show RHEED patterns for the Ga_2O_3 thin films as grown on bare STO along STO ⟨100⟩ and ⟨110⟩ azimuths for a 20-nm film.

[0226] Figures 24C and 24D show the same azimuths as in Figures 24A and 24B for a 50-nm film.

[0227] Figures 25A-25C depict results of ex situ XRD to characterize the crystal structure of Ga_2O_3 thin films.

[0228] Figures 26A-26C show cross-sectional TEM images (Figures 26A and 26B) and Fast Fourier Transform (Figure 26C) to characterize the epitaxial texture of the Ga_2O_3 thin films.

[0229] Figures 27A and 27B are structural models showing lattice matching for β-Ga_2O_3 ($\bar{1}12$) and (100), respectively.

[0230] Figures 28A and 28B are RHEED pattern to characterize the structural, morphology, and thickness for STO <100> and STO <110>, respectively, taken with a 15 keV electron beam of $Ga_2O_3/SrTiO_3/Si$.

[0231] Figure 29A depicts XRD patterns showing a θ-2θ diffractogram of a 15 nm film of Ga_2O_3 grown by PAMBE at 775 °C on the STO (100) buffer layer on Si (001).

[0232] Figures 29B and 29C depict XRD patterns showing θ-2θ diffractogram of in-plane XRD scans along STO [110] and [100], respectively.

[0233] Figure 30A depicts an XRR curve of Ga_2O_3 grown on STO-buffered Si.

[0234] Figure 30B depicts a low-magnification TEM image of a 15-nm Ga_2O_3 film grown at 775 °C on STO-buffered Si (001) projected along the Si (110) [110] zone-axis (equivalent to the STO (100) [100] zone-axis).

[0235] Figure 31 depicts a plot of surface energies of several surface terminations along the (100), ($\bar{1}12$), ($\bar{2}01$), (310) and (101) surfaces with respect to the Ga chemical potential where 0 and -4.65 eV represent Ga-rich and O-rich environments, respectively.

[0236] Figures 32A-32C depict cross-section TEM images taken along the STO [100] zone axis at progressively higher magnification, as indicted by the scale bar.

[0237] Figure 32D depicts the Fast Fourier Transform of Figure 32C.

[0238] Figure 33 depicts an indexing of Fast Fourier Transform of a TEM image of 50-nm Ga_2O_3 film, consistent with the model of four rotational in-plane variants for the (100) and ($\bar{1}12$) basal growth planes

[0239] Figures 34A-34C depicts plots of XPS data taken *in situ* after PAMBE growth of a 50 nm gallia film on STO with a VG Scienta spectrometer with monochromatic A1-Kα and R3000 hemispherical analyzer at 200 eV pass energy.

[0240] Figures 35A and 35B illustrate a reciprocal space simulation β-Ga_2O_3 (100) and ($\bar{1}12$) basal in the (*hk*0) plane of STO.

[0241] Figures 36A-36C provide tables of the fitted XRD peak positions and plane spacings along with and their deviation from the bulk values of β-Ga_2O_3 from Figures 25A-25C.

[0242] Figures 37A-37D illustrate mutual orientation of the parallelepipeds for the unit cells of (100)-β-Ga_2O_3 and (001)-STO.

[0243] Figure 38A depicts a plot showing the spectrum from the high binding energy side of the O 1*s* XPS peak.

[0244] Figure 38B depicts a plot showing the EEL spectrum from REELS experiments with low-incidence-angle electrons at 1.9 keV recorded under normal exit with a Staib Auger Probe.[143].

[0245] Figures 39A-39C illustrate surfaces before and after relaxation superimposed for the (100) (Figure 39A), (100)-A (Figure 39B), and $(\bar{1}12)$ (Figure 39C) mixed terminations.

[0246] Figures 40A and 40B illustrate a wafer according to some embodiments of the present technology.

[0247] Figure 41 provides examples of combining oxides with semiconductors epitaxially.

[0248] Figures 42A-42E illustrate difficulties of oxide/semiconductor epitaxy that may arise from strain, thermal mismatch, wetting, and symmetry effects, as well as steps.

[0249] Figure 43A shows the measured Ga flux in the absence of O-plasma of 1.35 Å/min (average min 20 to 44).

[0250] Figure 43B shows the measured GaO_x flux of 3.95 Å/min (average min 20 to 38), showing an increase in the accumulation rate by a factor of ~2.9 in the presence of O-plasma.

[0251] Figures 44A-44C provide results of the analysis of the RHEED patterns in an example.

[0252] Figures 45A-45C provide XPS results of the analysis in an example.

[0253] Figure 46 provides XRR results of the analysis in an example.

[0254] Figures 47A and 47B illustrate differences between the crystal structures of β-Ga_2O_3 and γ-Ga_2O_3.

[0255] Figure 48 shows that the example provides a single domain structure 5.5% mismatch (compressive), which can be denoted as γ-Ga_2O_3 (001)[001]/STO(001)[100].

[0256] Figure 49 illustrates expected epitaxy for β-Ga_2O_3 on STO(001), which is the same as that observed on MgO (100) substrates, for an example.

[0257] Figure 50 shows the expected 4-domain structure of β-Ga_2O_3 (100)[020] on STO(100)[110].

[0258] Figures 51A and 51B depict plots of out-of-plane (oop) XRD results for the example with sample label AF99.

[0259] Figures 52A and 52B depict combined in-plane 2q□/f plots for the example taken along two different azimuths.

[0260] Figures 53A-53D depict peak decompositions of each of the four features in Figures 52A and 52B.

[0261] Figure 54 is a diagram of an epi-Ga_2O_3 Power MOSFET, according to some embodiments of the present technology.

[0262] Figure 55 is a diagram of a Ga_2O_3 vertical rectifier, according to some embodiments of the present technology.

[0263] Figures 56 and 57 depict flowcharts of methods for manufacturing a wafer, according to some embodiments of the present technology.

[0264] The drawings have not necessarily been drawn to scale. Similarly, some components and/or operations may be separated into different blocks or combined into a single block for the purposes of discussion of some of the embodiments of the present technology. Moreover, while the technology is amenable to various modifications and alternative forms, specific embodiments have been shown by way of example in the drawings and are described in detail below. The intention, however, is not to limit the technology to the particular embodiments described. On the contrary, the technology is intended to cover all modifications, equivalents, and alternatives falling within the scope of the technology as defined by the appended claims.

DETAILED DESCRIPTION

[0265] Various embodiments of the present technology generally relate to silicon (Si)-based semiconductor manufacturing. More specifically, some embodiments of the present technology relate to systems and methods for integrating gallium oxide thin films on silicon (001) via a buffer layer.

[0266] The challenge of epitaxial integration is the structural difference between silicon and gallium oxide. Si has a crystal structure with cubic symmetry, whereas β-Ga_2O_3 has monoclinic symmetry. This symmetry mismatch will unavoidably lead to a multi-orientation growth of epitaxial domains [18, 19]. Crystal grain boundaries between epitaxial domains and defects arising from the lattice mismatch to the substrate can be pernicious to the electronic properties of the epilayer. Therefore, it appears paramount for device applications to increase crystal quality by reducing the defect densities and increasing the grain sizes of hetero-epitaxially grown gallium oxide. Molecular beam epitaxy (MBE) is a method of choice for such integration due to its unparalleled atomistic control [20]. A buffer layer on Si is required since growth of Ga_2O_3 is not possible by MBE without an activated oxygen source (plasma or ozone) [15], which would inevitably oxidize the pristine Si surface, forming amorphous SiO_2 and inhibiting epitaxy. Additionally, Ga_2O_3 is not thermodynamically stable on Si and will form SiO_2 spontaneously [21]. Hence, a buffer layer is needed to obtain epitaxial films. Conventional MBE is an inherently slow growth method (typically ~1 nm/min) and hence can only be useful to deposit a template, which can then be used as a seed layer to create (compensation-)doped device layers of appropriate thickness (usually several to tens of μm in case of Ga_2O_3 vertical Schottky barrier diodes[22]) by a faster growth method like metal organic vapor phase epitaxy (MOVPE) or hydride vapor phase epitaxy (HVPE) [2], or recently described suboxide-MBE (SMBE) [23].

[0267] In the following description, for the purposes of explanation, numerous specific details are set forth in order to provide a thorough understanding of embodiments of the present technology. It will be apparent, however, to one skilled in the art that embodiments of the present technology may be practiced without some of these specific details.

[0268] The phrases "in some embodiments," "according to some embodiments," "in the embodiments shown," "in other embodiments," and the like generally mean the particular feature, structure, or characteristic following the phrase is included in at least one implementation of the present technology and may be included in more than one implementation. In addition, such phrases do not necessarily refer to the same embodiments or different embodiments.

EXAMPLE 1: Gallia on Alumina-Buffered Silicon

Experimental Conditions

[0269] In an embodiment of the present technology, a 5 nm γ-Al_2O_3 (111) layer was deposited on a 2 inch diameter Si (001) substrate with 2 x 1 surface reconstruction, akin to references [60-62]. Figures 1A-1D depict reflection high-energy electron diffraction (RHEED) patterns at different stages of growth: Figure 1A is the Si (001) 2x1 surface after SiO_2 desorption with Sr along Si [110] azimuth; Figure 1B is the post-growth surface of 5 nm e-beam-evaporated γ-Al_2O_3 (111) grown at 840 °C along Si [100] azimuth with 12-fold rotational symmetry; Figure 1C is the post-growth surface of 21 nm gallia (Ga_2O_3) grown at 670 °C along Si [100] azimuth; and Figure 1D is the post-growth surface of additional 45 nm Ga_2O_3 grown at 630 °C along Si [100] azimuth. The RHEED pattern after growth showed a 12-fold symmetry and is shown along with the 2 x 1 Si surface in Figures 1C and 1D. Details of the growth and characterization by RHEED, x-ray reflectivity (XRR), x-ray photoelectron spectroscopy (XPS) and x-ray diffraction (XRD) are detailed in the section below entitled "Supplemental Material For Example 1." As discussed in greater detail there, the characterization results are in good agreement with what is reported in the literature [60-63, 67].

[0270] Following the characterization, the alumina ("Al_2O_3")-buffered 2 inch Si wafer was re-loaded into the ultra-high vacuum (UHV) system after *ex situ* cleaning with acetone, 2-propanol, de-ionized water, drying with N_2 and UV/ozone for 30 min. Ga_2O_3 was then deposited at 670 °C substrate temperature. Ga (99.99% purity) was evaporated from a dual filament (hot lip) effusion cell held at 880 °C, and an O plasma was generated by an rf-plasma source operated at 2.0 x 10^{-5} torr O_2 partial pressure and 200 W plasma power. The total pressure was monitored by an ion gauge located in the upper part of the molecular-beam epitaxy (MBE) chamber (above the sample), whereas a residual gas analyzer/quadrupole mass spectrometer (RGA/QMS) located at the side of the chamber (below the sample) measured an O_2 to O ratio of approximately 10, from which an absolute O flux of ~10 $nm^{-2}s^{-1}$ is estimated. The sample exposed to oxygen plasma was annealed for 30 min at 670 °C prior to growth. The Ga_2O_3 deposition rate on the quartz crystal microbalance (QCM) sensor before the anneal was 3.15 Å/min.

[0271] The film was grown for 174.5 min for a nominal Ga_2O_3 thickness of 55 nm. Post-growth RHEED showed a streaky surface with qualitatively similar pattern as the underlying γ-Al_2O_3, although with more modulation along the streaks as shown in Figure 1C. XPS determined a stoichiometric Ga_2O_3 and

revealed a sample that was thicker than the information depth in XPS (> 5 $\lambda \approx 10$ nm, λ is the kinetic-energy-dependent effective attenuation length for photoelectrons in Ga_2O_3 [68]), i.e., no substrate signal (Al or Si) was seen in the spectra. XRR determined an actual thickness of 20.6 nm for the stoichiometric Ga_2O_3 layer, resulting in an average sticking coefficient of 38 % for the given growth conditions (XPS and XRR data are discussed below in "Supplemental Material For Example 1").

[0272] The resulting Ga_2O_3 film was too thin for comprehensive characterization with a laboratory x-ray diffractometer (Al and Ga are weak Rayleigh x-ray scatterers [69]). Hence, additional Ga_2O_3 was deposited. The 2 inch wafer was first diced into 10x10 mm^2 pieces. After dicing, a 10x10 mm^2 piece obtained from the center of the wafer was re-cleaned following the above cleaning protocol and loaded into UHV on a molybdenum sample holder. After a 40 min anneal at 630 °C in oxygen plasma, an additional Ga_2O_3 layer was deposited at the lower substrate temperature of 630 °C to enhance the sticking probability [70], with GaO_x rate ~ 0.3 nm/min, at otherwise identical growth conditions for 256 min (76.8 nm additional Ga_2O_3 nominally). The XRR revealed an additional Ga_2O_3 thickness of 45 nm (see "Supplemental Material For Example 1," below), indicating an increased average sticking probability of 59 %, leading to a total film thickness of ~66 nm, sufficiently thick for XRD characterization. RHEED post-growth shown in Figure 1D displays a less streaky pattern with strong modulation along the streaks. This change in the RHEED pattern could be related to decrease in crystalline quality at the lower growth temperature, or due to surface roughening as the film thickness increased. XPS showed again stoichiometric Ga_2O_3 (see "Supplemental Material For Example 1," below).

[0273] In order to identify the polymorph and orientation of the stoichiometric and crystalline Ga_2O_3 layer, an *ex situ* $\theta/2\theta$ XRD scan with sample alignment to Si (004) was conducted on a Rigaku Ultima IV diffractometer with Cu-Kα anode, parallel beam geometry (multilayer mirror), and a 2-bounce Ge monochromator. The scan was recorded with slit settings of 1.0 mm for the divergence slit and 0.5 mm for both scattering and receiving slits, without the use of Soller slits. The settings were chosen to enhance the weak film signal and allow the observation of lattice planes that have normals slightly tilted away from the Si (001) surface. A 5.0 mm height-limiting slit was used to limit the spread of the beam perpendicular to the scattering plane and keep the x-ray beam from spilling over the sample edges. Figure 2 depicts a symmetric $\theta/2\theta$ coupled XRD scan with sample aligned to Si (004). Six film peaks are apparent and are attributed to the β-Ga_2O_3 polymorph labeled by their Miller indices. The scan shown in Figure 2 reveals six clearly identifiable film peaks along with the Si (004) substrate peak.

Results and Discussion

[0274] Fitting of the peak profiles to pseudo-Voigt functions is presented in Figures 21A-21F, and discussed in greater detail, below, in the section entitled "Supplemental Material For Example 1." By analysis of the respective integrated peak areas and 2θ positions, we conclude the presence of the harmonics of the β-Ga_2O_3 polymorph {310}, (101) and $(\bar{2}01)$ plane families, with estimated scattering

volume fractions of 71%, 13% and 16% for the three phases. With this model, the agreement between calculated and experimental intensities is reasonable - see Table 1, below.

(h k l)	$2\theta_{bulk}$ [°]	$2\theta_{exp}$ [°]	$\Delta 2\theta$ [°]	d_{bulk} [Å]	d_{exp} [Å]	Δd [Å]	ΣI_β	I_{exp}
$(\bar{2}\ 0\ 1)$	18.94	18.80	0.14	4.68	4.72	-0.04	1.00	1.00
(3 1 0)	37.30	37.23	0.07	2.41	2.41	-0.00	0.17	0.17
$(\bar{4}\ 0\ 2)$, (2 0 2)	38.42, 38.43	38.17	0.25, 0.26	2.34, 2.34	2.36	-0.01, -0.01	0.50	0.50
$(\bar{6}\ 0\ 3)$	59.14	58.84	0.30	1.56	1.57	-0.01	0.79	0.82
(6 2 0)	79.50	79.46	0.04	1.20	1.21	-0.00	0.17	0.20
$(\bar{8}\ 0\ 4)$, (4 0 4)	82.29, 82.32	x	x	1.17, 1.17	x	x	0.04	x
$(\overline{10}\ 0\ 5)$	110.67	110.10	0.62	0.94	0.94	-0.00	0.29	0.35
$(0\ 0\ 4)_{Si}$	69.120	69.140	0.020	1.3579	1.3576	0.003	x	x

Table 1: Experimental and bulk structure Bragg angles, lattice constants, and integrated peak intensities for the 66 nm β-Ga_2O_3 film on Al_2O_3/Si. The ΣI_β column for the expected intensity is based on the summed intensities for 71%, 13% and 16% scattering volume fractions for the {310}, (101) and $(\bar{2}01)$ out-of-plane orientations, respectively. Intensity values are normalized to the $(\bar{2}01)$ reflection.

[0275] The volume fractions obtained indicate that there are differences in nucleation and growth rate for the different basal growth planes. A non-uniform vertical distribution of the three out-of-plane orientations is also possible. By using the full-width-at-half-maxima of the peak profiles in the Debye-Scherrer equation, the coherence length of the scattering crystallites along the out-of-plane direction is estimated to be ~21 nm for the $(\bar{2}01)$ reflection, ~19 nm for the (310) reflection, ~24 nm for the $(\bar{4}02)$/(202) reflection. It is evident from Table 1 that the peaks of the $(\bar{2}01)$ and (101) phases show larger 2θ shifts from the bulk value when compared with {310}. This difference could be explained by a difference in strain values leading to differing lattice relaxation behavior. Probable orientations of other Ga_2O_3 polymorphs can be excluded as majority phases due to the absolute peak positions and relative peak areas (see Table 5, below, in the section entitled "Supplemental Material For Example 1"). The {310}, (101) and $(\bar{2}01)$ planes are plausible basal growth planes for growth on γ-Al_2O_3 (111) due to their local oxygen arrangement, as will be described below. Evidence for a thin interlayer of γ-Ga_2O_3 (111) could not be found from the θ/2θ diffractogram of Figure 2.

[0276] The crystal structure of β-Ga_2O_3 has a low symmetry, base-centered monoclinic $C2/m$ space group (12) with only one mirror plane (perpendicular to *b*-axis in standard setting [71]), one two-fold rotation axis (parallel to *b*-axis), and an inversion center (origin) as its non-trivial symmetry operations. However, β-Ga_2O_3 is characterized by oxygen ions forming a sublattice with a distorted fcc arrangement [72], where the smaller gallium ions fill interstitial spaces of tetrahedral (Ga1) or octahedral (Ga2) symmetry. Figure 3 illustrates the relationship between the *conventional* monoclinic unit cell with lattice

vectors *a*, *b*, *c*, and the distorted oxygen fcc sublattice of β-Ga_2O_3. A possible oxygen face-centered cubic (fcc) unit cell is highlighted by the yellow cage (labeled 3010 in Figure 3), tetrahedrally bonded Ga1 ions are in blue (labeled 3020 in Figure 3), octahedrally bonded Ga2 ions in green (labeled 3030 in Figure 3), and O ions are in red (labeled 3040 in Figure 3), and the monoclinic unit cell is highlighted by its parallelepiped. The crystal structure of β-Ga_2O_3 alongside with a visualization of the polyhedral Ga-O bonding, and the relationship of the *conventional* monoclinic unit cell to the oxygen ion distorted fcc sublattice, are pictured in Figure 3.

[0277] By looking at the distorted tetrahedra (blue, labeled 3050 in Figure 3) and octahedra (green, labeled 3060 in Figure 3) formed by the Ga-O bonds centered around the Ga ions in Figure 3 it can be seen that the structure *locally* exhibits a pseudo-three-fold symmetry for oxygen ions contained on the face planes of the polyhedra. Overall, there are four distinct sets of parallel face planes to the polyhedra, which mark planes of *local* (*approximate*) three-fold symmetry for the oxygen ions contained in the face planes. The sets of parallel face planes are *approximated* by the crystallographic planes $(\bar{2}01)$, (101), (310) and $(\bar{3}10)$ when given by their Miller indices. The latter two are crystallographically equivalent, related by mirror symmetry and henceforth summarized as $\{310\}$. Diffraction peaks for these planes are the ones observed in the θ/2θ diffractogram of Figure 3. However, growth along $\{310\}$ and along its negative $\{\overline{3}10\}$ give rise to two crystallographically distinct twin orientations, the twin variant arises by a 180° rotation about the *c*-axis (which is not a space group symmetry operation of β-Ga_2O_3). Hence, there are four *distinct* growth planes: $(\bar{2}01)$, (101), $\{310\}$ and $\{\overline{3}10\}$. The existence of a $\{310\}$ twin variant is not immediately obvious, but its existence is revealed by the pole figure pattern presented below.

[0278] The basal growth planes under discussion can also be thought as of being the close-packing planes of the distorted fcc O sublattice of β-Ga_2O_3, i.e. the planes that are perpendicular to the body-diagonal directions of the fcc cage in Figure 3. This is visualized in Figure 4, which illustrates the close-packing planes of the distorted oxygen sublattice of β-Ga_2O_3: $(\bar{2}01)$, (101), and (310), where the O ions contained in the (310) plane are highlighted in gold (labeled 4010 in Figure 4)for illustration of their nearly equilateral triangular arrangement in the plane. In Figure 4, oxygen ions contained in the (310) plane are shown in gold (labeled 4010 in Figure 4) to show their triangular arrangement in the plane. The triangular arrangement is also highlighted by the polyhedron faces shown in green (labeled 4020 in Figure 4) and blue (labeled 4030 in Figure 4), some of which are intersecting the (310) plane. If we mirror the (310) about the mirror plane perpendicular to the *b*-axis, we obtain the $(\bar{3}10)$ plane (not shown), which is crystallographically identical to the (310) plane. However, as described in greater detail herein, the (310) gives rise to a twin variant in the texture on γ-Al_2O_3 (111).

[0279] Due to the missing *global* three-fold symmetry (indeed absence of any non-trivial rotational symmetry) of β-Ga_2O_3 when rotated about the basal growth plane normals, each distinct growth plane should give rise to a *minimum* of six in-plane variants of β-Ga_2O_3 when grown on the six-fold symmetric

surface of γ-Al_2O_3 (111) shown in Figures 14A and 14B, as discussed in greater detail, below, in the section entitled "Supplemental Material for Example 1" [18, 19]. Combined with the two in-plane variants of γ-Al_2O_3 (111) observed on Si (001), there should be a minimum of 4 (# distinct growth planes) x 6 (# film rotations with respect to ("w.r.t.") substrate) x 2 (# substrate orientations) = 48 crystallographically distinct in-plane variants of β-Ga_2O_3 observable for this thin film.

[0280] Figures 5A-5C illustrate representative interface models between the γ-Al_2O_3 (111) substrate and locally epitaxial β-Ga_2O_3 domain variants: Figure 5A is (101); Figure 5B is $(\bar{2}01)$; and Figure 5C is {310}. The oxygen ions of each structure (red and purple spheres, respectively labeled 5010 and 5020 in Figures 5A-5C) are matched in position in the interface plane. The matching is not perfect for the bulk structures, and compressive strain is indicated near the interface for β-Ga_2O_3. Each epitaxial orientation domain gives rise to 6 in-plane variants which are obtained by rotating the β-Ga_2O_3 by multiples of 60° about the out-of-plane direction.

[0281] Representative atomistic models of feasible β-Ga_2O_3/γ-Al_2O_3 interfaces with alignment of the oxygen ions in the interface plane are presented in Figures 5A-5C with their crystallographic orientation relationship expressed as follows:

[0282] [010] β-Ga_2O_3 (101) ‖ $\langle 1\bar{1}0\rangle$ γ-Al_2O_3 (111) (Figure 5A);

[0283] [010] β-Ga_2O_3 $(\bar{2}01)$ ‖ $\langle 1\bar{1}0\rangle$ γ-Al_2O_3 (111) (Figure 5B);

[0284] [001] β-Ga_2O_3 {310} ‖ $\langle 1\bar{1}0\rangle$ γ-Al_2O_3 (111) (Figure 5C); and

[0285] [001] β-Ga_2O_3 $\{\overline{31}0\}$ ‖ $\langle 1\bar{1}0\rangle$ γ-Al_2O_3 (111) (twin of Figure 5C obtained by 180° rotation about the β-Ga_2O_3 *c*-axis).

[0286] The crystallographic relationships between γ-Al_2O_3 and Si are $\langle 11\bar{2}\rangle$ γ-Al_2O_3 (111) ‖ [100] Si (001) and $\langle 1\bar{1}0\rangle$ γ-Al_2O_3 (111) ‖ [100] Si (001) [60]. From Figures 5A-5C it can be seen that the oxygen atoms at the interface do not align perfectly when using the bulk structures. Hence, compressive strain and structural distortions are expected near the interface in the thin films due to the larger bond lengths in Ga_2O_3.

[0287] To confirm the presence of 48 in-plane variants, a full pole figure scan with $2\theta_{Bragg}$ angle of 31.7° was conducted on the Rigaku Ultima IV diffractometer with use of parallel beam in a non-coplanar measurement geometry with an in-plane detector axis [73]. The scan was done with 2.5° vertical Soller slits on both source and detector sides, 0.5 mm divergence slit, 5.0 mm width-limiting slit, 1.0 mm receiving slit, and 1.0 mm scattering slit. A thin Ni foil was used to block out Cu-Kβ radiation. The 2θ angle of 31.7° corresponds to the (002) and $(20\bar{2})$ reflections of β-Ga_2O_3, which are strong intensity reflections of β-Ga_2O_3 with only two-fold multiplicity, which makes them suitable for a pole figure scan. Figure 6 is a pole figure at 2θ = 31.7° of (002) and $(20\bar{2})$ Bragg reflections of β-Ga_2O_3. The polar angle is mapped linearly onto the radial axis and extends from 0° (north pole) to 90° (equator). The experimental measurement grid is overlaid on the data, as well as the expected peak positions based on the bulk lattice constants of β-Ga_2O_3 utilizing the model of 12 in-plane variants for each of the four

distinct out-of-plane orientations of (101), $(\bar{2}01)$, {310} and $\{\overline{3}10\}$. The β-Ga_2O_3 peaks are labeled with the notation hkl_n, where hkl are the Miller indices of the reflection, and the integers $n \in [0,11]$ denote the twelve rotational variants for each out-of-plane orientation (101), $(\bar{2}01)$, {310} and $\{\overline{3}10\}$ (color-code and numbering legend is shown in the lower left corner of Figure 6).

[0288] The resulting pole figure is shown in Figure 6 along with an overlay of a grid of azimuthal and polar coordinates used in the experiment, and of the calculated peak coordinates as dots (in red in colorized version) based the bulk structure lattice constants and the model of 48 in-plane variants oriented with respect to the Si substrate, as described above.

[0289] The polar angle (measured from the north pole downwards) is represented linearly on the radial axis of the plot of Figure 6 and was measured in steps of 2.0°. To avoid total external reflection at large polar angles a minimum incidence angle of 0.4° was set in the measurement software. A polar angle of 0° corresponds to the Si [001] out-of-plane direction. The azimuthal angle was measured in steps of 2.5°, and an azimuthal angle of 0° corresponds to the Si [110] in-plane direction. The intensity was recorded for 5 seconds per grid point and is represented as the intensity value (in gray value) in Figure 6. The maximum of the recorded intensity was 553 counts in the raw data. For a neater display, and to partially account for change in sampling volume and absorption with polar angle, the intensity was scaled by multiplication with the cosine of the polar angle, which is to first order proportional to the reciprocal of the absorption factor in this measurement geometry [73, 74], and then normalized by the resulting maximum. To explain the pole figure pattern fully we had to include the β-Ga_2O_3 $(40\bar{1})$ reflection, which is the closest nearby reflection in terms of Bragg scattering angle at $2\theta = 30.5°$, for the {310} and the $\{\overline{3}10\}$ orientations. The azimuthal arrangement of those $(40\bar{1})$ reflections suggests the presence of both twin variants. Due to their relative angles with respect to the growth plane normals, the (002) and $(20\bar{2})$ peaks arising from different domain variants overlap nearly on top of each other. The β-Ga_2O_3 peaks are labeled with the notation hkl_n, where hkl are the Miller indices of the reflection, the integers $n \in [0,11]$ denote the twelve rotational variants for each out-of-plane orientation (101), $(\bar{2}01)$, {310} and $\{\overline{3}10\}$. Additionally, we note the observation of four Si (111) reflections at polar angles of 54.7° labelled with purple-colored indices (6050). The Si (111) 2θ value is 29.3°, but its tail is picked up in this scan since it is a strong peak. γ-Al_2O_3 (220) is at $2\theta = 32.0°$, but not detected in this scan because of low intensity owing to the buffer layer thickness of only 5 nm. The qualitative and quantitative agreement between the calculated peak coordinates and the peak coordinates of the experimental data is reasonable when considering the finite angular step size (for simulated pole positions, see Table 6, below, in the section entitled "Supplemental Material for Example 1"). Pole figures of plausible lattice orientations of other Ga_2O_3 polymorphs (as mentioned above) give a qualitatively and quantitatively very distinct pattern for the Bragg angle under consideration. The pole diagram of Figure 6 therefore substantiates our model of the β-Ga_2O_3 polymorph with 48 domain variants. Deviations from the calculated peak positions can likely be explained by strain-induced deformations or by slight tilt and twist misorientations of the film.

The angular resolution and step size of the scan are not sufficient to quantify strain or tilt and twist misorientations.

[0290] The morphology of the □-Ga_2O_3 thin films was observed using an image-corrected FEI Titan 80-300 high-resolution electron microscope (HREM) operated at 300 kV and a probe-corrected JEOL ARM200F scanning transmission electron microscope (STEM) operated at 200 kV. Suitable cross-section samples were prepared in the form of thin (50-100 nm) lamellae using focused-ion-beam milling and lift-out techniques, and all images were recorded with the incident electron beam aligned parallel with a Si [110] zone axis.

[0291] Figures 7A and 7B depict STEM and TEM images, respectively, of the present technology. Specifically, Figure 7A is a bright-field STEM image showing cross-section of gallium oxide film grown on Si (001) substrate with thin alumina buffer layer, and Figure 7B is a high-resolution TEM image showing region of gallium oxide film adjacent to alumina buffer layer. The inset of Figure 7B shows corresponding Fast Fourier Transform (FFT)- arrows that indicate spots corresponding to β-Ga2O3 $(2\bar{0}1)$-type lattice spacings with a measured lattice spacing of 4.70 Å. Figure 7A is a bright-field STEM image showing a representative cross section of the gallium oxide film. The contrast variations across the field of view are consistent with the multi-grain nature of the film predicted by the XRD data, while the unevenness of the top surface confirms the view that the growth rate of different crystallites depends on their relative orientation. The film thickness was estimated to be in the range of 65-70 nm, in close agreement with the XRR data. Figure 7B shows an enlarged HREM view of the gallium oxide film close to the region of alumina-oxide buffer layer. The crystallinity of the film is clearly evident, as also shown by the inset FFT of Figure 7B, and strong film texture is also apparent both in the image and in the FFT (see arrowed spots). Moreover, the TEM images in Figure 7 show no evidence that the β-Ga_2O_3 film is layered (in the sense that different basal growth planes $(\bar{2}01), (101), (310)$ are not visibly stacked on top of each other).

[0292] Depending on the growth method and temperature, different ratios of $(\bar{2}01)$, (101), and 310 are observed when β-Ga_2O_3 is grown on sapphire, with some studies describing the observation of $(\bar{2}01)$ only [13, 34, 36, 37, 39, 40, 43, 45, 48-50, 52, 55, 57, 75-77]. This could be due to differences in dependence of the nucleation and growth rate of the individual planes on the growth temperature. A speculated growth temperature dependence of the observed planes could be related to the microscopic growth kinetics or to the surface energies of the individual planes. The surface energies for the $(\bar{2}01)$, (101), and (310) planes were calculated using density functional theory as detailed, below, in the section entitled "Supplemental Material for Example 1." The (101) plane has a significantly higher surface energy of ~1.5 Jm^{-2} than the $(\bar{2}01)$ plane with ~0.8 Jm^{-2}; these compare favorably with the literature values of ~1.8 Jm^{-2} and ~0.9 Jm^{-2} , respectively [78]. A calculation of the surface energy of (310) plane has to our knowledge so far not been published, here we have calculated a minimal surface energy of ~2.1 Jm^{-2} under O-rich conditions for a non-stoichiometric slab. This surface energy is larger

than for both $(\bar{2}01)$ and (101). The surface energies of different planes of β-Ga_2O_3 have been positively correlated with the growth rates for PAMBE on these planes [79]. No obvious correlation is seen between the surface energies and the volume fractions for the film documented here. However, the (310) shows the largest surface energy and the largest volume fraction by far implicating such a relationship could exist to some degree in this thin film. Based on different growth rates, one can expect film roughening with increasing film thickness due to different growth rates of the distinct growth planes present in the film. Further work should seek to reduce the number of in-plane variants by utilizing vicinal Si (001) substrates akin to reference [49], and adjusting the growth temperature and growth conditions to see if the occurrence of the amount of distinct growth planes can also be reduced in order to prevent film roughening and achieve the goal of increased crystal grain size.

Concluding Remarks for Example 1

[0293] In conclusion, strongly textured growth of β-Ga_2O_3 with $(\bar{2}01)$, (101), and {310} orientations was demonstrated on a two-domain γ-Al_2O_3 (111) e-beam evaporated buffer on Si (001). Structural order in the film texture is achieved by continuation of the oxygen sublattice from the γ-alumina buffer layer into the β-gallia film with three distinct growth planes that correspond to the close-packing planes of the oxygen sublattice of β-Ga_2O_3 plus one twin variant $\{\overline{3}10\}$. Each basal growth plane gives rise to 6 in-plane variants for each of the two in-plane orientations of the γ-Al_2O_3 pseudo-substrate, resulting in a total of 48 rotational domain variants. The structural integration of β-Ga_2O_3 onto Si (001) is of technological relevance as it would enable Ga_2O_3-based semiconductor devices on Si semiconductor technology, large scale wafer substrates, and the use of heat transfer technologies that are employed for Si-based high-power electronics for use in Ga_2O_3-based high-power applications. This work shows that, in principle, such a structural integration is possible and serves as a proof of concept, addressing the challenges of Si oxidation, thermodynamic instability of a Ga_2O_3/Si interface and the symmetry and lattice mismatch between Ga_2O_3 and Si. The PAMBE-grown thin films could serve as templates for a faster growth technique such as MOVPE, HVPE [2], or recently described SMBE [23], and thus enable large scale integration with Ga_2O_3 thicknesses appropriate for power-device applications.

Supplemental Material for Example 1

[0294] This Supplemental Material contains additional data and analysis for the above described Example 1, including growth rate analysis by QCM and XRR, stoichiometry analysis by *in situ* XPS, additional XRD experiments and supporting analysis and supplemental tables for the XRD data of this Example 1, a further discussion on the growth model and the oxygen to gallium ratio, and finally density functional theory surface energy calculations of growth surfaces discussed above.

[0295] Figure 8 is a plot demonstrating the sample heating mechanism in the MBE consists of a silicon carbide heater that is placed above the sample backside and heats the sample backside and sample holder radiatively. The sample temperatures in this Example 1 are temperatures of the SiC heater read out by a thermocouple corrected by the displayed calibration curve. The calibration curve relates the actual

growth temperature on the sample surface to the manipulator setpoint temperature. The calibration curve was obtained by aiming a pyrometer through a viewport in the MBE chamber located below the sample at the growth side of a 20x20 cm^2 Si sample attached with a spring clip on the sample backside to a molybdenum sample holder.

XPS data analysis

[0296] For a homogenous thin film *f* containing the element *f*1 with smooth coverage on the substrate *s* containing the element *s*1 we can write for the ratio $A_{f,f1nl}/A_{s,s1n'l'}$ of measured photoelectron intensity of subshell *nl* of element *f*1 to the measured photoelectron intensity of subshell *n'l'* of element *s*1 [80]:

$$\frac{A_{f,f1nl}}{A_{s,s1n'l'}} = \frac{T(EK_{f1,nl})}{T(EK_{s1,n'l'})}\frac{\lambda_f(EK_{f1,nl})}{\lambda_s(EK_{s1,n'l'})}\frac{1-\exp\left[-\frac{d}{\lambda_f(EK_{f1,nl})}\right]}{\exp\left[-\frac{d}{\lambda_f(EK_{s1,n'l'})}\right]}\frac{\sigma_{f1,nl}}{\sigma_{s1,n'l'}}\frac{n_{f1}}{n_{s1}}\frac{\rho_f/M_f}{\rho_s/M_s} \quad (1)$$

[0297] Here T is the analyzer response function also denoted as transmission function, $EK_{f1,nl}$ is the kinetic energy of the ejected photoelectron from element *f*1 and subshell *nl*, λ_f (λ_s) is the effective attenuation length (EAL) for electrons in the film (substrate), d is the film thickness, $\sigma_{f1,nl}$ is the photoelectric cross section of element *f*1 and subshell *nl*, M_f (M_s) is the molar mass of the molecules comprising the film (substrate) material, n_{f1} (n_{s1}) is the stoichiometric coefficient of element *f*1 (*s*1) in the molecules comprising the film (substrate). This equation can be solved numerically as an estimate of the thin film thickness d, as long as $d \lesssim 5\lambda$. The transmission function of our VG Scienta spectrometer was characterized, for the used experimental conditions, by a method devised by the National Physical Laboratory (NPL) of the United Kingdom [81], where survey spectra from *in situ* Ar sputter-cleaned copper, silver and gold samples were acquired and then referenced back to a spectrum determined on a well characterised spectrometer at NPL. The binding energy (BE) scale was calibrated using the Au $4f_{7/2}$, Ag $3d_{5/2}$ and Cu $2p_{3/2}$ core-levels [82]. The EAL is estimated by using the so-called CS2-formula [80, 83]. For the theoretical photoelectric cross-sections we use the Scofield values [84].

[0298] Once the thickness d of the film layer is known (by the above estimate or another more accurate method like XRR) we can evaluate the stoichiometry of the film. The ratio of the stoichiometric coefficients n_{f2}/n_{f1} of elements *f*1 and *f*2 contained in the film layer is given by [80]:

$$\frac{n_{f2}}{n_{f1}} = \frac{A_{f,f2n'l'}}{A_{f,f1nl}}\frac{T(EK_{f1,nl})}{T(EK_{f2,n'l'})}\frac{\lambda_f(EK_{f1,nl})}{\lambda_f(EK_{f2,n'l'})}\frac{1-\exp\left[-\frac{d}{\lambda_f(EK_{f1,nl})}\right]}{1-\exp\left[-\frac{d}{\lambda_f(EK_{f2,n'l'})}\right]}\frac{\sigma_{f1,nl}}{\sigma_{f2,n'l'}} \quad (2)$$

[0299] Using this approach of determining the stoichiometry from fundamental parameters we found that it is necessary to adjust the O 1*s* Scofield cross-section [84], empirically to 0.75 times its tabulated value for a variety of investigated oxides (including Ga_2O_3, Al_2O_3, $SrTiO_3$, La_2O_3, Nb_2O_5) in order to arrive at the correct oxygen to metal ratio for these materials.

γ-Al_2O_3 growth on Si (001)

[0300] Silicon (001) wafers with 2 inch diameter (50.8 mm), n-type phosphorous doped, single-side polished of 200 μm thickness were used as substrates (Virginia Semiconductor). The substrates were *ex situ* cleaned by immersion in solvent and sonication for 10 min each with acetone, 2-propanol and de-ionized water. Thereafter the substrate was blow dried with N_2 and exposed to an ozone/UV treatment for 15 min to break-up residual hydrocarbons on the surface, after which the substrate was loaded into the UHV system on a molybdenum sample holder without backplate. The UHV system consisted of a DCA MBE chamber connected via a buffer line to a VG Scienta XPS system. The SiO_2 layer was desorbed *in situ* in the MBE chamber using the Sr desorption method [85], resulting in a 2x1 surface reconstruction of Si (001) observed by reflection high-energy electron diffraction (RHEED) shown in Figure 1A.

[0301] Figure 9 is a plot depicting alumina rate via e-beam evaporation measured by QCM at an e-gun voltage of 7.75 kV and an emission current of 50 mA resulting in an oxygen partial pressure of ~10^{-7} torr without supplying additional oxygen in the form of molecular O_2 gas. The rate of about 3.9 Å/min, and also the O_2 partial pressure resulting from the alumina evaporation were very stable over time. After the aforementioned Sr desorption, the sample was then heated to the deposition temperature of 840 °C. Al_2O_3 was deposited by e-beam evaporation with an acceleration voltage of 7.75 kV and an emission current of 50 mA, which resulted in a very stable alumina deposition rate of 3.9 Å/min determined by a quartz crystal microbalance placed near the substrate before growth (Figure 9), and an oxygen partial pressure of ~10^{-7} torr measured by a residual gas analyzer/quadrupole mass spectrometer (RGA/QMS) and by an ion gauge.

[0302] Figures 10A-10D depict XPS data taken *in situ* after growth of e-beam evaporated alumina on clean Si (001) with a VG Scienta spectrometer with monochromatic Al-Kα and R3000 hemispherical analyzer at 200 eV pass energy. Figure 10A is a survey spectrum showing no impurity elements or surface contamination within the accuracy of XPS. Figure 10B is the O 1s core-level. Figure 10C shows the Si 2*s*, Al 2*s*, Si 2*p* and Al 2*p* core-levels, indicating a thin layer of aluminum oxide on Si without the presence of Si-O bonds at the interface. Al 2*s* sits on the plasmon loss peak of Si 2*p*. Figure 10D is the low count and low-resolution valence band spectrum from the survey spectrum of Figure 10A (step size 1 eV). Figure 11 depicts plots of XRR data (dots in upper panel plot, in blue) and GenX [89] simulation (curves, in red, in upper and lower panels) of Al_2O_3/Si. The simulation parameters are 5.0 nm Al_2O_3 thickness. Surface roughness σ value of 5.8 Å and a molecular density of 0.020 Al_2O_3 formula units per $Å^3$, very close to the bulk value of 0.021 Al_2O_3 formula units per $Å^3$ of γ-Al_2O_3. The Si substrate roughness value was modeled with σ = 1.4 Å.

[0303] The alumina source consisted of alumina pellets (1-3 mm pieces of 99.99% purity). Alumina was deposited on the substrate at 840°C without supplying additional oxygen for two hours. This resulted in a stoichiometric Al_2O_3 layer of 5.0 nm without the formation of SiO_2 at the Al_2O_3/Si interface as determined *ex situ* by x-ray reflectivity (XRR) and *in situ* by x-ray photoelectron spectroscopy (XPS)

(see Figures 10A-10D and 11, and Tables 2, 3 and 4, below). The determined thickness amounts to an average sticking probability for alumina on silicon of about 11% under the given growth conditions. It is speculated that the high substrate temperature protects the Si surface from oxidation by residual oxygen generated by e-beam irradiation of the alumina source but also leads to re-evaporation of arriving alumina/aluminum suboxide. The RHEED pattern after growth, displayed in Figure 1B, repeats every 30° and therefore shows a 12-fold rotational symmetry. The streaky 12-fold RHEED pattern indicates the formation of a smooth γ-Al_2O_3 (111) with two in-plane variants, as described previously [86].

[0304] Figure 12 depicts results of in-plane XRD coupled $2\theta_\chi/\varphi$ scan of 5 nm thick Al_2O_3/Si conducted on the Rigaku Ultima IV with in-plane arm, using parallel beam, Ni Cu-Kβ filter and 0.5° vertical Soller slits on source and detector sides. The incidence angle was 0.3° slightly above the critical angle of bulk Al_2O_3 for Cu-Kα radiation. The Q-vectors were parallel to [100] Si (red curve 1210) and 30° off from [100] Si (blue curve **1220**). The peak positions were fitted by pseudo-Voigt functions. For γ-Al_2O_3 ($4\bar{4}0$) along $[100]_{Si}$ + 30°: $2\theta_\chi$ = 67.091°, d = 1.394 Å → γ-Al_2O_3 a = 7.886 Å, FWHM = 1.13° → crystallite size ~83 Å. For γ-Al_2O_3 ($4\bar{4}0$) along $[100]_{Si}$: $2\theta_\chi$ = 67.114°, d = 1.394 Å → γ-Al_2O_3 a = 7.886 Å, FWHM = 1.39° → crystallite size ~67 Å. For Si (004) along $[100]_{Si}$: $2\theta_\chi$ = 69.173°, d = 1.357 Å → Si a = 5.428 Å, FWHM = 0.51° (limited by in-plane Soller slit resolution of 0.5° Soller slits) → crystallite size ~190 Å (very underestimated due to low in-plane resolution).

[0305] Figure 13 depicts the $\theta/2\theta$ out-of-plane diffraction pattern of the 5 nm film of alumina on Si (001). Due to the small film thickness we have used widely open slits with a 2 mm divergence slit and 1 mm receiving and scattering slits, hence a broad base to the Si (004) peak. The Si (004) was not scanned fully to avoid detector saturation. We see two film peaks that we attribute to γ-Al_2O_3 (222) and γ-Al_2O_3 (444). Due to the low signal to noise ratio we refrained from peak fitting and determination of the lattice constant. Combined with the quantitative result from the in-plane XRD and the twelve-fold symmetry in RHEED, this qualitative result confirms the thin film's structure to be the γ-Al_2O_3 polymorph in (111)-orientation with two in-plane variants, consistent with the literature reports for similarly grown alumina films on Si (001) [86,88,90,91].

[0306] The diffraction patterns discussed above with reference to Figures 12 and 13 are consistent with previous findings [86], and suggest the coexistence of two γ-Al_2O_3 (111) || Si (001) in-plane variants, offset by 30° from each other, with $\langle 11\bar{2}\rangle$ γ-Al_2O_3 || [100] Si and $\langle 1\bar{1}0\rangle$ γ-Al_2O_3 || [100] Si. This geometry results in a surface consisting of equilateral triangles of oxygen ions, as displayed in Figure 14.

[0307] The γ-Al_2O_3 lattice constant was calculated as a_{Al2O3} = 7.89 Å by measuring ($4\bar{4}0$) reflections with in-plane XRD shown in this supplemental material for Example 1 and assuming all three crystal axes are equally strained or relaxed, without non-cubic deformation. This value is within the range of reported γ-Al_2O_3 bulk lattice constants from 7.84 Å to 7.98 Å [87], and in excellent agreement with the

reported value of (7.90 ± 0.11) Å found for a similarly grown 6 nm γ-Al_2O_3 (111) thin film on Si (001) [86].

Peak label	Experimental BE [eV]	Literature BE [88] γ-Al_2O_3/Si(111) [eV]	FWHM fit [eV]	Raw Area A [cps eV]	Photoelectric cross-section σ^5	EAL λ [83] [nm]	Transmission function [arb. units]
Al 2*p*	75.61	75.50	1.56	8253.5	0.5371	2.21	80.2
Si 2*p*	99.23	99.35	1.09	1901.6	0.817	2.19	81.6
Al 2*s*	120.42	x	2.31	11558.2	0.753	2.15	83.1
Si 2*s*	150.40	x	1.27	1465.2	0.955	2.12	85.4
O 1*s*	532.23	x	1.88	48922.8	2.20*	1.62	100.5

Table 2: XPS data of 5 nm Al_2O_3 film on Si including values obtained from peak fitting of the data shown in Figures 10A-10D. The BE position of Si 2*p* indicates that no Si-O bonds are formed at the interface. The raw area denotes the integrated peak area after Tougaard background subtraction. The Scofield elemental subshell cross-sections are relative to C 1*s*. *The O 1*s* cross-section had to be empirically corrected, after measuring a range of sesquioxide compounds (including Ga_2O_3, Al_2O_3, $SrTiO_3$), to a common value of 0.75 times the tabulated value of 2.93 [84], to obtain correct stoichiometries.

d [nm]	Al 2*p*	Al 2*s*	O 1*s*
Si 2*p*	5.1	5.1	5.1
Si 2*s*	5.8	5.8	5.8

Table 3: Al_2O_3 film thickness *d* in nm estimated using equation (1) and values from Table 2. The thickness values estimated using Si 2*p* agree well with the result of 5.0 nm from XRR in Figure 11. The thickness values using Si 2*s* are somewhat overestimated compared to XRR, which could be due to an underestimation of the integrated Si 2*s* peak area owing to its smaller signal to noise ratio in the spectrum of Figure 10C.

n_O/n_{Al}	O 1*s*
Al 2*p*	1.48
Al 2*s*	1.51

Table 4: Stoichiometric ratios n_O/n_{Al} of oxygen to aluminum in the alumina thin film determined using equation (2) and values from Table 2 and a alumina thickness d = 5.0 nm (from XRR - see Supplemental Figure 11). The film stoichiometry, within the error of XPS, has the ideal sesquioxide value of stoichiometric Al_2O_3 with $n_O/n_{Al} = 1.50$.

[0308] Figures 14A and 14B are top-views of the oxygen-terminated surface of γ-Al_2O_3 (111). Note the bulk structure of γ-Al_2O_3 has $\bar{3}$ symmetry, but the terminating O layer taken by itself and unreconstructed is 6-fold symmetric with the O ions being arranged in a hexagonal surface net. Two rotational variants are observed by RHEED and XRD giving rise to an apparent 12-fold pseudo-symmetry of the RHEED pattern in Figure 1B. The triangular faces of the oxygen polyhedra surrounding the partially occupied Al cation sites are contained in the (111) surface plane. Figure 14C is a side-view of the oxygen-terminated surface of γ-Al_2O_3 (111).

Ga_2O_3 growth and characterization

[0309] Figure 15A depicts a plot of gallia rate as measured by quartz crystal microbalance (QCM) at $2x10^{-5}$ torr molecular oxygen pressure and 200 W rf-plasma power and a Ga cell temperature of 880 °C, assuming a mass density of 5.95 g cm^{-3}. The Ga cell charge was held at 900 °C for 40 min prior to each growth run before igniting the oxygen plasma to outgas the charge. The rate at 880 °C is stable over time apart from fluctuations about the mean of 3.15 Å/min and was also very similar between different growth runs. It can be assumed that the Ga arriving to the QCM sensor held at room temperature in the presence of O-plasma forms an oxide of Ga_2O_3 stoichiometry and represents the maximum growth rate achievable with the given Ga cell temperature and O plasma settings [92]. When assuming all the Ga arriving at the QCM sticks under O-plasma conditions the measured Ga flux is ~ 0.2 $nm^{-2}s^{-1}$. It should be mentioned that the inferred Ga flux from the QCM rate when measured without the presence of O-plasma was usually about a factor of ~0.5 lower than the Ga flux inferred form the Ga_2O_3 rate for Ga deposition in presence of O-plasma (both Ga metal and Ga_2O_3 have nearly identical mass density, the only parameter needed for the thickness measurements of thin films by the QCM was therefore unchanged). This is likely because elemental Ga has a large surface tension and hence is not sticking well without the presence of atomic oxygen flux.

[0310] Figure 15B depicts a plot of the gallia deposition rate measured by the QCM increases with increasing Ga effusion cell temperature for fixed oxygen plasma settings of 200 W rf-plasma power and 2.0 10^{-5} torr O_2 pressure. The increase in deposition rate can be modeled by an $\sim exp[-E_0/k_BT]$ law (see fit in the graph). The "activation" energy E_0 was fit to ~1.7 eV. The increase of gallia growth rate with increase in Ga effusion cell temperature under unchanged oxygen plasma conditions constitutes an oxygen rich growth regime. This observation is consistent with the Ga to O ratio inferred from the growth model by Vogt and Bierwagen as discussed below (under Figure 20).

[0311] Figures 16A-16E depict XPS data taken *in situ* after 1st PAMBE growth of gallia at 670 °C on γ-Al_2O_3(111)(5nm)/Si(001) with a VG Scienta spectrometer with monochromatic Al-Kα and R3000 hemispherical analyzer at 200 eV pass energy. Figure 16A is the survey spectrum; no core-levels of Al or Si are observed, the film is therefore thicker than the information depth of the film layer (>5 EAL), no impurity elements or surface contamination within the accuracy of XPS. Figure 16B is Ga $2p_{3/2}$ deep core-level. Figure 16C is the O 1*s* core-level. Figure 16D is the Ga 3*p* core-level. Figures 16E is the valence band region with semi-core O 2*s* and Ga 3*d* states. For the quantification of oxygen to gallium ratio in the gallia film we used the O 1*s*, Ga 3*p* and Ga $2p_{3/2}$ core-levels. The oxygen and gallium percentages using O 1*s* and Ga 3*p* are 60 % and 40 %. The oxygen and gallium percentages using O 1*s* and Ga $2p_{3/2}$ are 58 % and 42 %. Hence within the accuracy of XPS the film is stoichiometric Ga_2O_3. We also recorded the semi-core and valence band region. We did not use the semi-core states Ga 3*d* and O 2*s* for quantification since they are already subject to non-negligible hybridization.

[0312] Figure 17 depicts XRR data (dots in upper panel plot, in blue) and GenX [89] simulation (curves, in red, in upper and lower panels) of Ga_2O_3/Al_2O_3/Si according to the present technology. The simulation parameters are 20.9 nm Ga_2O_3 thickness, surface roughness σ value of 14.4 Å and a molecular density of 0.019 Ga_2O_3 formula units per $Å^3$, identical to the bulk value of 0.019 Ga_2O_3 formula units per $Å^3$ of β-Ga_2O_3 and γ-Ga_2O_3. The tabulated density values of α-Ga_2O_3 are denser with 0.021 Ga_2O_3 formula units per $Å^3$, but they have been recorded under elevated pressures and are likely different in thin film form. The fit was somewhat improved if the alumina layer was reduced in thickness compared to the 5.0 nm used as thickness parameter in the simulation of the curve shown in Figure 11, this could indicate intermixing of Al and Ga near the Ga_2O_3/Al_2O_3 interface. We also needed to increase the Si substrate roughness which could indicate oxidation of Si near the Al_2O_3/Si interface by oxygen diffusion through the thin alumina layer when taken into air for a prolonged time, cleaning with ozone or annealing in oxygen plasma.

[0313] Figures 18A-18E depict XPS data taken *in situ* after 2nd PAMBE growth of additional gallia at 630 °C on Ga_2O_3(21nm)/γ-Al_2O_3(111)(5nm)/Si(001) with a VG Scienta spectrometer with monochromatic Al-Kα and R3000 hemispherical analyzer at 200 eV pass energy. Figure 18A is a survey spectrum showing no impurity elements or surface contamination within the accuracy of XPS. Figure 18B is Ga $2p_{3/2}$ deep core-level. Figure 18C is O 1*s* core-level. Figure 18D is Ga 3*p* core-level. Figure 18E is valence band region with semi-core O 2*s* and Ga 3*d* states. For the quantification of oxygen to gallium ratio in the gallia film we used the O 1*s*, Ga 3*p* and Ga $2p_{3/2}$ core-levels. The oxygen and gallium percentages using O 1*s* and Ga 3*p* are 59 % and 41 %. The oxygen and gallium percentages using O 1*s* and Ga $2p_{3/2}$ are 57 % and 43 %. Hence within the accuracy of XPS the film is stoichiometric Ga_2O_3 (possibly slightly oxygen deficient). We also recorded the semi-core and valence band region. We did not use the semi-core states Ga 3*d* and O 2*s* for quantification since they are already subject to non-negligible hybridization.

[0314] Figure 19 depicts a plot of the Kiessig fringe spacing, which indicates a total Ga_2O_3 thickness of 66 nm.

[0315] Figure 20 depicts a plot of the sticking probability as a function of sample temperature in the PAMBE-growth of Ga_2O_3 after the model by Vogt and Bierwagen [92]. Within the macroscopic kinetic growth model for the PAMBE growth of Ga_2O_3 (in a first approximation independent of the substrate and crystal structure) [92], a volatile suboxide Ga_2O evaporates from heated surfaces and limits the sticking probability below 100% and hence reduces the growth rate below the maximum possible growth rate at lower growth temperature (or higher O flux). The Ga_2O_3 growth rate Γ is described by a dependence on the activated O-flux Φ_O, the Ga flux Φ_{Ga} and the sample temperature T. We define the sticking probability as Γ/Γ_{max}, where Γ_{max} is the maximum growth rate achievable at low growth temperature. Our results for the different sticking coefficients obtained at 630 °C and 670 °C agree qualitatively with this model, however, the 1st sticking probability is also related to nucleation on the substrate and therefore the model [92] may not be applicable yet. If we quantitatively apply the model to the 2nd sticking probability of 59%, a Ga flux of 0.2 $nm^{-2}s^{-1}$, and the substrate temperature of 630 °C we can then use the model to constrain the activated O flux impinging on the sample (the only uncertain growth parameter): Both curves are for a Ga flux of 0.2 $nm^{-2}s^{-1}$ (measured by QCM); the red curve **2010** is for an O-flux of 10 $nm^{-2}s^{-1}$ (RGA estimate), and the blue curve is for an O-flux of 1.85 $nm^{-2}s^{-1}$, which was chosen such that the curve intersects 59 % at a temperature of 630 °C. The obtained activated O flux of ~1.85 $nm^{-2}s^{-1}$ is about an order of magnitude lower than the estimate from the RGA O partial pressure. With this choice for the blue curve **2020** it appears that, if the inferred O-flux is correct, the 1st sticking probability of 38% at 670 °C is higher than what the curve predicts. This could be related to an enhanced sticking probability in the initial nucleation of Ga_2O_3 on the Al_2O_3/Si substrate. The growth rate Γ was given as an algebraic solution to simplified rate equations in a dynamic equilibrium [92], as (beware of some typos in the original reference):

$$\Gamma(\Phi_{Ga}, \Phi_O, \Upsilon, A) = A^{-1}\left(\Upsilon - \frac{3}{4}\Phi_{Ga}^2 + \Phi_{Ga}\Phi_O - \frac{1}{12}(2\Phi_O - A)^2\right),$$

$$A(\Phi_{Ga}, \Phi_O, \Upsilon) = \left(72\Upsilon\Phi_O - (3\Phi_{Ga} - 2\Phi_O)^3 + \sqrt{108}\left(\Upsilon\left(16\Upsilon^2 - 4\Upsilon\left(9\Phi_{Ga}^2 - 12\Phi_{Ga}\Phi_O - 8\Phi_O^2\right) + (\Phi_{Ga} - 2\Phi_O)(3\Phi_{Ga} - 2\Phi_O)^3\right)\right)^{1/2}\right)^{1/3},$$

$$\Upsilon(\phi_{Ga}, \phi_O, T) = \Upsilon_0 \exp\left[\frac{-\left(E_0 - \zeta\frac{\Phi_{Ga}}{\Phi_O}\right)}{k_B T}\right],$$

[0316] with model and fitting constants $\Upsilon_0 = \exp[37.1]$, $E_0 = 2.93$ eV, $\zeta = 0.90$ eV.

[0317] Figures 21A-21F depict plots of Pseudo-Voigt function fits of x-ray diffraction θ/2θ reflections from the 66 nm β-Ga_2O_3 thin film. Based on the absolute peak positions and lattice parameters and relative areas under the curves the most likely assignments of the diffraction peaks are the β-Ga_2O_3 {310} (green), (101) (blue) and ($\bar{2}$01) (blue) families of reflections. The Si (004) peak (red) is at 2θ = 69.14°, slightly off from the bulk value of 69.12° (see Table I), which indicates a small instrumental offset of

0.02°. In the symmetric θ/2θ geometry with the use of an incident beam monochromator, the integrated reflection intensity per unit scattering volume at scattering angle 2θ for a crystal slab of thickness *t*, based on the kinematic approximation, is proportional to [93]:

$$I_{hkl}(\theta) \propto \frac{1 + A\cos^2 2\theta}{1 + A} \frac{1}{\sin 2\theta} |F_{hkl}|^2 \left(1 - \exp\left[\frac{-2\mu t}{\sin\theta}\right]\right), \quad (3)$$

[0318] where the first factor is the polarization factor for the incident x-rays and $A = \cos^2 2\theta_M$, with $\theta_M = 22.6°$ being the Bragg angle of the Ge (220) channel cut monochromator, polarization correction due to the multilayer mirror can be neglected due to the small x-ray incidence angle onto the multilayer mirror [94], the second factor is often called Lorentz factor and stems from the change of variables from reciprocal or wavenumber coordinates to angular coordinates in the integration of the lattice interference function [95], $|F_{hkl}|^2$ is the modulus square of the structure factor for the given reflection, the last factor accounts for a change in sampling volume and x-ray pathlength with change in incident and exit angles, where μ is the linear absorption coefficient for x-rays of Cu-Kα energy in the crystal slab. Evaluating the intensities of the harmonics of the {310}, (101) and $(\bar{2}01)$ reflections with regards to equation (3) we obtain scattering volume fractions for the three phases of 71%, 13% and 16%. The structure factors were calculated with the software Vesta [96], based on an imported structure file obtained from entry #1638495 of reference [87]. The linear attenuation coefficient is based on interpolated mass absorption coefficients tabulated in [97] and assuming a mass density of 5.95 g cm^{-3} for Ga_2O_3.

Label	*Peak* 1	*Peak* 2	*Peak* 3	*Peak* 4	*Peak* 5	*Peak* 6	*Peak* 7
$2\theta_{exp}$ [°]	18.80	37.23	38.17	58.84	79.46	x	110.10
Q_{exp}/Q_0	1.00	1.95	2.00	3.01	3.91	x	5.02
d_{exp} [Å]	4.72	2.41	2.36	1.57	1.21	x	0.94
I	1.00	0.17	0.50	0.82	0.20	x	0.35
(h k l)	x	x	$(0\,0\,.\,6)_\alpha$	x	x	$(0\,0\,.\,12)_\alpha$	x
$2\theta_{bulk}$ [°]	x	x	40.24	x	x	86.96	x
Q_{bulk}/Q_0	x	x	2.11	x	x	4.21	x
d_{bulk} [Å]	x	x	2.24	x	x	1.12	x
I	x	x	1.00	x	x	0.09	x
(h k l)	$(1\,1\,1)_\gamma$	x	$(2\,2\,2)_\gamma$	$(3\,3\,3)_\gamma$	x	$(4\,4\,4)_\gamma$	$(5\,5\,5)_\gamma$
$2\theta_{bulk}$ [°]	18.64	x	37.80	58.14	x	80.76	108.20
Q_{bulk}/Q_0	0.99	x	1.98	2.97	x	3.97	4.96
d_{bulk} [Å]	4.76	x	2.38	1.59	x	1.19	0.95
I	0.94	x	1.00	0.90	x	0.31	0.27
(h k l)	$(0\,0\,2)_\kappa$	x	$(0\,0\,4)_\kappa$	$(0\,0\,6)_\kappa$	x	$(0\,0\,8)_\kappa$	$(0\,0\,10)_\kappa$
$2\theta_{bulk}$ [°]	19.12	x	38.80	59.76	x	83.26	112.30
Q_{bulk}/Q_0	1.02	x	2.03	3.05	x	4.07	5.08
d_{bulk} [Å]	4.76	x	2.32	1.55	x	1.16	0.93
I	1.00	x	0.95	0.25	x	0.23	0.04
(h k l)	$(\bar{2}\,0\,1)_\beta$	x	$(\bar{4}\,0\,2)_\beta$	$(\bar{6}\,0\,3)_\beta$	x	$(\bar{8}\,0\,4)_\beta$	$(\bar{10}\,0\,5)_\beta$
$2\theta_{bulk}$ [°]	18.94	x	38.42	59.14	x	82.30	110.70

Q_{bulk}/Q_0	1.01	x	2.01	3.02	x	4.03	5.04
d_{bulk} [Å]	4.68	x	2.34	1.56	x	1.17	0.94
I	1.00	x	0.32	0.79	x	0.03	0.29
(h k l)	x	x	$(2\,0\,2)_\beta$	x	x	$(4\,0\,4)_\beta$	x
$2\theta_{bulk}$ [°]	x	x	38.42	x	x	82.32	x
Q_{bulk}/Q_0	x	x	2.01	x	x	4.07	x
d_{bulk} [Å]	x	x	2.34	x	x	1.17	x
I	x	x	0.23	x	x	0.01	x
(h k l)	x	$(3\,1\,0)_\beta$	x	x	$(6\,2\,0)_\beta$	x	x
$2\theta_{bulk}$ [°]	x	37.30	x	x	79.50	x	x
Q_{bulk}/Q_0	x	1.96	x	x	3.92	x	x
d_{bulk} [Å]	x	2.41	x	x	1.20	x	x
I	x	0.04	x	x	0.04	x	x

Table 5: List of experimental θ/2θ Bragg peak positions and intensities of Ga_2O_3/γ-Al_2O_3(111)/Si(001) and literature bulk Bragg peak positions* and their expected intensities after equation (S.3) (unit volume) for plausible Ga_2O_3 polymorph orientations based on structure symmetry and previous reports. Experimental peak intensities are normalized to the strongest film peak (Peak 1). Bulk peak intensities are normalized to the strongest peak contained in the table for a particular polymorph, i.e. the relative intensities for the bulk structures are only meaningful within the same polymorph. By means of the normalization Q/Q_0 (with $Q_0 = d(\text{Peak } 1)^{-1}$) we can identify harmonic peaks in the experimental data set: Hence, peaks 1, 3, 4, and 7 are most likely harmonics of the same plane family, and likewise Peaks 2 and 5 are likely harmonics of the same plane family. By using this Q/Q_0 ratio we can see that: The α-polymorph in (00.1)-orientation at first sight can be excluded based on lattice constants, but caution has to be taken since the bulk data is for the high-pressure phase and is likely different in thin film form. However, based on intensities this polymorph and orientation can likely be excluded. The γ-, κ-, and β-polymorphs in the given orientations are all likely candidates based on their Q/Q_0 values. However, we also see that within the considered possibilities, the harmonic Peaks 2 and 5 are only explained well by β-Ga_2O_3 in (310)-orientation. Based on intensities, a mixture of β-Ga_2O_3 epitaxial orientation variants seems to explain the data best. The absence of Peak 6 in the experimental data seems plausible for β Ga_2O_3 due to the low intensity of the $(\bar{8}04)/(404)$ peaks; this is not so for γ- and κ-polymorphs. Therefore, we deem it highly likely that all peaks originate from β-Ga_2O_3. This is corroborated by the elevated growth temperatures and the pole figure scan shown in the main text of the article. By means of the pole figure scan we can exclude significant volume fractions of the α-, γ- and κ-polymorphs and confirm β-Ga_2O_3 with 48 epitaxial orientation variants as described in the main article.

*entries: #1638495, #1638490, # 1638497 and #1812181 in reference [87] .

[0319] We would like to mention here that the presence of the (101) phase can be easily overlooked in a θ/2θ scan since its peaks overlap with the peaks of the $(\bar{2}01)$ phase. Only a careful analysis of the

relative peak intensity ratios and relative peak positions of the harmonic reflections belonging to the same plane family can reveal the corresponding phase's volume fraction. For instance in the recent work [98] the observation of the disappearing of $(\bar{2}01)$ and $(\bar{6}03)$ peaks, and reduction of the $(\bar{4}02)$ peak in β-Ga_2O_3 films grown at elevated growth temperature by PAMBE on sapphire substrate have been interpreted as a reduction in crystal quality of the epilayer. However, in consideration of the overlap of $(\bar{4}02)$ and (202) peaks the data could also be interpreted as a suppression of the $(\bar{2}01)$ phase and instead emergence of (101) as dominant phase, since the (202) is the only harmonic of (101) with substantial diffraction intensity - see Figure 21B and Table 5. If the {310} phase was also present the (310) peak, owing to its small structure factor, should show up as a weak shoulder to the left of the $(\bar{4}02)$ and (202) peaks. Since the (620) peak is even weaker the {310} phase can also easily be missed for a thin film in a low resolution θ/2θ scan.

	0	1	2	3	4	5	6	7	8	9	10	11
$(40\bar{1})_{(101)}\theta$	84.0	84.0	84.0	84.0	84.0	84.0	84.0	84.0	84.0	84.0	84.0	84.0
$(40\bar{1})_{(101)}\phi$	-45.0	-15.0	15.0	45.0	75.0	105.0	135.0		-	-	-	-75.0
$(\bar{2}02)_{(101)}\theta$	50.0	50.0	50.0	50.0	50.0	50.0	50.0	50.0	50.0	50.0	50.0	50.0
$(\bar{2}02)_{(101)}\phi$		165.0	-	-	-	-75.0	-45.0	-15.0	15.0	45.0	75.0	105.0
$(002)_{(101)}\theta$	22.5	22.5	22.5	22.5	22.5	22.5	22.5	22.5	22.5	22.5	22.5	22.5
$(002)_{(101)}\phi$		165.0	-	-	-	-75.0	-45.0	-15.0	15.0	45.0	75.0	105.0
$(\bar{4}01)_{(\bar{2}01)}\theta$	23.4	23.4	23.4	23.4	23.4	23.4	23.4	23.4	23.4	23.4	23.4	23.4
$(\bar{4}01)_{(\bar{2}01)}\phi$		165.0	-	-	-	-75.0	-45.0	-15.0	15.0	45.0	75.0	105.0
$(\bar{2}02)_{(\bar{2}01)}\theta$	22.5	22.5	22.5	22.5	22.5	22.5	22.5	22.5	22.5	22.5	22.5	22.5
$(\bar{2}02)_{(\bar{2}01)}\phi$	-45.0	-15.0	15.0	45.0	75.0	105.0	135.0		-	-	-	-75.0
$(002)_{(\bar{2}01)}\theta$	50.0	50.0	50.0	50.0	50.0	50.0	50.0	50.0	50.0	50.0	50.0	50.0
$(002)_{(\bar{2}01)}\phi$	-45.0	-15.0	15.0	45.0	75.0	105.0	135.0		-	-	-	-75.0
$(40\bar{1})_{(310)}\theta$	58.3	58.3	58.3	58.3	58.3	58.3	58.3	58.3	58.3	58.3	58.3	58.3
$(40\bar{1})_{(310)}\phi$		-	-	-98.6	-68.6	-38.6	-8.6	21.4	51.4	81.4	111.0	141.0
$(20\bar{2})_{(310)}\theta$	81.7	81.7	81.7	81.7	81.7	81.7	81.7	81.7	81.7	81.7	81.7	81.7
$(20\bar{2})_{(310)}\phi$	-	-	-86.0	-56.0	-26.0	4.0	34.0	64.0	94.0	124.0	154.0	-
$(002)_{(310)}\theta$	81.7	81.7	81.7	81.7	81.7	81.7	81.7	81.7	81.7	81.7	81.7	81.7
$(002)_{(310)}\phi$	56.0	86.0	116.0	146.0	176.0	-	-	-94.0	-64.0	-34.0	-4.0	26.0
$(\bar{4}01)_{(\bar{3}10)}\theta$	58.3	58.3	58.3	58.3	58.3	58.3	58.3	58.3	58.3	58.3	58.3	58.3
$(\bar{4}01)_{(\bar{3}10)}\phi$	98.6	129.0	159.0	-	-	-	-81.4	-51.4	-21.4	8.6	38.6	68.6
$(\bar{2}02)_{(\bar{3}10)}\theta$	81.7	81.7	81.7	81.7	81.7	81.7	81.7	81.7	81.7	81.7	81.7	81.7
$(\bar{2}02)_{(\bar{3}10)}\phi$	56.0	86.0	116.0	146.0	176.0	-	-	-94.0	-64.0	-34.0	-4.0	26.0
$(00\bar{2})_{(\bar{3}10)}\theta$	81.7	81.7	81.7	81.7	81.7	81.7	81.7	81.7	81.7	81.7	81.7	81.7
$(00\bar{2})_{(\bar{3}10)}\phi$	-	-	-86.0	-56.0	-26.0	4.0	34.0	64.0	94.0	124.0	154.0	-

Table 6: Expected pole figure coordinates of the relevant β-Ga_2O_3 reflections, based on the orientational model presented in the main text for each of the twelve in-plane variants arising from the four out-of-plane orientations (101), $(\bar{2}01)$, {310} and $\{\bar{3}10\}$, and based on bulk lattice constants of β-Ga_2O_3. In each row the upper angle is the polar angle θ in degree (measured from the north pole downwards) and

the lower angle in the azimuthal angle ϕ in degree. A polar angle of 0° corresponds to the Si [001] out-of-plane direction and an azimuthal angle of 0° corresponds to the Si [110] in-plane direction.

Supplementary Density Functional Theory Calculations

[0320] Density functional theory (DFT), as implemented in the Vienna ab initio Simulation Package (VASP) code, is used to perform all calculations [99]. The Perdew-Burke-Ernzerhof (PBE) generalized-gradient approximation (GGA) is used for the exchange correlation energy functional. We use projector-augmented-wave potentials [100], to describe Ga and O with a cut-off energy of 500 eV for bulk optimizations. The valence electron configurations used are $4s^2 3d^{10} 4p^1$ for Ga and $2s^2 2p^4$ for O. Each self-consistent electronic calculation is converged to within 10^{-6} eV per cell, and the ionic relaxation is iterated until the forces are less than 0.01 eV/Å. For the Brillouin zone integration of bulk Ga_2O_3 (space group $C2/m$, 12), a 5x9x11 Monkhorst-Pack grid is used. For bulk Ga (space group $Abma$, 64), a 12×12×12 Monkhorst-Pack k-point mesh is used.

[0321] The lattice parameters calculated for bulk Ga_2O_3 are a = 12.445, b = 3.084 Å, c = 5.876 Å, and β = 103.73°, which compare favorably with the experimental values of a = 12.22 Å, b = 3.04 Å, c = 5.80 Å and β = 103.75° [101], and theoretical values of a = 12.446, b = 3.083 Å, c = 5.876 Å, and β = 103.70° [102].

[0322] To create the slabs, we used surface-oriented basis transformations on the conventional unit cell using methods described in reference [103]. The transformation matrices used are shown in Table 7, below. Each unit cell is repeated along the c-axis to create a 15-20 Å thick supercell and a 15 Å vacuum is added to create the slab. For slab optimizations, a 600 eV energy cutoff is used, and the convergence criteria are the same as those used for the bulk optimizations. For Brillouin zone integration of the $(\bar{2}01)$, (310), and (101) slabs, 7x7x1, 5x7x1, and 5x25x1 Monkhorst-Pack k-point meshes are used, respectively.

[0323] We calculate the surface energies using the following equation,

$$\Upsilon_{surface} = \frac{1}{2A}\left[E_{slab} - N_{Ga}(E_{Ga} + \mu_{Ga}) - \frac{1}{2}N_O(E_{O_2} + \mu_{O_2})\right]$$

[0324] In this equation, $\Upsilon_{surface}$ is the surface energy, A is the surface area with a factor of 2 accounting for both surfaces, E_{slab} is the energy of the Ga_2O_3 slab, N_X is the number of X atoms in the Ga_2O_3 slab, E_X is the energy of one unit cell of bulk X, and μ_X is the chemical potential of bulk or molecular X.

[0325] To simplify the number of variables in this equation, we use the relationship:

$$E_{Ga_2O_3} + \mu_{Ga_2O_3} = 2(E_{Ga} + \mu_{Ga}) + \frac{3}{2}(E_{O_2} + \mu_{O_2})$$

[0326] We assume that the surface is in equilibrium with its own bulk, hence $\mu_{Ga_2O_3}$ is equal to 0 eV. The formation energy of Ga_2O_3 is defined as $E_f = E_{Ga_2O_3} - 2E_{Ga} - \frac{3}{2}E_{O_2}$. Using this definition and rearranging the equation above, we get the relationship $\mu_{Ga} = \frac{1}{2}\left(E_f - \frac{3}{2}\mu_{O_2}\right)$. We can then allow the chemical potential to vary over the range $0 \leq \mu_{O_2} \leq \frac{2}{3}E_f$, where $\mu_{O_2} = 0$ eV represents oxygen-rich

conditions and $\mu_{O_2} = \frac{2}{3}E_f$ represents Ga-rich conditions. We determined that the formation energy of Ga_2O_3 is -9.31 eV, which is less stable than the experimental value of -11.3 eV [104], but comparable to the formation energy value of -9.3 eV calculated by Zacherle et. al [102].

[0327] Figures 22A-22C illustrate ideally terminated surfaces with lattice planes marking the terminations studied. To the left of each slab, the top and bottom axes correspond to the axes for the β-Ga_2O_3 conventional unit cell and the axes for the slab, respectively. Ga and oxygen atoms are labeled 2201 and 2203, respectively. In Figure 22A, the dark blue 2205 (pink 2210) plane marks the Ga-terminated (O-terminated) surface along the (310) surface termination. For the $(\bar{2}01)$ plane, we studied two distinct O-terminations and two distinct Ga-terminations denoted by the labels (A) and (B) in Figures 22B. (b) The dark blue (2220), pink (2230), light blue (2240), red (2250), and green (2260) planes mark the O-terminated (A), Ga-terminated (A), O-terminated (B), Ga-terminated (B), and mixed-terminated surfaces along the $(\bar{2}01)$ surface termination, respectively. In Figure 22C, the dark blue 2270 (pink 2280) plane marks the O-terminated (mixed-terminated) surface along the (101) surface termination.

[0328] Figures 23A-23C illustrate lowest energy terminations before and after relaxation superimposed for the (310) O-termination (Figure 23A), $(\bar{2}01)$ mixed-termination (Figure 23B), and (101) O-termination (Figure 23C). In Figures 23A-23C, 2310 (gray) denotes Ga atoms before relaxation, 2320 (green) denotes Ga atoms after relaxation, 2330 (white) denotes oxygen atoms before relaxation, and 2340 (red) denotes oxygen atoms after relaxation. To the left of each slab, the top and bottom axes correspond to the axes for the β-Ga_2O_3 conventional unit cell and the axes for the slab, respectively.

[0329] To determine the lowest energy surface reconstruction of the (310) plane, we studied one Ga-terminated and one O-terminated surface (Figure 22A). The average surface energy of the O-terminated surface (Figure 23A) is 4.267 J m^{-2}, which is higher than the surface energy value of 3.671 J m^{-2} of the Ga-terminated surface. For the $(\bar{2}01)$ plane, we studied five surface terminations shown in Figure 22B. The lowest value for the surface energy is 0.768 J m^{-2} and this was achieved with the mixed termination (Figure 23B). Although a different calculation method was used, the surface energy and relaxation energy we determined is comparable to the values reported by Schewski et. al [105]. For the (101) plane, we studied a mixed-terminated surface and an O-terminated surface (Figure 22C). The surface energy of the O-terminated surface (Figure 23B) is 1.510 J m^{-2}, which is slightly lower than the surface energy of 1.573 J m^{-2} for the mixed-terminated surface. The values we calculated are comparable to the surface energy value of 1.5-2 J m^{-2} reported by Schewski et. al [105].

Surface termination	Transformation matrix
$(\bar{2}01)$	$\begin{pmatrix} 0.5 & 0.5 & 1 \\ -0.5 & 0.5 & -1 \\ 0 & 0 & 1 \end{pmatrix}$

(310)	$\begin{pmatrix} -0.5 & 1.5 & 0 \\ 0 & 0 & 1 \\ 0 & 1 & 0 \end{pmatrix}$
(101)	$\begin{pmatrix} 1 & 0 & -1 \\ 0 & 1 & 0 \\ 1 & 0 & 4 \end{pmatrix}$

Table 7: Transformation matrices used to create surface-oriented unit cells along the $(\bar{2}01)$, (310), and (101) planes.

Surface	Termination	Environment	Surface energy before relaxation	Average surface energy before relaxation	Surface energy after relaxation	Average surface energy after relaxation	Relaxation energy
$(\bar{2}01)$	Ga (A)	Ga-rich	1.320	2.937	1.204	2.821	0.116
		O-rich	4.554		4.438		
$(\bar{2}01)$	O (A)	Ga-rich	7.347	5.730	5.212	3.595	2.135
		O-rich	4.113		1.978		
$(\bar{2}01)$	Ga (B)	Ga-rich	1.276	2.893	1.211	2.828	0.065
		O-rich	4.510		4.445		
$(\bar{2}01)$	O (B)	Ga-rich	7.268	5.651	7.014	5.397	0.254
		O-rich	4.034		3.780		
$(\bar{2}01)$	Mixed	Ga- or O-rich	2.100	–	0.768	–	1.332
(310)	Ga	Ga-rich	1.796	3.995	1.472	3.671	0.324
		O-rich	6.194		5.870		
(310)	O	Ga-rich	9.618	7.418	6.466	4.267	3.151
		O-rich	5.219		2.068		
(101)	Mixed	Ga- or O-rich	2.724	–	1.573	–	1.150
(101)	O	Ga- or O-rich	3.431	–	1.510	–	1.920

Table 8: Computed surface energies (J m^{-2}) for the ideally terminated and reconstructed surfaces.

EXAMPLE 2: Gallia on STO-Buffered Silicon

[0330] For epitaxial integration, a buffer layer is essential since the interface between Ga_2O_3 and Si is not thermodynamically stable [126]. Integration via an oxide buffer layer is therefore an important step that provides a high-quality, well-defined template layer for subsequent growth by a faster method such as chemical vapor deposition (CVD), metal-organic CVD (MOCVD), or the recently reported suboxide

MBE [127-129]. $SrTiO_3$ (001) can be routinely epitaxially integrated onto Si (001) [130], and hence it could act as a buffer layer for growth of Ga_2O_3 on Si, which would then lead to the availability of large scale Ga_2O_3 epitaxial films. Electrical transport properties of β-Ga_2O_3 films grown on STO (100) were recently reported by Wang et al. and we expect films grown on STO-buffered Si to behave similarly [131].

[0331] Here we report the deposition of β-Ga_2O_3 thin films grown on both STO (001) and STO-buffered Si (001) substrates using PAMBE and investigate their structural properties in detail. STO has the attraction of being one of the few oxide materials that can routinely be directly integrated with Si (001) [130]. Since it can be *n*-type doped with Nb [132], STO can also function in the dual role of epitaxial template layer for Ga_2O_3 and as conductive bottom electrode. The β-Ga_2O_3 thin films have been characterized by RHEED, XPS, XRD, XRR, reflection electron-energy-loss spectroscopy (REELS), and TEM.

Experimental Conditions

[0332] In an embodiment of the present technology, single-side-polished STO (001) substrates with dimensions of 10x10x0.5 mm^3 were cleaned *ex situ* in acetone, 2-propanol, and de-ionized water, each for 10 min in an ultrasonic bath. The samples were loaded into the MBE growth chamber (base pressure $5x10^{-10}$ torr) on Mo sample holders held in place by a Mo spring clip exerting pressure onto the backside of the sample, and a ~0.5 mm protruding lip on the growth side of the sample. The sample was heated radiatively from the backside via a SiC heating coil placed above the sample with a set point of 775 °C (corresponding to a calibrated substrate temperature of ~670 °C measured for a Si substrate with a pyrometer) in an oxygen plasma for 30 min. The oxygen plasma was generated by an Oxford Applied Research HD25 radio-frequency plasma generator at 200 W forward power and 2.0 x 10^{-5} torr nominal O_2 pressure measured by an ion gauge located at the top of the growth chamber. A residual gas analyzer (RGA) located on the sidewall of the chamber confirmed that O_2 was the predominant gas species, with an atomic oxygen amount of about 10% at the RGA position. Before introducing oxygen into the chamber, the dual filament Ga effusion cell was heated to 900 °C and outgassed for 20 minutes. The cell temperature was then lowered to 880 °C and the Ga rate was measured in the high-vacuum atmosphere of typically low 10^{-8} torr (caused by the hot effusion cell, and predominantly H_2 as measured by the RGA) by a QCM. Typical metal growth rates at this cell temperature were about 1 Å/min. After ignition of the oxygen plasma, the Ga rate was measured again, usually achieving a deposition rate that was a factor of ~2.8 higher than for the bare Ga rate (using the same density setting for the QCM of 5.95 g/cm^3 since Ga and Ga_2O_3 densities are nearly identical). This difference is most likely due to a lower sticking coefficient of bare Ga due to larger surface tension. The Ga_2O_3 growth was performed under the same Ga cell and O-plasma conditions at a manipulator set-point temperature of 775 °C. This growth temperature was selected as it is the highest temperature that gives unity sticking coefficient for our oxygen flux, based on the model developed by Vogt and Bierwagen [133]. Higher substrate temperatures

provide better epitaxy but should not be too high as to result in significant Ga suboxide desorption. The STO buffer layer on Si was grown on a 2-inch Si (001) wafer [132], and the Ga_2O_3 film was grown on this pseudo-substrate under nominally the same conditions as used for the bare STO substrates. The QCM-measured GaO_x growth rate matched the observed rate of Ga_2O_3 on bare STO, as confirmed by *ex situ* XRR thickness measurements. The film surfaces grown on bare STO were monitored *in situ* during growth by RHEED with a 21-keV electron beam and *in situ* after growth in a secondary analysis chamber with a 15-keV electron beam for the STO-Si substrate. The thin film stoichiometry was measured *in situ* and post-growth by XPS with monochromatic Al-Kα and a VG Scienta R3000 hemispherical analyzer set at 200-eV pass energy and 0.8-mm slit size. The sample grown on STO-Si was also studied by REELS with 1.9-keV electrons and a Staib Auger probe. To determine the sample thickness, morphology, and crystal structure, XRD and XRR measurements were performed *ex situ* on a Rigaku Ultima IV diffractometer (Cu-Kα). TEM observations were made using an image-corrected Titan 80-300 operated at 300 kV.

Results

[0333] Figures 24A and 24B show RHEED patterns for the Ga_2O_3 thin films as grown on bare STO along STO ⟨100⟩ and ⟨110⟩ azimuths for a 20-nm film, while Figures 24C and 24D show the same azimuths for a 50-nm film. For each of those figures, the Ga_2O_3 films were grown on STO at 775 °C. Each of the RHEED patterns show four-fold symmetry upon azimuthal rotation of the sample. The horizontal spot spacings were used to infer the in-plane lattice spacings at the film surface after calibration to the known STO substrate spacings and are given as insets in each figure. The RHEED patterns have a spot-like nature indicating a slightly rough film surface or small lateral crystal grain size. It is apparent that the thicker film shows more modulation along the RHEED streaks, suggesting surface roughening with increasing film thickness. The RHEED patterns formed within minutes after deposition was initiated, and they confirmed that the sample surface remained crystalline throughout growth. Each pattern shows 4-fold symmetry, commensurate with the substrate symmetry on the high-symmetry azimuths. The horizontal streak spacing, indicating lattice spacings perpendicular to the electron beam direction, was determined by calibration to the substrate lattice constant of a = 3.905 Å. The RHEED streaks of the 50-nm film show stronger modulation along their length than observed for the 20-nm film, indicating a rougher surface; this is corroborated by XRR and cross-sectional TEM (see discussion of Figures 32A-32D and 33, below).

[0334] XPS measurements conducted *in situ* after growth indicated stoichiometric Ga_2O_3 films, as shown in Figures 34A-34C and discussed below. To characterize the crystal structure of the thin films, XRD was performed *ex situ*, and the results are shown in Figures 25A-25C for the 50-nm Ga_2O_3 film grown by PAMBE at 775 °C on STO (001). Figures 25A displays a 2θ-θ out-of-plane diffraction pattern with the diffraction vector $\vec{Q}$ aligned along STO [001]; Figures 25B and 25C show $2\theta_\chi$-ϕ in-plane diffraction patterns taken at a grazing angle of incidence of 0.325°, with $\vec{Q}$ aligned along STO [100] in

Figure 25B, and along STO [110] in Figures 25C. The diffraction patterns are indexed by the Miller indices of the observed substrate and film reflections. These reflections are assigned to the β-Ga_2O_3 polymorph with (100) and $(\bar{1}12)$ out-of-plane orientation for this basal-plane thin-film growth. The presence of (100) follows from the peak positions and the peak area ratios of the harmonics in Figures 25A [134], whereas the presence of $(\bar{1}12)$ was corroborated from in-plane XRD measurements in Figures 25B and 25C due to overlapping peaks in Figure 25A [134]. The observed diffraction peaks are consistent with each of the two growth planes having four rotational domain variants aligned with the STO substrate, as shown in a reciprocal space simulation in Figures 35A and 35B, discussed below. The epitaxial relationships observed can be written as: β-Ga_2O_3 (100) [010] ‖ $SrTiO_3$ (001) ⟨110⟩, and β-Ga_2O_3 $(\bar{1}12)$ $[0\bar{2}1]$ ‖ $SrTiO_3$ (001) ⟨100⟩. The $(\bar{1}12)$ peak has a structure factor that is about one fifth of the (400) peak. Therefore, despite the smaller relative peak height in Figure 25A, a significant fraction of the sampled crystalline volume is crystalized in the $(\bar{1}12)$-orientation. A deconvolution by peak fitting of the (600) and $(\bar{1}12)$ peaks, and the (12 0 0) and $(\bar{2}24)$ peaks, is complicated by overlaps with the strong substrate signal and the broad width and small relative intensity of the film peaks. Considering the peak height ratio of the (12 0 0) and $(\bar{2}24)$ peaks (Figures 25A) in comparison with the β-Ga_2O_3 powder pattern intensity ratio as a rough approximation for the volume fractions in the thin film scattering volume, the volume fraction of the (100)-orientation is estimated to be about 3 times greater than that of the $(\bar{1}12)$-orientation. The prominent (400) peak in Figures 25C is asymmetric which could indicate a strain gradient of the plane spacing along the growth direction. The fitted XRD peak positions and plane spacings along with and their deviation from the bulk values of β-Ga_2O_3 from Figures 25A-25C are given in the tables provided in Figures 36A-36C, discussed below.

[0335] The epitaxial texture of the films is confirmed by cross-sectional TEM images displayed in Figures 26A-26C. Figure 26A is a low-magnification TEM image of a 20 nm Ga_2O_3 film grown at 775 °C, as observed along the [100] zone axis of STO. Figure 26B is a high-magnification TEM image, where the film appears ordered with atomic planes running parallel and perpendicular to the substrate film interface. Figure 26C is an FFT of the image in Figure 26B; spots originating from the Ga_2O_3 thin film are consistent with the model obtained from XRD. The crystallinity in the film extends from the substrate up to the film surface, but strong granularity of the film is apparent, indicating a small crystal grain size of ~ 5-10 nm, and leads to the observation of Moiré patterns in some regions due to overlap in the electron-beam direction. Figure 26A shows a low magnification image and reveals an uneven film surface, while the high-magnification image in Figure 26B shows atomic planes of the film running parallel and perpendicular to the substrate surface, closely aligned with the substrate planes. In Figure 26C, the FFT spots can be indexed by reference to the STO substrate peaks and by the prominent β-Ga_2O_3 peaks, which are consistent with the XRD data.

[0336] Based on the observed epitaxial relationships, a structural model is presented in Figures 27A and 27B. Lattice matching is illustrated for β-Ga_2O_3 $(\bar{1}12)$ in Figure 27A and (100) in Figure 27B

surface-oriented cells placed on top of STO (001). The conventional cells of β-Ga_2O_3 in $(\bar{1}12)$-orientation or (100)-orientation are also shown in relation to the surface-oriented cells (details can be found in Figures 37A-37D, discussed below). The surface-oriented cells are shifted from the STO (001) surface by half a STO unit cell for clarity. The implied atomic bonding at the interface is not necessarily representative of the actual experimental bonding geometry and needs further investigation. However, the O and Sr-O sub-lattice matching can be seen to play an important role for the epitaxial relationships. The β-Ga_2O_3 $(\bar{1}12)$ surface-oriented cell was constructed such that the $\vec{a}_S$ and $\vec{b}_S$ lattice vectors are: 1) contained in the $(\bar{1}12)$ plane of the conventional cell; 2) enclose an angle of nearly 90° (89.989°); and 3) have the shortest lengths compatible with this structural arrangement. Their lengths are a_S = 23.75 Å and b_S = 8.40 Å, leading to lattice mismatches of -1.2 % and -2.4 % with respect to the STO 6x2 surface cell shown in Figure 27A. The surface-oriented cell of β-Ga_2O_3 (100) is obtained by relabeling the unit cell vectors such that the $\vec{a}_S$ and $\vec{b}_S$ lattice vectors are contained in the (100) plane of the conventional cell, and by doubling the cell along the original [010] direction. The lattice mismatch is then given with regards to a $(\sqrt{2}\,x\,\sqrt{2})R(45°)$ surface cell of STO as -9.0 % for a_S = 6.08 Å and -4.8 % for b_S = 5.81 Å. The additional domain orientations of β-Ga_2O_3 $(\bar{1}12)$ and (100) can be obtained by rotating the depicted surface-cells by multiples of 90° about the STO [001] direction.

[0337] Motivated by the epitaxial matching, despite rotational symmetry mismatch, of monoclinic β-Ga_2O_3 and cubic $SrTiO_3$ (001), we have performed epitaxial integration with a 2-inch-diameter Si (001) wafer using a $SrTiO_3$ buffer layer under nominally identical growth conditions as used for the bare STO substrate. The structural, morphology, and thickness characterization results are shown in Figures 28A, 28B, 29A-29C, 30A and 30B. Figures 28A and 28B are RHEED images for STO <100> and STO <110>, respectively, taken with a 15 keV electron beam of Ga_2O_3/$SrTiO_3$/Si. The RHEED pattern of Figure 28 is qualitatively similar to the RHEED patterns of Ga_2O_3 grown on bulk STO, as shown in Figures 24A-24D. Differences in brightness and contrast are likely due to the use of a different RHEED chamber system with smaller electron beam energy, and larger wafer size allowing shallower incidence angle.

[0338] Figure 29A depicts XRD patterns showing a θ-2θ diffractogram of a 15 nm film of Ga_2O_3 grown by PAMBE at 775 °C on the STO (100) buffer layer on Si (001). The diffractogram of Figure 29A looks very similar to the diffraction patterns of Ga_2O_3 directly grown on STO, except for the finite-size oscillations of the STO (001) and (002) peaks and the presence of the Si substrate peaks. Figures 29B and 29C depict XRD patterns showing θ-2θ diffractogram of in-plane XRD scans along STO [110] and [100], respectively. The STO peaks are comparatively weak relative to the bulk substrate scans in Figures 25B and 25C. However, the same Ga_2O_3 peaks appear as for the case of the STO bulk substrate, although with different intensity ratios.

[0339] Figure 30A depicts an XRR curve of Ga_2O_3 grown on STO-buffered Si. The simulation (red curve 3010) reveals a thickness of 15.4 nm for Ga_2O_3 and 18.2 nm for STO, which is consistent with the high resolution TEM cross-section images. Figure 30B depicts a low-magnification TEM image of a 15-

nm Ga_2O_3 film grown at 775 °C on STO-buffered Si (001) projected along the Si (110) [110] zone-axis (equivalent to the STO (100) [100] zone-axis). Columnar growth of Ga_2O_3 is observed along with a Moiré pattern caused by the overlap of granular but ordered crystallites. A thin SiO_2 interlayer can be observed between STO and the Si substrate.

[0340] Additional electron-energy-loss spectroscopy (EELS) experiments were performed on the β-Ga_2O_3 film grown on Si. A band gap of 4.5-5.2 eV is extracted from the fits, consistent with literature data for Ga_2O_3 [106]. For details see Figures 38A and 38B, discussed below.

Discussion

[0341] Unlike the MOCVD growth of Ga_2O_3 on STO [122], in the present study we observe crystallization of Ga_2O_3 as-grown with the use of MBE and growth temperature of 670°C. Beside the (100)-orientation, we additionally observe the $(\bar{1}12)$ out-of-plane orientation of β-Ga_2O_3. The STO in this study is TiO_2-terminated due to the water treatment of the surface [135]. The TiO_2-plane contains an oxygen surface net that is like the face of an oxygen-based *fcc* cell and hence provides a template layer for the β-Ga_2O_3 distorted *fcc* oxygen sublattice. This *fcc* oxygen-sub-lattice of β-Ga_2O_3 has its six cube faces roughly aligned with the plane families {100}: (100), $(\bar{1}00)$; and $\{\bar{1}12\}$: $(\bar{1}12)$, $(1\bar{1}2)$, $(11\bar{2})$, and $(\bar{1}\bar{1}2)$. Furthermore, the Ga-O bonds of the distorted oxygen octahedra about the octahedral Ga2 sites of β-Ga_2O_3 are roughly aligned with the normal vectors of these planes. Hence, epitaxy on a cubic (001) substrate like $SrTiO_3$ is expected to be determined by the matching of these sub-lattice planes with the substrate basal plane in a "cube-on-cube" manner, and the octahedral cation-oxygen bonding direction being continued across the interface.

[0342] The $(\bar{1}12)$ family of surfaces do not appear to have been reported as growth surfaces for β-Ga_2O_3 bulk growth or epitaxy in the literature, and it is also not a commonly known surface cut for bulk substrates [107]. This may indicate that they are high energy surfaces, which is partially corroborated by the observations in this study that they are observed at high growth temperature. To support this assessment, we performed a detailed theoretical analysis. Using density functional theory, we calculated the surface energies of the (100) and $(\bar{1}12)$ surface terminations of β-Ga_2O_3.

[0343] To calculate the surface energy, we used the following relation:

$$\gamma_{surface} = \frac{1}{2A}\left[E_{slab} - N_{Ga}(E_{Ga} + \mu_{Ga}) - \frac{1}{2}N_O(E_{O_2} + \mu_{O_2})\right]$$

[0344] In this equation, $\gamma_{surface}$ is the surface energy, A is the surface area with a factor of 2 accounting for the top and bottom surfaces, E_{slab} is the energy of the Ga_2O_3 slab, N_{Ga} (N_O) is the number of Ga (O) atoms in the Ga_2O_3 slab, E_{Ga} (E_{O_2}) is the energy of one unit cell of bulk Ga (molecular O_2), and μ_{Ga} (μ_{O_2}) is the chemical potential of bulk Ga (molecular O_2). To simplify the number of variables in this equation, we use the relationship:

$$E_{Ga_2O_3} + \mu_{Ga_2O_3} = 2(E_{Ga} + \mu_{Ga}) + \frac{3}{2}(E_{O_2} + \mu_{O_2})$$

[0345] The details of the methods used for these calculations are outlined, below, in the section entitled "Supplemental Material for Example 2." For the (100) surface, we used two stoichiometric slabs and found that the surface energy of the mixed-terminated surface is 0.5 J/m^2 and it is 0.8 J/m^2 for the O-terminated surface. The surface energy values we have calculated are lower than the values reported by Bermudez [136] who used different computational methods. However, we do find that the 0.3 J/m^2 difference in energy between the (100)-A and (100)-B is comparable to the energy difference of 0.5 J/m^2 reported by Bermudez. To our knowledge, calculations of the $(\bar{1}12)$ surface termination have not been reported previously. For the $(\bar{1}12)$ termination, we used a non-stoichiometric slab with a mixed-termination and found the surface energy is 4.0 J/m^2 in a Ga-rich environment and 2.0 J/m^2 in an O-rich environment. This suggests that thermodynamics would not favor the $(\bar{1}12)$ termination. However, thermal expansion mismatch and lattice mismatch to the substrate, or symmetry considerations as well as growth kinetics, could also play a crucial role in the observation of this growth surface for β-Ga_2O_3 on STO (001).

[0346] Figure 31 depicts a plot of surface energies of several surface terminations along the (100), $(\bar{1}12)$, $(\bar{2}01)$, (310) and (101) surfaces with respect to the Ga chemical potential where 0 and -4.65 eV represent Ga-rich and O-rich environments, respectively. In Figure 31, we compare the surface energies of the (100) and $(\bar{1}12)$ surfaces to several other β-Ga_2O_3 surface terminations we have previously reported [125], and confirm that the (100) mixed terminated surface is the most energetically stable surface termination under Ga- or O- rich environments whereas the $(\bar{1}12)$ surface termination is not energetically favorable when solely considering surface energies.

[0347] The horizontal RHEED spot spacings in Figures 24A and 24C along STO [100]-azimuths are 2.1 ± 0.1 Å, commensurate with either β-Ga_2O_3 {11-2} planes of bulk lattice spacing 2.098 Å (for (100)-oop-orientation) or {600} of 1.979 Å (for {-112} oop-orientation). The lattice spacings in Figure 24B and 24D along STO [110]-azimuths are 2.9 ± 0.1 Å, commensurate with either β-Ga_2O_3 {020} of 1.518 Å and {-1,0,2} of 2.903 Å (for {100}-oop-orientation), or β-Ga_2O_3 {7,-1,-2} of 1.440 Å and {5,1,2} of 1.440 Å (for {-112}-oop-orientation). The RHEED analysis is complicated by the multi-domain structure of the film and the large quantitative error inherent to this method, but the observed spacings are in good agreement with the expected values in comparison with the other structural results from XRD and TEM.

[0348] The epitaxial growth of (100) β-Ga_2O_3, even in the case of homo-epitaxy on a non-vicinal substrate, gives rise to stacking faults and twin boundaries (mirror about (100) with a *c*/2-glide) [137]. The mirror twin and stacking faults could possibly be avoided by using a vicinal (100) substrate with off-cut along $[00\bar{1}]$ at an optimal angle of ~6°. Such substrates give rise to terrace steps formed by the energetically low $(\bar{2}01)$ surface facet (~0.8 J/m^2) of 1 ML height (1 ML = 5.8 Å) preventing the stacking faults, as opposed to the high-energy (001) surface facet (~1.25 J/m^2) for off-cut along [001] which shows 1-2 ML step heights [137]. Such faceting could also be a contributing factor to the roughening

observed in these Ga_2O_3 thin films with increasing film thickness. For the hetero-epitaxy of β-Ga_2O_3 on STO (001), additional defects are expected based on the in-plane lattice mismatch and stacking faults due to the non-commensurate terrace step height of a_{STO} / 2 for mixed-terminated STO or a_{STO} for singly terminated STO. Further, in-plane rotational variants are observed, due to the higher four-fold symmetry of STO in the growth plane compared to the low symmetry of monoclinic β-Ga_2O_3 [138, 139]. It should be mentioned that the (100) planes have a stacking height of 11.9 Å ~3 a_{STO} = 11.7 Å. Thus, in order to avoid stacking faults for (100) β-Ga_2O_3 it could be useful to achieve a step bunching of 3-unit-cell height on a vicinal STO substrate. The vicinal substrate could further contribute to reducing the number of in-plane variants of β-Ga_2O_3. Such an approach, using a vicinal substrate to suppress in-plane variants, has been used successfully in the hetero-epitaxy of β-Ga_2O_3 on corundum Al_2O_3 [127]. The ML height for the $(\bar{1}12)$ planes is ~ 2.1 Å and is therefore better matched to a single multiple of a_{STO}. We have observed no evidence for any γ -Ga_2O_3 interlayer by TEM or XRD.

Concluding Remarks for Example 2

[0349] In summary, we have demonstrated the successful epitaxial integration of β-Ga_2O_3 on $SrTiO_3$ (001) and $SrTiO_3$-buffered Si (001). The films are crystalline as grown. Two basal growth planes (100) and $(\bar{1}12)$ of β-Ga_2O_3, each with four in-plane rotational domain variants, are observed. Small crystal grains result from the symmetry and lattice mismatch between film and substrate. STO serves as a buffer layer to prevent Si oxidation and reaction between Ga_2O_3 and Si during growth and also acts as a template to guide oxide-on-oxide epitaxial growth. The epitaxial integration of Ga_2O_3 with Si serves as a template layer for subsequent fast deposition methods and could enable the fabrication of large area wafers that in turn could advance Ga_2O_3-based technologies.

Supplemental Material for Example 2

[0350] This supplementary material for Example 2 provides additional supporting figures and tables, electron energy loss spectroscopy measurements, and for the details of density functional calculations.

Additional TEM Analysis

[0351] Figures 32A-32C depict cross-section TEM images taken along the STO [100] zone axis at progressively higher magnification, as indicted by the scale bar. Figure 32D depicts the FFT of Figure 32C.

[0352] Figure 33 depicts an indexing of FFT of a TEM image of 50-nm Ga_2O_3 film, consistent with the model of four rotational in-plane variants for the (100) and $(\bar{1}12)$ basal growth planes.

X-ray photoelectron spectroscopy

[0353] Figures 34A-34C: XPS data taken *in situ* after PAMBE growth of a 50 nm gallia film on STO with a VG Scienta spectrometer with monochromatic A1-Kα and R3000 hemispherical analyzer at 200 eV pass energy. Figure 34A is a survey spectrum, no core-levels of Sr or Ti are observed, the film is therefore thicker than the information depth of the film layer (>5 EAL), no impurity elements or surface contamination within the accuracy of XPS. Figure 34B is the O 1*s* core-level. Figure 34C is the Ga 3*p*

core-level. For the quantification of oxygen to gallium ratio in the gallia film we used the O 1*s* and Ga 3*p* core-levels. We obtain a ratio of 1.52, i.e., the oxygen and gallium percentages are 60 % and 40 %. Hence within the accuracy of XPS the film is stoichiometric Ga_2O_3.

X-ray analysis details

[0354] Figures 35A and 35B: Reciprocal space simulation β-Ga_2O_3 (100) and $(\bar{1}12)$ basal in the (*hk*0) plane of STO. Each out-of-plane orientation should give rise to four rotational variants due to symmetry mismatch between the β-Ga_2O_3 growth planes and STO (001) [140, 141]. The color of the reciprocal lattice points fades between white and either orange or green, and the fading scales with the square of the structure factor for the given reflection. Lattice spacings consistent with the ones expected based on this model are observed along the anticipated directions in the in-plane XRD of Figures 25A-25C and the RHEED images of Figures 24A-24D.

[0355] The fitted peak positions and plane spacings in Figure 25A-25C are given in Figures 36A-36C, discussed below, along with their deviation from the bulk values of β-Ga2O3. The assigned Miller indices are consistent with the reciprocal space simulation shown in Figure 33. The fitted peak areas are not reported for the in-plane measurements since, in Figures 25B and 25C, those strongly depend on the incidence angle of the x-rays with respect to the film surface. The incident angle was set at $\omega \approx 0.325°$ but may slightly change upon azimuthal rotation of the sample during measurement resulting in a non-constant incidence angle.

[0356] Figures 36A, 36B and 36C provide tables of fitted peak positions and determined lattice spacing from the peaks in Figures 25A, 25B and 25C, respectively. The peak assignments are labelled by their Miller indices and association with the basal growth plane is color-coded. The lattice spacing deviations from the bulk values are also given. Black/red/blue refers to peaks from the STO layer; orange is for peaks from β-Ga_2O_3 (100); and green is for peaks from β-Ga_2O_3 $(\bar{1}12)$.

Lattice matching

[0357] These cells shown in Figures 27A and 27B were obtained using the transformations given in Table 9, below, acting on the basis vectors of the conventional unit cell.

Surface Termination	Transformation Matrix *P*
$(\bar{1}12)$	$\begin{pmatrix} 2 & 0 & 0 \\ 0 & 2 & 1 \\ 1 & -1 & 0 \end{pmatrix}$
(100)	$\begin{pmatrix} 0 & 0 & 1 \\ 2 & 0 & 0 \\ 0 & 1 & 0 \end{pmatrix}$

Table 9. Transformation matrices P used to create surface-oriented basis ($\vec{a}_S$, $\vec{b}_S$, $\vec{c}_S$) vectors of the cells depicted in Figures 27A and 27B from the conventional basis ($\vec{a}$, $\vec{b}$, $\vec{c}$) according to the transformation $(\vec{a}_S, \vec{b}_S, \vec{c}_S) = (\vec{a}_S, \vec{b}_S, \vec{c}_S)\boldsymbol{P}$.

[0358] Figures 37A-37D illustrate mutual orientation of the parallelepipeds for the unit cells of (100)-β-Ga_2O_3 and (001)-STO. In Figure 37A, the *b*-axis points along STO [1-10] and the *c*-axis along STO [110]. In Figures 37B-37D, epitaxial variants are related by a rotation about the *z*-axis of $\phi = n \cdot 90°$. The orientation of the conventional cell parallelepiped corresponding to (1-1-2)-β-Ga2O3 is not as easy to picture: The first variant corresponds to a -90° rotation about the *y*-axis of the β-Ga2O3 parallelepiped in Figure 37A, indicated by the rotating arrow. The other in-plane variants of (1-1-2) are also related by 90°- rotations about the *z*-axis.

Electron Energy Loss Spectroscopy

[0359] Additional electron-energy-loss spectroscopy (EELS) experiments were performed on the β-Ga_2O_3 film grown on Si. Figure 38A depicts a plot showing the spectrum from the high binding energy side of the O 1*s* XPS peak. The loss onset is fitted by straight lines and a band gap of 4.5-5.2 eV is extracted from the fits, consistent with literature data for Ga_2O_3.[142] Figure 38B depicts a plot showing the EEL spectrum from REELS experiments with low-incidence-angle electrons at 1.9 keV recorded under normal exit with a Staib Auger Probe.[143] (The negative intensity is attributed to a detector aberration). The band gap is underestimated due to the lower resolution of the measurement compared to Figure 38A. The qualitative shape of the curve, however, agrees very well with the literature.[144, 145] For Figure 38A, the EEL spectrum was obtained from the low kinetic energy side of the O 1*s* core-level in XPS withmonochromatic Al-Kα and recorded with a VG Scienta R3000 analyzer with 200-eV pass energy and 0.8-mm slit size. For Figure 38B, the EEL spectrum was obtained from REELS experiment with low-incidence-angle electrons at 1.9 keV recorded under normal exit.

Density Functional Theory Calculations

[0360] To perform our calculations, we used density functional theory (DFT) as implemented in the Vienna ab Initio Simulation Package (VASP).[146] For the exchange energy correlation functional,we used the generalized-gradient approximation (GGA) parametrized by Perdew-Burke-Ernerhof (PBE). We use a cutoff energy of 500 eV for all bulk optimizations and 600 eV for all slab calculations. We use projector-augmented-wave potentials [147] to describe Ga and O and the valence electron configurations used are $4s^2 3d^{10} 4p^1$ for Ga and $2s^2 2p^4$ for O. Each self-consistent electronic calculation is converged to within 10^{-6} eV per cell, and the ionic relaxation is iterated until the forces are less than 0.01 eV/Å. For the Brillouin zone integration of bulk Ga_2O_3 (space group *C2/m*) and bulk Ga (space group *Abma*), 5×9×11 and 12×12×12 Monkhorst-Pack k-point grids are used, respectively. The lattice parameters calculated for bulk Ga_2O_3 are a = 12.445, b = 3.084 Å, c = 5.876 Å, and β = 103.73°, which compare

favorably with the experimental values of a = 12.22 Å, b = 3.04 Å, c = 5.80 Å, and β = 103.75° [148] and theoretical values of a = 12.446, b = 3.083 Å, c = 5.876 Å, and β = 103.70°.[149]

Surface Termination	Transformation Matrix P
$(\bar{1}12)$	$\begin{pmatrix} -0.5 & -1.5 & -1 \\ 0.5 & -0.5 & 0 \\ 0 & 0 & -1 \end{pmatrix}$
(100)	$\begin{pmatrix} 0 & 1 & 0 \\ 0 & 0 & 1 \\ 1 & 0 & 0 \end{pmatrix}$

Table 10: Transformation matrices used to create surface-oriented unit cells along the $(\bar{1}12)$ and (100) planes.

[0361] The transformation matrices used to create unit cells for each surface were derived using the methods described in reference [150] and are provided in Table 10. For Brillouin zone integration of the (100) and $(\bar{1}12)$ slabs, 5×9×1 and 5×7×1 Monkhorst-Pack k-point meshes are used, respectively. Each slab was built using a supercell and vacuum regions that are at least 10 Å thick. Figures 39A-39C illustrate surfaces before and after relaxation superimposed for the (100) (Figure 39A), (100)-A (Figure 39B), and $(\bar{1}12)$ (Figure 39C) mixed terminations. To determine the lowest energy surface reconstruction of the (100) plane, we study the two stoichiometric mixed-terminated surfaces, shown in Figures 39A and 39B. For the $(\bar{1}12)$ plane, we study one nonstoichiometric mixed-terminated surface shown in Figure 39C.

Surface	**Environment**	**Surface energy before relaxation**	**Surface energy after relaxation**	**Relaxation energy**
(100)-A	-	1.264	0.774	0.490
(100)-B	-	0.688	0.459	0.229
(112)	Ga-rich	4.919	3.976	0.943
	O-rich	2.933	1.990	

Table 11: Computed surface energies (J m^{-2}) for the ideally terminated and reconstructed surfaces.

[0362] To calculate the surface energy values listed in Table 11, we used the following relation:

$$\gamma_{surface} = (1/2A)\,[E_{slab} - N_{Ga}(E_{Ga} + \mu_{Ga}) - (1/2)N_O(E_{O2} + \mu_{O2})]$$

[0363] In this equation, $\gamma_{surface}$ is the surface energy, A is the surface area with a factor of 2 accountingfor the top and bottom surfaces, E_{slab} is the energy of the Ga_2O_3 slab, N_{Ga} (N_O) is the number of Ga (O) atoms in the Ga2O3 slab, E_{Ga} (E_{O2}) is the energy of one unit cell of bulk Ga (molecular O2), and μ_{Ga} (μ_{O2}) is the chemical potential of bulk Ga (molecular O_2).

[0364] To simplify the number of variables in this equation, we use the relationship:

$$E_{Ga2O3} + \mu_{Ga2O3} = 2(E_{Ga} + \mu_{Ga}) + (3/2)(E_{O2} + \mu_{O2})$$

[0365] Assuming the surface is in equilibrium with its own bulk, $\mu_{Ga_3O_3}$ is equal to 0 eV. We define the formation energy of Ga_2O_3 as $E_f = E_{Ga_3O_3} - 2E_{Ga} - \frac{3}{2}E_{O_2}$. Using this definition and rearranging the previous equation, we define the chemical potential of bulk Ga as $\mu_{Ga} = \frac{1}{2}\left(E_f - \frac{3}{2}\mu_{O_2}\right)$. We can then allow the chemical potential to vary over the range $0 \leq \mu_{O_2} \leq \frac{2}{3}E_f$, where $\mu_{O_2} = 0$ eV and $\mu_{O_2} = \frac{2}{3}E_f$ represent O-rich and Ga-rich conditions, respectively. We determined that the formation energy of Ga_2O_3 is -9.31 eV which is comparable to the formation energy value of -9.3 eV calculated by Zacherle et al. [149], but lower in magnitude compared to the experimental value of -11.3 eV [151].

EXAMPLE 3: Extension Cases For Examples 1-2

[0366] We present a route to integrate crystalline gallium oxide grown epitaxially on a silicon (001) substrate via an epitaxial strontium titanate (STO) buffer layer. Specifically, we produce samples with the following layer stack: silicon (001) substrate/thin film $SrTiO_3$ (buffer layer)/thin film Ga_2O_3. Such a materials system could be used as a seed layer for thick bulk-like MOCVD-grown Ga_2O_3 films or layers directly integrated on silicon, or can yield, via an etching process, free-standing gallium oxide films that can be transferred to other substrates. Gallium oxide is likely to find use in a wide variety of microelectronic (e.g., integrated circuits), micro-electromechanical system (MEMS), optoelectronic and power-electronics applications and devices. The STO buffer can be as thin as 5 nm or can be thicker (up to 20 nm) while the Ga_2O_3 epitaxial seed layer can range from 20 nm to 100 nm.

[0367] The layer stack according to the present technology has not previously been prepared, to the best of our knowledge. Present technologies for power-electronics applications tend to focus on millimeter-sized bulk-crystals of Ga_2O_3 grown by conventional crystal growth methods or thin films grown on isostructural substrates. The hetero-epitaxial integration of Ga_2O_3 onto silicon allows processing of gallium oxide technology in state-of-the-art semiconductor fabs specialized in the processing of silicon devices on large scale wafer diameters allowing for cost-effective production.

[0368] Ga_2O_3 cannot be directly grown on silicon due to a thermodynamically unstable interface favoring the formation of SiO_2 hence the $SrTiO_3$ seed, or buffer, layer is a crucial part of the present technology of epitaxial integration ofGa_2O_3 directly onto Si. The layer stacks according to the present technology enable the growth of large scale Ga_2O_3 bulk-like films on the Si wafer platform by serving as a template for subsequent fast deposition techniques like MOCVD or sputtering. An additional etching and polishing process could produce large scale free-standing Ga_2O_3 films that can be layer transferred

to other substrates for use in power-electronics devices. Power-electronics devices may require large area, bulk-like, Ga_2O_3 crystals and therefore a substrate like silicon that is available in large wafer diameters (200-300 mm) is more suitable than the available isostructural substrates commonly used for hetero-epitaxy of Ga_2O_3. "Bulk-like" in this context refers to the Ga_2O_3 being epitaxial rather than polycrystalline, and with thicknesses on the order of microns.

[0369] The present technology has the advantage of integrating the wide-gap semiconductor Ga_2O_3 directly on the Si semiconductor platform for which many etching and processing technologies are widely available. The current hetero-epitaxial growth of Ga_2O_3 are limited to the small wafer sizes of the currently availablesubstrate materials.

[0370] Since the silicon/STO platform is not very well lattice matched to Ga_2O_3, initially grown films are defective. However, if they act as a seed layer for further deposition of Ga_2O_3 by MOCVD or a similar method, this problem can be overcome as it is expected that the crystalline quality will drastically improve with increasing film thickness as long as there is a highly ordered nucleation layer. Furthermore, post-processing methods like annealing can further improve crystalline quality and polishing or etching can smoothen out a rough surface of such grown films to obtain high-quality free-standing Ga_2O_3 or Si/STO/Ga_2O_3 stacks. Another method to improve the lattice matching is to use a compositionally graded $Al_xGa_{1-x}O_3$ alloy as the initial seed layer, as Al_2O_3 has a smaller lattice constant more closely-matched with STO.

[0371] Ga_2O_3 is a material with prospective use in high-power-electronics. In order to be useful for power- electronics applications, bulk-size crystals are needed. The size of currently grown epitaxial thin films is limited by the substrate wafer size.

[0372] The present technology comprises the epitaxial integration of a Ga_2O_3 layer on a silicon (001) substrate by means of a thin $SrTiO_3$ buffer layer. The present technology also enables the integration and processing of Ga_2O_3 directly into the silicon processing line and allows for growth on large scale wafer substrates.

[0373] Layer stacks according to the present technology would allow the growth of large scale Ga_2O_3 bulk-like films on the Si wafer platform, which are required for power-electronics applications of Ga_2O_3. The present technology opens the door for a multitude of new use cases that have not yet been considered. Ga_2O_3 is also a potential semiconductor for optoelectronic applications due to its large bandgap which makes it transparent into the UV range. The epitaxial integration onto silicon layer enables the construction of a wide range of novel devices relying on the electronic and optical properties of Ga_2O_3. Potential examples include field-effect transistors, semiconductor devices, and sensor technology.

[0374] Figures 40A and 40B illustrate a wafer according to some embodiments of the present technology. In one embodiment, as shown in Figure 40A, the buffer layer is STO deposited onto Si (001) according to the present technology. In an example, Ga_2O_3 is then deposited onto the STO layer. In another embodiment, as shown in Figure 40B, STO is deposited onto Si (001) and then a layer of γ-

Al_2O_3 is then deposited onto the STO layer. In an example, Ga_2O_3 is then deposited onto the aforementioned Al_2O_3 layer.

[0375] Figure 41 provides examples of combining oxides with semiconductors epitaxially. As described in A.A. Demkov and A.B. Posadas, "Integration of Functional Oxides with Semiconductors," Spring, New York (2014), Si has been combined with perovskites and bixbyites. Other examples include spinel ($MgAl_2O_4$, γ -Al_2C), fluorite (e.g., CaF_2, ZrO_2), and rocksalt (e.g., MgO). Germanium has been combined with $BaTiO_3$ and Gd_2O_3. Silicon carbide has been combined with MgO and $LiNbO_3$.

[0376] As shown in Figures 42A-42E, difficulties of oxide/semiconductor epitaxy may arise from strain, thermal mismatch, wetting, and symmetry effects, as well as steps.

[0377] In one embodiment, gallia was grown on STO buffered Si under the following process conditions. The STO-buffered Si wafer was *ex situ* cleaned (acetone, 2-propanol, distilled water, each for minutes in sonicator). UHV was loaded on a molybdenum sample holder. Degassing was performed under O-plasma exposure (200W, $3x10^{-5}$ torr O_2 partial pressure). Ga_2O_3 growth was done at 775 °C with O-plasma and Ga cell temperature of 880 °C. Then, a cool down in O-plasma to 200 °C was done. *In situ* analysis included RHEED and XPS (using floodgun), and *ex situ* measurements were done using AFM, XRR and XRD. Figures 43A and 43B provide results of QCM flux measurements according to the example, where the Ga density used was 5.95 g/cm^3 for QCM (Ga metal and Ga_2O_3 densities are almost identical). Figure 43A shows the measured Ga flux in the absence of O-plasma of 1.35 Å/min (average min 20 to 44), while Figure 43B shows the measured GaO_x flux of 3.95 Å/min (average min 20 to 38), showing an increase in the accumulation rate by a factor of ~2.9 in the presence of O-plasma.

[0378] Figures 44A-44C provide results of the analysis of the RHEED patterns in the example. For the analysis of the RHEED patterns, diffraction patterns emerged after ~5 min of film growth in the example. Extracted plane spacings (normalized to STO [110] azimuth) were consistent with (001)-oriented γ-Ga_2O_3 or a 4-domain (100)-oriented β-Ga_2O_3. Figure 44A shows the STO layer [110] azimuth from which the spot spacing is calibrated. Figure 44B shows the b-Ga_2O_3 [020] / g-Ga_2O_3 [440] azimuth with a measured spacing of 1.46 Å, while Figure 44C shows the b-Ga_2O_3 [11-2] / g-Ga_2O_3 [400] azimuth with a measured spacing of 2.05Å.

[0379] Figures 45A-45C provide XPS results of the analysis in an example. The XPS results demonstrated a stoichiometry of O:Ga = ~60:40 (from O 1s & Ga 3p). The XPS results further showed a valence band shape characteristic of Ga_2O_3.

[0380] Figure 46 provides XRR results of the analysis in the example. The data are shown as blue dots while the model fit is the solid red line (4610). The model fit indicates a 21 nm thickness for the Ga_2O_3 layer with a surface roughness of 11 Å.

[0381] Figures 47A and 47B illustrate differences between the crystal structures of β-Ga_2O_3 and γ-Ga_2O_3. As shown in this figure, γ-Ga_2O_3 can be considered a defective spinel structure with fractional occupancies.

[0382] Figure 48 shows that the example provides a single domain structure 5.5% mismatch (compressive), which can be denoted as γ-Ga_2O_3 (001)[001]/STO(001)[100].

[0383] Figure 49 illustrates expected epitaxy for β-Ga_2O_3 on STO(001), which is the same as that observed on MgO (100) substrates, for an example.

[0384] (100)-oriented β-Ga_2O_3 thin film is formed on the (100) MgO substrate with a fourfold domain structure rotated every 90°. In addition, the c-axis direction of β-Ga_2O_3 was parallel to the <011> direction of MgO. These results were the same as that observed for the crystal orientation of β-Ga_2O_3 formed on the (100) MgO substrate, as shown in reference [66], although different methods for film formation were employed. This should show the in-plane spacings (020) and (11-2) in RHEED & XRD at ~45° (actual separation 46.3°) azimuthal direction.

[0385] Figure 50 shows the expected 4-domain structure of β-Ga_2O_3 (100)[020] on STO(100)[110].

[0386] Table 11, below, provides the expected 2θ peak positions in an out-of-plane XRD scan for the example.

LAMBA = 1.5406 Å

- STO:
  - (001) = 22.7535
  - **(002) = 46.4721**
  - (003) = 72.5668
  - (004) = 104.192
- γ-Ga_2O_3:
  - **(004) = 43.9301**
  - (008) = 96.849
- β-Ga_2O_3:
  - (200) = 14.9088
  - **(400) = 30.0778**
  - **(600) = 45.811**
  - (800) = 62.5237
  - (1000) = 80.8855

Table 11: Expected 2θ peaks out-of-plane

[0387] Figures 51A and 51B depict plots of out-of-plane (oop) XRD results for the example with sample label AF99. The plot on the left of Figure 51A is the normal out of plane XRD identifying the presence of both b- and g-Ga_2O_3. The contour plot on the bottom right is a reciprocal space map of the scanned region. Some instrumental artifacts ("streaks") are observable and identified as well.

[0388] Figures 52A and 52B depict combined in-plane 2q□/f plots for the example taken along two different azimuths. The blue curves (5210) are taken along the STO [100] azimuth, while the red curves (5220) are taken along the STO [110] azimuth. Figure 52A is a plot on a linear scale, while Figure 52B

provides curves 5230 (same data as 5210) and 5240 (same data as 5220) plotted on a log scale to better see the film peaks, which are to the left of the intense, narrow substrate peaks.

[0389] Figures 53A-53D depict peak decompositions of each of the four features in Figures 52A and 52B. The peaks are color-coded with the following scheme. Orange refers to g-Ga_2O_3, green is b-Ga_2O_3, blue is STO, and purple is unidentified. These results confirm the presence of both phases of Ga_2O_3.

[0390] Measured XRD reflections in the example indicated a mix of β and γ polymorphs. The following relation provides lattice constants *d* obtained from the Miller indices (*hkl*) for a monolithic crystal:

$$\frac{1}{d^2} = h^2\frac{1}{a^2 sin^2\beta} + k^2\frac{1}{b^2} + l^2\frac{1}{c^2 sin^2\beta} + h \cdot l \frac{\cos\beta}{acsin^2\beta}$$

[0391] where

$$\frac{1}{a^2 sin^2\beta} \equiv \xi_1\,, \qquad \frac{1}{b^2} \equiv \xi_2\,, \qquad \frac{1}{c^2 sin^2\beta} \equiv \xi_3\,, \text{and} \qquad \frac{\cos\beta}{acsin^2\beta} \equiv \xi_4$$

[0392] and where

$$\xi_4 = \sqrt{\xi_1\xi_3}\cos\beta$$

[0393] For the γ polymorph, *a* = 8.01 Å (in-plane 20 nm film), and *a* = 8.3 Å (oop RSM 50 nm film), compared to the bulk value of 8.23 Å. For the β polymorph, reflections were not sufficient to determine all lattice parameters (need on more lattice parameter off-symmetry). The *b* lattice parameter can be extracted as 2.99 Å (20 nm film), compared to the bulk value of 3.04 Å.

EXAMPLE 4: Extension Cases For Examples 1-3

[0394] Interfacing between the monoclinic β-gallia and silicon requires a buffer that grows epitaxially on silicon while at the same time having structural commonality with the β-gallia crystal structure. $SrTiO_3$ (STO) is well-known to be able to grow epitaxially on Si(100) also with 100 orientation. The *b* lattice vector and twice the *c* lattice vector match reasonably well with the STO (110) spacing. Thus, the β-Ga_2O_3 may grow with its *bc*-plane epitaxially aligned on the STO (001) surface with a 45° rotation. Additionally, the oxygen sublattice in this orientation of β-Ga_2O_3 is only a slightly distorted continuation from that in STO, which can allow for a low energy interface.

[0395] Another approach is to grow a buffer layer that has a crystal structure which Ga_2O_3 can also take. While the β-gallia structure is unique to Ga_2O_3, Ga_2O_3 can also undergo the corundum (α), spinel (γ), and bixbyite (d) crystal structures. Both spinel (γ-Al_2O_3) and bixbyite (rare earth oxides) materials have been demonstrated as epitaxial films on Si(100) previously. Such buffers may force the Ga_2O_3 to initially take these alternative crystal structures and transition to its normal β-gallia structure as it grows thicker. Because the atomic distortions among the different polymorphs is not large, such buffers may enable the continuation of the atomic structure from the buffer to the β-gallia structure. In the case of γ-Al_2O_3, it has been reported that when grown on Si(100), it initially grows pseudomorphically as γ-Al_2O_3 (100), but surface energy considerations cause it to transition to (111) orientation. The oxygen framework of γ-Al_2O_3 (111) (which is the same as corundum 0001) induces the (-201) plane of β-gallia to form in order to continue the oxygen sublattice via a γ-Ga_2O_3 (111) transition layer. The same

mechanism is expected in the case of a bixbyite oxide (e.g., Gd_2O_3 or Er_2O_3) where the transition is through a thin layer of Δ-Ga_2O_3.

[0396] In some embodiments, use of compositional grading in the case of spinel or bixbyite buffers may alleviate lattice mismatch. For example, after the γ-Al_2O_3 layer, one may then switch to an intermediate $AlGaO_3$ composition before putting pure Ga_2O_3. In another embodiment, one can also use continuously graded layers $Al_xGa_{2-x}O_3$ with x going from 1 to 0 smoothly, The same concept can be used for bixbyite oxides, e.g., Gd_2O_3 initially then $GdxGa_{2-x}O_3$ then Ga_2O_3. Additionally, use of vicinal surfaces may eliminate other domains, as discussed above in Example 2.

EXAMPLE 5: Applications to Power Electronics

[0397] Larger breakdown fields can lead to the miniaturization of power electronic devices with associated reductions in cost and weight. The enhanced radiation hardness of Ga_2O_3 [6] additionally makes it suitable for space applications. Today an estimated 30 % of all electricity flows through power electronics and this is projected to reach 80 % in the future [7]. Efficient n-type doping of Ga_2O_3 can be achieved by Si, Ge, Sn and Nb incorporation [3]. Recently p-type doping with H has been demonstrated [8]. This, in combination with a way to create shallow p-type doping, could lead to realization of new kinds of optoelectronics operating in the deep-UV due to the large band gap of Ga_2O_3.

[0398] Figure 54 is a diagram of transistor-type power electronic device 5400 embodied as an epi-Ga_2O_3 Power MOSFET, according to some embodiments of the present technology. In some embodiments, such a transistor 5400 may include an Si carrier 5410 serving the function of a substrate as well as a heat spreader. Transistor 5400 may include an epi-oxide buffer layer 5420 formed atop the Si carrier 5410, as shown in Figure 54. In an example, Si carrier 5410 with epi-oxide buffer 5420 formed thereon may together comprise a wafer 5425 according to the present technology. In one example, epi-oxide buffer 5420 may be formed, at least in part, of at least one thin film layer of alumina formed on the Si carrier 5410, as described herein, for instance, with reference to Examples 1 and 6. In another example, epi-oxide buffer 5420 may be formed, at least in part, of at least one thin film layer of epitaxial STO formed on the Si carrier 5410, as described above, for instance, with reference to Examples 2 and 6 (see, e.g., Figure 40A). In another example, epi-oxide buffer 5420 may be formed, at least in part, of at least one thin film layer of epitaxial STO formed on the Si carrier 5410, and then at least one layer of γ-Al_2O_3 deposited onto the STO layer(s), as described above, for instance, with reference to Examples 3 and 6 (see, e.g., Figure 40B). In still another example, epi-oxide buffer 5420 may be formed, at least in part, of at least one thin film layer of epitaxial STO formed on the Si carrier 5410, and then at least one layer of a rare earth oxide, alumina, a gallium-rare earth oxide alloy, and/or a gallium-aluminum oxide alloy, as described above, for instance, with reference to Examples 4 and 6. In any of the aforementioned examples described above with reference to Figure 54, the wafer 5425 may also include the thin film 5430 including a gallium oxide formed on the epi-oxide buffer layer 5420. Wafer 5425 may be manufactured for use in transistor 5400 using any of the processes or methods as described herein according to the present technology.

[0399] One or more additional layers of gallia may be formed on the thin film 5430 including a gallium oxide. In the embodiment illustrated in Figure 54, a first layer 5435 is, or includes, undoped epitaxial Ga_2O_3 formed on the aforementioned thin film 5430. Next, at least a second layer 5440 is, or includes, lightly doped epitaxial Ga_2O_3 formed on the aforementioned first layer 5435. In the example shown in Figure 54, the second layer 5440 is formed on the first layer 5435 over only a portion of the first layer 5435, so as to leave at least one (e.g., bordering) space(s). As such, transistor 5400 also includes at least one n+ block 5450 also formed atop portion(s) of the second layer 5440.

[0400] In some embodiments, as shown for example in Figure 54, transistor 5400 may include a source 5460 formed atop a first n+ block 5450 and a drain 5470 formed atop a second n+ block 5450. In an example, an alumina layer 5480 may be formed atop another portion of the aforementioned second layer 5440. Transistor 5400 may also include a gate 5490 formed atop the alumina layer 5480. In power electronic devices according to the present technology embodied in transistor 5400 or equivalent devices readily envisaged and practiced by persons having ordinary skill in the art without undue experimentation, components such as the aforementioned source 5460, drain 5470 and gate 5490, and their functional equivalents, may receive and/or transmit electric current during operation of the power electronic device. Accordingly, such components may be referred to herein as means for transmitting and/or receiving a first, and at least a second, electric current coupled (e.g., electrically) to and/or from one or more portions of wafer 5425, as shown for example in Figure 54.

[0401] Figure 55 is a diagram of rectifier-type power electronic device 5400 embodied as a Ga_2O_3 vertical rectifier, according to some embodiments of the present technology. In some embodiments, such a rectifier 5500 may include a heavily doped (n+) Si carrier 5510. In a example, Si carrier 5510 may serve the function of a substrate as well as a heat spreader. Rectifier 5500 may include an epi-oxide buffer layer 5520 formed atop the Si carrier 5510, as shown in Figure 55. In an example, Si carrier 5510 with epi-oxide buffer 5520 formed thereon may together comprise a wafer 5525 according to the present technology. In one example, epi-oxide buffer 5520 may be formed, at least in part, of at least one thin film layer of alumina formed on the Si carrier 5510, as described herein, for instance, with reference to Examples 1 and 6. In another example, epi-oxide buffer 5520 may be formed, at least in part, of at least one thin film layer of epitaxial STO formed on the Si carrier 5510, as described above, for instance, with reference to Examples 2 and 6 (see, e.g., Figure 40A). In another example, epi-oxide buffer 5520 may be formed, at least in part, of at least one thin film layer of epitaxial STO formed on the Si carrier 5510, and then at least one layer of γ-Al_2O_3 deposited onto the STO layer(s), as described above, for instance, with reference to Examples 3 and 6 (see, e.g., Figure 40B). In still another example, epi-oxide buffer 5420 may be formed, at least in part, of at least one thin film layer of epitaxial STO formed on the Si carrier 5510, and then at least one layer of a rare earth oxide, alumina, a gallium-rare earth oxide alloy, and/or a gallium-aluminum oxide alloy, as described above, for instance, with reference to Examples 4 and 6. In any of the aforementioned examples described above with reference to Figure 55, the wafer 5525 may also include the thin film 5530 including a gallium oxide formed on the epi-oxide buffer layer

5520. Wafer 5525 may be manufactured for use in rectifier 5500 using any of the processes or methods as described herein according to the present technology.

[0402] One or more additional layers of gallia may be formed on the thin film 5530 including a gallium oxide. In the embodiment illustrated in Figure 55, at least one layer 5540 is, or includes, lightly Si-doped epitaxial Ga_2O_3 (thickened) formed on the aforementioned thin film 5530. In some embodiments, as shown for example in Figure 55, rectifier 5500 may include a bottom contact 5550 formed beneath Si carrier 5510 and a top contact 5560 formed atop the layer(s) 5540 of lightly Si-doped epitaxial Ga_2O_3 (thickened). In power electronic devices according to the present technology embodied in rectifier 5500 or equivalent devices readily envisaged and practiced by persons having ordinary skill in the art without undue experimentation, components such as the aforementioned contacts 5550 and 5560, and their functional equivalents, may receive and/or transmit electric current during operation of the power electronic device. Accordingly, such components may be referred to herein as means for transmitting and/or receiving a first, and at least a second, electric current coupled (e.g., electrically) to and/or from one or more portions of wafer 5525, as shown for example in Figure 55.

[0403] Epitaxial growth onto Si (001) wafers would open up numerous avenues for the large scale integration but, unfortunately, Ga_2O_3 cannot be directly grown on Si. In additional to the examples of power electronics devices described above with reference to Figures 54 and 55, a person of ordinary skill in the art is expected to readily envisage, and practice without undue experimentation, Si-based optoelectronic, MEMS, switching devices combined with a Ga_2O_3-based rectifier, monolithically integrated on a Si bulk substrate, and manufactured according to the present technology.

EXAMPLE 6: Wafer Manufacturing Methods

[0404] Figure 56 depicts a flow chart of a method 5600 for manufacturing a wafer, according to some embodiments of the present technology. With further reference to the foregoing figures and accompanying description thereof, method 5600 may include the step of forming 5710, on a silicon substrate, a buffer layer including a thin film of epitaxial strontium titanate (STO). Method 5600 may also include the step of forming 5620 a thin film including a gallium oxide on the buffer layer.

[0405] In one embodiment, forming 5610 the buffer layer may include the steps of: forming a first layer including STO on the silicon substrate; and forming a second layer including an aluminum oxide on the first layer. In an example, the step of forming 5620 the thin film including the gallium oxide may include forming the thin film including the gallium oxide on the second layer. In an example, forming the second layer including the aluminum oxide on the first layer may including forming the second layer including gamma-aluminum oxide (γ-Al_2O_3). In another example, forming the thin film including the gallium oxide may include hetero-epitaxially integrating the thin film including the gallium oxide onto the silicon substrate via the buffer layer.

[0406] In some embodiments, method 5600 may further include forming 5630 one or more additional layers of gallium oxide on the thin film including the gallium oxide. In an example, forming 5630 the one or more additional layers of gallium oxide includes growing the one or more additional layers of

gallium oxide on the thin film including the gallium oxide using a process including chemical vapor deposition. In another example, forming 530 the one or more additional layers of gallium oxide may include the steps of: forming at least a first layer of the one or more additional layers of gallium oxide as a layer of an aluminum-gallium alloy oxide formed on the thin film including the gallium oxide; and forming at least a second layer of the one or more additional layers of gallium oxide on the layer of the aluminum-gallium alloy oxide. In yet another example, method 5600 may additionally include at least one of the following steps: etching, polishing, and annealing, at least a portion of the one or more additional layers of gallium oxide. In still another example, the step of forming 5630 the one or more additional layers of gallium oxide includes forming at least a portion of the one or more layers of gallium oxide as bulk-like crystals of gallium oxide.

[0407] In any of the embodiments and examples as described herein with reference to Figure 56, method 5600 may further include the step of forming at least one of: a microelectronic device, an optoelectronic device, a micro-electromechanical system (MEMS), a field-effect transistor, a sensor, and a semiconductor device, in or on: the thin film including the gallium oxide, or the one or more additional layers of gallium oxide. Also, in any of the above described embodiments and examples described with reference to Figure 56, method 5600 may also include the step of operably coupling one or more components of a power electronics device to: the thin film including the gallium oxide, or the one or more additional layers of gallium oxide.

[0408] any of the embodiments and examples as described herein with reference to Figure 56, the forming 5610 step of method 5600 may include forming the buffer layer on a silicon (001) substrate. In an example, the forming 5620 step of method 5600 may include forming at least a portion of the thin film including the gallium oxide as gamma-gallium oxide (γ-Ga_2O_3). In another example, the forming 5620 step of method 5600 may include forming at least a portion of the thin film including the gallium oxide as beta-gallium oxide (β-Ga_2O_3), either instead of or in addition to forming the at least a portion of the thin film including the gallium oxide as gamma-gallium oxide.

[0409] Figure 57 depicts a flow chart of a method 5700 for manufacturing a wafer, according to some embodiments of the present technology. With further reference to the foregoing figures and accompanying description thereof, method 5700 may include the step of forming 5710, on a silicon substrate, a buffer layer including an epitaxial thin film of an aluminum oxide, or a rare earth oxide. Method 5700 may also include the step of forming 5720 a thin film including a gallium oxide on the buffer layer.

[0410] In a first embodiment, forming 5710 the buffer layer in method 5700 may include forming the buffer layer including the epitaxial thin film of aluminum oxide. In an example, the aluminum oxide for the forming 5710 step of method 5700 may be, or may include, gamma-aluminum oxide (γ-Al_2O_3). In another embodiment, the aluminum oxide for the forming 5710 step of method 5700 may be, or may include, an aluminum-gallium oxide alloy, either instead of or in addition to the aforementioned gamma-aluminum oxide.

[0411] In some embodiments, the method 5700 step of forming 5710 the buffer layer may further include the steps of: forming a first layer including the aluminum oxide on the silicon substrate; and forming at least a second layer of an aluminum-gallium alloy oxide on the first layer. In an example, the step of forming 5720 the thin film including the gallium oxide may include forming the thin film including the gallium oxide on the at least a second layer.

[0412] In a second embodiment, forming 5710 the buffer layer in method 5700 may include forming the buffer layer including the epitaxial thin film of the rare earth oxide. In an example, the rare earth oxide may be, or may include, gadolinium oxide (Gd_2O_3). In another example, the rare earth oxide may be, or may include, erbium oxide (Er_2O_3), either instead of, or in addition to, gadolinium oxide. In yet another example, the rare earth oxide may be, or may include, a gallium-rare earth alloy oxide.

[0413] In some embodiment, the method 5700 step of forming 5710 the buffer layer may further include the steps of: forming a first layer including the rare earth oxide on the silicon substrate; and forming at least a second layer of a gallium-rare earth alloy oxide on the first layer. In an example, the step of forming 5720 the thin film including the gallium oxide may include forming the thin film including the gallium oxide on the at least a second layer.

[0414] In either of the first or second embodiments, or any of the above described examples thereof, the forming 5710 step of method 5700 may include forming the buffer layer as a compositionally graded buffer layer. Also, in either the first or second embodiments, or any of the above described examples thereof, forming 5720 the thin film including the gallium oxide may include hetero-epitaxially integrating the thin film including the gallium oxide onto the silicon substrate via the buffer layer.

[0415] Additionally, in either of the first or second embodiments, or any of the above described examples thereof, method 5700 may also include forming 5730 one or more additional layers of gallium oxide on the thin film including the gallium oxide. In an example, forming 5730 the one or more additional layers of gallium oxide may include growing the one or more additional layers of gallium oxide on the thin film including the gallium oxide using a process including chemical vapor deposition. In another example, method 5700 may also include at least one of the following steps: etching, polishing, and annealing, at least a portion of the one or more additional layers of gallium oxide. In yet another example, forming 5730 the one or more additional layers of gallium oxide may include forming at least a portion of the one or more layers of gallium oxide as bulk-like crystals of gallium oxide.

[0416] In examples where the buffer layer is, or includes, the epitaxial film of aluminum oxide, forming 5730 the one or more additional layers of gallium oxide on the thin film including the gallium oxide may include the steps of: first forming at least one layer including an aluminum-gallium alloy oxide on the thin film including the gallium oxide; and second forming at least one additional layer including the one or more additional layers of gallium oxide on the at least one layer. In examples where the buffer layer includes the epitaxial film of the rare earth oxide, forming 5730 the one or more additional layers of gallium oxide on the thin film including the gallium oxide may include the steps of: first forming at least one layer including a rare earth-gallium alloy oxide on the thin film including the gallium oxide; and

second forming at least one additional layer including the one or more additional layers of gallium oxide on the at least one layer.

[0417] In either of the first or second embodiment, or any of the above described examples thereof, the method 5700 may further include the step of at least one of: a microelectronic device, an optoelectronic device, a micro-electromechanical system (MEMS), a field-effect transistor, a sensor, and a semiconductor device, formed in or on: the thin film including the gallium oxide, or the one or more additional layers of the gallium oxide. Also, in either the first or second embodiment, or any of the above described examples, thereof, method 5700 may further include the step of operably coupling one or more components of a power electronics device to: the thin film including the gallium oxide, or the one or more additional layers of gallium oxide.

[0418] In either of the first or second embodiment, or any of the above described examples thereof, the forming 5710 step of method 5700 may include forming the buffer layer on a silicon (001) substrate. In an example, the forming 5720 step of method 5700 may include forming at least a portion of the thin film including the gallium oxide as gamma-gallium oxide (γ-Ga_2O_3). In another example, the forming 5720 step of method 5700 may include forming at least a portion of the thin film including the gallium oxide as beta-gallium oxide (β-Ga_2O_3), either instead of or in addition to forming the at least a portion of the thin film including the gallium oxide as gamma-gallium oxide.

CONCLUSION

[0419] Unless the context clearly requires otherwise, throughout the description and the claims, the words "comprise," "comprising," and the like are to be construed in an inclusive sense, as opposed to an exclusive or exhaustive sense; that is to say, in the sense of "including, but not limited to." As used herein, the terms "on," “connected,” or “coupled” means having any attachment, connection or coupling, either direct or indirect, between two or more elements; the attachment, coupling. or connection between the elements can be physical, logical, or a combination thereof. Similarly, the phrase “directly on” means a direct attachment, connection, or coupling without any intermediate elements, layers, etc. Additionally, the words "herein," "above," "below," and words of similar import, when used in this application, refer to this application as a whole and not to any particular portions of this application. Where the context permits, words in the above Detailed Description using the singular or plural number may also include the plural or singular number respectively. The word "or," in reference to a list of two or more items, covers all of the following interpretations of the word: any of the items in the list, all of the items in the list, and any combination of the items in the list.

[0420] The above Detailed Description of examples of the technology is not intended to be exhaustive or to limit the technology to the precise form disclosed above. While specific examples for the technology are described above for illustrative purposes, various equivalent modifications are possible within the scope of the technology, as those skilled in the relevant art will recognize. For example, while processes or blocks are presented in a given order, alternative implementations may perform routines having steps, or employ systems having blocks, in a different order, and some processes or blocks may

be deleted, moved, added, subdivided, combined, and/or modified to provide alternative or subcombinations. Each of these processes or blocks may be implemented in a variety of different ways. Also, while processes or blocks are at times shown as being performed in series, these processes or blocks may instead be performed or implemented in parallel, or may be performed at different times. Further any specific numbers noted herein are only examples: alternative implementations may employ differing values or ranges.

[0421] The teachings of the technology provided herein can be applied to other systems, not necessarily the system described above. The elements and acts of the various examples described above can be combined to provide further implementations of the technology. Some alternative implementations of the technology may include not only additional elements to those implementations noted above, but also may include fewer elements.

[0422] These and other changes can be made to the technology in light of the above Detailed Description. While the above description describes certain examples of the technology, and describes the best mode contemplated, no matter how detailed the above appears in text, the technology can be practiced in many ways. Details of the system may vary considerably in its specific implementation, while still being encompassed by the technology disclosed herein. As noted above, particular terminology used when describing certain features or aspects of the technology should not be taken to imply that the terminology is being redefined herein to be restricted to any specific characteristics, features, or aspects of the technology with which that terminology is associated. In general, the terms used in the following claims should not be construed to limit the technology to the specific examples disclosed in the specification, unless the above Detailed Description section explicitly defines such terms. Accordingly, the actual scope of the technology encompasses not only the disclosed examples, but also all equivalent ways of practicing or implementing the technology under the claims.

[0423] To reduce the number of claims, certain aspects of the technology are presented below in certain claim forms, but the applicant contemplates the various aspects of the technology in any number of claim forms. For example, various aspects may be presented in other system claims, composition of matter claims, method claims, or in other forms, such as being embodied in a means-plus-function claim. Any claims intended to be treated under 35 U.S.C. § 112(f) will begin with the words "means for", but use of the term "for" in any other context is not intended to invoke treatment under 35 U.S.C. § 112(f). Accordingly, the applicant reserves the right to pursue additional claims after filing this application to pursue such additional claim forms, in either this application or in a continuing application.

CLAIMS

What is claimed is:

1. A wafer comprising:
a silicon substrate;
a buffer layer including a thin film of epitaxial strontium titanate (STO) formed on the silicon substrate; and
a thin film including a gallium oxide formed on the buffer layer.

2. The wafer of claim 1, wherein the buffer layer further includes:
a first layer including STO formed on the silicon substrate; and
a second layer including an aluminum oxide formed on the first layer,
and wherein the thin film including the gallium oxide is formed on the second layer.

3. The wafer of claim 2, wherein the aluminum oxide includes gamma-aluminum oxide (γ-Al_2O_3).

4. The wafer of claim 2, wherein the aluminum oxide includes an aluminum-gallium alloy oxide.

5. The wafer of any one of claims 1-4, wherein the thin film including the gallium oxide is integrated hetero-epitaxially onto the silicon substrate via the buffer layer.

6. The wafer of any one of claims 1-5, further comprising one or more additional layers of a gallium oxide formed on the thin film including the gallium oxide.

7. The wafer of claim 6, wherein the one or more additional layers of the gallium oxide are grown using chemical vapor deposition.

8. The wafer of claim 6, wherein at least a first layer of the one or more additional layers of the gallium oxide includes a layer of an aluminum-gallium alloy oxide formed on the thin film including the gallium oxide, and wherein at least a second layer of the one or more additional layers of the gallium oxide is formed on the layer of the aluminum-gallium alloy oxide.

9. The wafer of claim 1 or claim 6, further comprising at least one of: a microelectronic device, an optoelectronic device, a micro-electromechanical system (MEMS), a field-effect transistor, a sensor, and a semiconductor device, formed in or on: the thin film including the gallium oxide, or the one or more additional layers of the gallium oxide.

10. The wafer of claim 1 or claim 6, further comprising one or more components of a power electronics device operably coupled to: the thin film including the gallium oxide, or the one or more additional layers of gallium oxide.

11. The wafer of claim 6, wherein at least a portion of the one or more additional layers of gallium oxide is at least one of: etched, polished, and annealed.

12. The wafer of claim 6, wherein at least a portion of the one or more layers of gallium oxide includes bulk-like crystals of gallium oxide.

13. The wafer according to any one of claims 1-12, wherein the silicon substrate includes silicon (001).

14. The wafer of any one of claims 1-13, wherein at least a portion of the thin film including the gallium oxide is gamma-gallium oxide (γ-Ga_2O_3).

15. The wafer of any one of claims 1-13, wherein at least a portion of the thin film including the gallium oxide is beta-gallium oxide (β-Ga_2O_3).

16. A power electronics device comprising:

the wafer of any one of claims 1-15;

means for receiving a first electric current coupled to a first portion of the wafer; and

means for transmitting a second electric current coupled to a second portion of the wafer.

17. The power electronics device of claim 16 further comprising at least one of structural and functional components of: a rectifier, or a transistor.

18. A method comprising:

forming, on a silicon substrate, a buffer layer including a thin film of epitaxial strontium titanate (STO); and

forming a thin film including a gallium oxide on the buffer layer.

19. The method of claim 18, wherein forming the buffer layer includes:

forming a first layer including STO on the silicon substrate; and

forming a second layer including an aluminum oxide on the first layer,

and wherein forming the thin film including the gallium oxide includes forming the thin film including the gallium oxide on the second layer.

20. The method of claim 19, wherein forming the second layer includes forming the second layer including gamma-aluminum oxide (γ-Al_2O_3).

21. The method of any one of claims 18-20, wherein forming the thin film including the gallium oxide includes hetero-epitaxially integrating the thin film including the gallium oxide onto the silicon substrate via the buffer layer.

22. The method of any one of claims 18-21, further comprising forming one or more additional layers of gallium oxide on the thin film including the gallium oxide.

23. The method of claim 22, wherein forming the one or more additional layers of gallium oxide includes growing the one or more additional layers of gallium oxide on the thin film including the gallium oxide using a process including chemical vapor deposition.

24. The method of claim 22, wherein forming the one or more additional layers of gallium oxide includes:

forming at least a first layer of the one or more additional layers of gallium oxide as a layer of an aluminum-gallium alloy oxide formed on the thin film including the gallium oxide; and

forming at least a second layer of the one or more additional layers of gallium oxide on the layer of the aluminum-gallium alloy oxide.

25. The method of claim 18 or claim 22, further comprising forming at least one of: a microelectronic device, an optoelectronic device, a micro-electromechanical system (MEMS), a field-effect transistor, a sensor, and a semiconductor device, in or on: the thin film including the gallium oxide, or the one or more additional layers of gallium oxide.

26. The method of claim 18 or claim 22, further comprising operably coupling one or more components of a power electronics device to: the thin film including the gallium oxide, or the one or more additional layers of gallium oxide.

27. The method of claim 22 further comprising at least one of: etching, polishing, and annealing, at least a portion of the one or more additional layers of gallium oxide.

28. The method of claim 22, wherein forming the one or more additional layers of gallium oxide includes forming at least a portion of the one or more layers of gallium oxide as bulk-like crystals of gallium oxide.

29. The method of any one of claims 18-28, wherein forming the buffer layer includes forming the buffer layer on a silicon (001) substrate.

30. The method of any one of claims 18-29, wherein forming the thin film including the gallium oxide includes forming at least a portion of the thin film including the gallium oxide as gamma-gallium oxide (γ-Ga_2O_3).

31. The method of any one of claims 18-29, wherein forming the thin film including the gallium oxide includes forming at least a portion of the thin film including the gallium oxide as beta-gallium oxide (β-Ga_2O_3).

32. A wafer comprising:

a silicon substrate;

a buffer layer formed on the silicon substrate, wherein the buffer layer includes an epitaxial thin film of an aluminum, or rare earth, oxide; and

a thin film including a gallium oxide formed on the buffer layer.

33. The wafer of claim 32, wherein the buffer layer includes the epitaxial thin film of aluminum oxide.

34. The wafer of claim 33, wherein the aluminum oxide includes gamma-aluminum oxide (γ-Al_2O_3).

35. The wafer of claim 33, wherein the aluminum oxide includes an aluminum-gallium oxide alloy.

36. The wafer of claim 33, wherein the buffer layer further includes:

a first layer including the aluminum oxide formed on the silicon substrate; and

at least a second layer of an aluminum-gallium alloy oxide formed on the first layer,

and wherein the thin film including the gallium oxide is formed on the at least a second layer.

37. The wafer of claim 32, wherein the buffer layer includes the epitaxial thin film of a rare earth oxide.

38. The wafer of claim 37, wherein the rare earth oxide includes gadolinium oxide (Gd_2O_3) or erbium oxide (Er_2O_3).

39. The wafer of claim 37, wherein the rare earth oxide includes a gallium-rare earth alloy oxide.

40. The wafer of claim 37, wherein the buffer layer further includes:

a first layer including the rare earth oxide formed on the silicon substrate; and

at least a second layer of a gallium-rare earth alloy oxide,

and wherein the thin film including the gallium oxide is formed on the at least a second layer.

41. The wafer of any one of claims 32-40, wherein the buffer layer is compositionally graded.

42. The wafer of any one of claims 32-41, wherein the thin film including the gallium oxide is integrated hetero-epitaxially onto the silicon substrate via the buffer layer.

43. The wafer of any one of claims 32-42, further comprising one or more additional layers of a gallium oxide formed on the thin film including the gallium oxide.

44. The wafer of claim 43, wherein the one or more additional layers of the gallium oxide are grown using chemical vapor deposition.

45. The wafer of claim 43, wherein the buffer layer includes an epitaxial film of aluminum oxide, and wherein at least a first layer of the one or more additional layers of the gallium oxide includes a layer of an aluminum-gallium alloy oxide formed on the thin film including the gallium oxide, and wherein at least a second layer of the one or more additional layers of the gallium oxide is formed on the layer of the aluminum-gallium alloy oxide.

46. The wafer of claim 43, wherein the buffer layer includes an epitaxial film of a rare earth oxide, and wherein at least a first layer of the one or more additional layers of the gallium oxide includes a layer of a rare earth-gallium alloy oxide formed on the thin film including the gallium oxide, and wherein at least a second layer of the one or more additional layers of the gallium oxide is formed on the layer of the rare earth-gallium alloy oxide.

47. The wafer of claim 32 or claim 43, further comprising at least one of: a microelectronic device, an optoelectronic device, a micro-electromechanical system (MEMS), a field-effect transistor, a sensor, and a semiconductor device, formed in or on: the thin film including the gallium oxide, or the one or more additional layers of the gallium oxide.

48. The wafer of claim 32 or claim 43, further comprising one or more components of a power electronics device operably coupled to: the thin film including the gallium oxide, or the one or more additional layers of gallium oxide.

49. The wafer of claim 43, wherein at least a portion of the one or more additional layers of gallium oxide is at least one of: etched, polished, and annealed.

50. The wafer of claim 43, wherein at least a portion of the one or more layers of gallium oxide includes bulk-like crystals of gallium oxide.

51. The wafer of any one of claims 32-50, wherein the silicon substrate includes silicon (001).

52. The wafer of any one of claims 32-51, wherein at least a portion of the thin film including the gallium oxide is gamma-gallium oxide (γ-Ga_2O_3).

53. The wafer of any one of claims 32-52, wherein at least a portion of the thin film including the gallium oxide is beta-gallium oxide (β-Ga_2O_3).

54. A power electronics device comprising:

the wafer of any one of claims 32-53;

means for receiving a first electric current coupled to a first portion of the wafer; and

means for transmitting a second electric current coupled to a second portion of the wafer.

55. The power electronics device of claim 54 further comprising at least one of structural and functional components of: a rectifier, or a transistor.

56. A method comprising:

forming, on a silicon substrate, a buffer layer including an epitaxial thin film of an aluminum, or rare earth, oxide; and

forming a thin film including a gallium oxide on the buffer layer.

57. The method of claim 56, wherein forming the buffer layer includes forming the buffer layer including the epitaxial thin film of aluminum oxide.

58. The method of claim 57, wherein the aluminum oxide includes gamma-aluminum oxide (γ-Al_2O_3).

59. The method of claim 57, wherein the aluminum oxide includes an aluminum-gallium oxide alloy.

60. The method of claim 57, wherein forming the buffer layer further includes:

forming a first layer including the aluminum oxide on the silicon substrate; and

forming at least a second layer of an aluminum-gallium alloy oxide on the first layer,

and wherein forming the thin film including the gallium oxide includes forming the thin film including the gallium oxide on the at least a second layer.

61. The method of claim 56, wherein forming the buffer layer includes forming the buffer layer including the epitaxial thin film of the rare earth oxide.

62. The method of claim 61, wherein the rare earth oxide includes gadolinium oxide (Gd_2O_3) or erbium oxide (Er_2O_3).

63. The method of claim 61, wherein the rare earth oxide includes a gallium-rare earth alloy oxide.

64. The method of claim 61, wherein forming the buffer layer further includes:

forming a first layer including the rare earth oxide on the silicon substrate; and

forming at least a second layer of a gallium-rare earth alloy oxide on the first layer,

and wherein forming the thin film including the gallium oxide includes forming the thin film including the gallium oxide on the at least a second layer.

65. The method of any one of claims 56-64, wherein forming the buffer layer includes forming the buffer layer as a compositionally graded buffer layer.

66. The method of any one of claims 56-65, wherein forming the thin film including the gallium oxide includes hetero-epitaxially integrating the thin film including the gallium oxide onto the silicon substrate via the buffer layer.

67. The method of any one of claims 56-66, further comprising forming one or more additional layers of gallium oxide on the thin film including the gallium oxide.

68. The method of claim 67, wherein forming the one or more additional layers of gallium oxide includes growing the one or more additional layers of gallium oxide on the thin film including the gallium oxide using a process including chemical vapor deposition.

69. The method of claim 67, wherein the buffer layer includes the epitaxial film of aluminum oxide, and wherein forming the one or more additional layers of gallium oxide on the thin film including the gallium oxide includes:

first forming at least one layer including an aluminum-gallium alloy oxide on the thin film including the gallium oxide; and

second forming at least one additional layer including the one or more additional layers of gallium oxide on the at least one layer.

70. The method of claim 67, wherein the buffer layer includes the epitaxial film of the rare earth oxide, and wherein forming the one or more additional layers of gallium oxide on the thin film including the gallium oxide includes:

first forming at least one layer including a rare earth-gallium alloy oxide on the thin film including the gallium oxide; and

second forming at least one additional layer including the one or more additional layers of gallium oxide on the at least one layer.

71. The method of claim 56 or claim 67, further comprising forming at least one of: a microelectronic device, an optoelectronic device, a micro-electromechanical system (MEMS), a field-effect transistor, a sensor, and a semiconductor device, formed in or on: the thin film including the gallium oxide, or the one or more additional layers of the gallium oxide.

72. The method of claim 56 or claim 67, further comprising operably coupling one or more components of a power electronics device to: the thin film including the gallium oxide, or the one or more additional layers of gallium oxide.

73 The method of claim 67 further comprising at least one of: etching, polishing, and annealing, at least a portion of the one or more additional layers of gallium oxide.

74. The method of claim 67, wherein forming the one or more additional layers of gallium oxide includes forming at least a portion of the one or more layers of gallium oxide as bulk-like crystals of gallium oxide.

75. The method of any one of claims 56-74, wherein forming the buffer layer includes forming the buffer layer on a silicon (001) substrate.

76. The method of any one of claims 56-75, wherein forming the thin film including the gallium oxide includes forming at least a portion of the thin film including the gallium oxide as gamma-gallium oxide (γ-Ga_2O_3).

77. The method of any one of claims 56-75, wherein forming the thin film including the gallium oxide includes forming at least a portion of the thin film including the gallium oxide as beta-gallium oxide (β-Ga_2O_3).

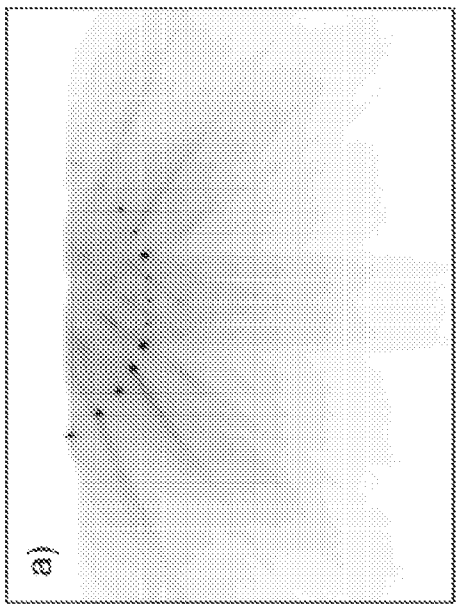

FIG. 1A

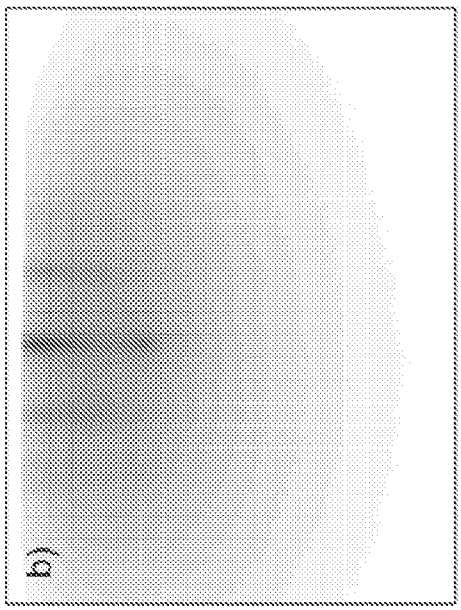

FIG. 1B

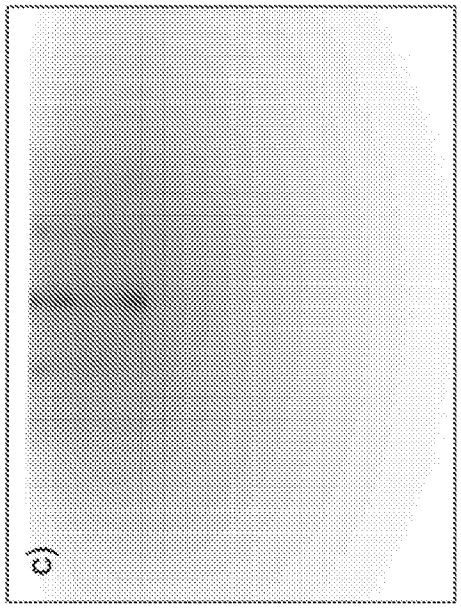

FIG. 1C

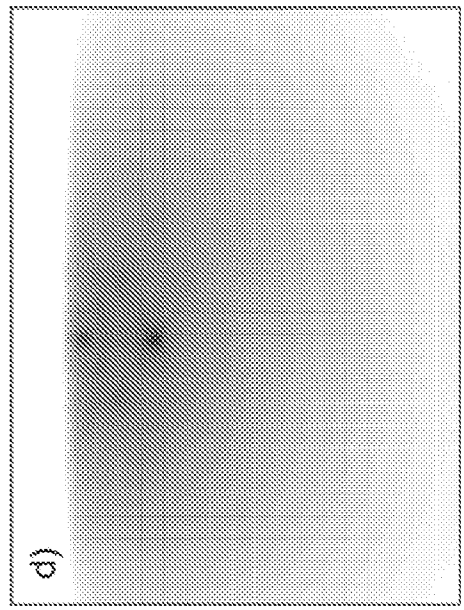

FIG. 1D

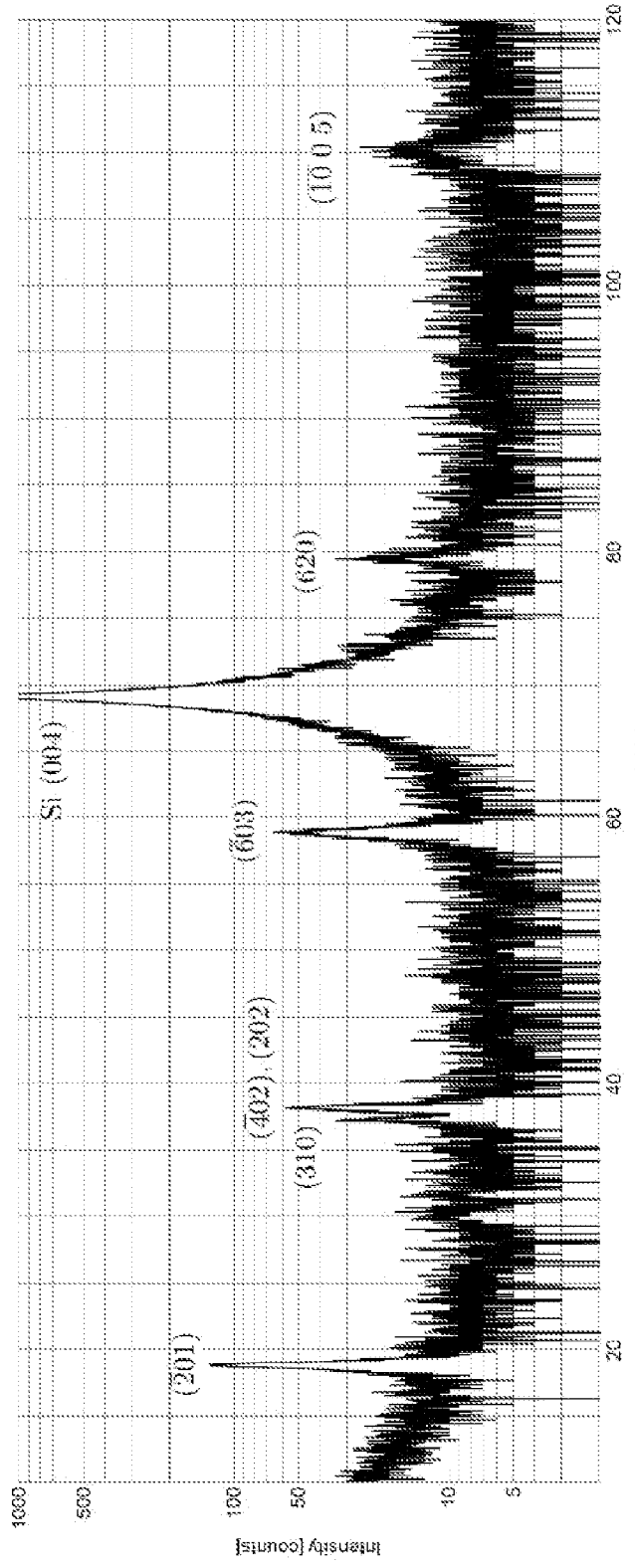
Intensity [counts]
1000
500
100
50
10
5
20
40
60
80
100
120
2θ [°]
Si (004)
(201)
(603)
(402), (202)
(310)
(620)
(10 0 5)

FIG. 2

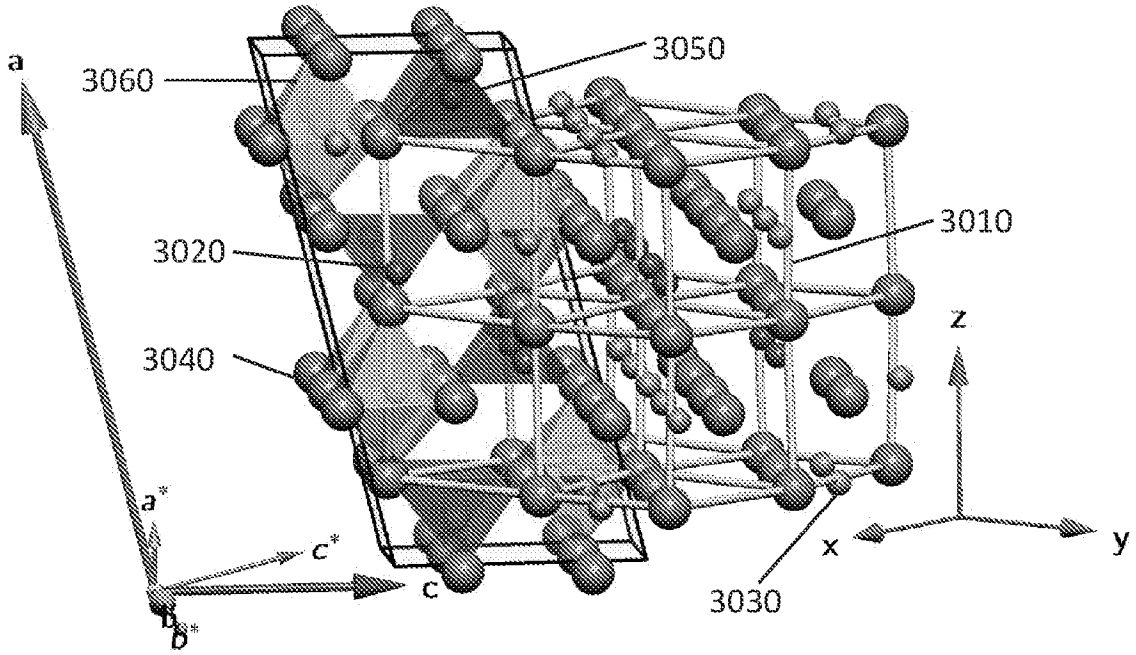
a
3060
3050
3020
3010
3040
z
a*
c*
c
x
y
3030
b*

FIG. 3

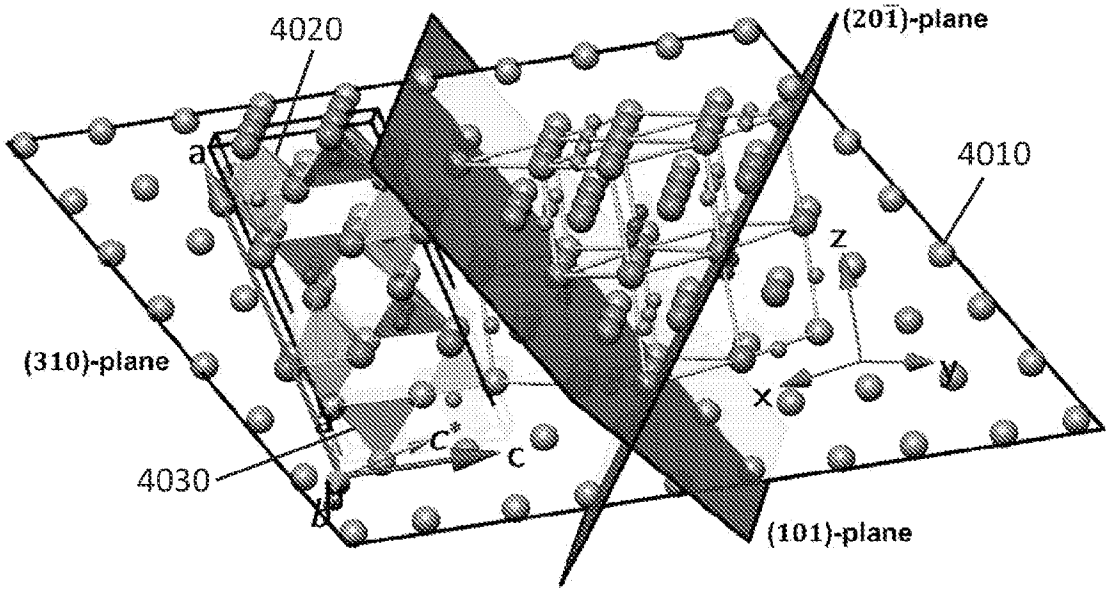
4020
(20$\bar{1}$)-plane
a
4010
z
(310)-plane
y
x
c*
c
4030
(101)-plane

FIG. 4

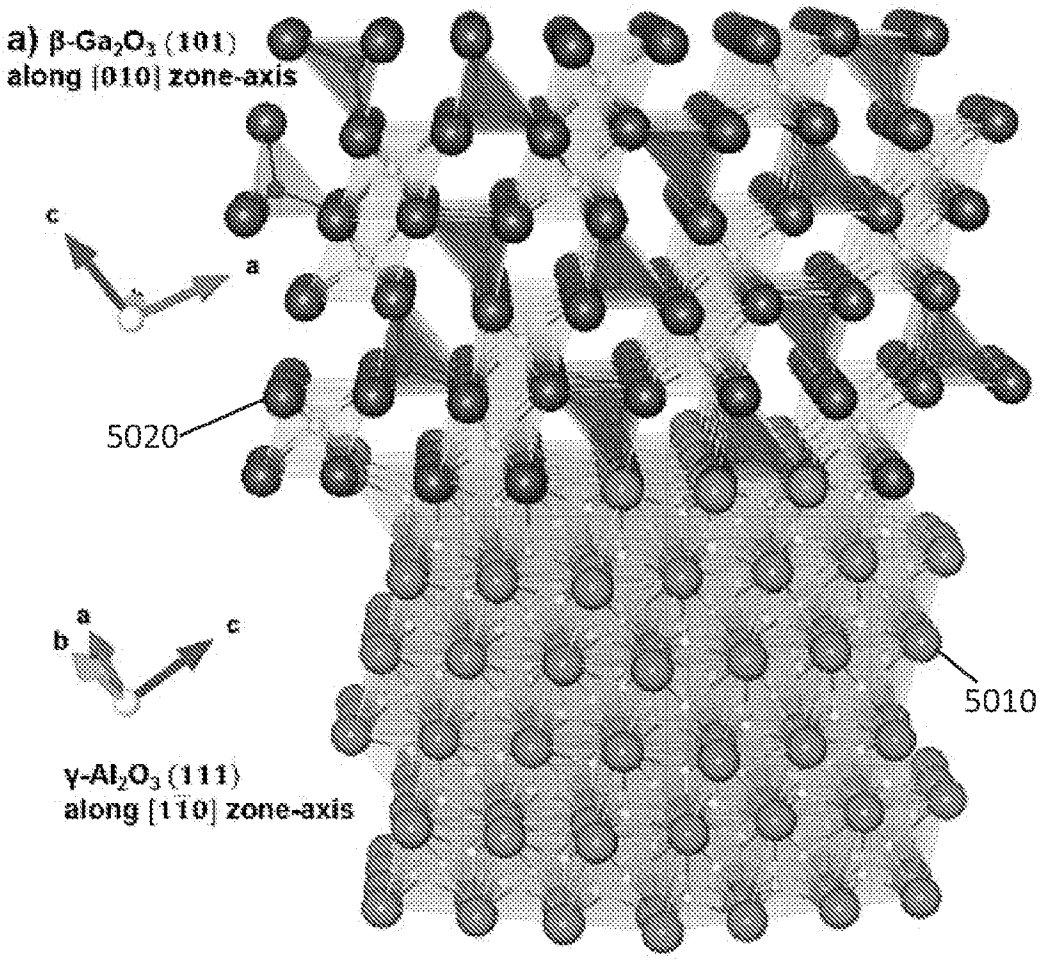
a) β-Ga2O3 (101)
along [010] zone-axis
c
a
5020
a
b
c
5010
γ-Al2O3 (111)
along [1$\bar{1}$0] zone-axis

FIG. 5A

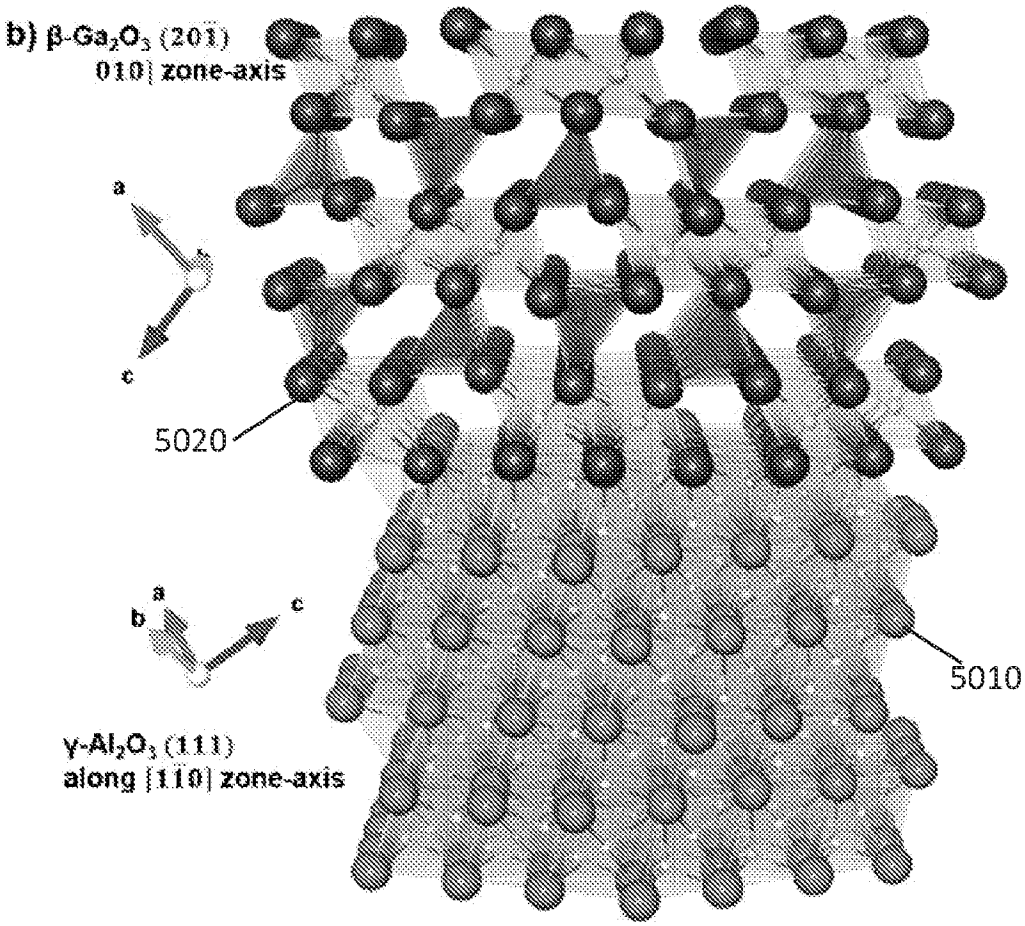
b) β-Ga2O3 (201)
010] zone-axis
a
c
5020
a
b
c
5010
γ-Al2O3 (111)
along [1$\bar{1}$0] zone-axis

FIG. 5B

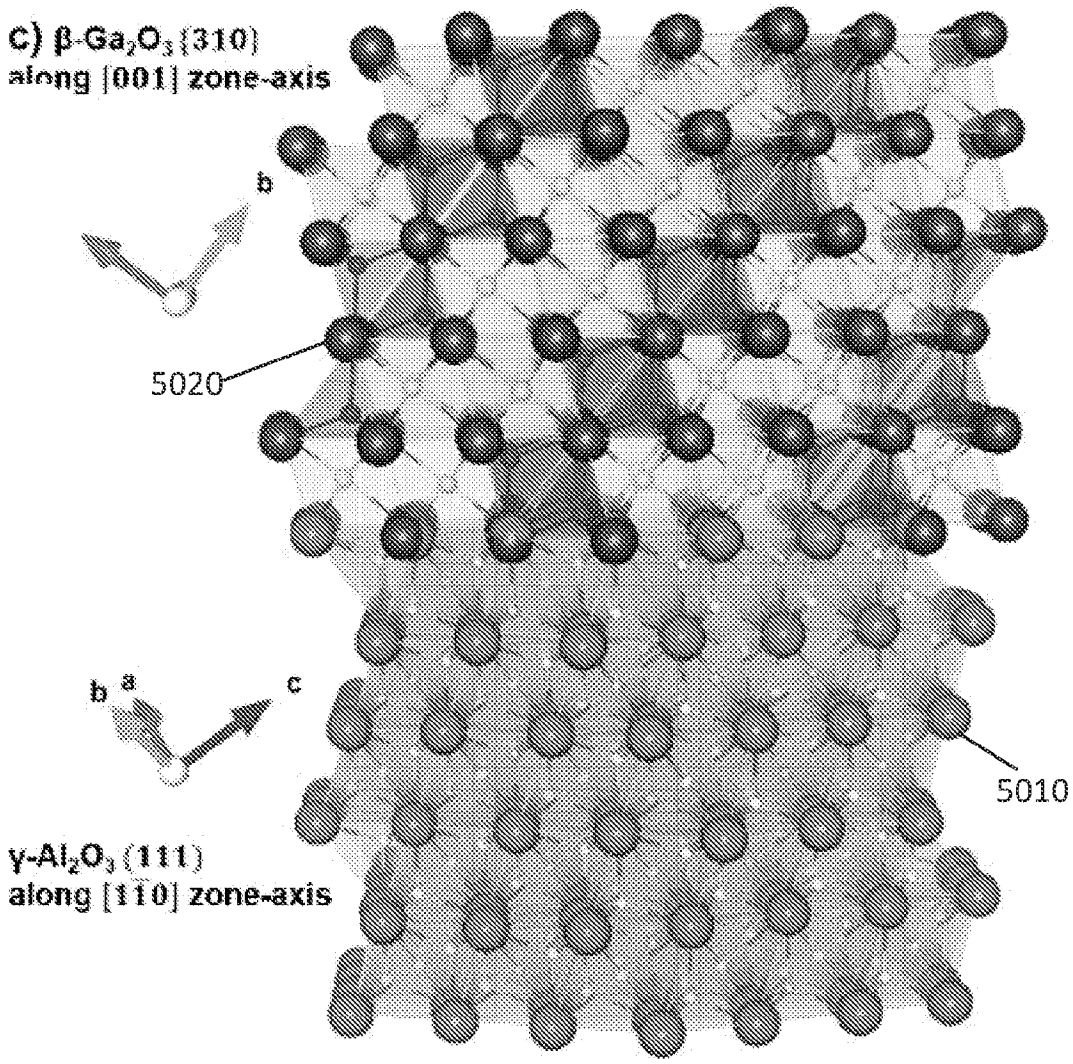
c) β-Ga2O3 (310)
along [001] zone-axis
b
5020
b
a
c
5010
γ-Al2O3 (111)
along [110] zone-axis

FIG. 5C

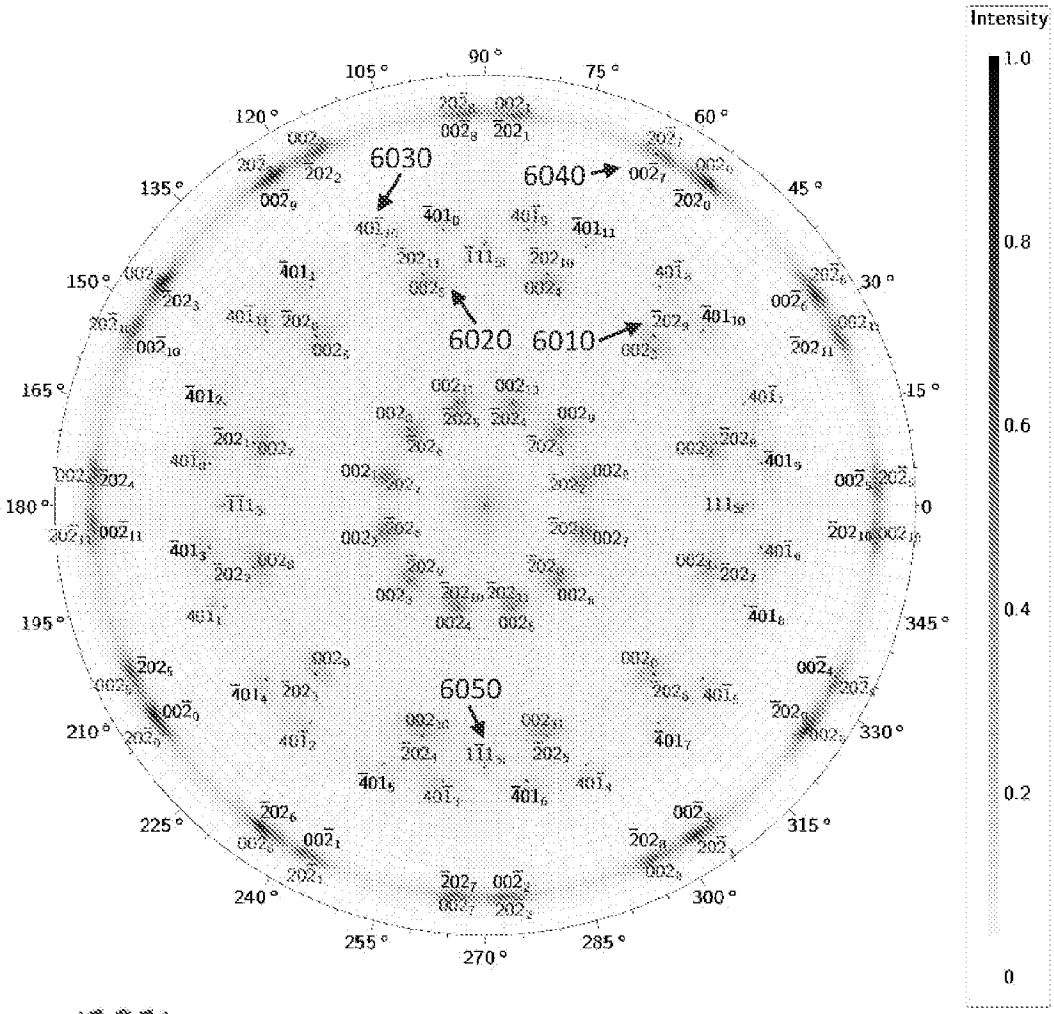

$(\bar{1}01)_{\beta-Ga2O3}$ - 6010
$(\bar{2}01)_{\beta-Ga2O3}$ - 6020
$\{310\}_{\beta-Ga2O3}$ - 6030
$\{\bar{3}\bar{1}0\}_{\beta-Ga2O3}$ - 6040
$(001)_{Si}$ - 6050

FIG. 6

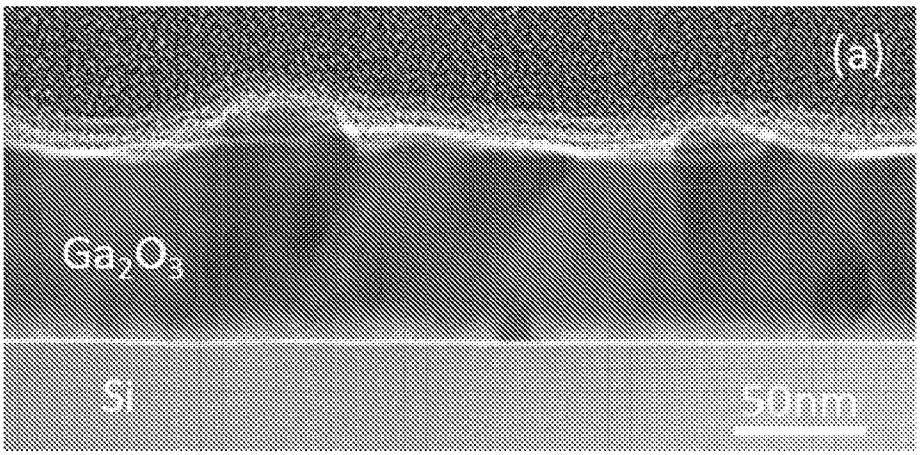

FIG. 7A

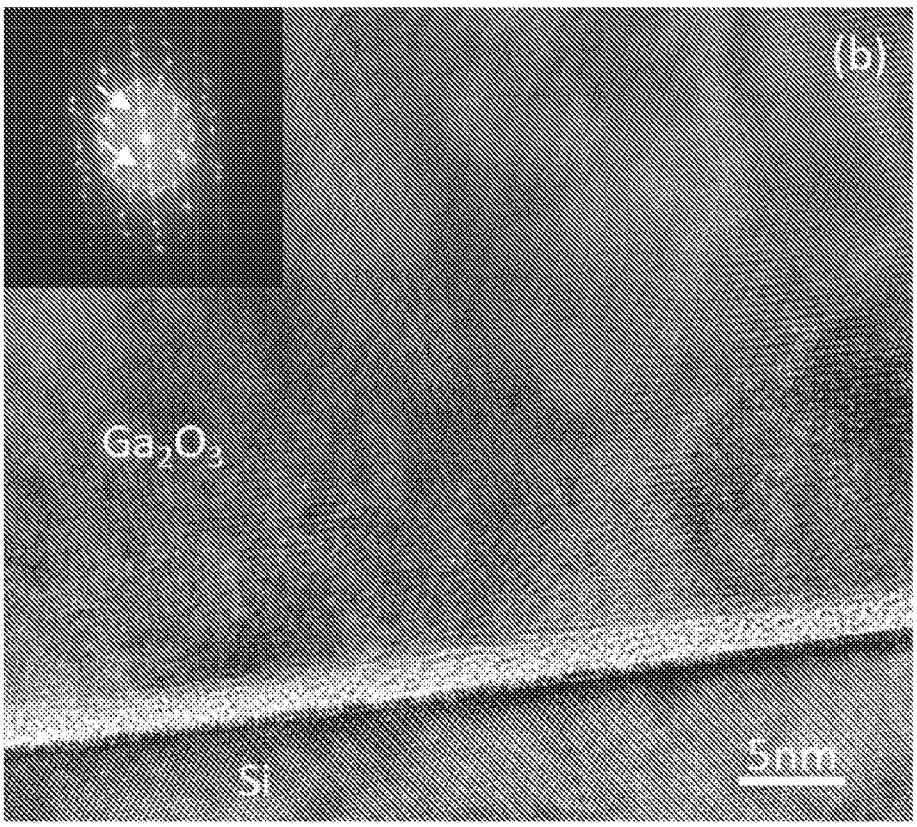

FIG. 7B

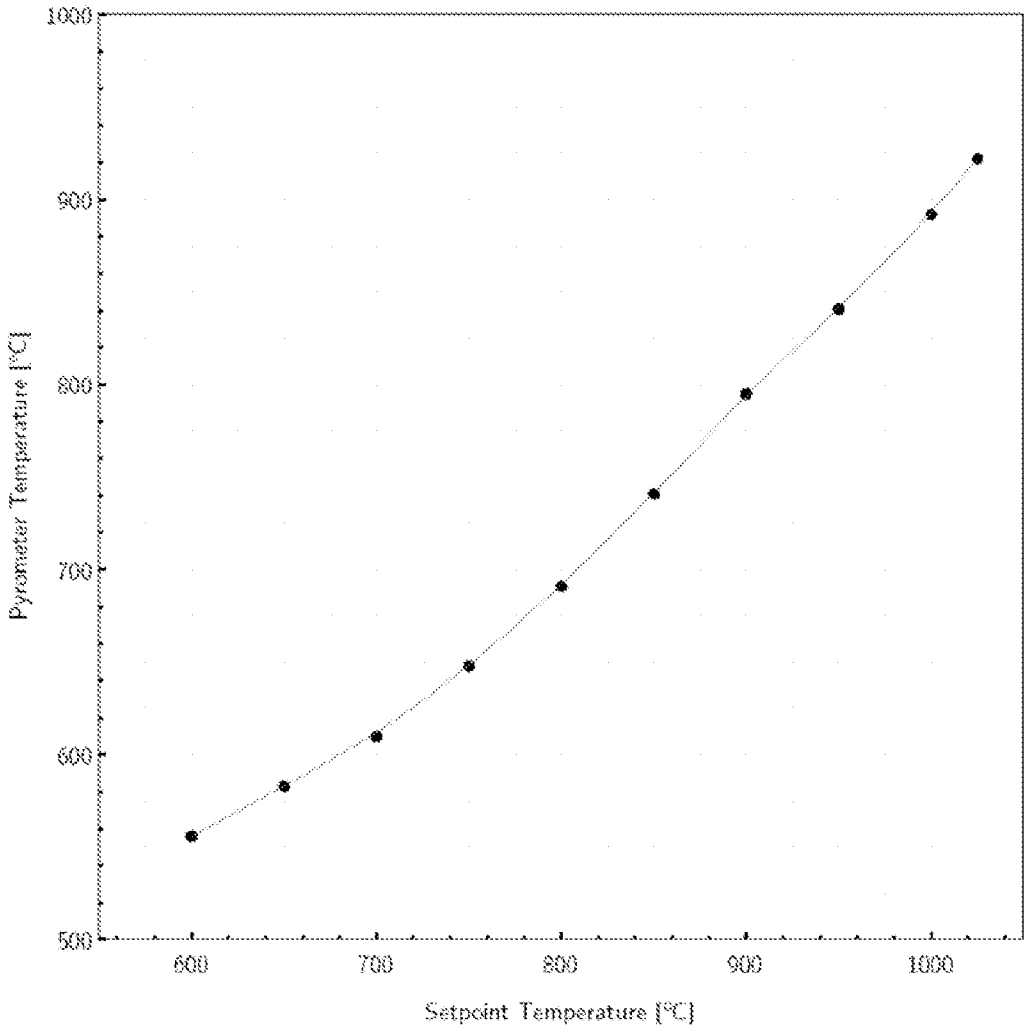
1000
900
800
700
600
500
Pyrometer Temperature [°C]
600
700
800
900
1000
Setpoint Temperature [°C]

FIG. 8

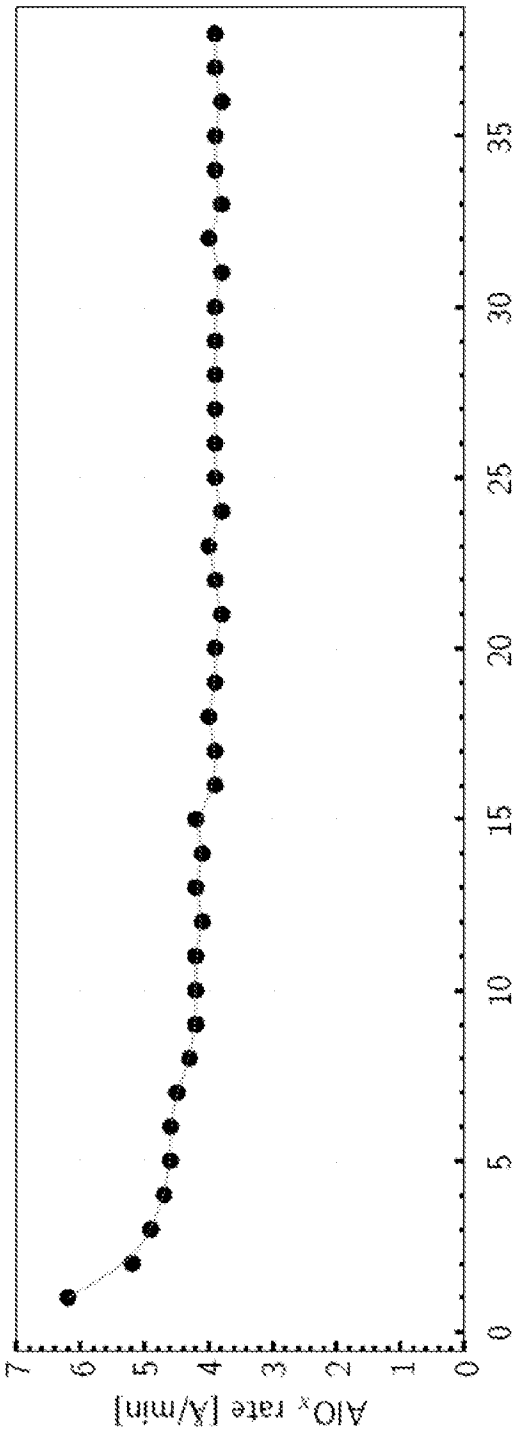

FIG. 9

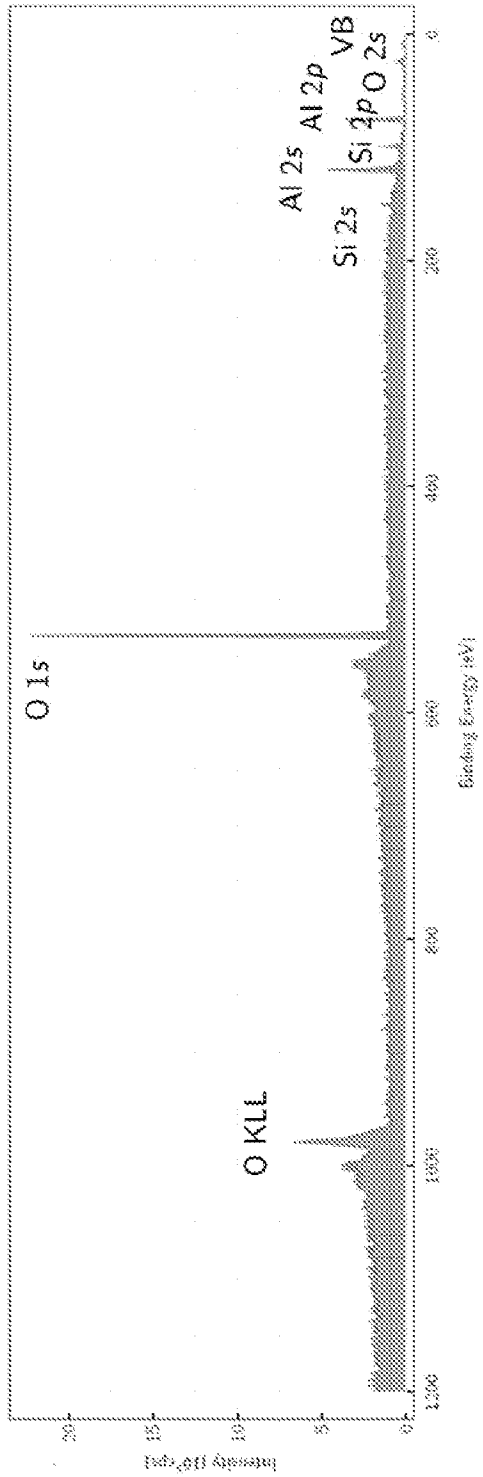
O 1s
O KLL
Al 2s
Al 2p
VB
Si 2s
Si 2p
O 2s
Intensity (10³ cps)
Binding Energy (eV)

FIG. 10A

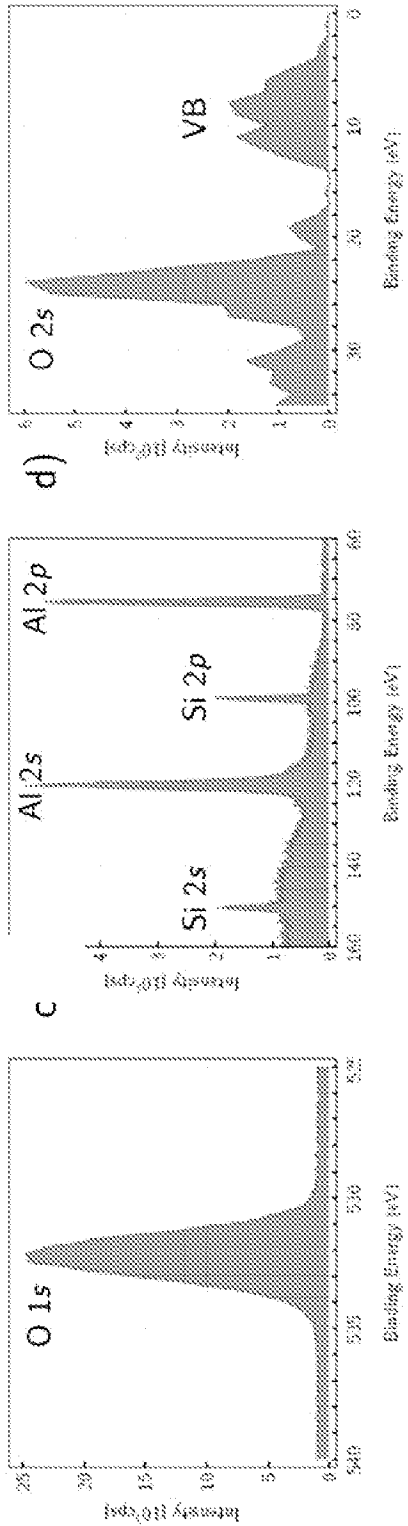

FIG. 10B

FIG. 10C

FIG. 10D

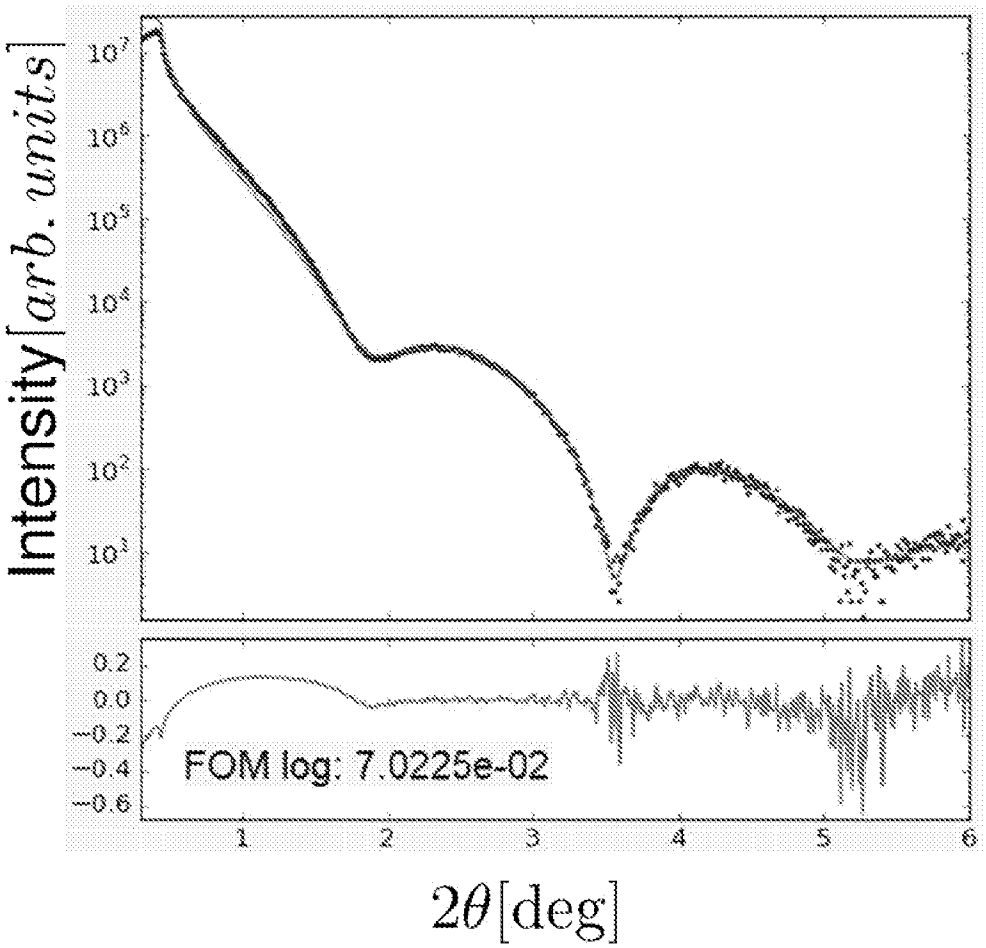
Intensity[arb. units]
10^7
10^6
10^5
10^4
10^3
10^2
10^1
0.2
0.0
−0.2
−0.4
−0.6
FOM log: 7.0225e-02
1
2
3
4
5
6
2θ[deg]

FIG. 11

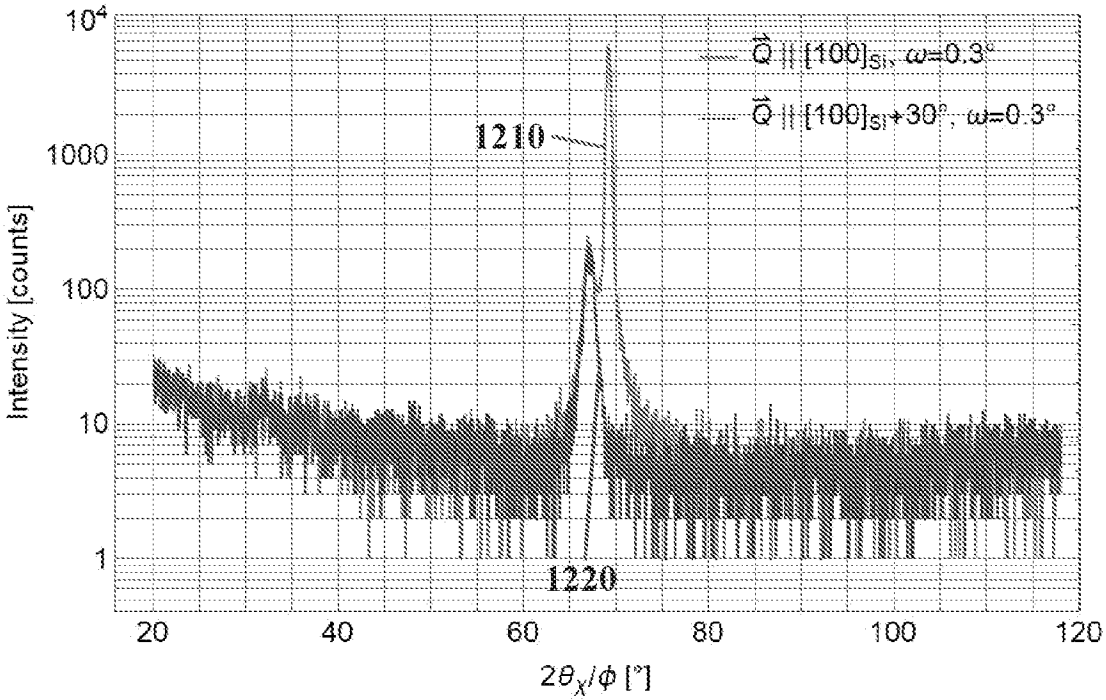
10^4
1000
100
10
1
Intensity [counts]
$\vec{Q}$ || [100]$_{Si}$, ω=0.3°
$\vec{Q}$ || [100]$_{Si}$+30°, ω=0.3°
1210
1220
20
40
60
80
100
120
$2\theta_\chi/\phi$ [°]

FIG. 12

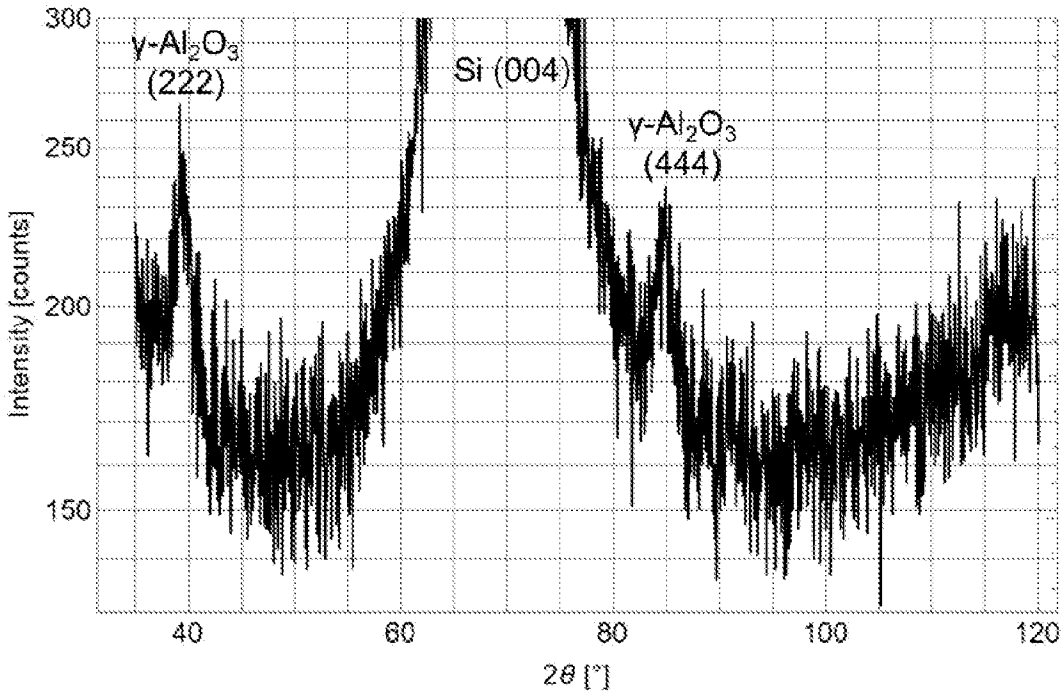
300
250
200
150
Intensity [counts]
γ-Al_2O_3 (222)
Si (004)
γ-Al_2O_3 (444)
40
60
80
100
120
2θ [°]

FIG. 13

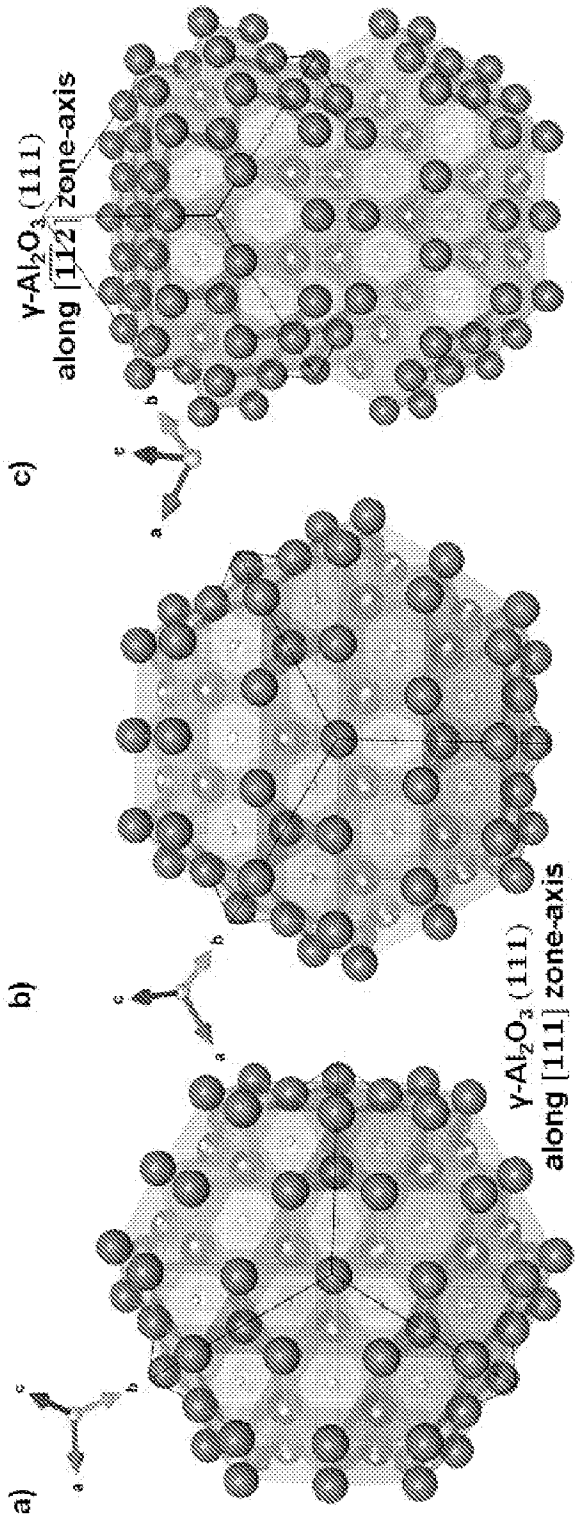

FIG. 14A FIG. 14B FIG. 14C

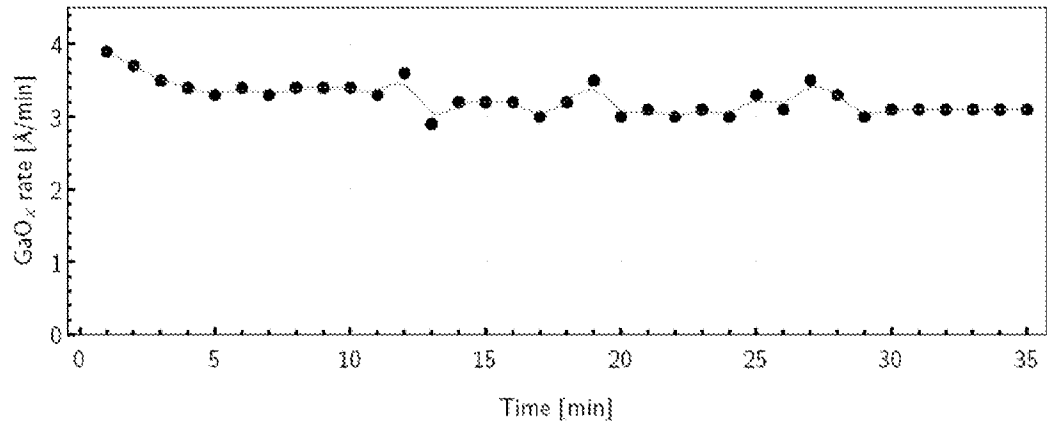

FIG. 15A

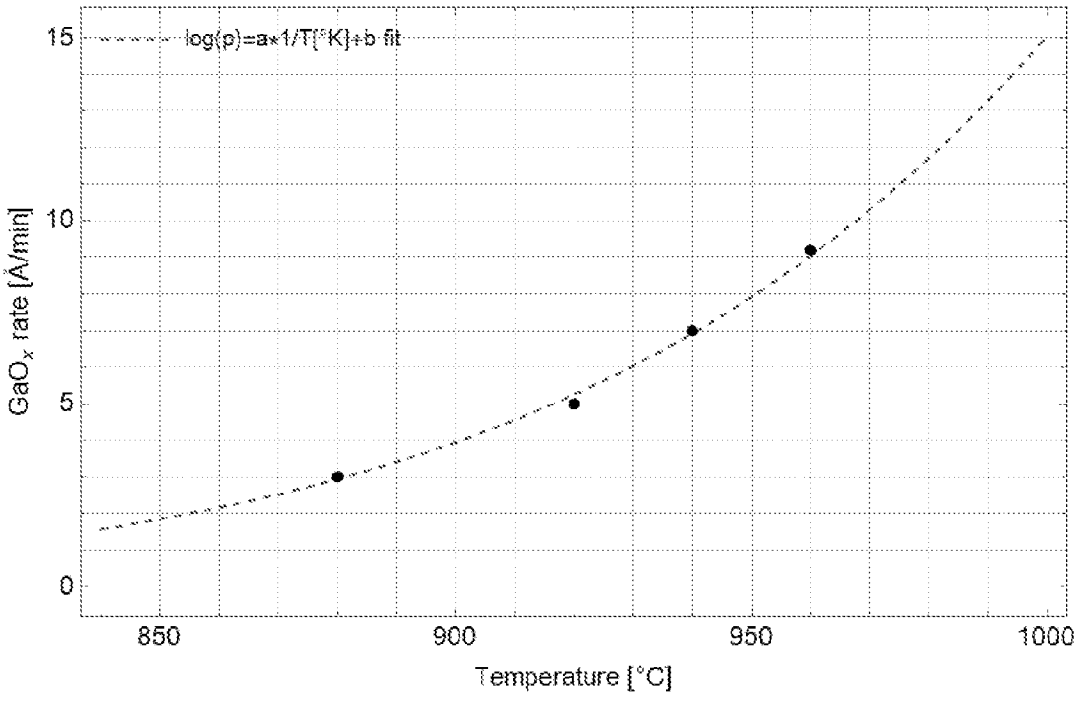

FIG. 15B

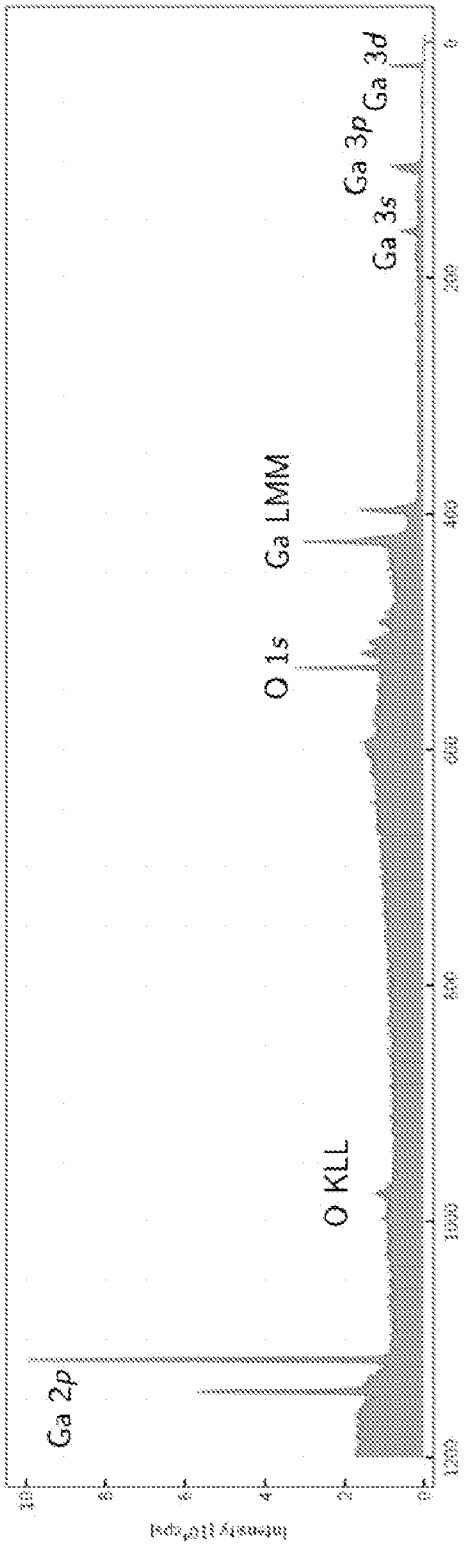
Ga 2p
O KLL
O 1s
Ga LMM
Ga 3s
Ga 3p
Ga 3d
Intensity (10^3 cps)
0
2
4
6
8
10
1200
1000
800
600
400
200
0

FIG. 16A

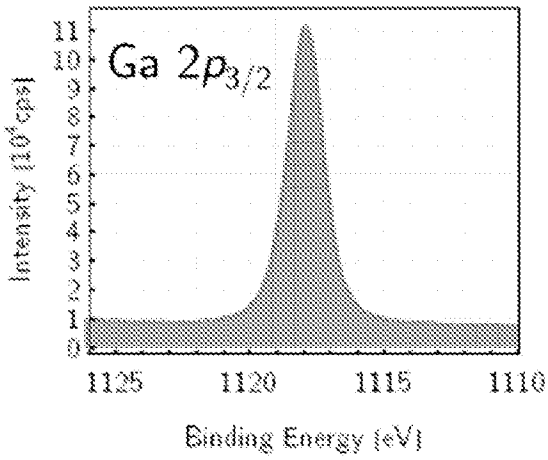

FIG. 16B

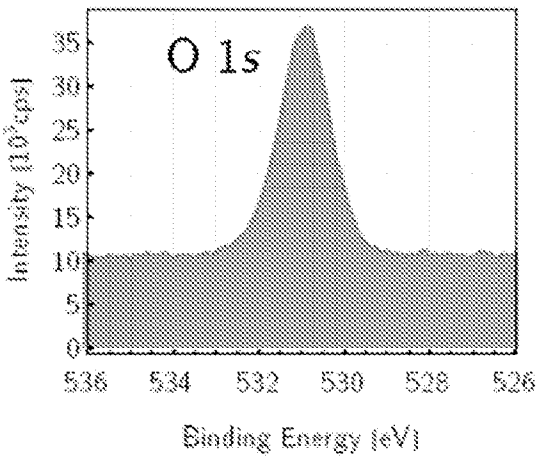

FIG. 16C

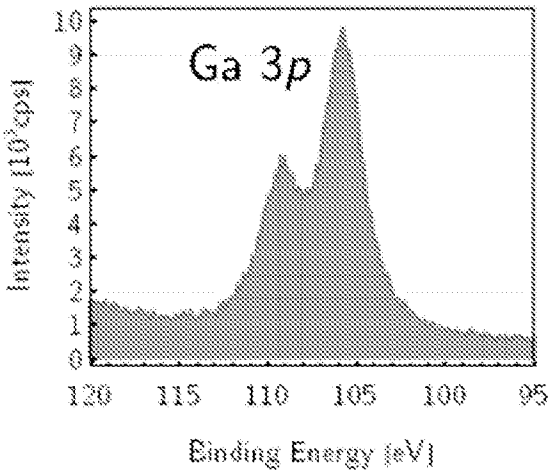

FIG. 16D

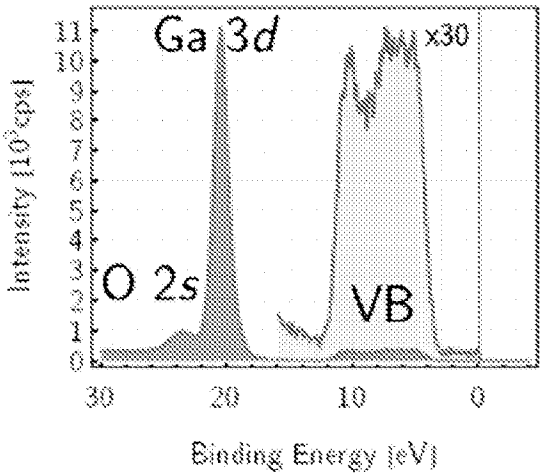

FIG. 16E

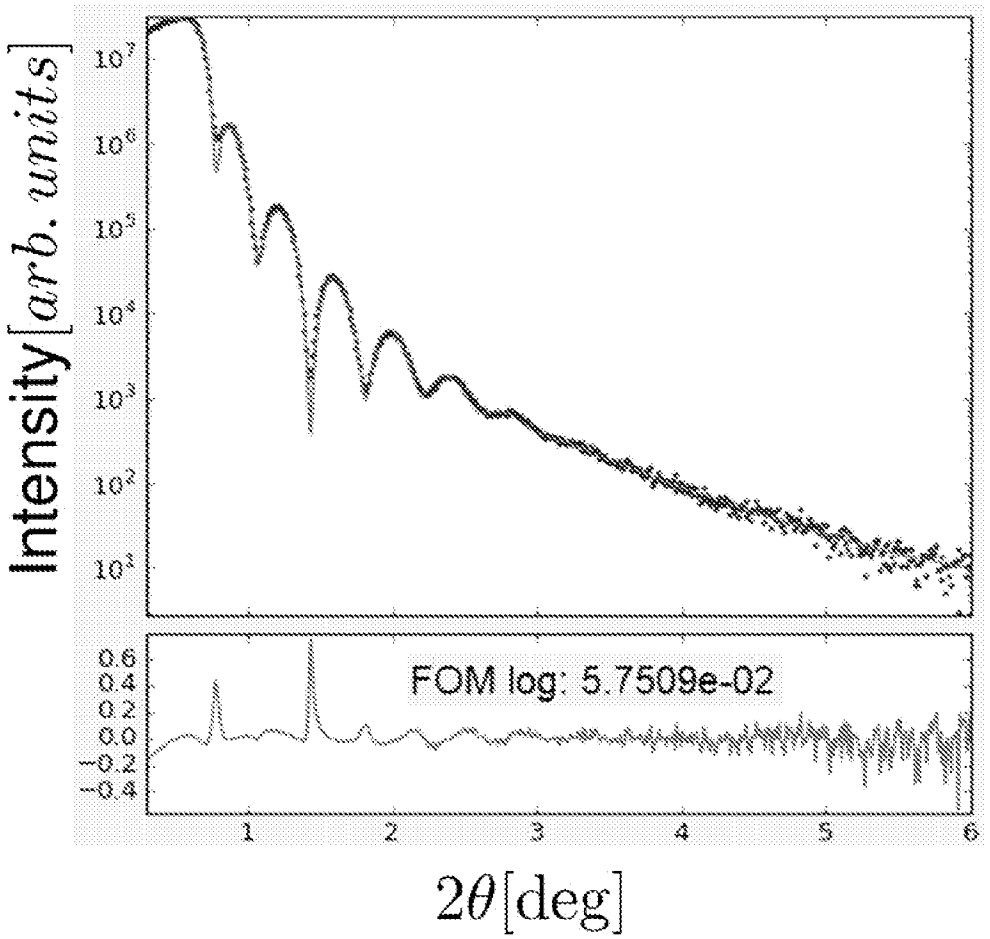
Intensity[arb. units]
10^7
10^6
10^5
10^4
10^3
10^2
10^1
FOM log: 5.7509e-02
0.6
0.4
0.2
0.0
−0.2
−0.4
1
2
3
4
5
6
2θ[deg]

FIG. 17

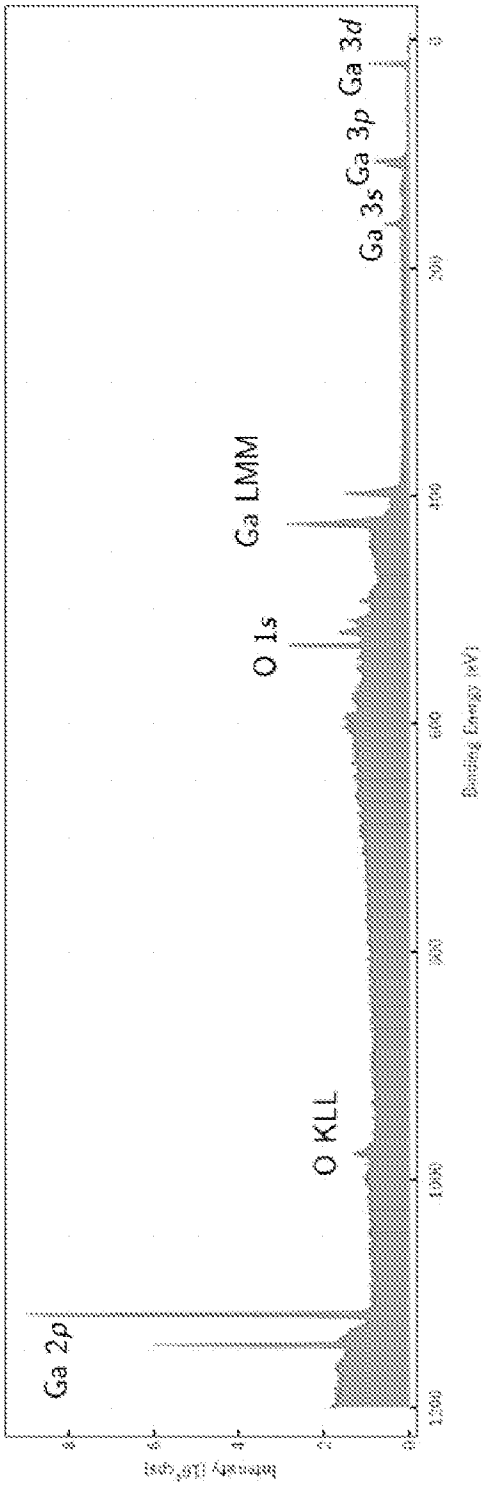

FIG. 18A

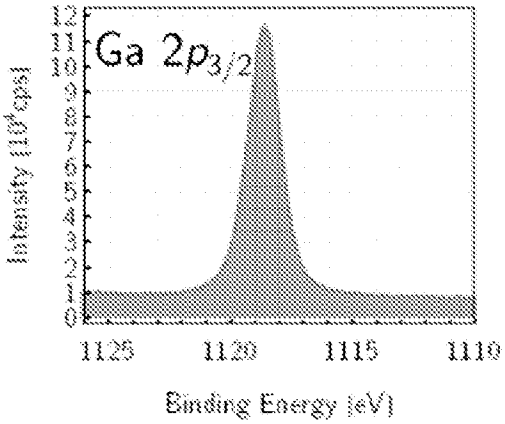

FIG. 18B

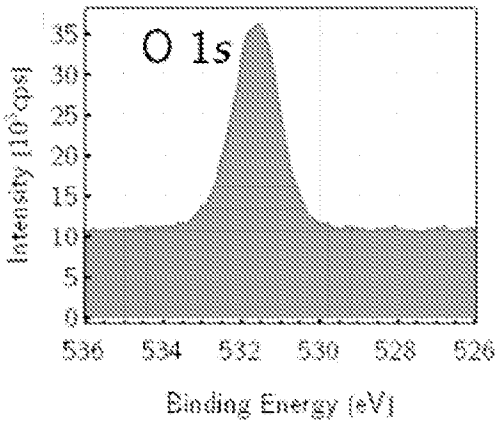

FIG. 18C

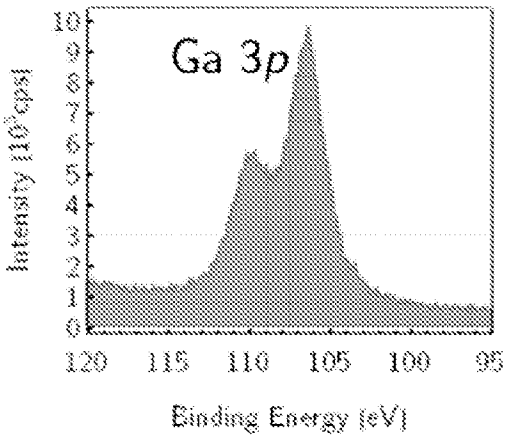

FIG. 18D

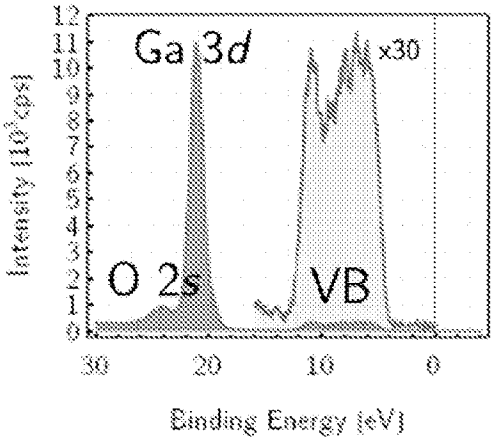

FIG. 18E

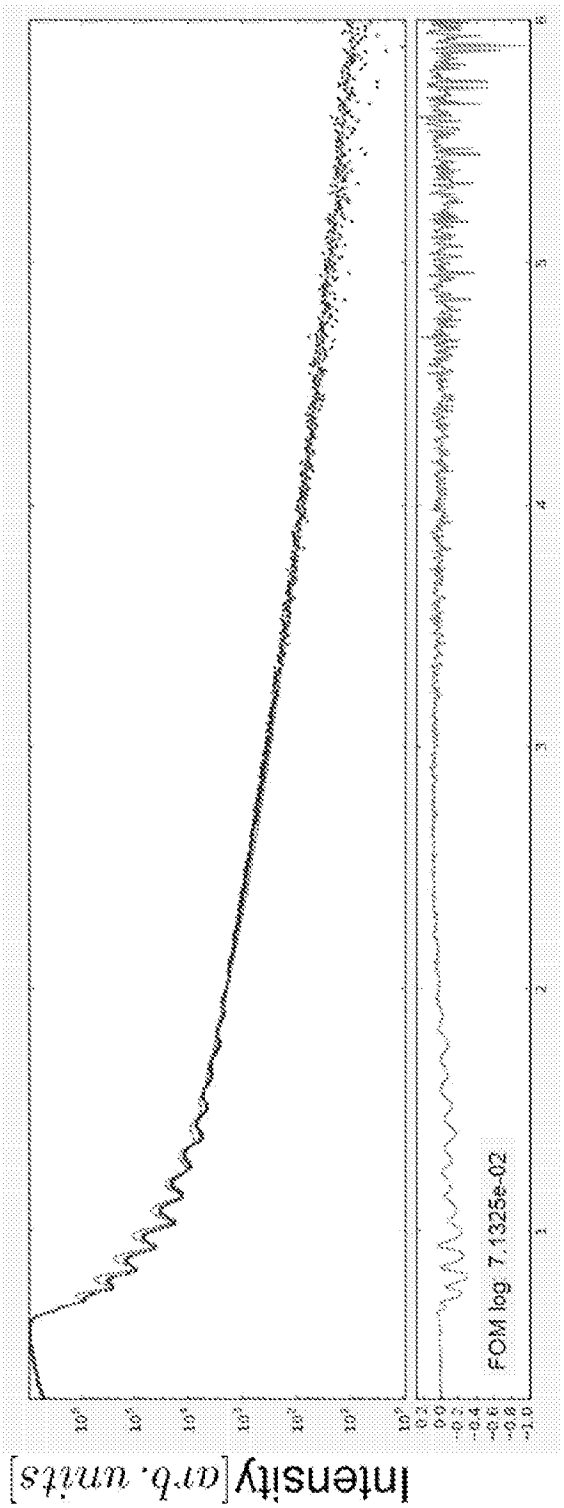

FIG. 19

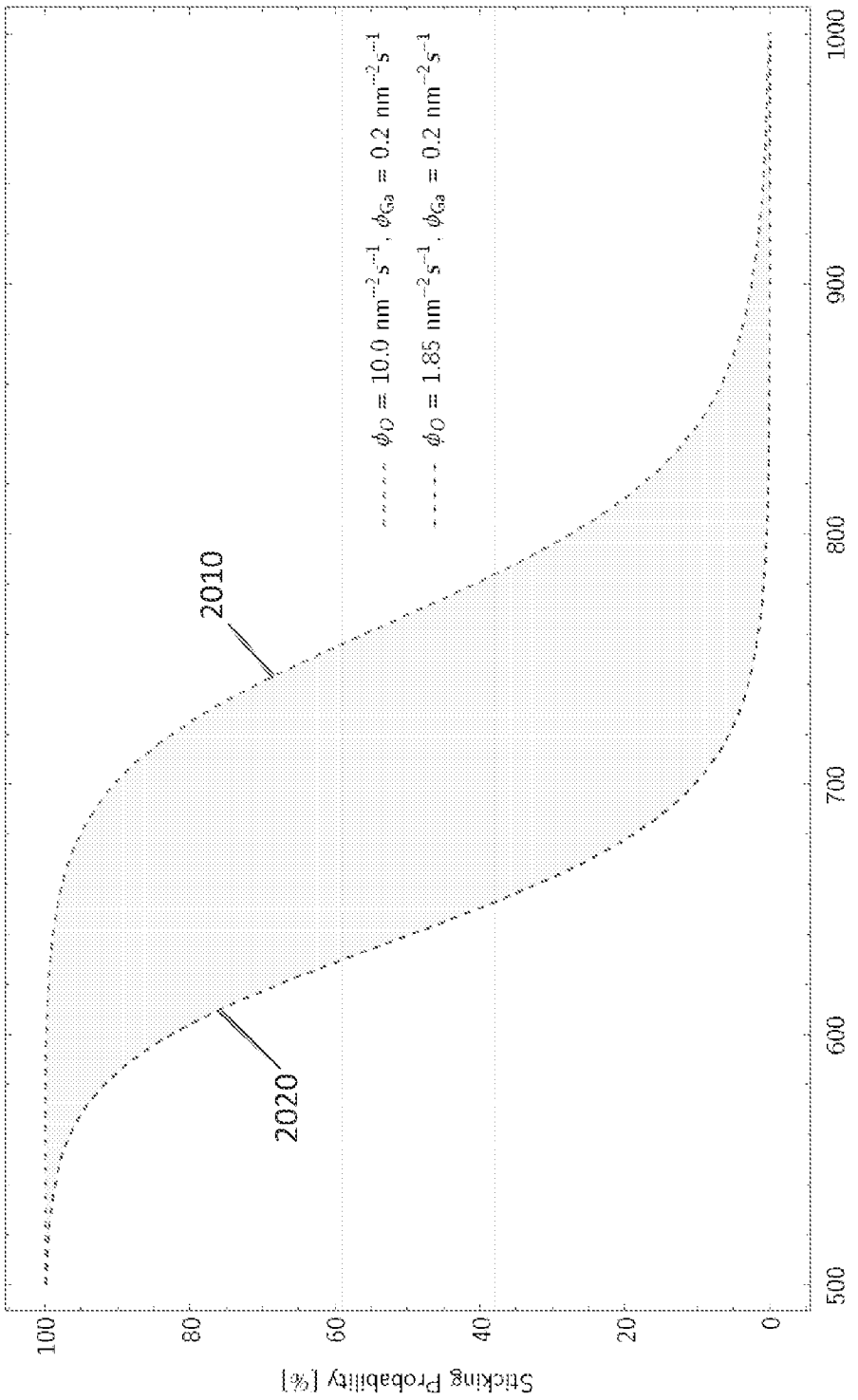
Sticking Probability [%]
100
80
60
40
20
0
500
600
700
800
900
1000
Temperature [°C]
2010
2020
ϕ_O = 10.0 nm^{-2}s^{-1}, ϕ_{Ga} = 0.2 nm^{-2}s^{-1}
ϕ_O = 1.85 nm^{-2}s^{-1}, ϕ_{Ga} = 0.2 nm^{-2}s^{-1}

FIG. 20

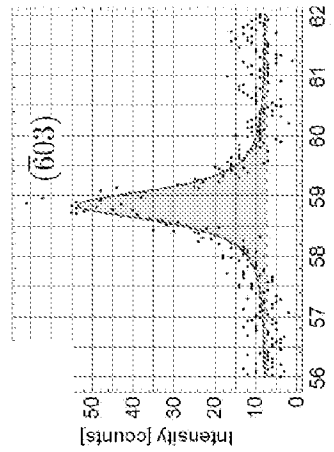

FIG. 21C

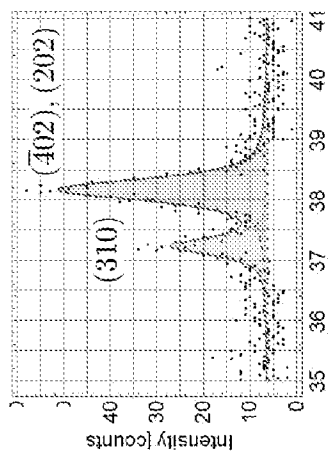

FIG. 21B

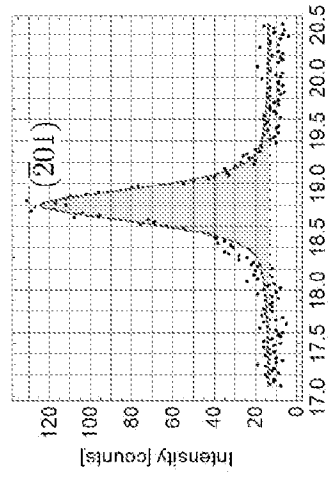

FIG. 21A

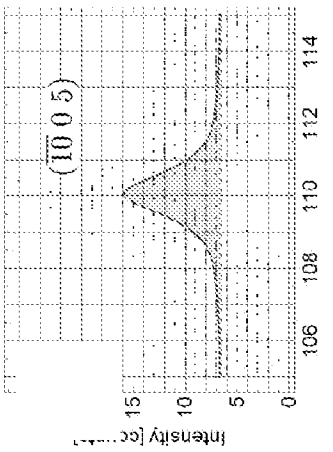

FIG. 21F

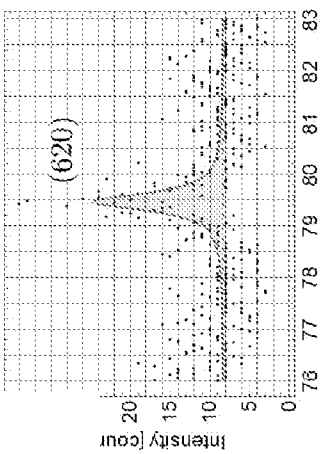

FIG. 21E

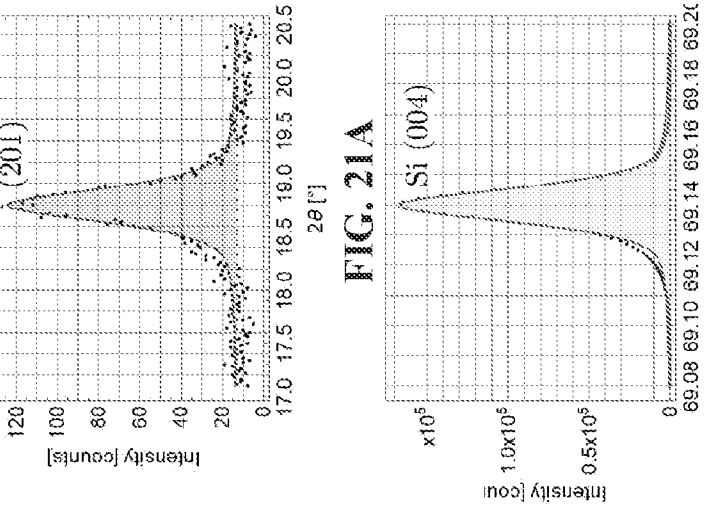

FIG. 21D

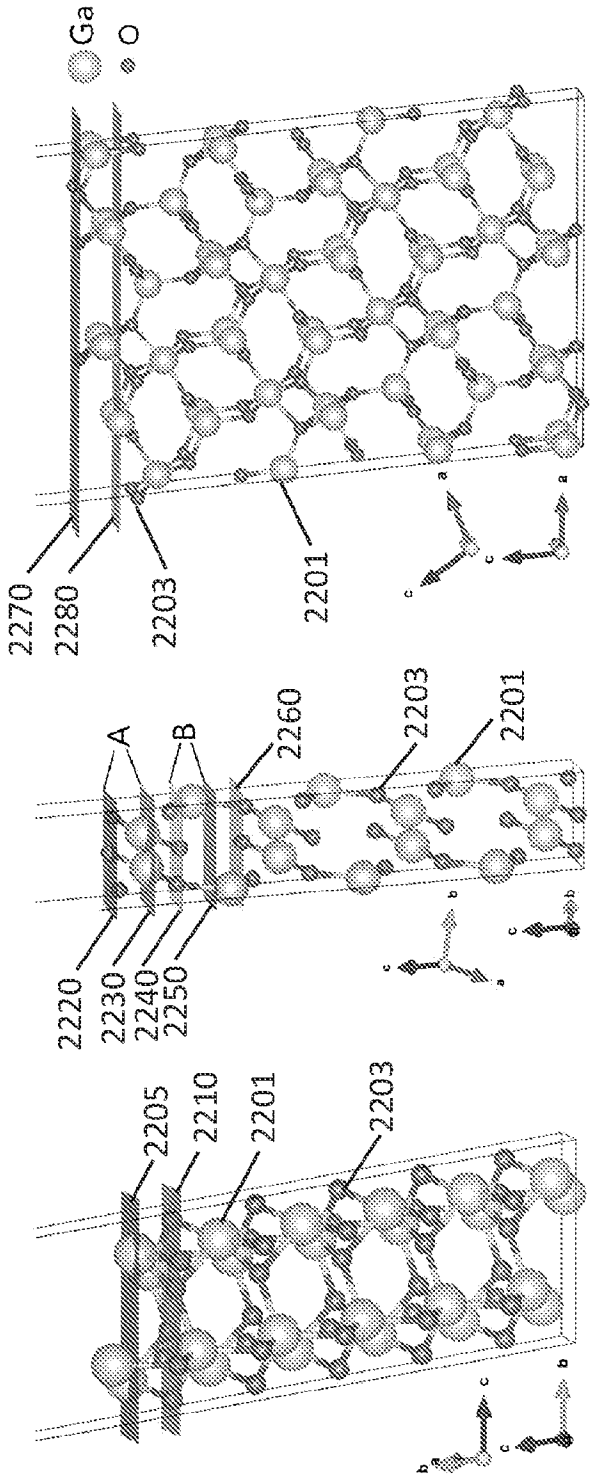

FIG. 22C

FIG. 22B

FIG. 22A

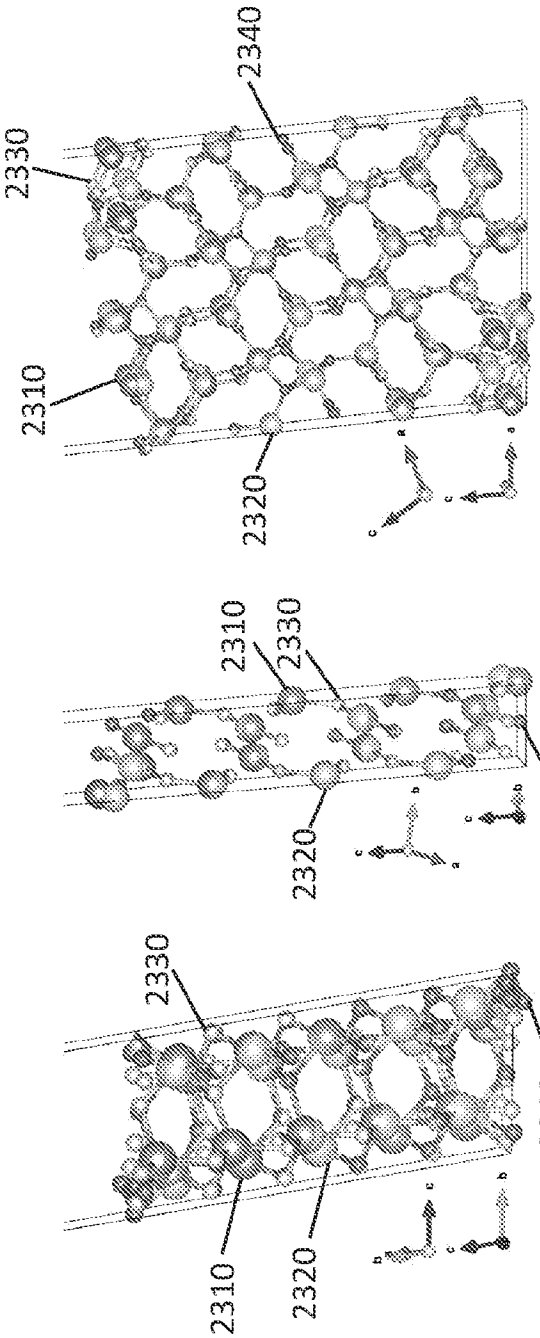

FIG. 23C

FIG. 23B

FIG. 23A

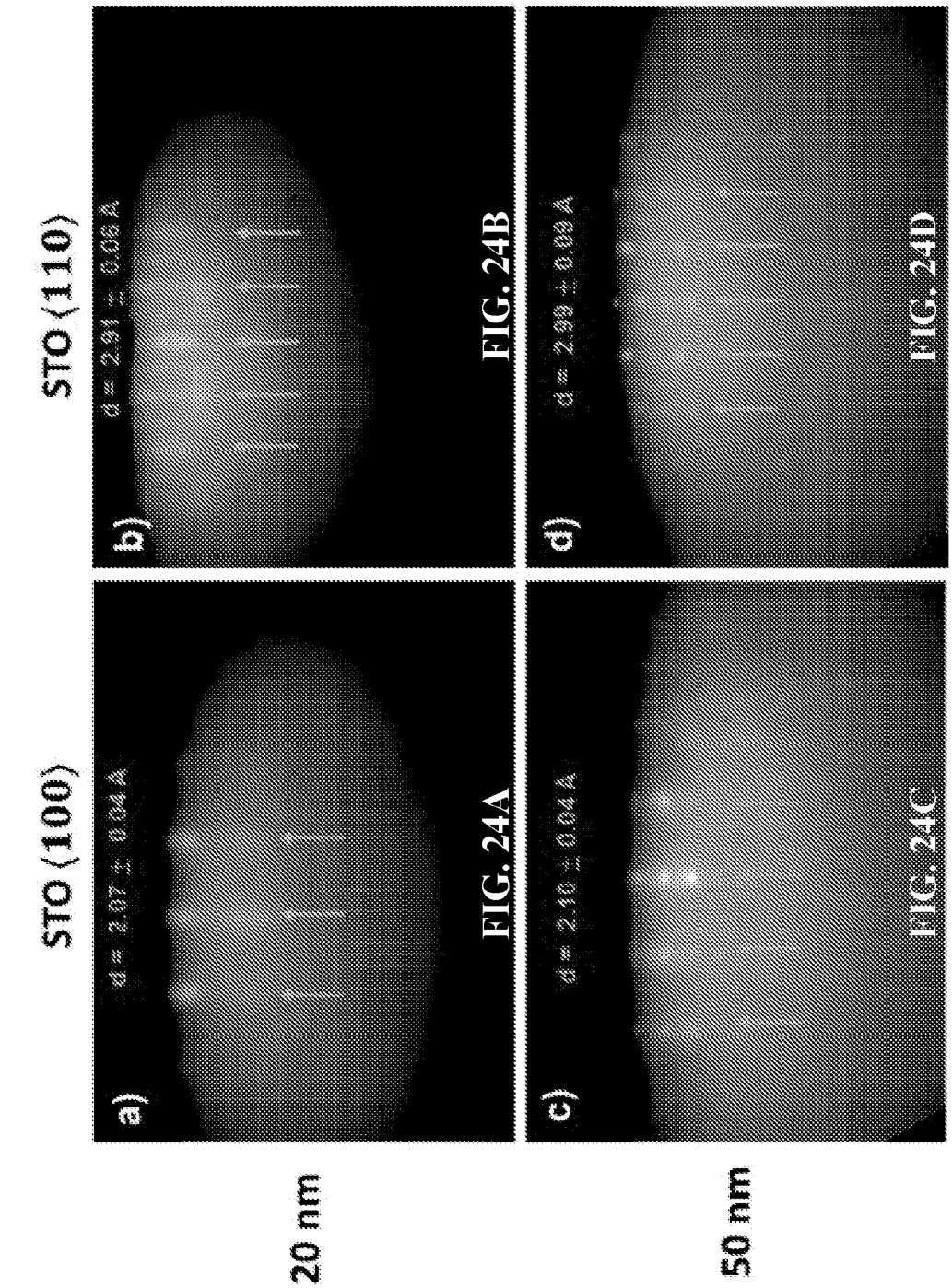

FIG. 24A

FIG. 24B

FIG. 24C

FIG. 24D

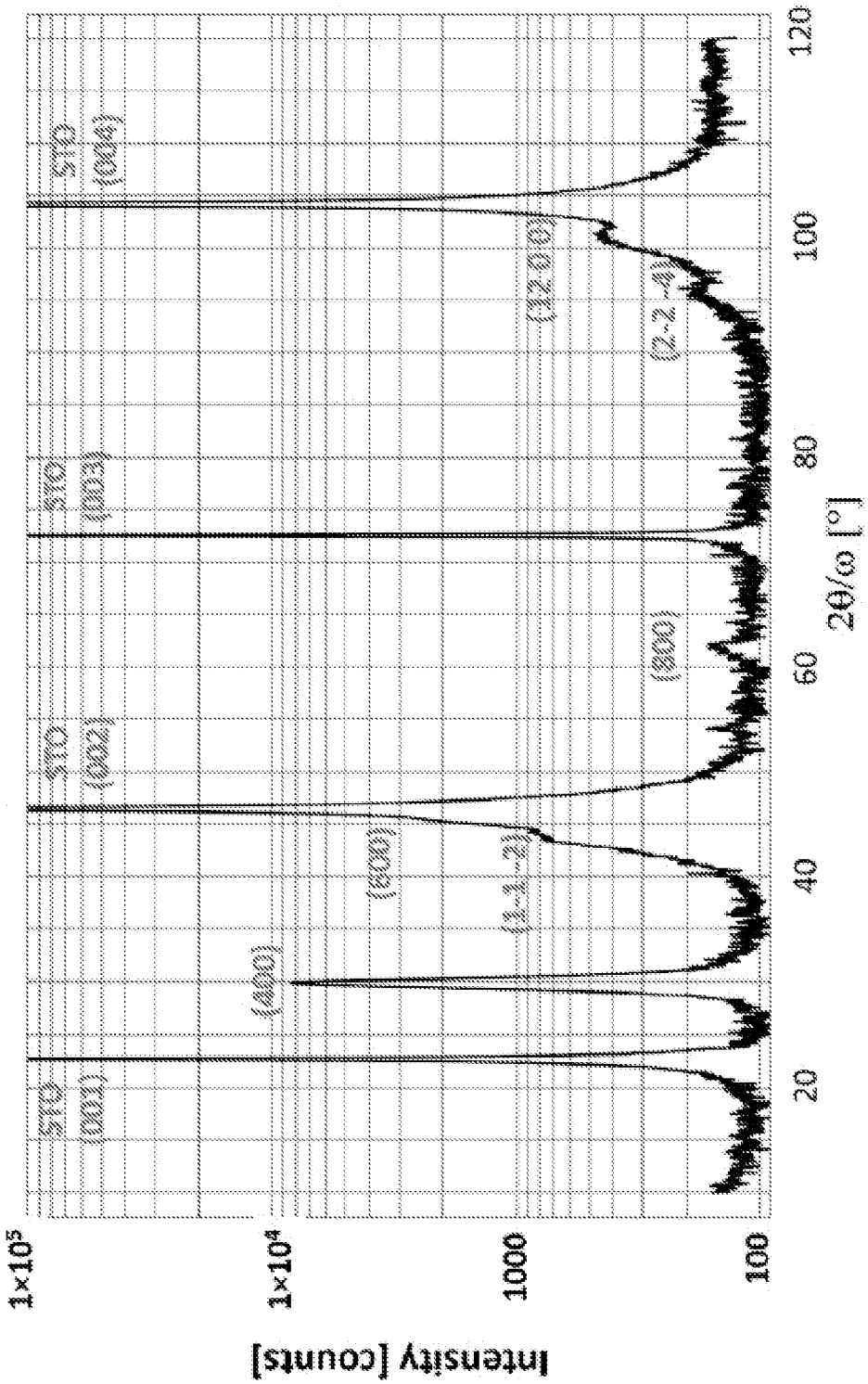
Intensity [counts]
1×10⁵
1×10⁴
1000
100
20
40
60
80
100
120
2θ/ω [°]
STO (001)
STO (002)
STO (003)
STO (004)
(400)
(200)
(1-1-2)
(800)
(12-10)
(2-2-4)

FIG. 25A

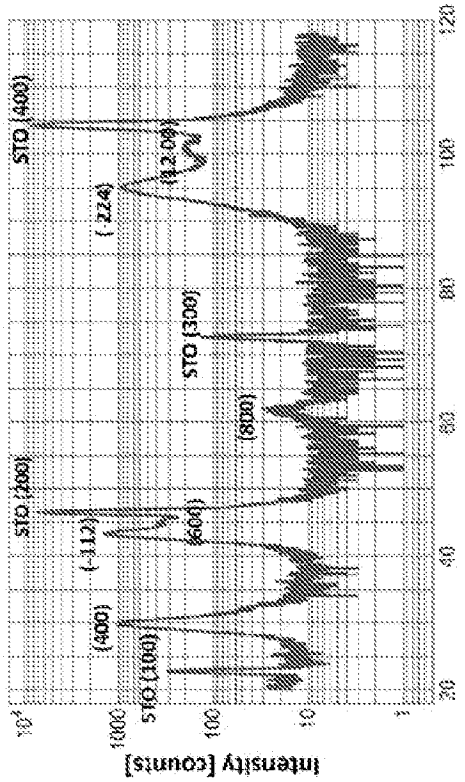

FIG. 25B

FIG. 25C

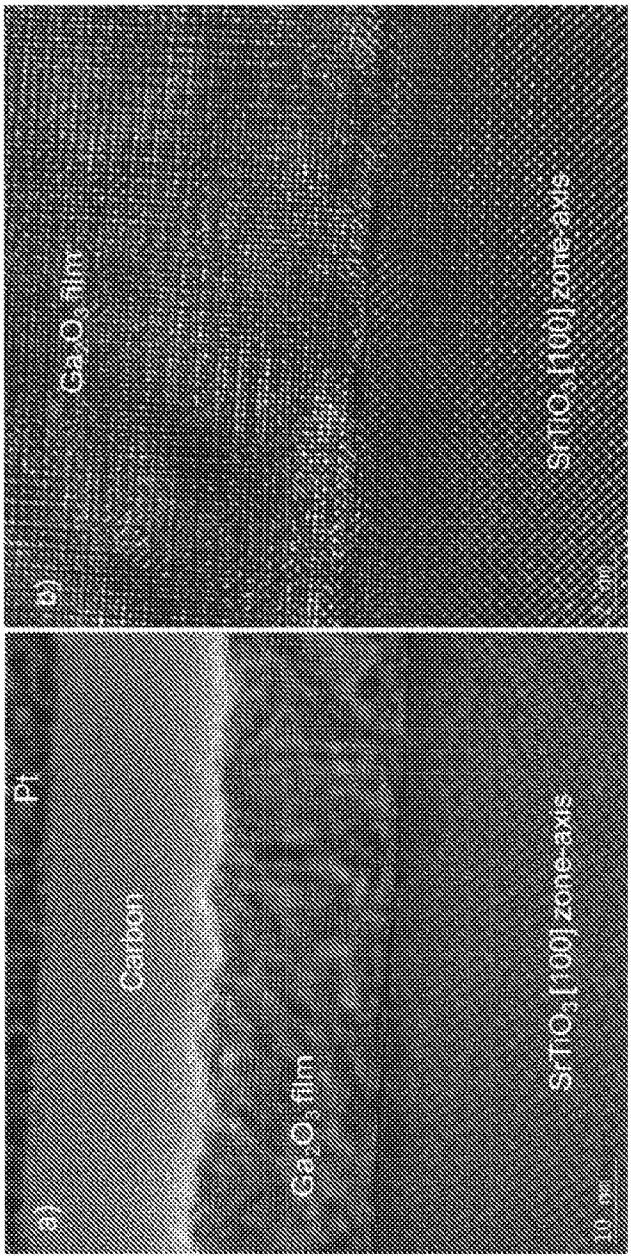

FIG. 26A

FIG. 26B

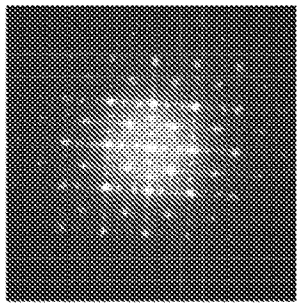

FIG. 26C

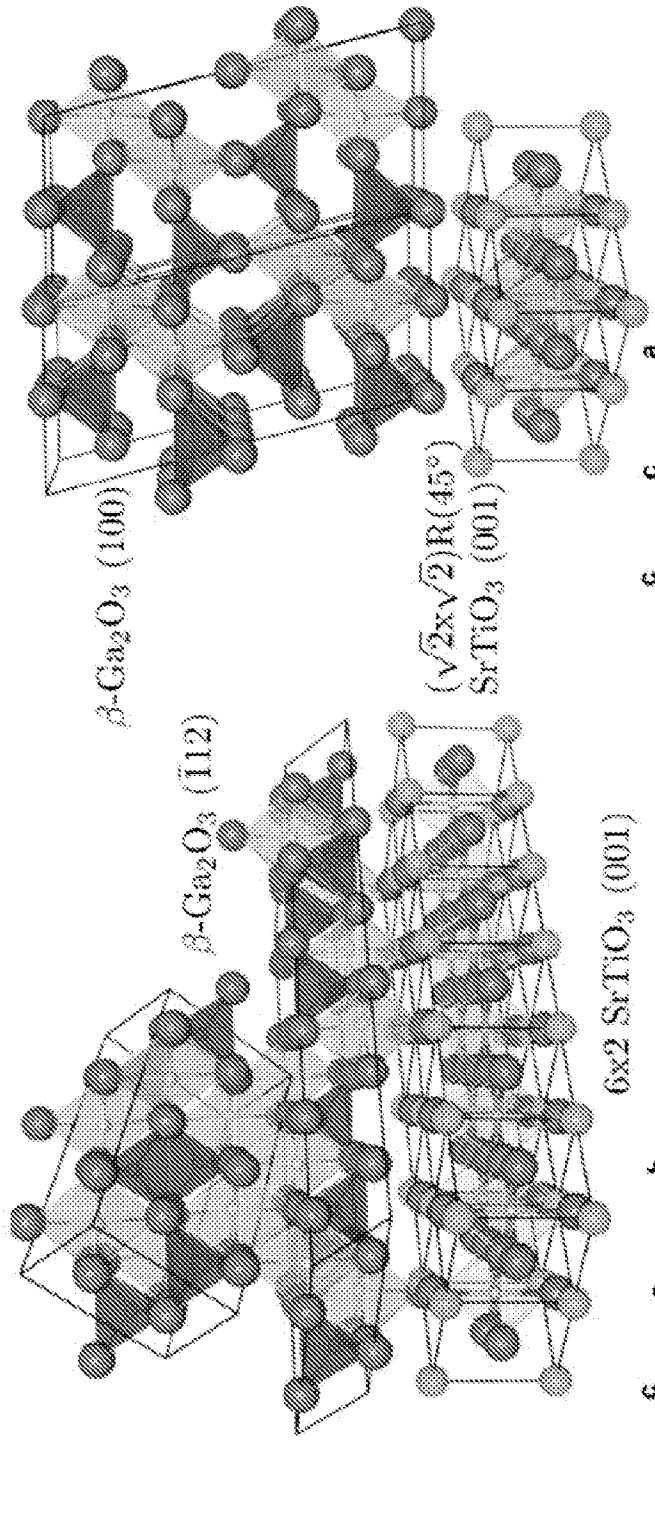

FIG. 27A

FIG. 27B

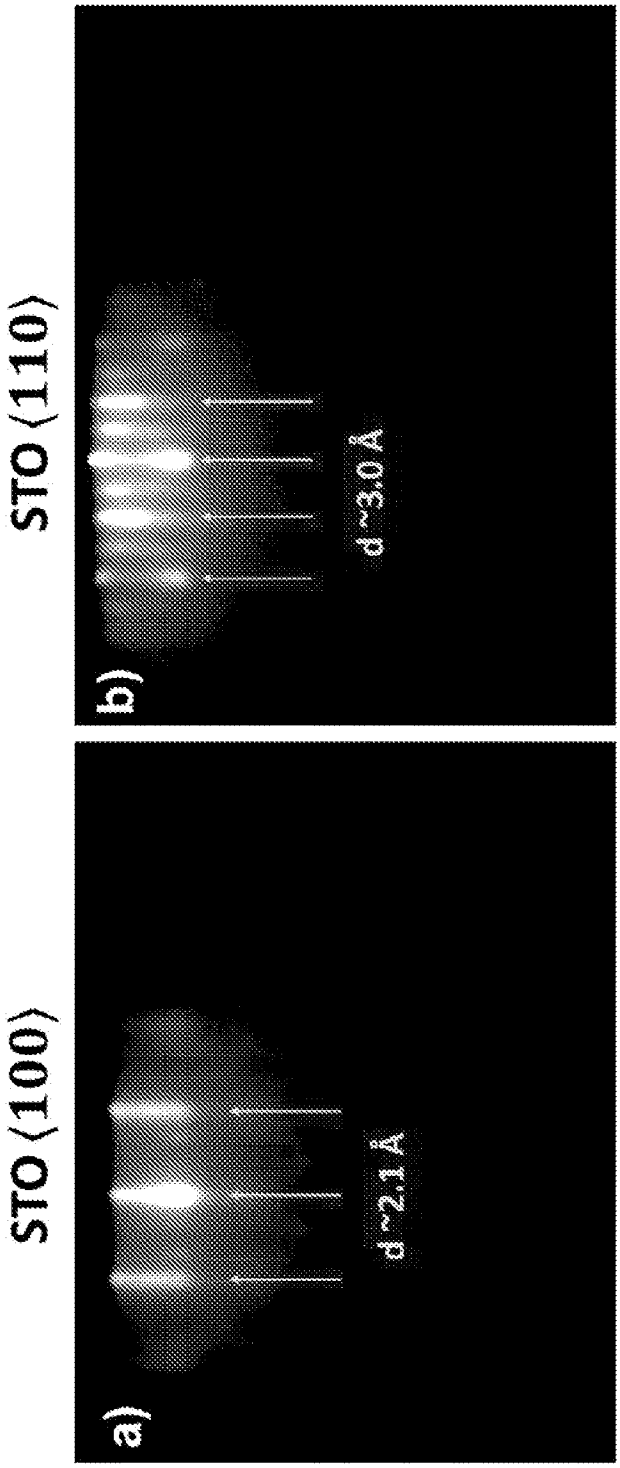

FIG. 28A

FIG. 28B

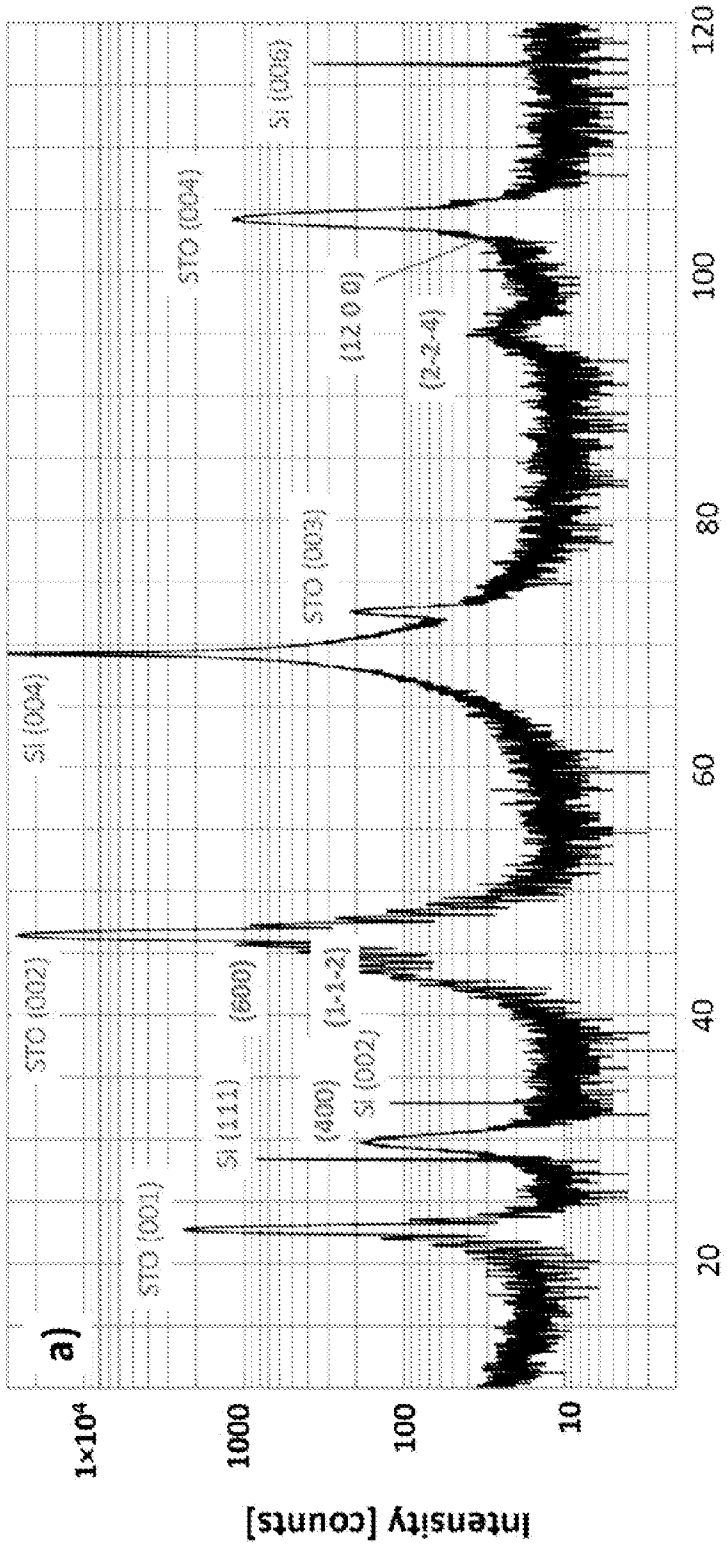
a)
STO (001)
STO (002)
Si (004)
Si (111)
(400)
(200)
Si (002)
(1-1-2)
STO (003)
(2-2-4)
(12 0 0)
STO (004)
Si (008)
1×10^4
1000
100
10
intensity [counts]
20
40
60
80
100
120
2θ/ω [°]

FIG. 29A

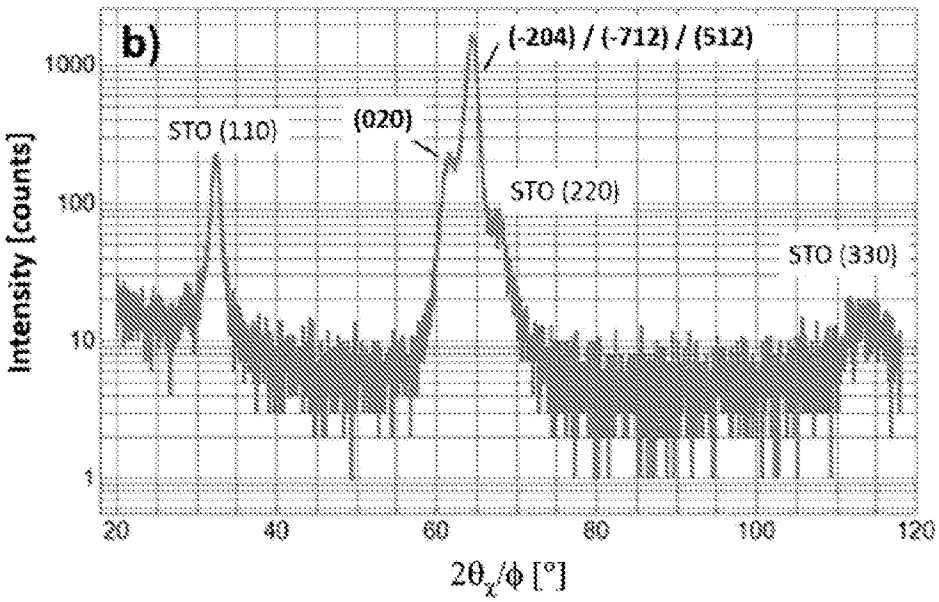

FIG. 29B

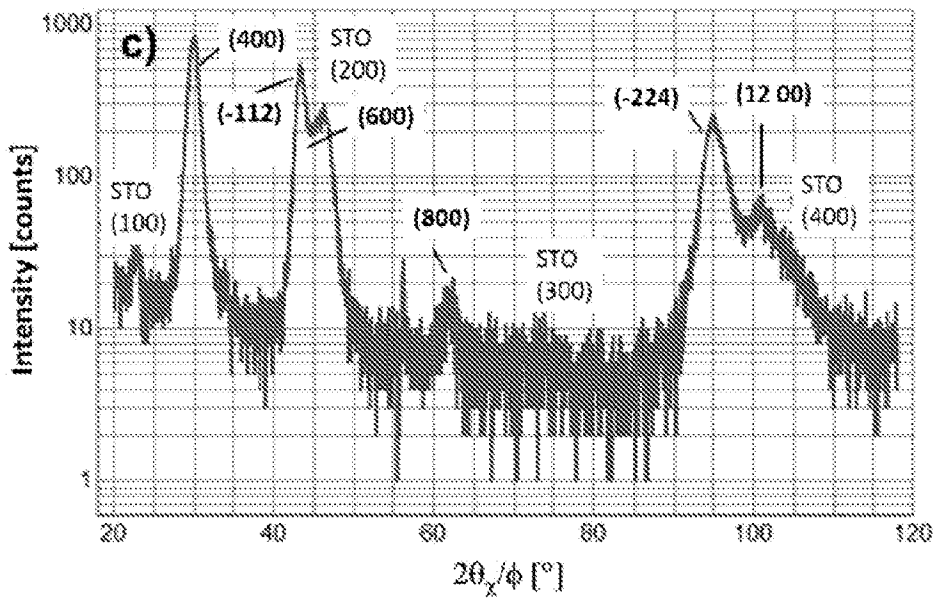

FIG. 29C

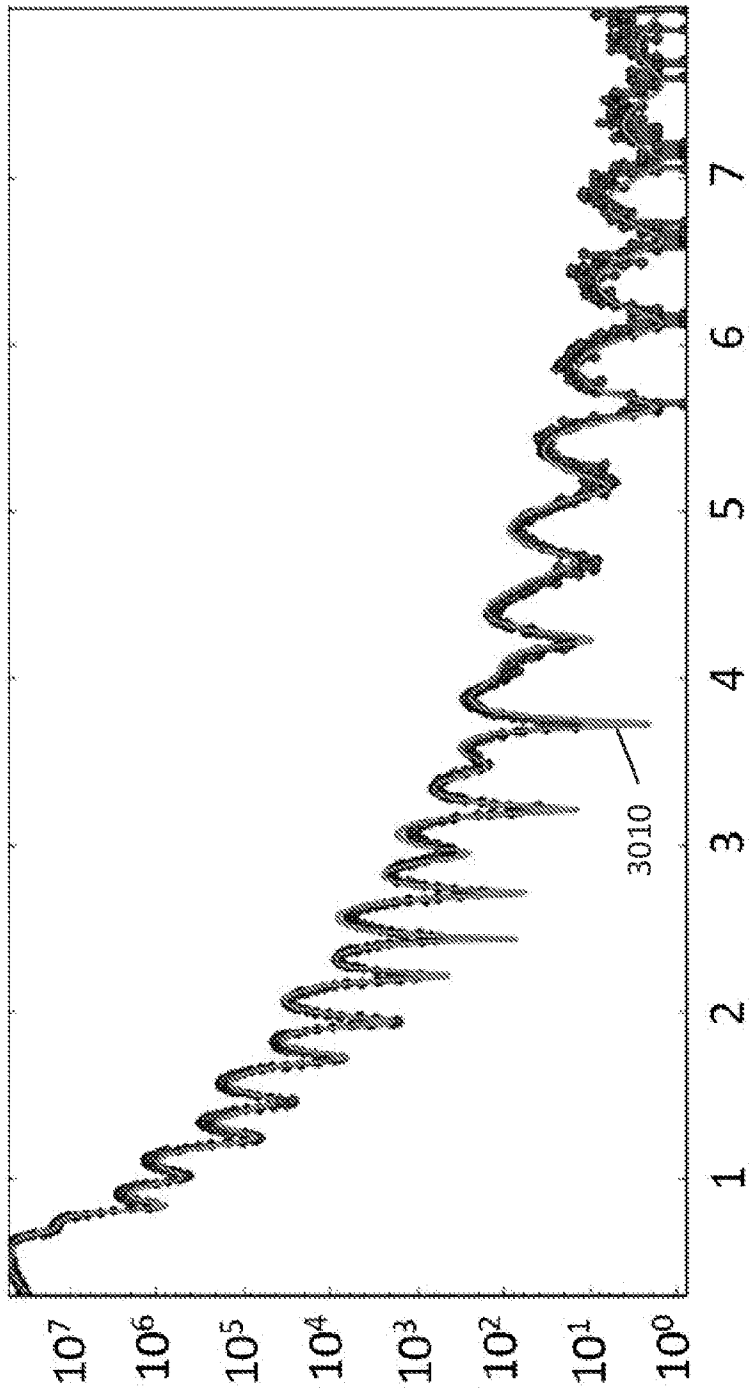

FIG. 30A

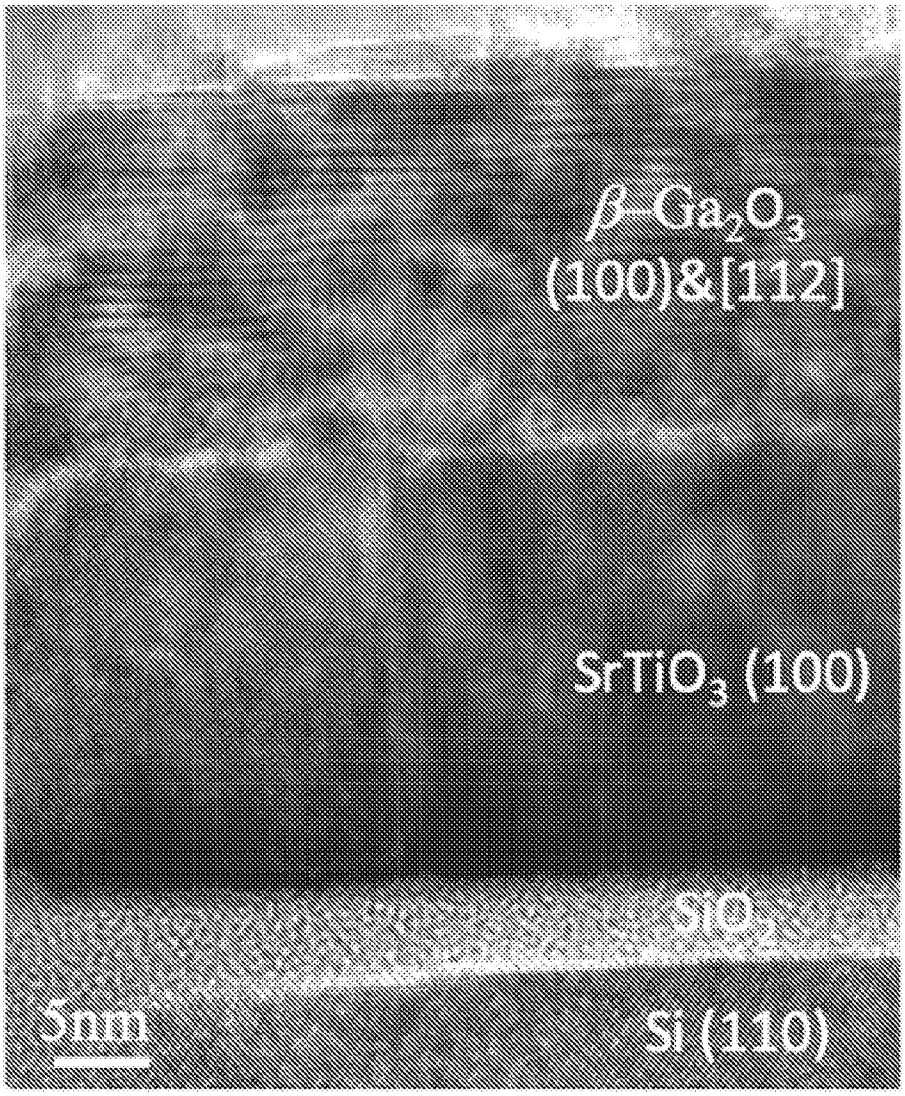

FIG. 30B

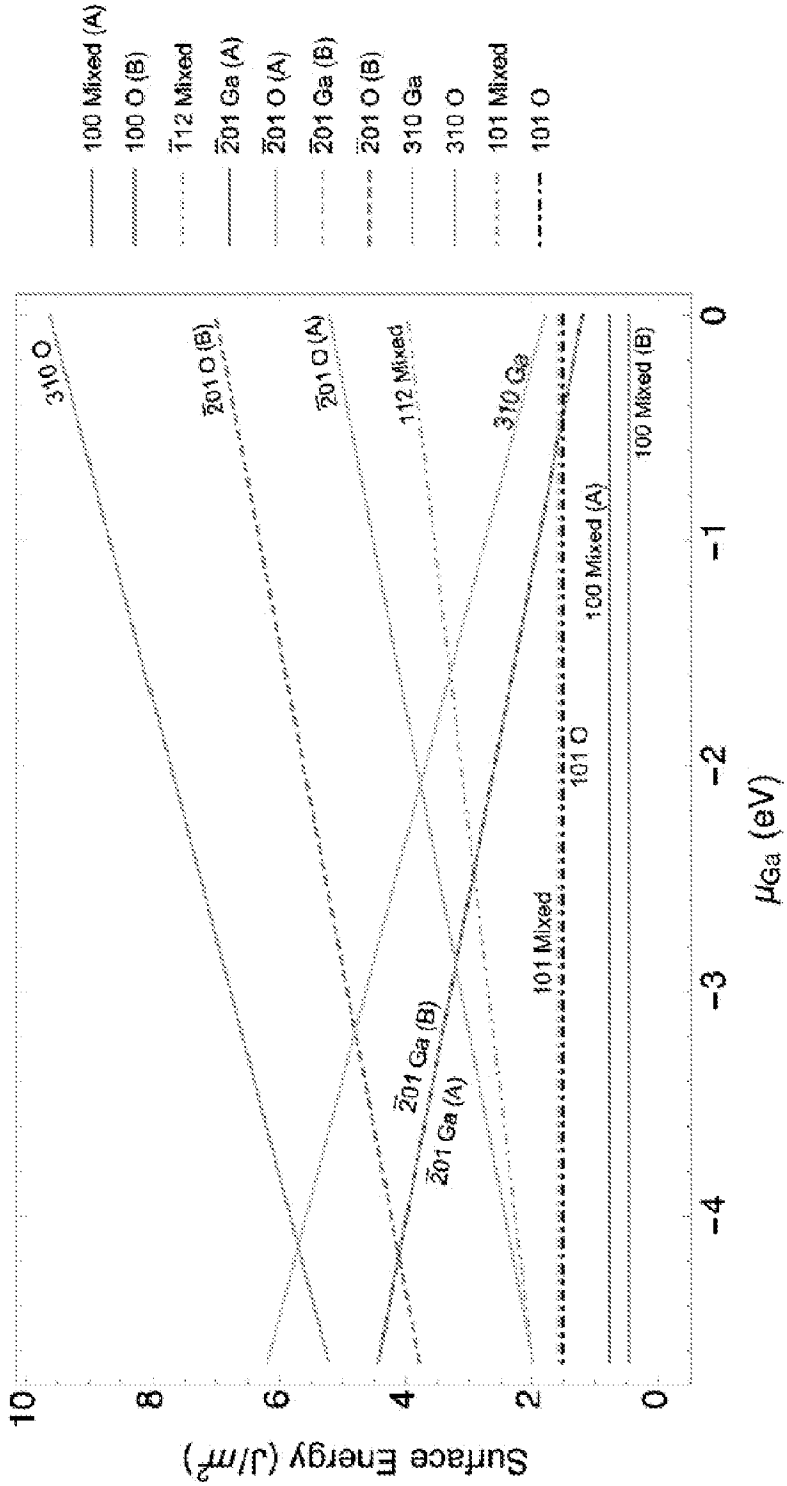
100 Mixed (A)
100 O (B)
$\bar{1}12$ Mixed
$\bar{2}01$ Ga (A)
$\bar{2}01$ O (A)
$\bar{2}01$ Ga (B)
$\bar{2}01$ O (B)
310 Ga
310 O
101 Mixed
101 O
Surface Energy (J/m^2)
μ_{Ga} (eV)
0
2
4
6
8
10
−4
−3
−2
−1
0

FIG. 31

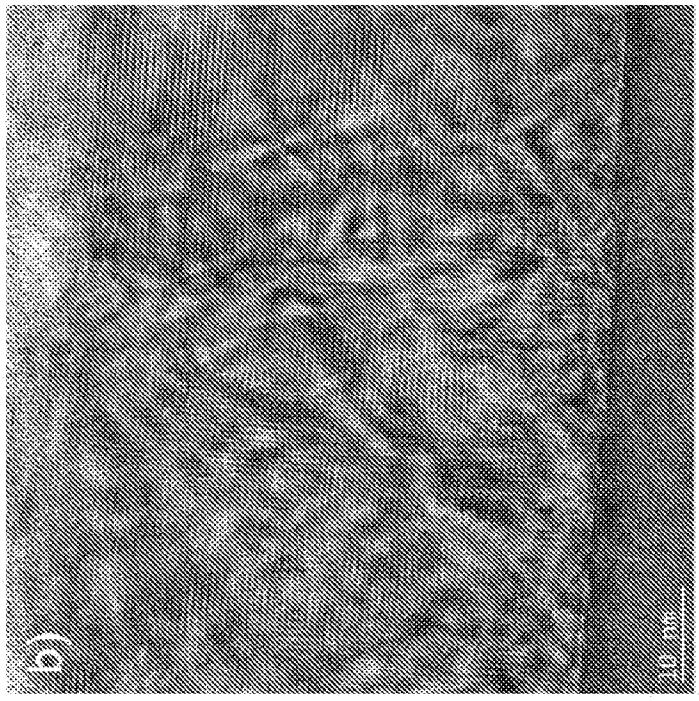

FIG. 32B

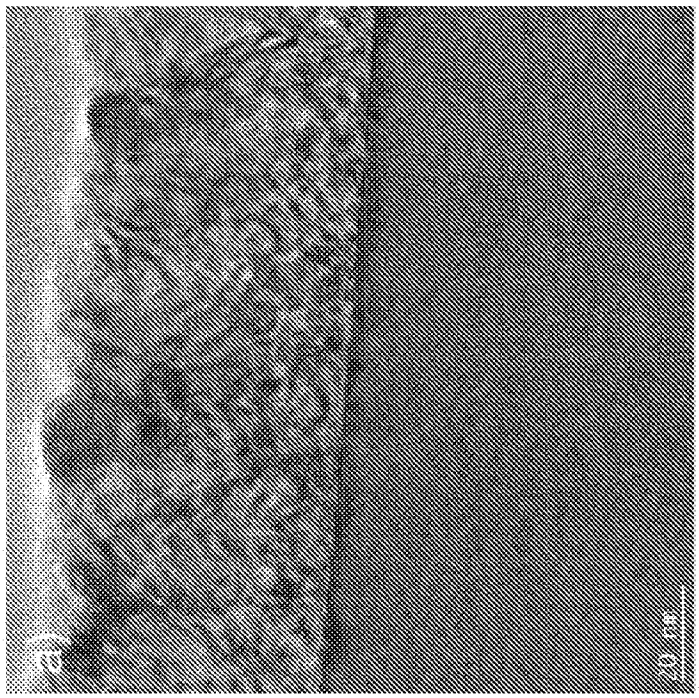

FIG. 32A

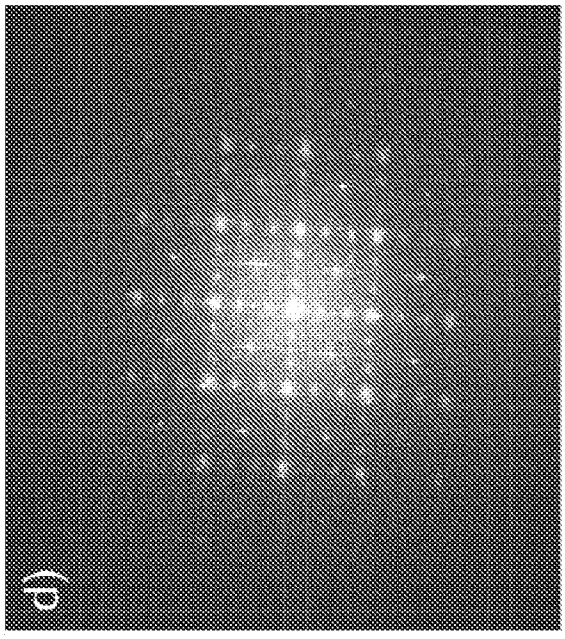

FIG. 32D

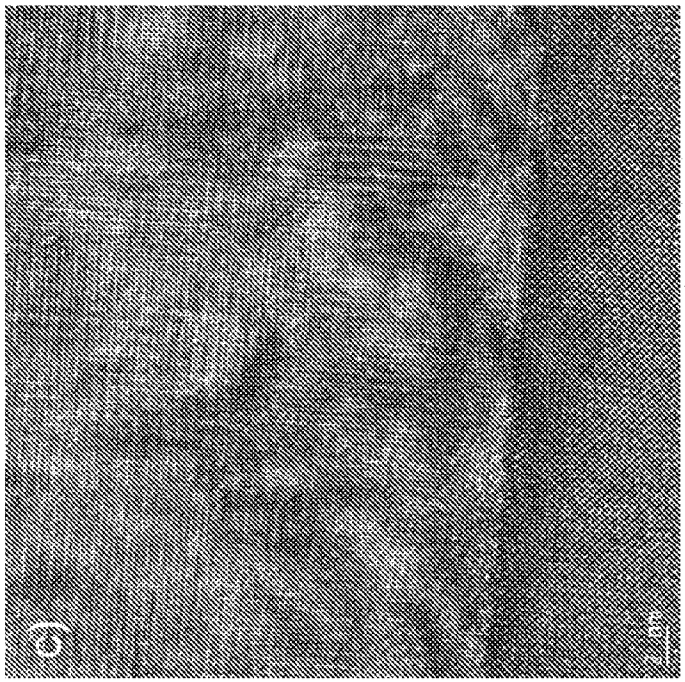

FIG. 32C

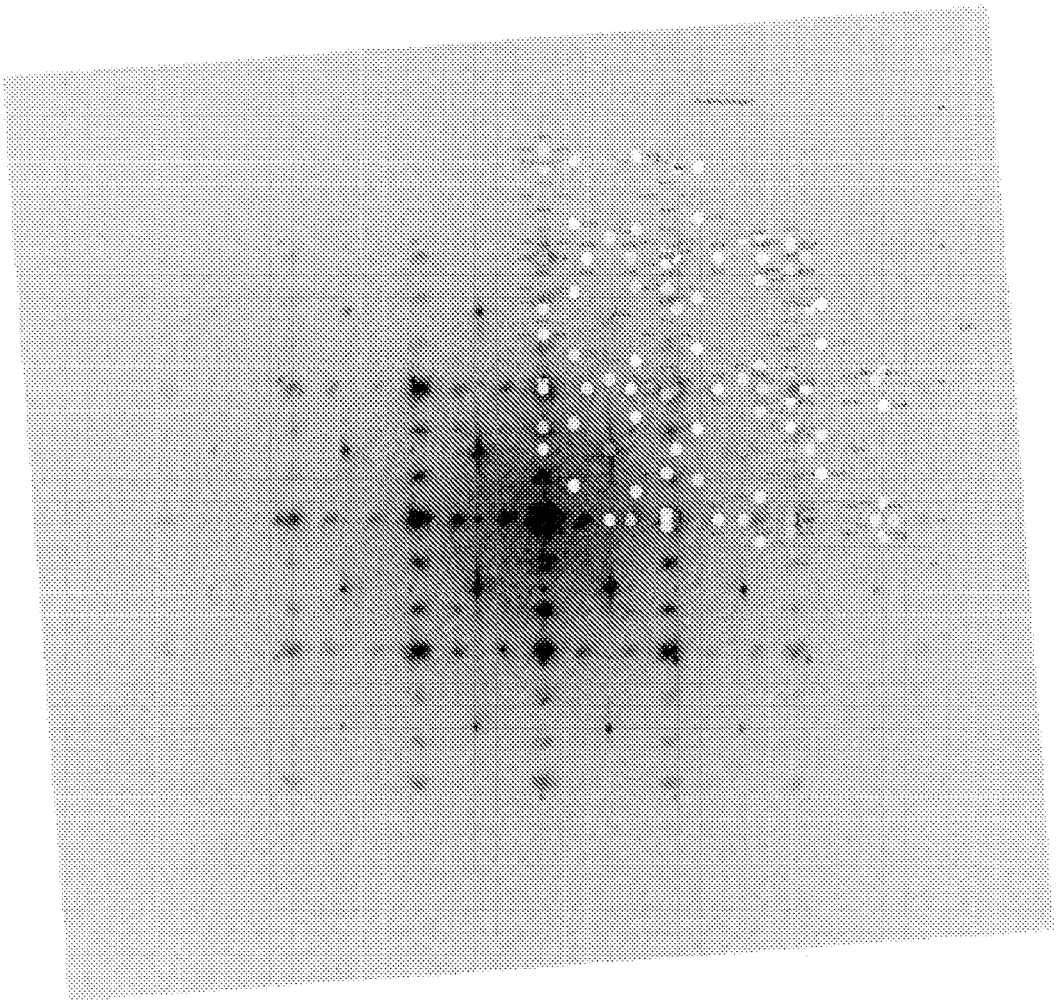

FIG. 33

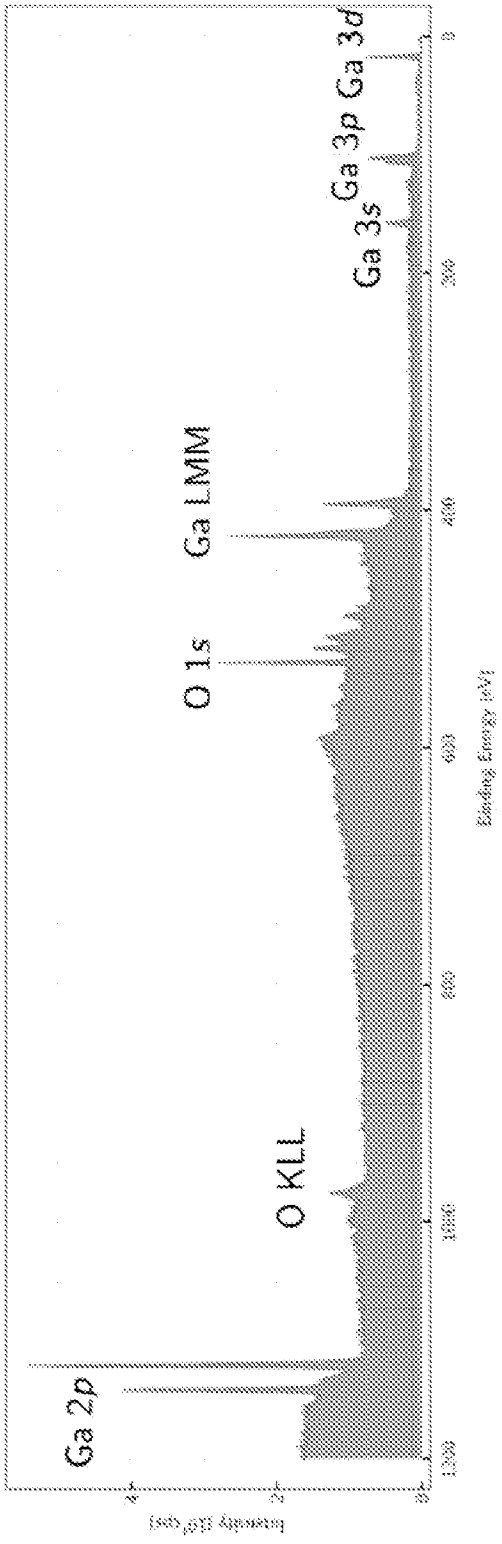

FIG. 34A

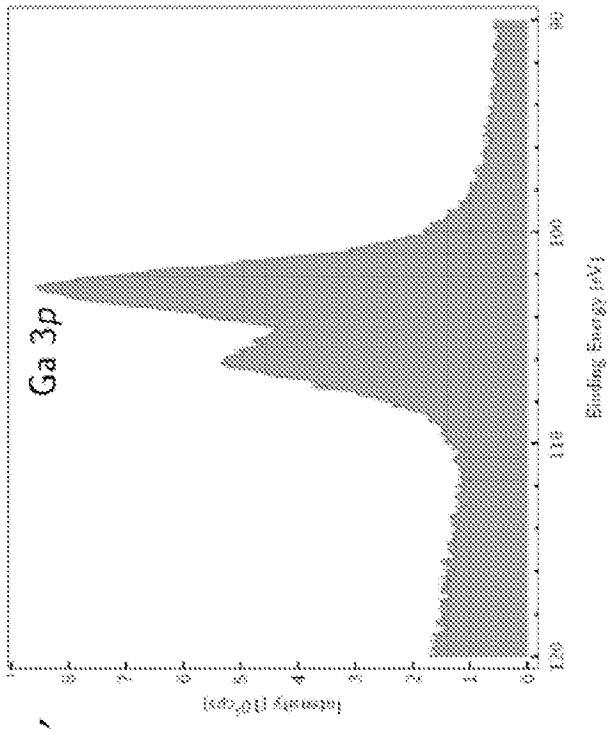

FIG. 34C

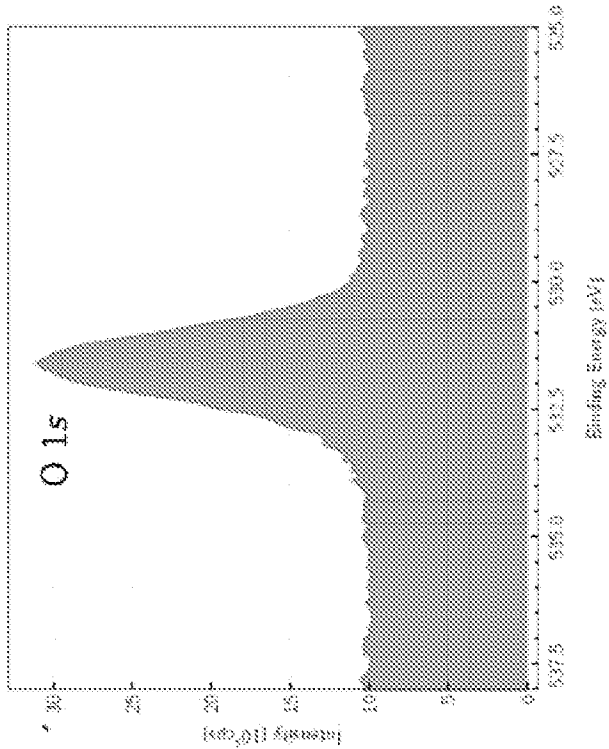

FIG. 34B

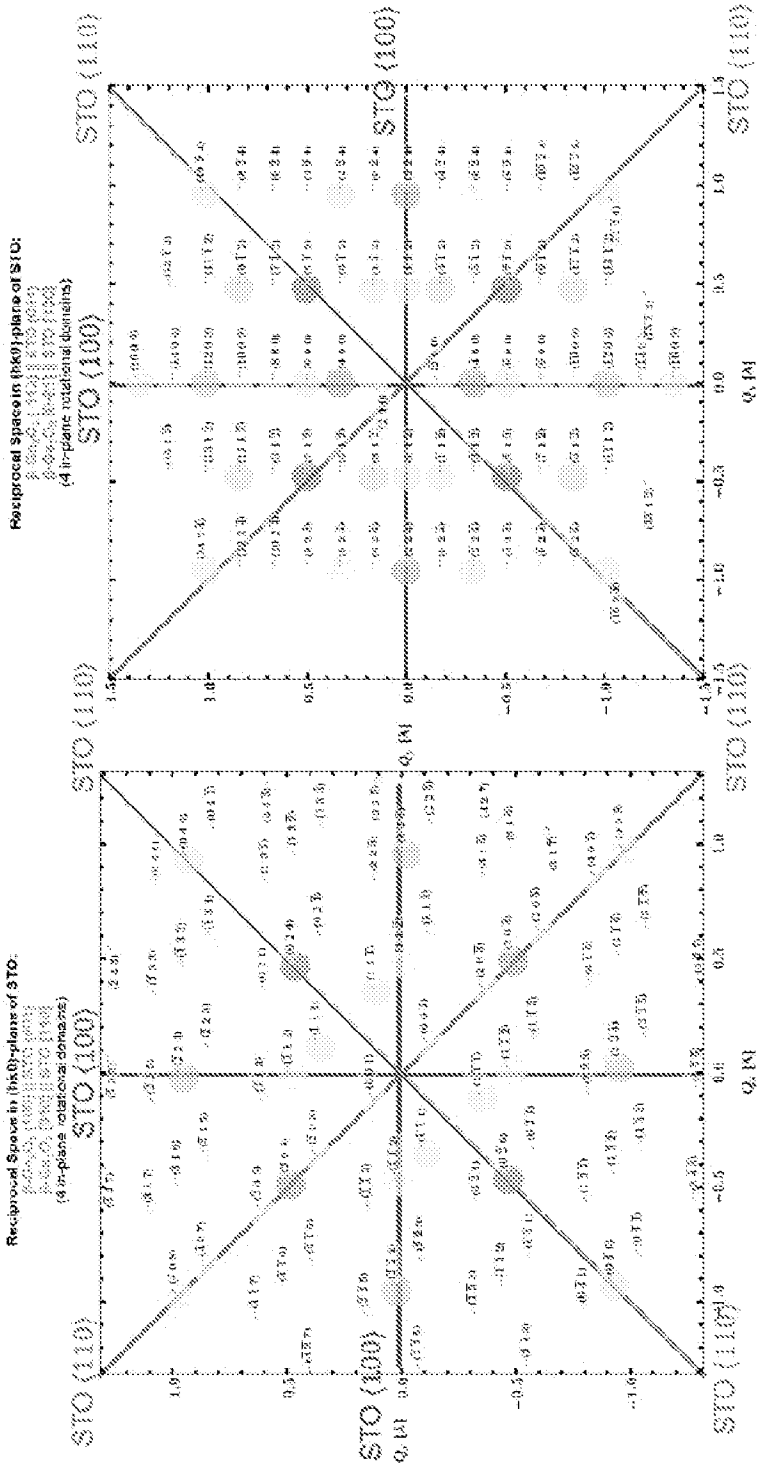

FIG. 35A

FIG. 35B

	2θ [°]	*d* [Å]	(*hkl*)	Δ*d* [Å]
a)	22.719	3.911	STO (001)	+0.006
	29.801	2.996	β-Ga_2O_3 (400)	+0.027
	46.442	1.954	STO (002)	+0.002
	61.745	1.501	β-Ga_2O_3 (800)	+0.017
	72.538	1.302	STO (003)	+0.000
	95.545	1.040	β-Ga_2O_3 ($\bar{2}$24)	-0.009
	101.220	0.997	β-Ga_2O_3 (12 0 0)	+0.007
	104.160	0.976	STO (004)	-0.000

FIG. 36A

	2θ [°]	*d* [Å]	(*hkl*)	Δ*d* [Å]
b)	32.408	2.760	STO (110)	-0.001
	61.412	1.509	β-Ga_2O_3 (020)	-0.009
	64.222	1.449	β-Ga_2O_3 ($\bar{2}$04)	-0.003
	64.222	1.449	β-Ga_2O_3 ($\bar{7}$12) & (512)	+0.009
	67.867	1.380	STO (220)	-0.001
	113.640	0.920	STO (330)	-0.000

FIG. 36B

	2θ [°]	*d* [Å]	(*hkl*)	Δ*d* [Å]
c)	22.742	3.907	STO (100)	+0.002
	30.864	2.989	β-Ga_2O_3 (400)	+0.020
	43.261	2.090	β-Ga_2O_3 ($\bar{1}12$)	-0.008
	43.261	2.090	β-Ga_2O_3 ($\bar{1}12$)	-0.008
	44.828	2.020	β-Ga_2O_3 (600)	+0.041
	46.492	1.952	STO (200)	-0.001
	61.698	1.502	β-Ga_2O_3 (800)	+0.018
	72.653	1.300	STO (300)	-0.002
	95.021	1.045	β-Ga_2O_3 ($\bar{2}24$)	-0.004
	95.021	1.045	β-Ga_2O_3 ($\bar{2}24$)	-0.004
	100.550	1.001	β-Ga_2O_3 (12 0 0)	+0.011
	104.230	0.976	STO (400)	-0.000

FIG. 36C

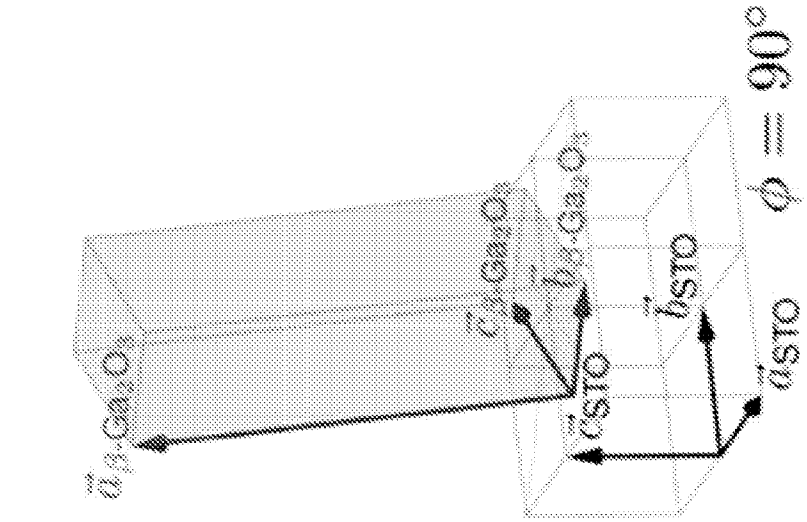

FIG. 37B

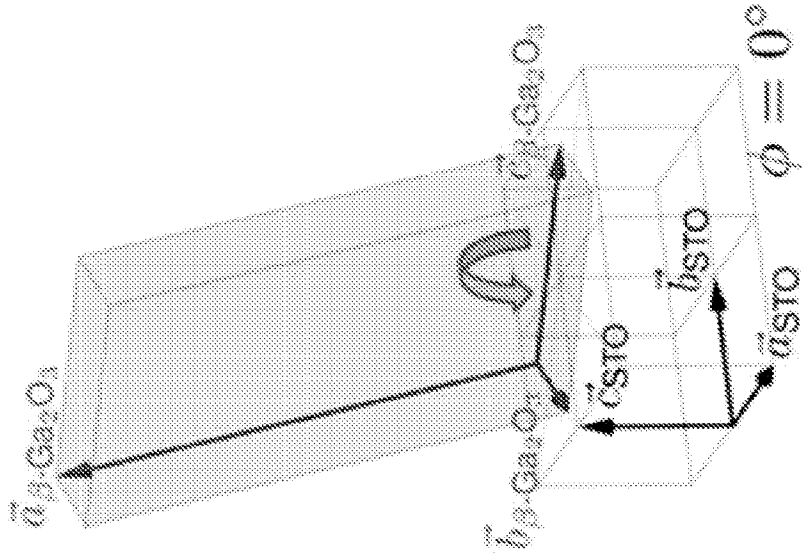

FIG. 37A

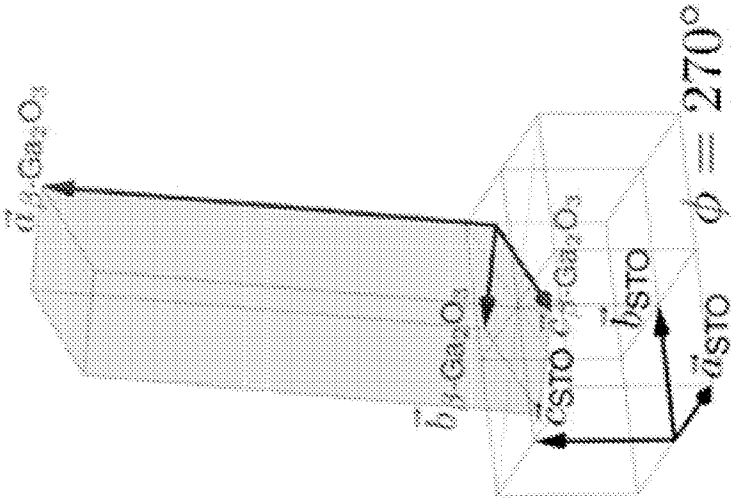

FIG. 37D

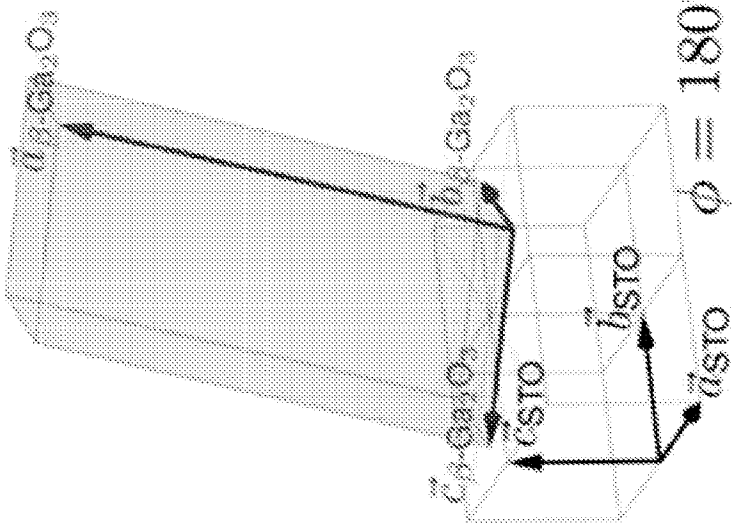

FIG. 37C

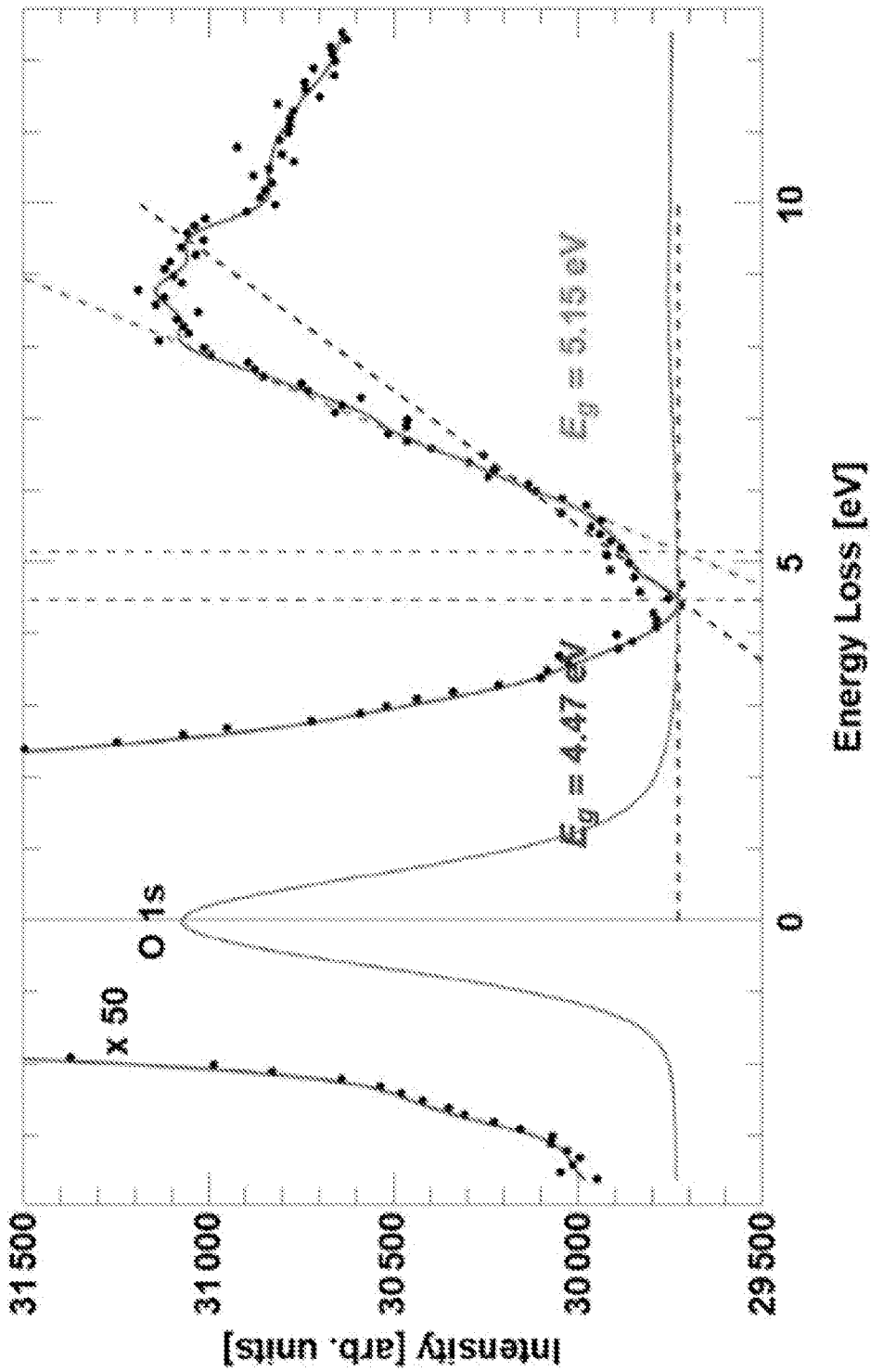
Intensity [arb. units]
31 500
31 000
30 500
30 000
29 500
x 50
O 1s
E_g = 4.47 eV
E_g = 5.15 eV
0
5
10
Energy Loss [eV]

FIG. 38A

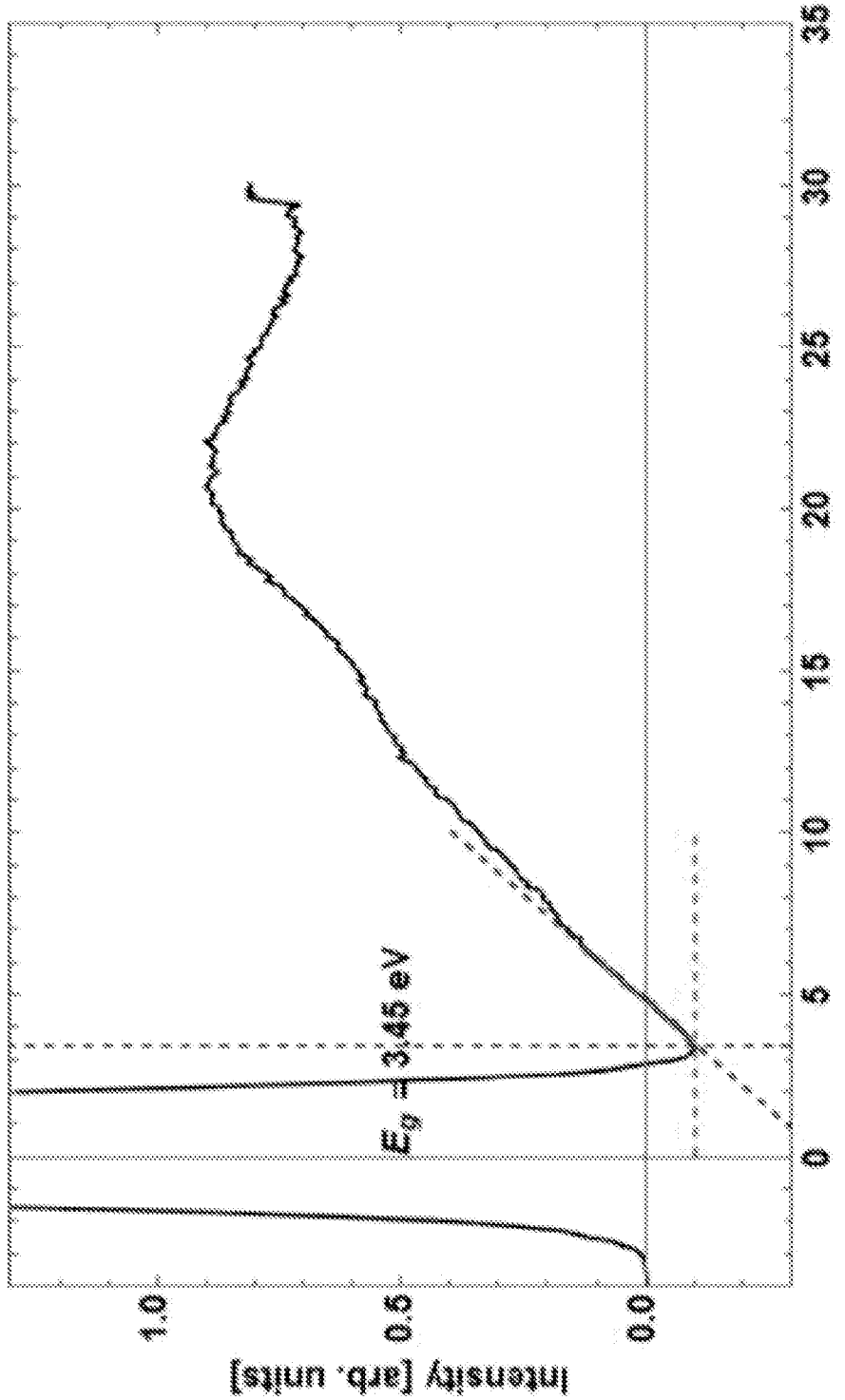
Intensity [arb. units]
1.0
0.5
0.0
0
5
10
15
20
25
30
35
Energy Loss [eV]
E_g = 3.45 eV

FIG. 38B

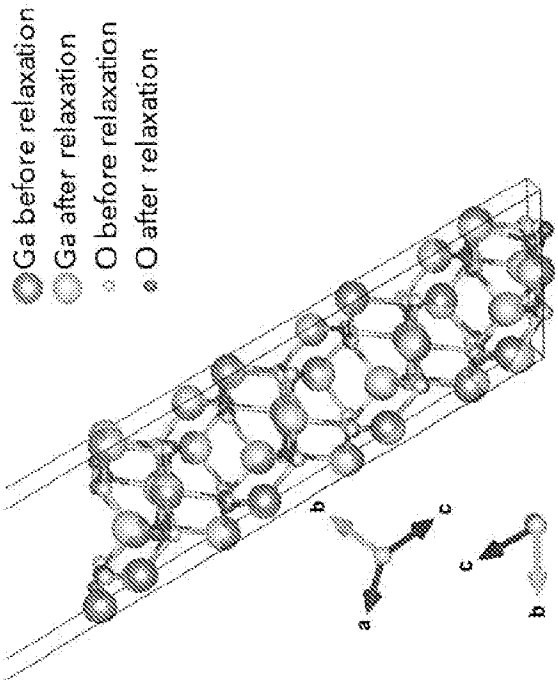

FIG. 39C

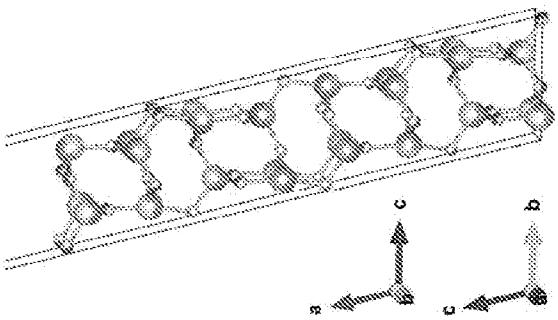

FIG. 39B

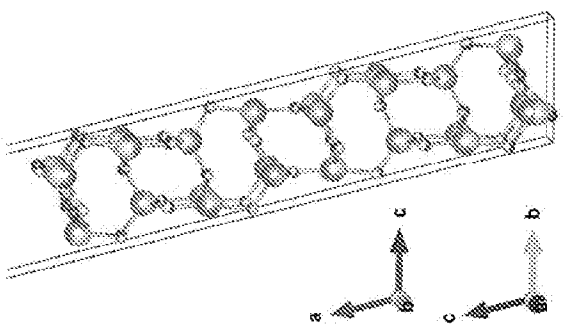

FIG. 39A

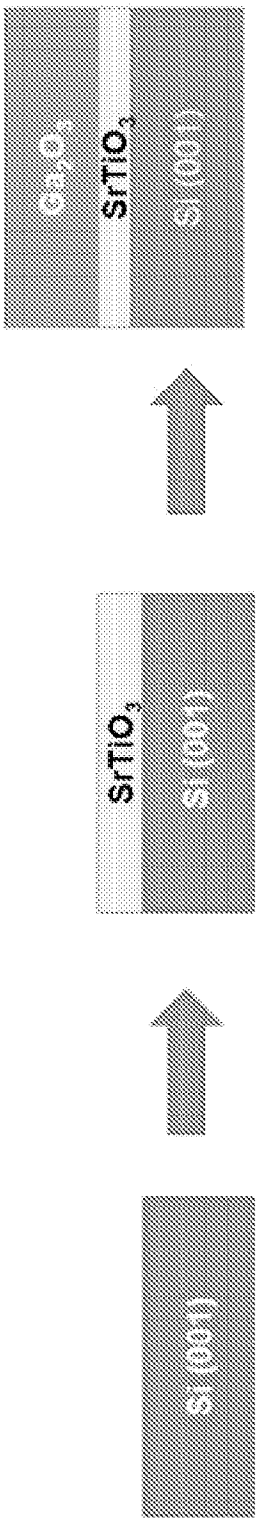

FIG. 40A

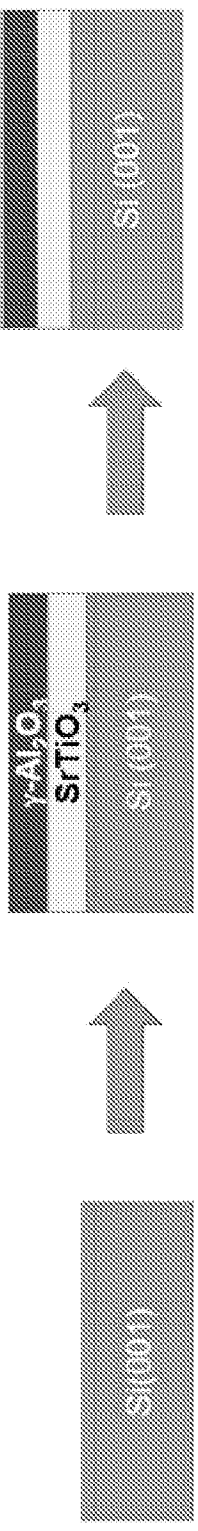

FIG. 40B

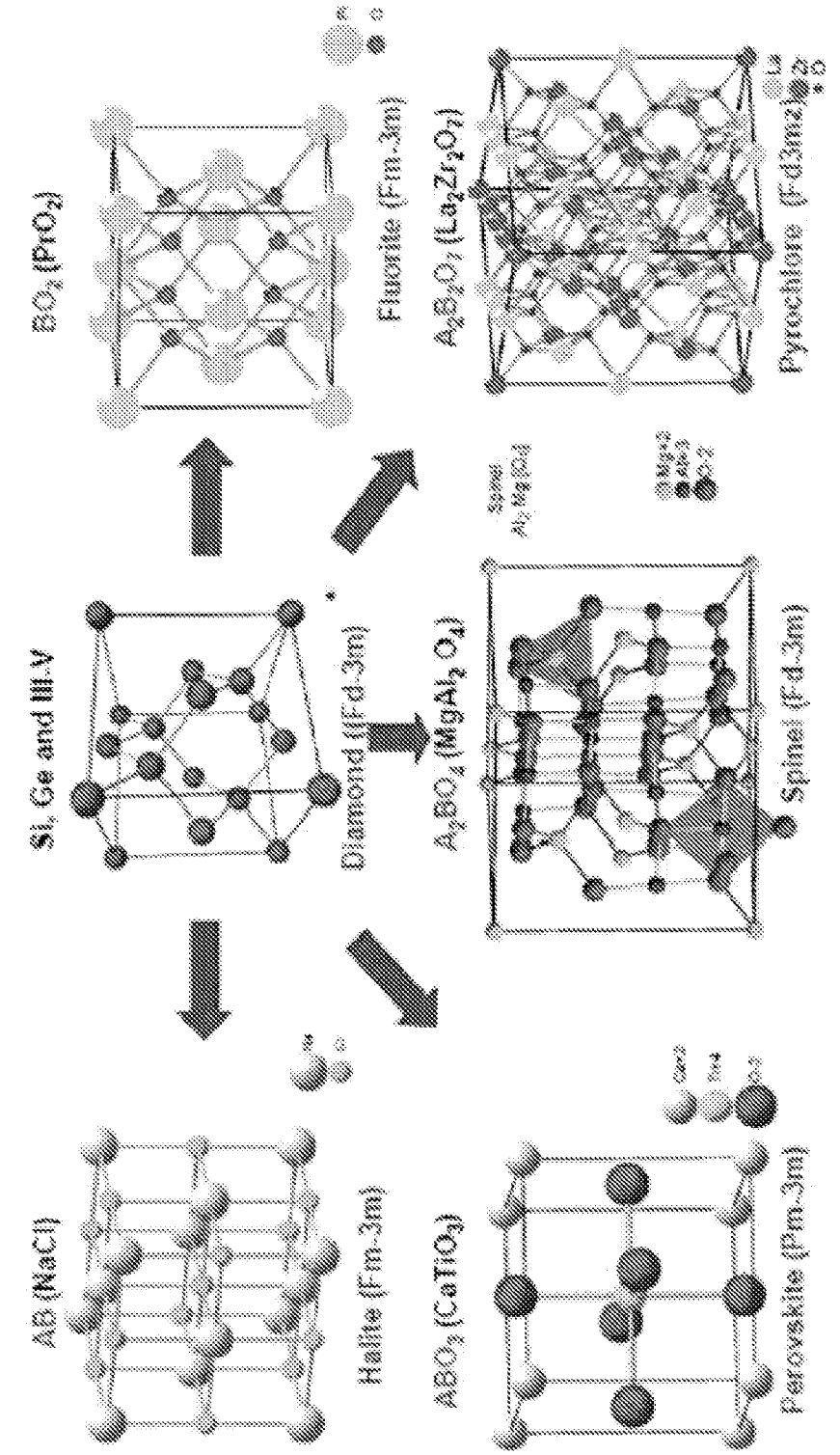
AB (NaCl)
Halite (Fm-3m)
ABO3 (CaTiO3)
Perovskite (Pm-3m)
Si, Ge and III-V
Diamond (Fd-3m)
A2BO4 (MgAl2O4)
Spinel (F-4-3m)
BO2 (PrO2)
Fluorite (Fm-3m)
A2B2O7 (La2Zr2O7)
Pyrochlore (Fd3ma)

FIG. 41

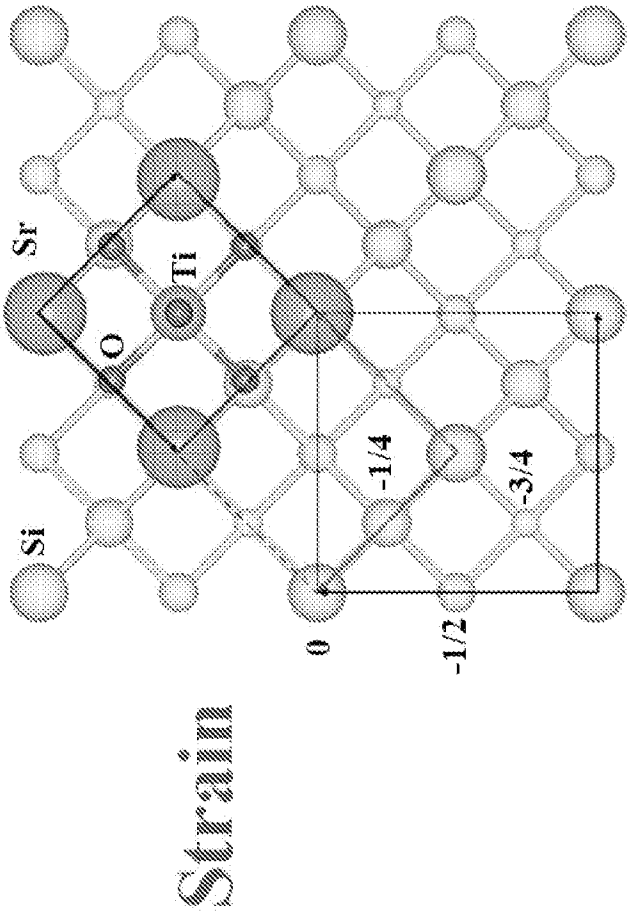
Sr
Ti
O
Si
-1/4
-3/4
0
-1/2
Strain

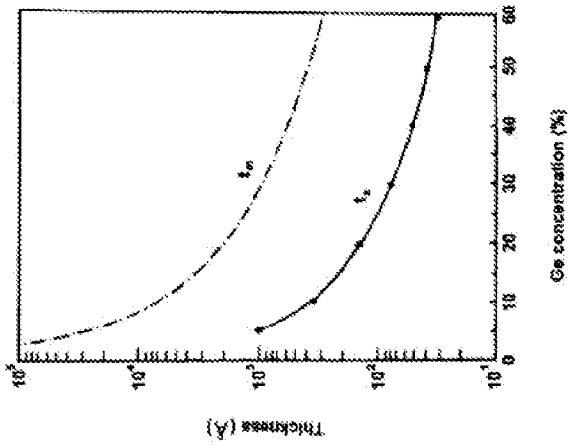
Thickness (Å)
Ge concentration (%)
0
10
20
30
40
50
60

FIG. 42A

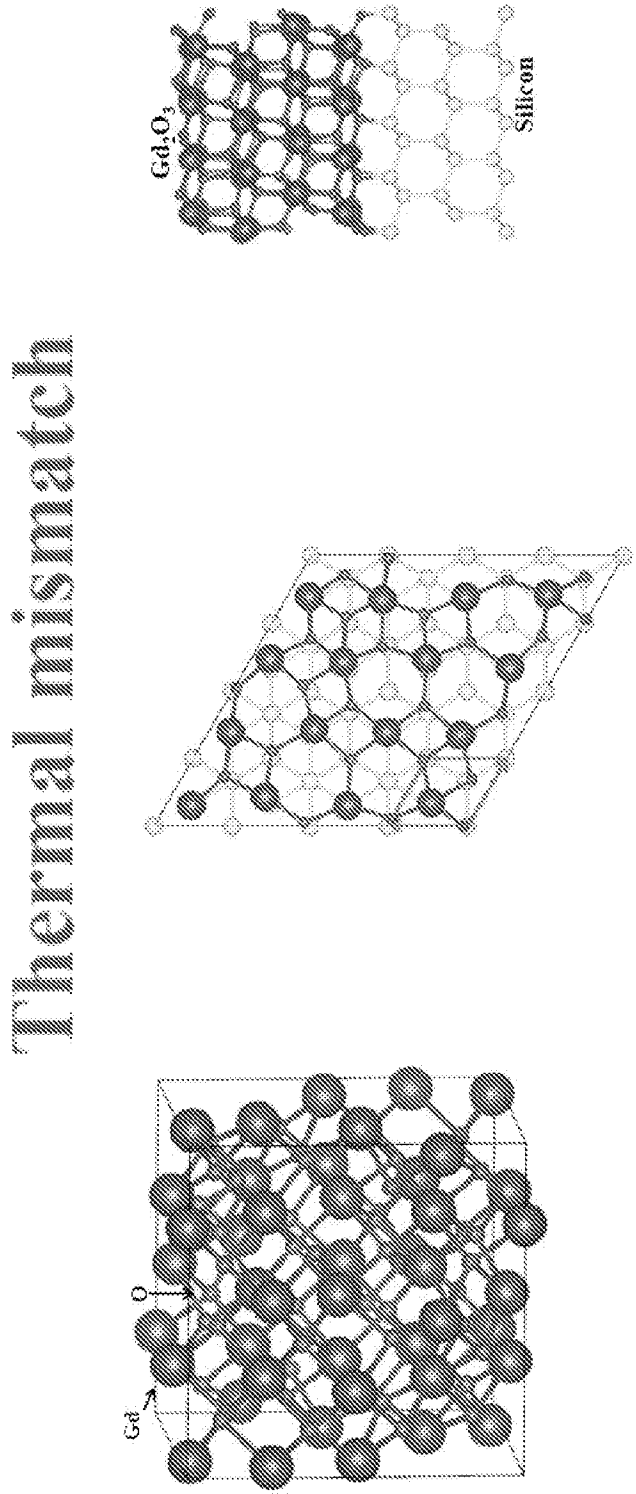

FIG. 42B

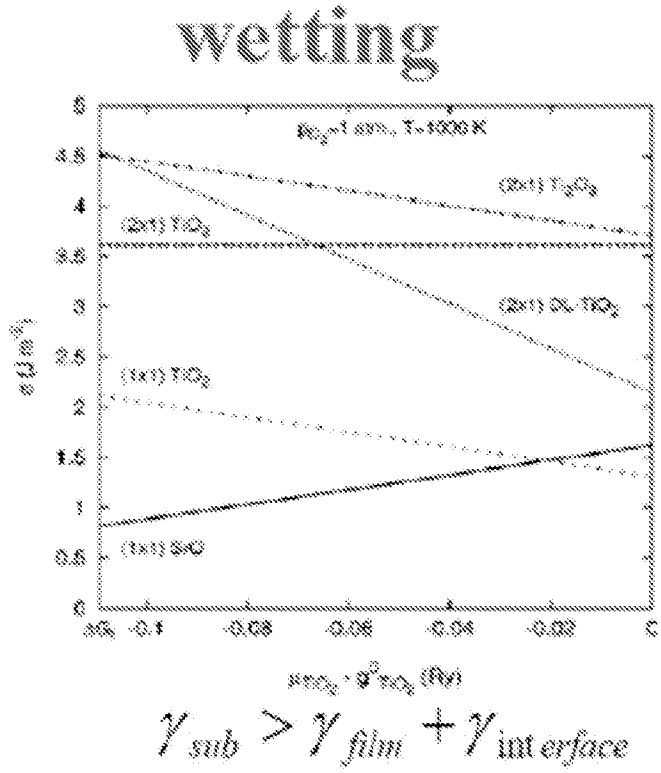

FIG. 42C

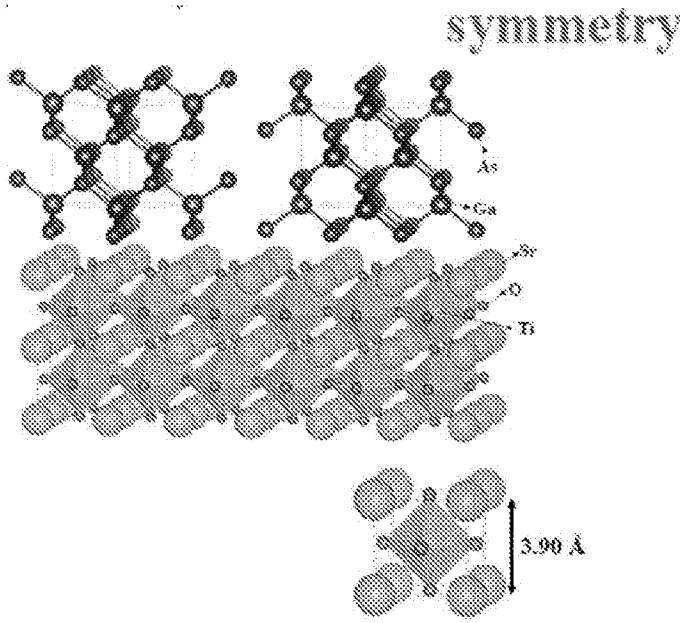

FIG. 42D

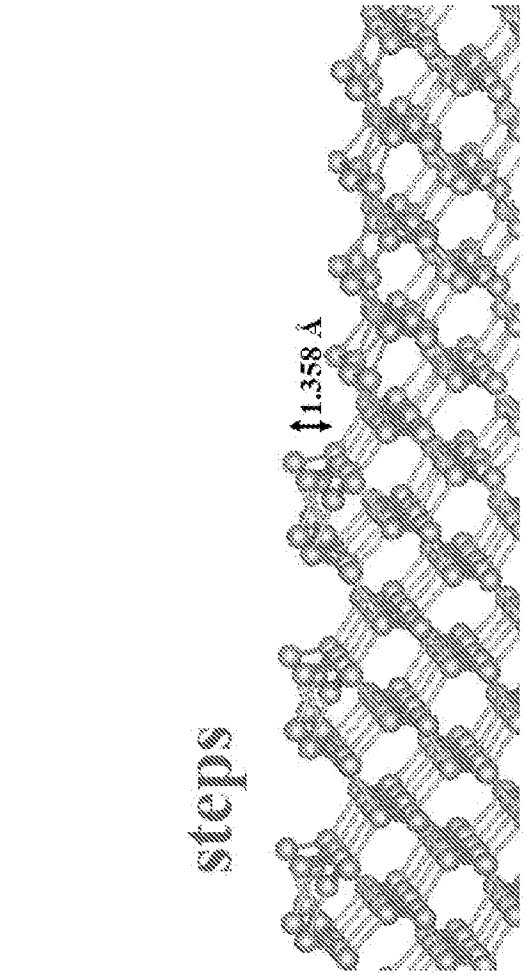

FIG. 42E

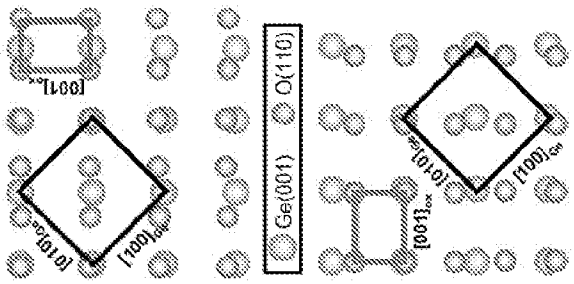

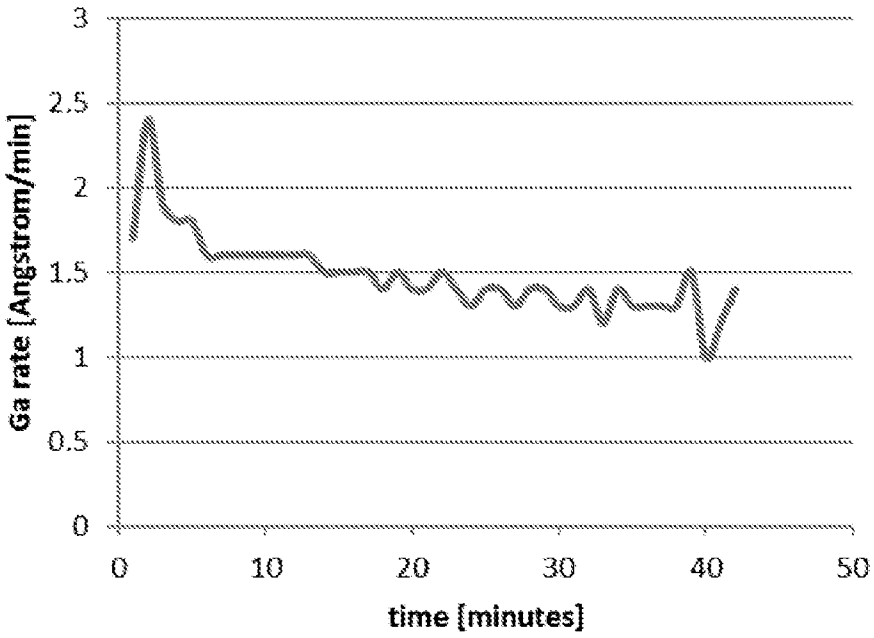

FIG. 43A

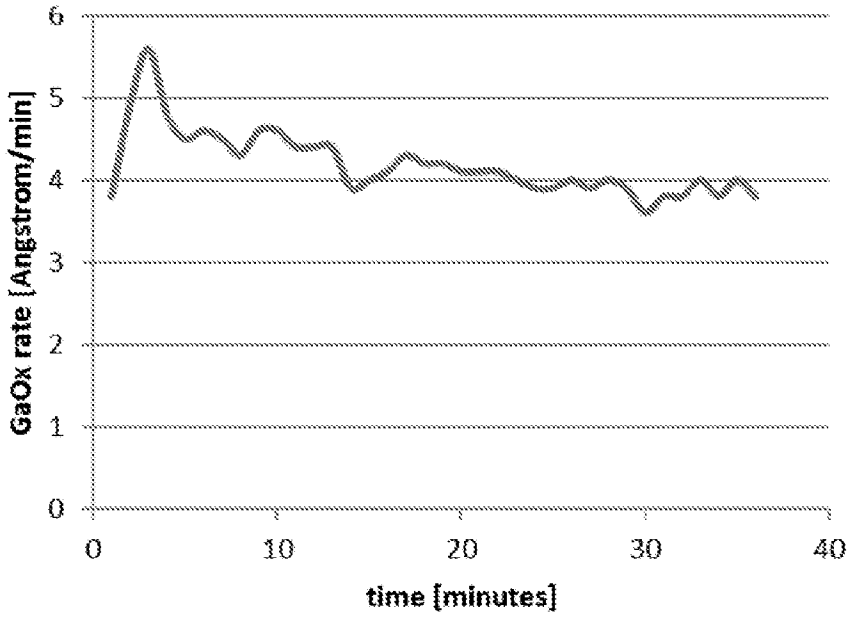

FIG. 43B

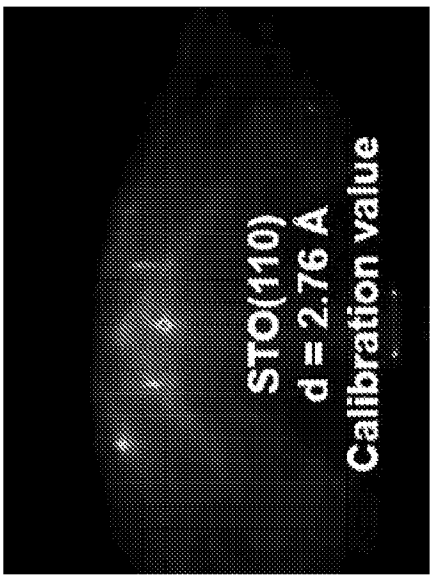

FIG. 44A

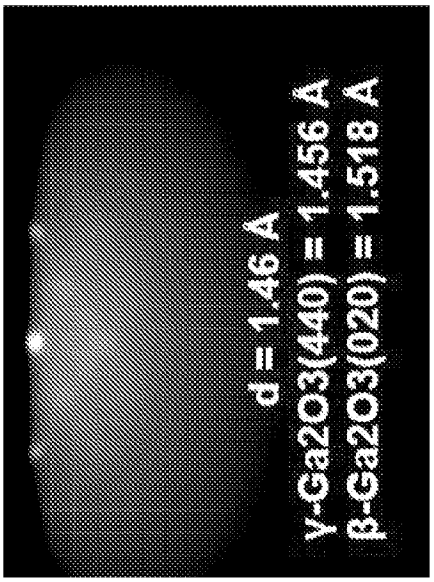

FIG. 44B

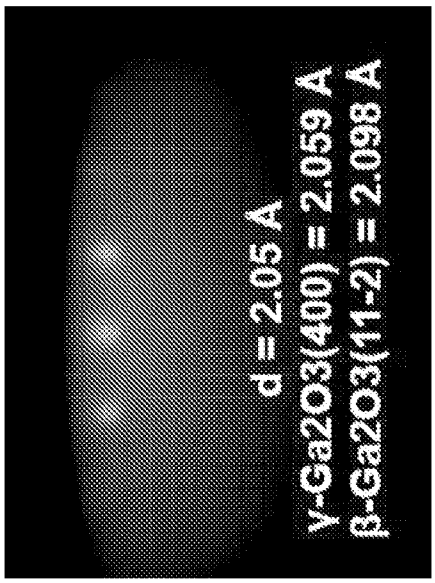

FIG. 44C

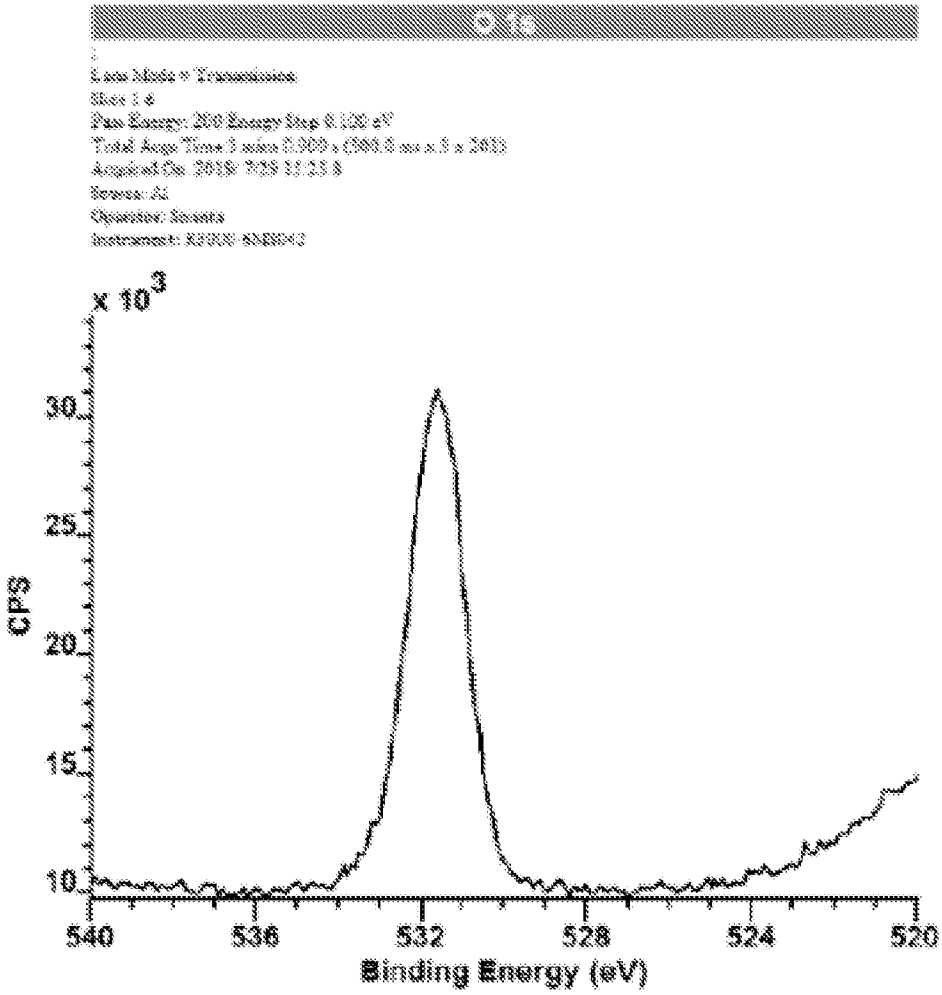
x 10^3
30
25
20
15
10
CPS
540
536
532
528
524
520
Binding Energy (eV)

FIG. 45A

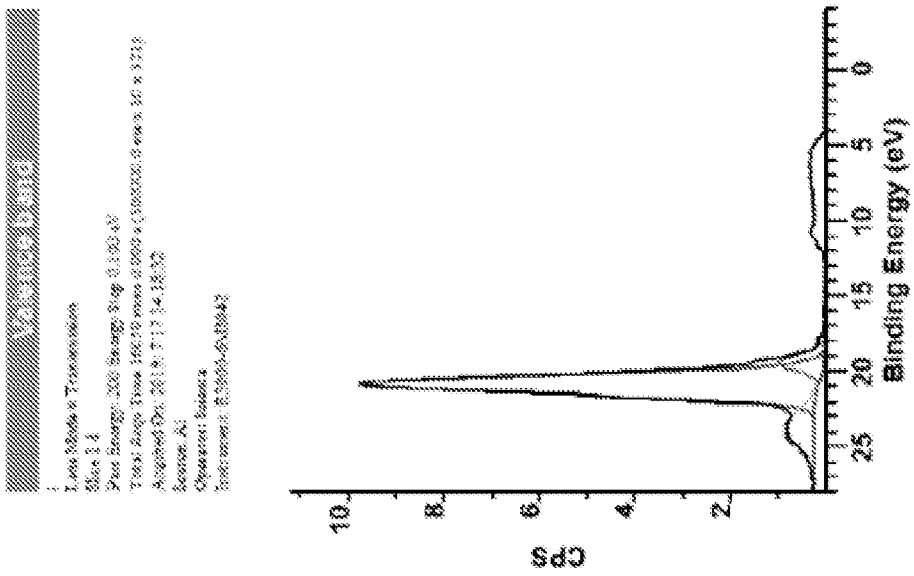

FIG. 45C

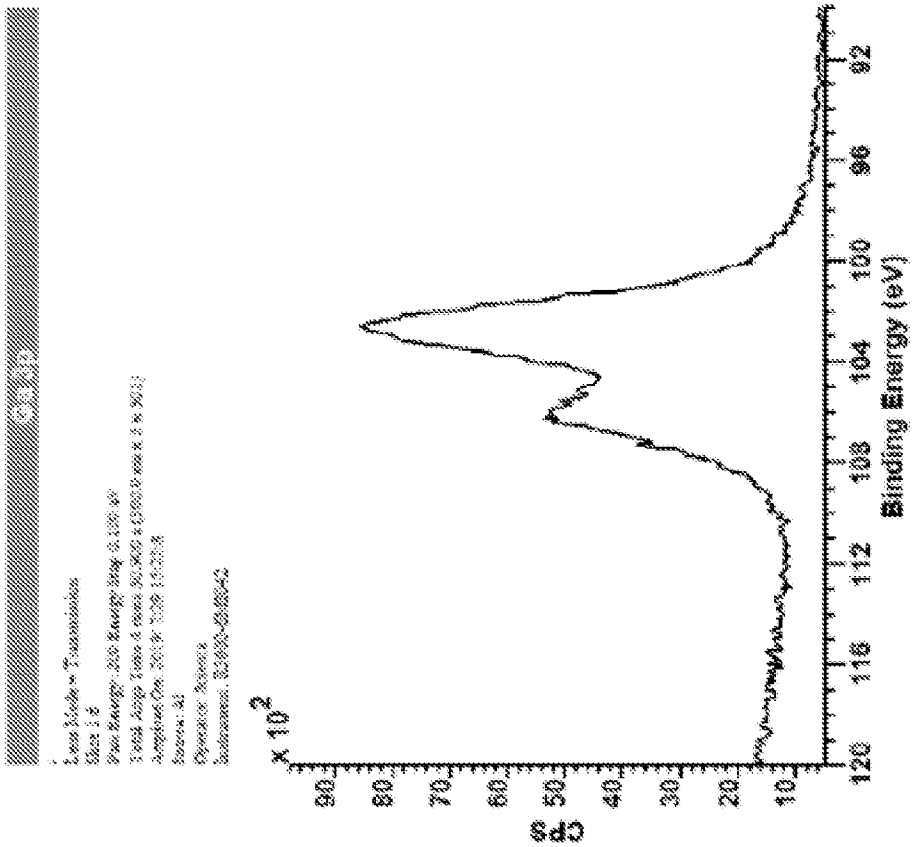

FIG. 45B

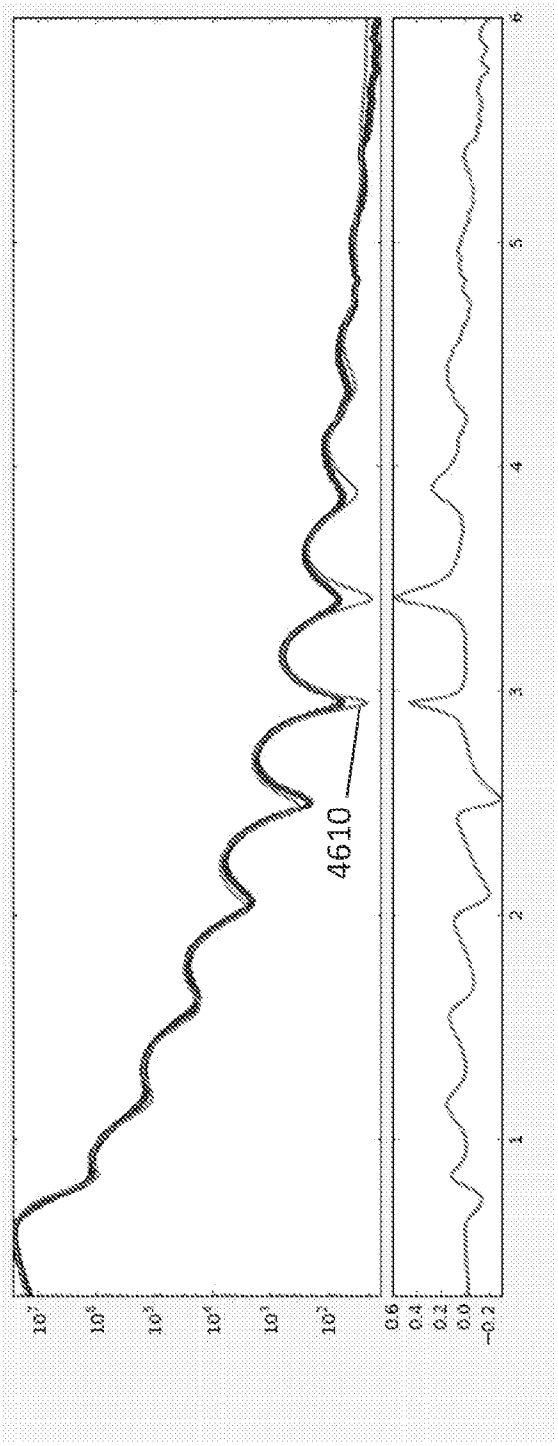

FIG. 46

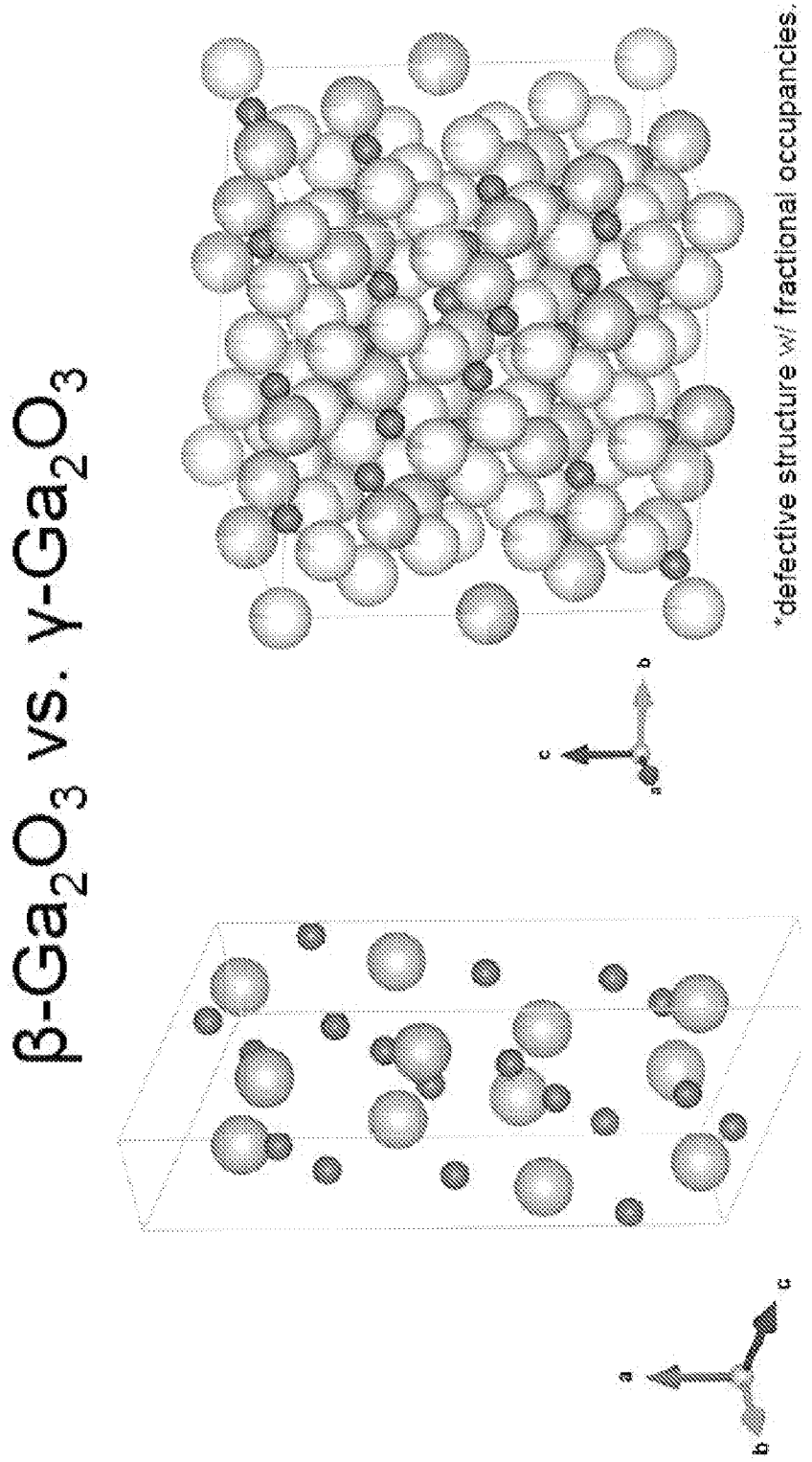

FIG. 47A

FIG. 47B

Single domain structure 5.5% mismatch
(compressive)
γ-Ga_2O_3(001)[100]/STO(001)[100]

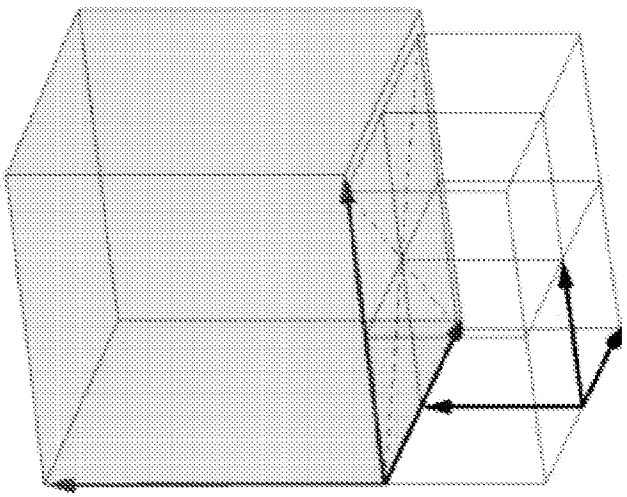

FIG. 48

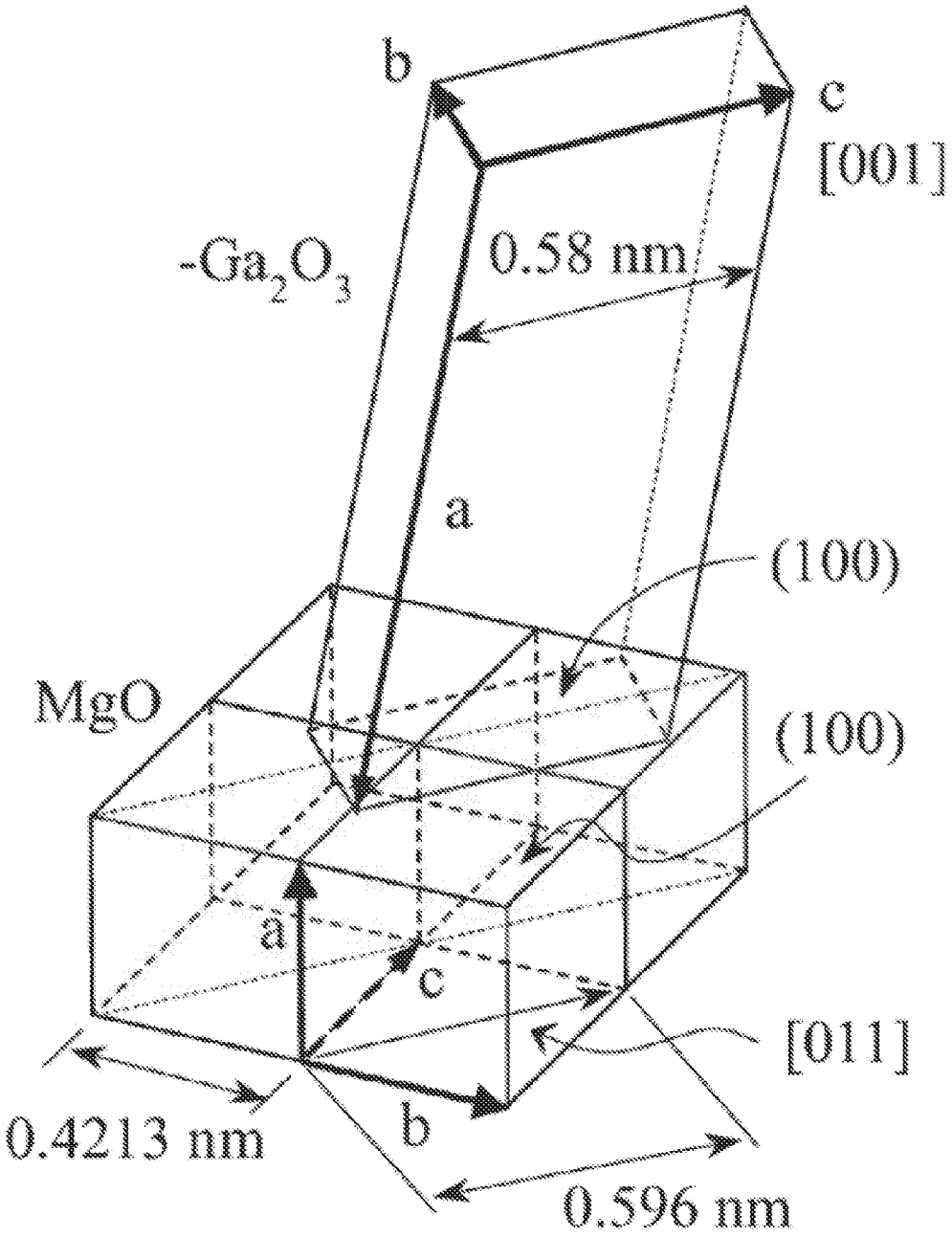

FIG. 49

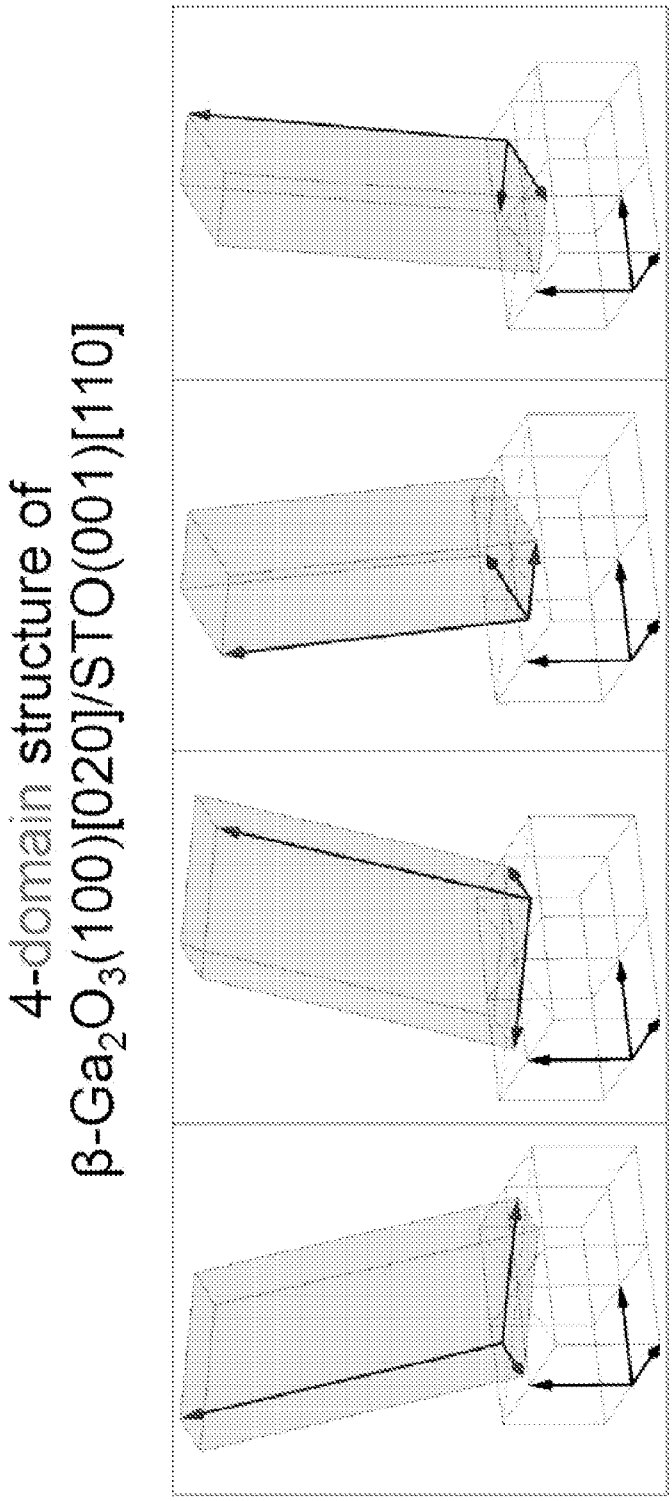

FIG. 50

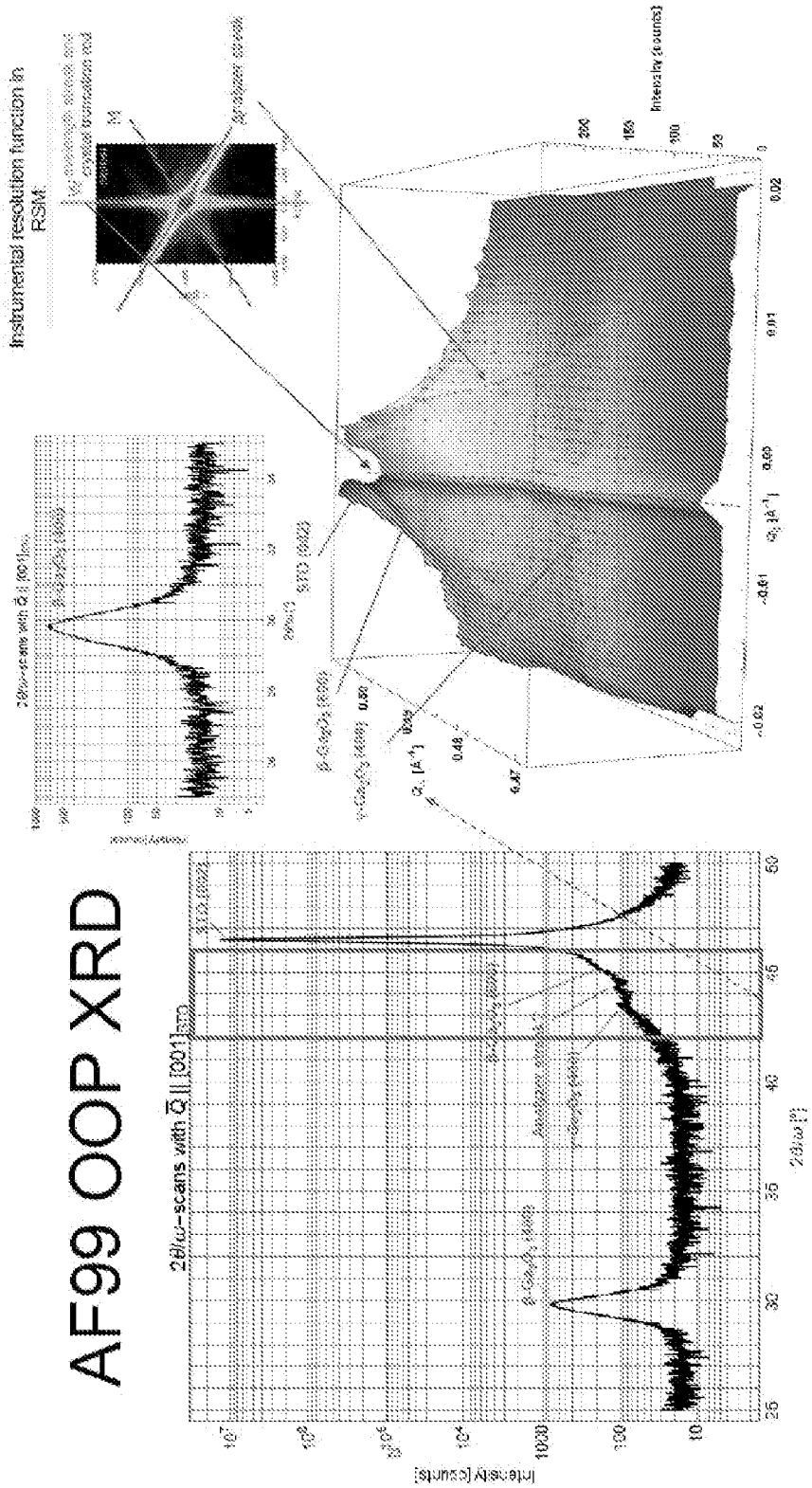
AF99 OOP XRD
2θ/ω-scans with Q ∥ [001]
Intensity [counts]
Instrumental resolution function in RSM
Intensity (counts)

FIG. 51A

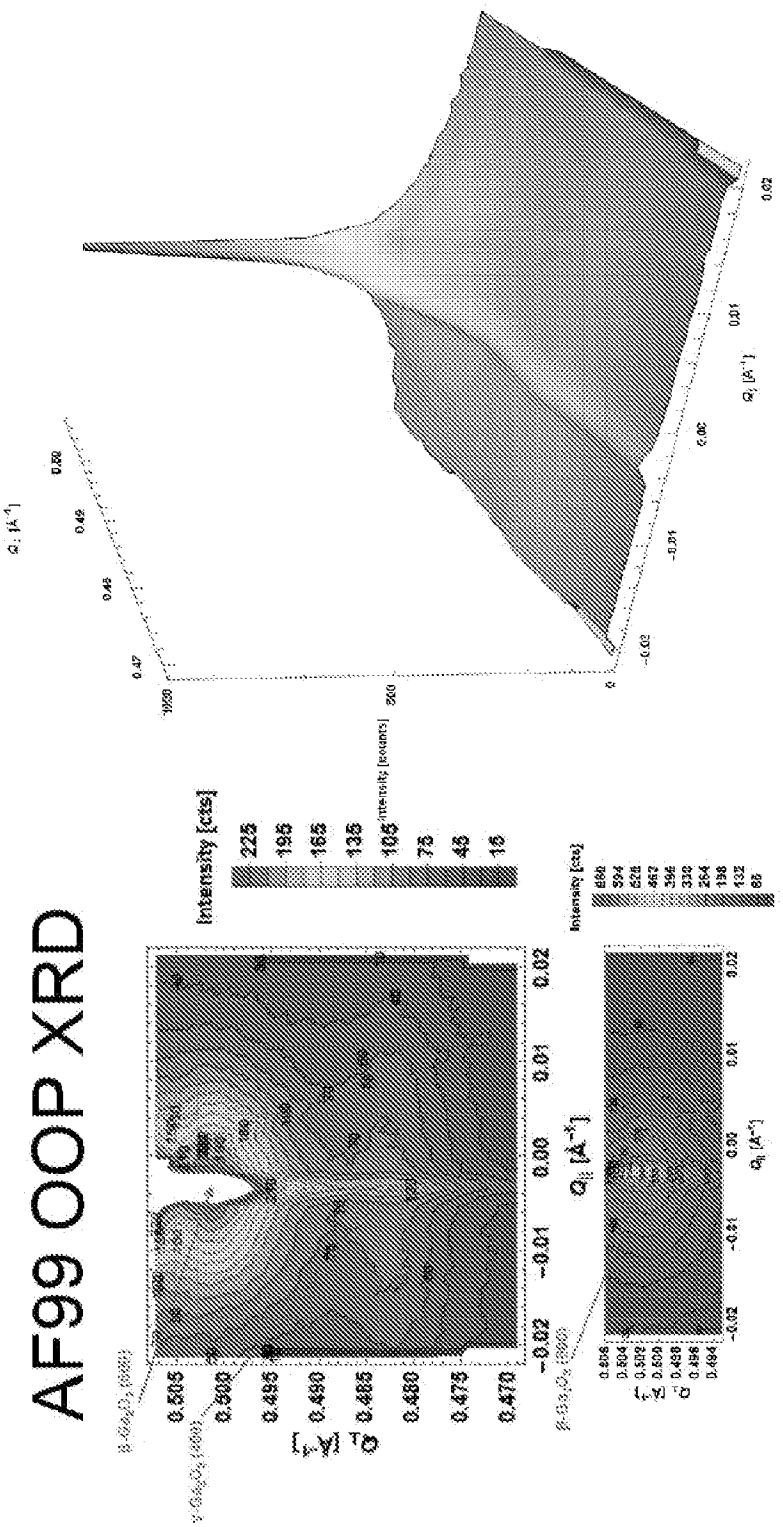
AF99 OOP XRD
Intensity [cts]
225
195
165
135
105
75
45
15
Q_z [Å^{-1}]
$Q_{||}$ [Å^{-1}]

FIG. 51B

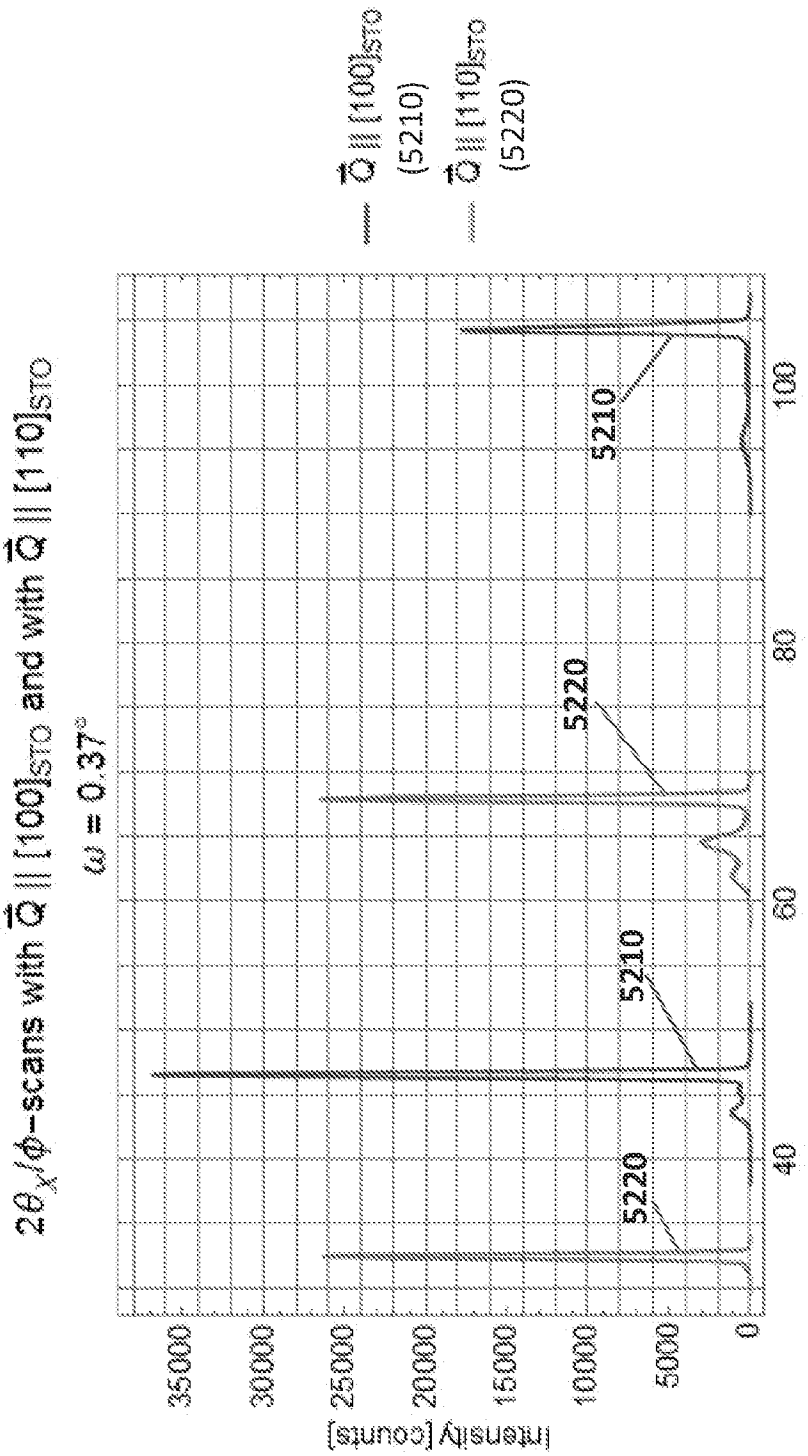
$2\theta_\chi/\phi$–scans with $\vec{Q} \parallel [100]_{STO}$ and with $\vec{Q} \parallel [110]_{STO}$
$\omega = 0.37°$
$\vec{Q} \parallel [100]_{STO}$ (5210)
$\vec{Q} \parallel [110]_{STO}$ (5220)
5210
5220
5210
5220
intensity [counts]
$2\theta_\chi/\phi$ [°]
0
5000
10000
15000
20000
25000
30000
35000
40
60
80
100

FIG. 52A

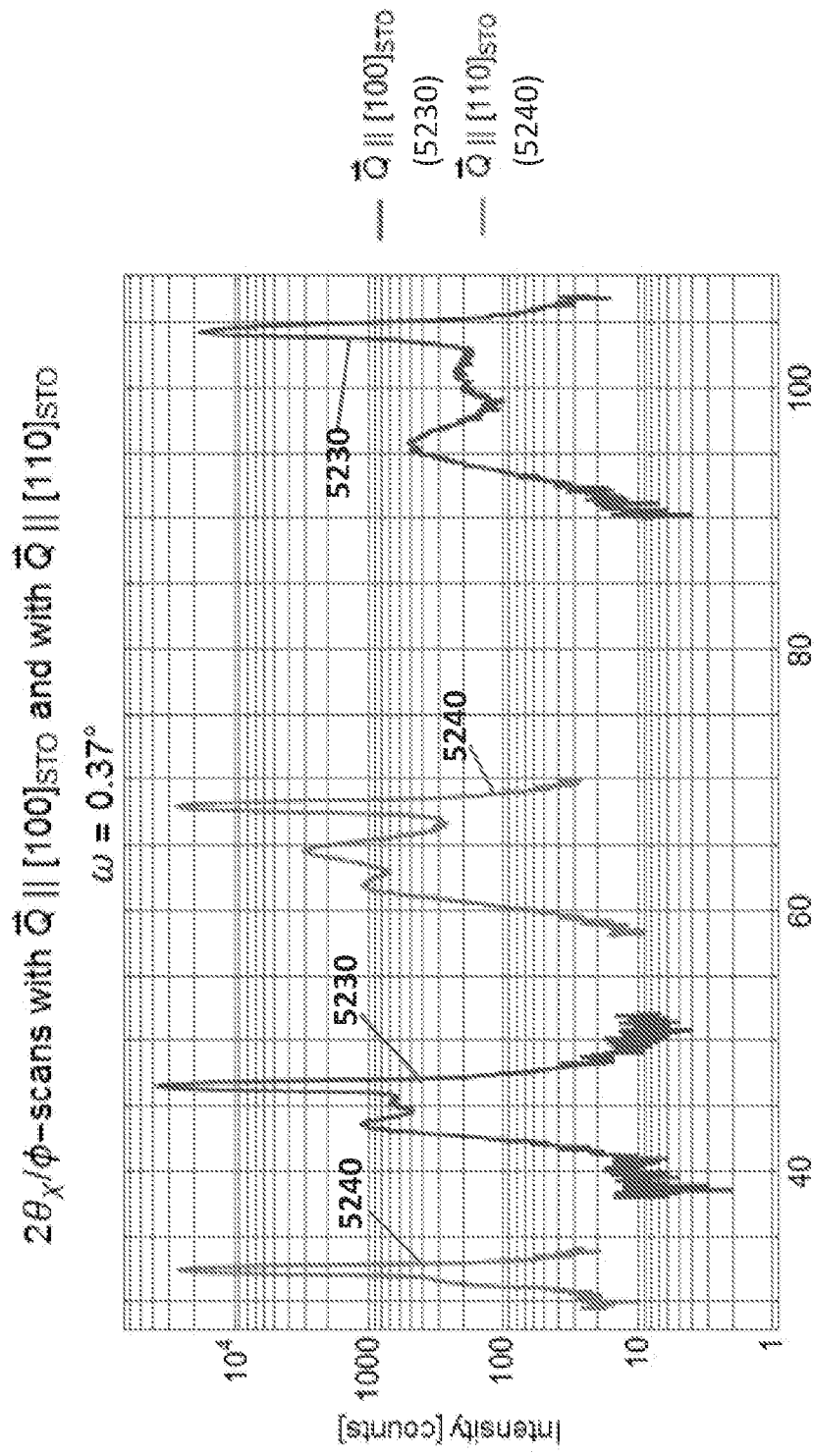
$2\theta_\chi/\phi$–scans with $\vec{Q} \parallel [100]_{STO}$ and with $\vec{Q} \parallel [110]_{STO}$
$\omega = 0.37°$
$\vec{Q} \parallel [100]_{STO}$ (5230)
$\vec{Q} \parallel [110]_{STO}$ (5240)
5230
5240
5230
5240
Intensity [counts]
10^4
1000
100
10
1
40
60
80
100
$2\theta_\chi/\phi$ [°]

FIG. 52B

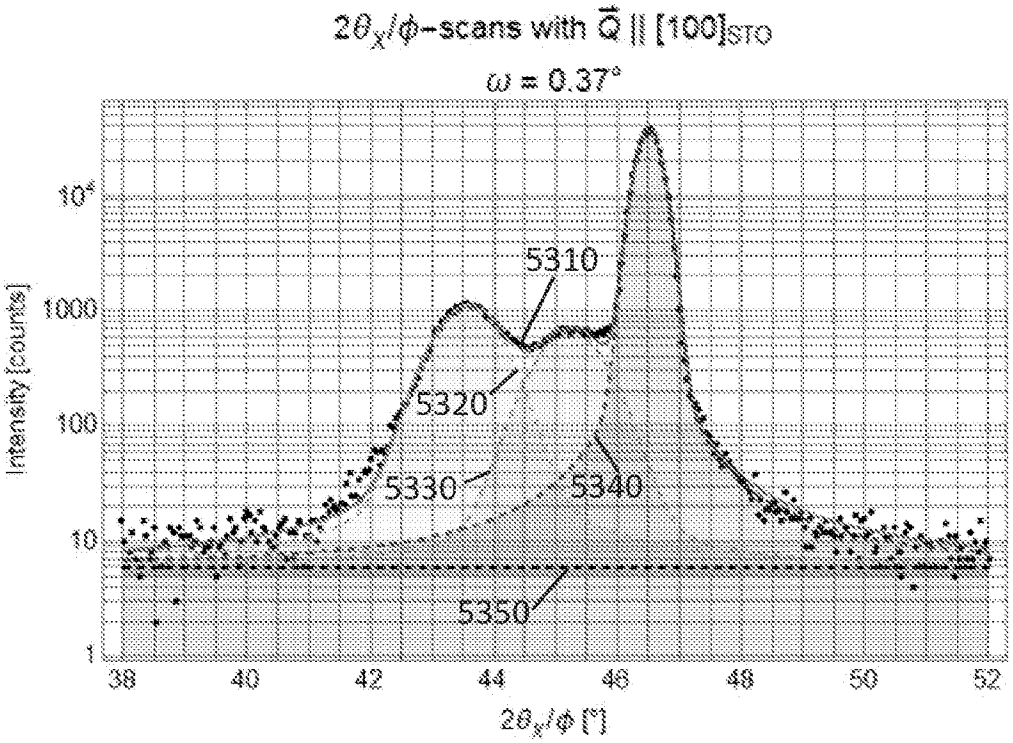

Envelope (5310)

film 1: (5320)

$2\theta_\chi$ = 43.578°, δ = 0.06°, σ = 0.46°, FWHM = 1.15°, crystallite size ~73. Å

film 2: (5330)

$2\theta_\chi$ = 46.236°, δ = 0.05°, σ = 0.50°, FWHM = 1.22°, crystallite size ~69. Å

STO (200): (5340)

$2\theta_\chi$ = 46.510°, δ = 0.01°, σ = 0.19°, FWHM = 0.45°

a_{STO} = 3.902 Å

background (5350)

FIG. 53A

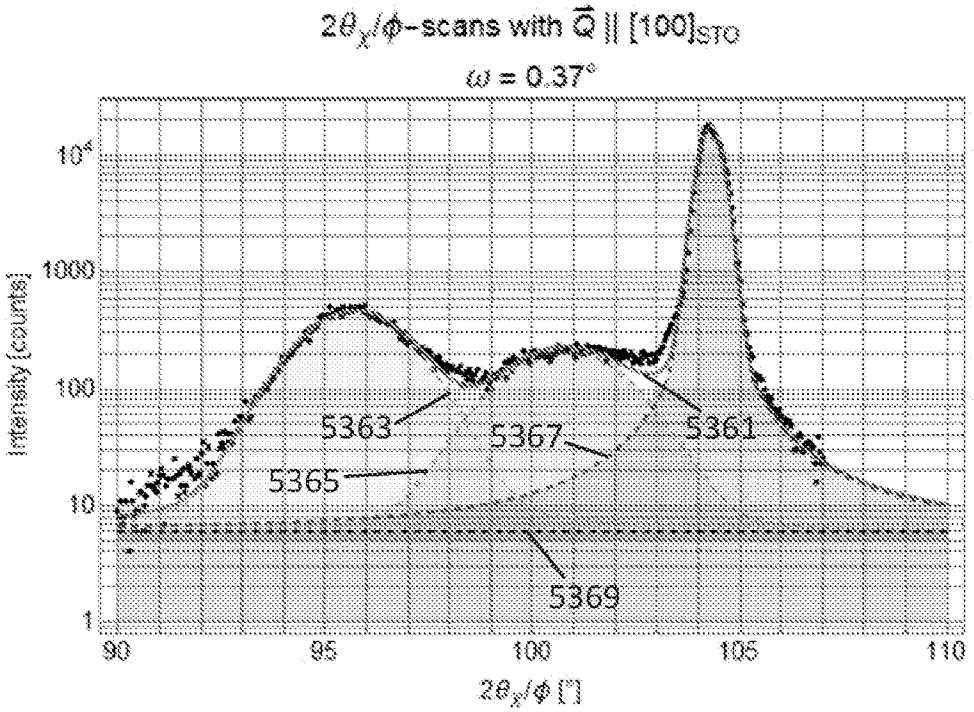

Envelope (5361)

film 1: (5363)

$2\theta_\chi$ = 95.712°, δ = 0.08°, σ = 1.19°, FWHM = 2.90°, crystallite size ~40. Å

film 2: (5365)

$2\theta_\chi$ = 100.750°, δ = 0.06°, σ = 1.36°, FWHM = 3.27°, crystallite size ~38. Å

STO (400): (5367)

$2\theta_\chi$ = 104.308°, δ = 0.02°, σ = 0.25°, FWHM = 0.63°

a_{STO} = 3.902 Å

background (5369)

FIG. 53B

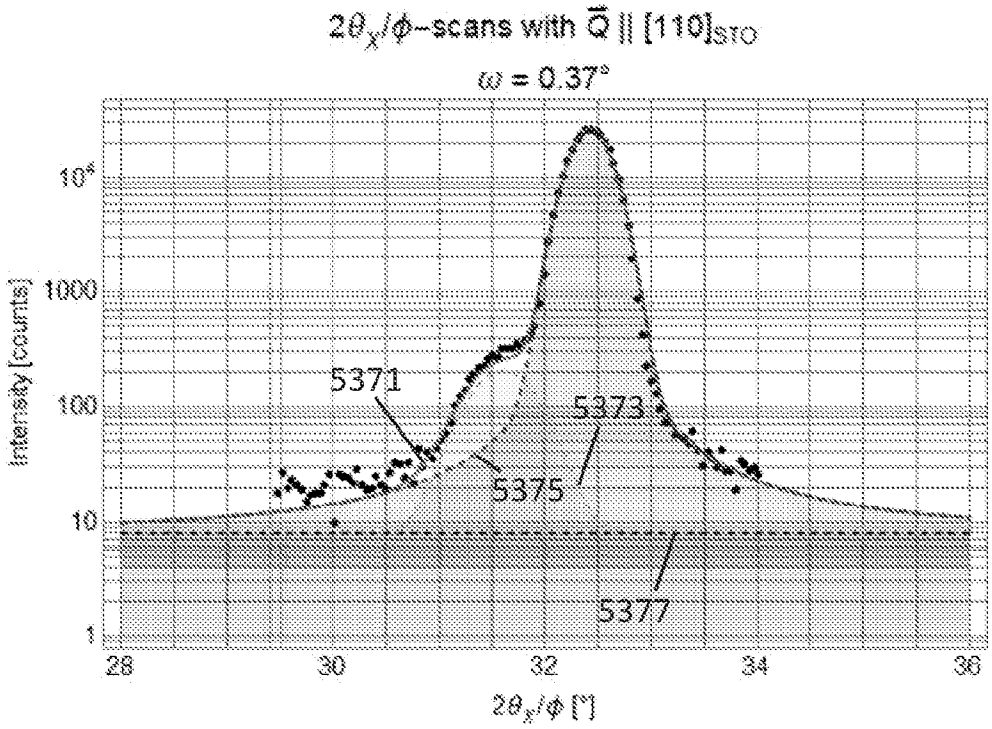

Envelope (5371)

film 1: (5373)

$2\theta_\chi$ = 31.600°, δ = 0.00°, σ = 0.30°, FWHM = 0.71°, crystallite size ~110.

STO (110): (5375)

$2\theta_\chi$ = 32.423°, δ = 0.01°, σ = 0.18°, FWHM = 0.43°

a_{STO} = 3.902 Å

background (5377)

FIG. 53C

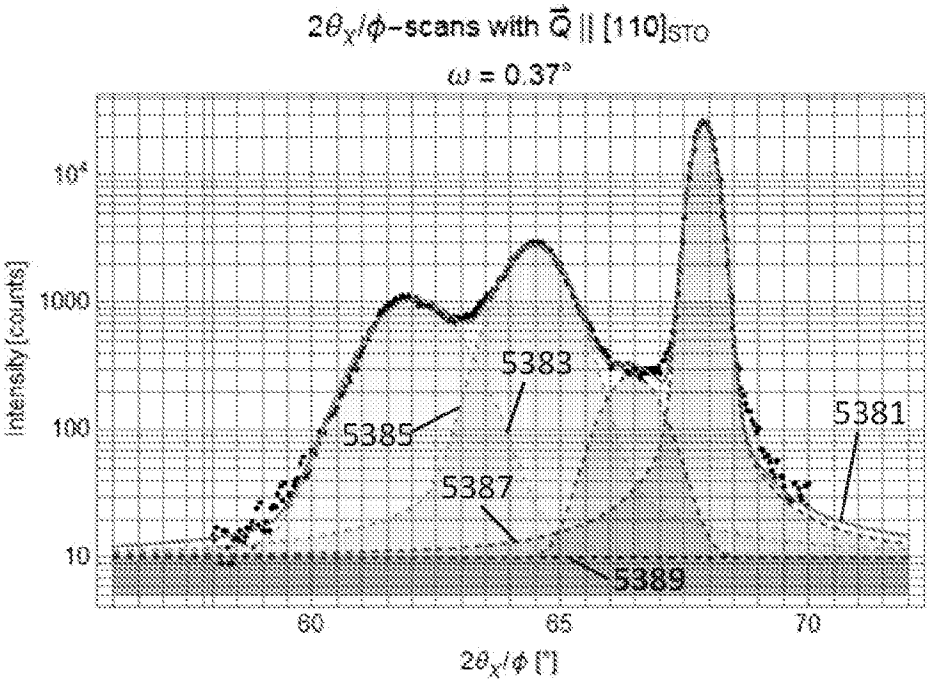

Envelope (5381)

film 1: (5383)

$2\theta_\chi$ = 62.022°, δ = 0.19°, σ = 0.68°, FWHM = 1.82°, crystallite size ~50. Å

film 2: (5385)

$2\theta_\chi$ = 64.478°, δ = 0.10°, σ = 0.57°, FWHM = 1.46°, crystallite size ~63. Å

STO (220): (5387)

$2\theta_\chi$ = 67.890°, δ = 0.01°, σ = 0.21°, FWHM = 0.50°

a_{STO} = 3.902 Å

background (5389)

FIG. 53D

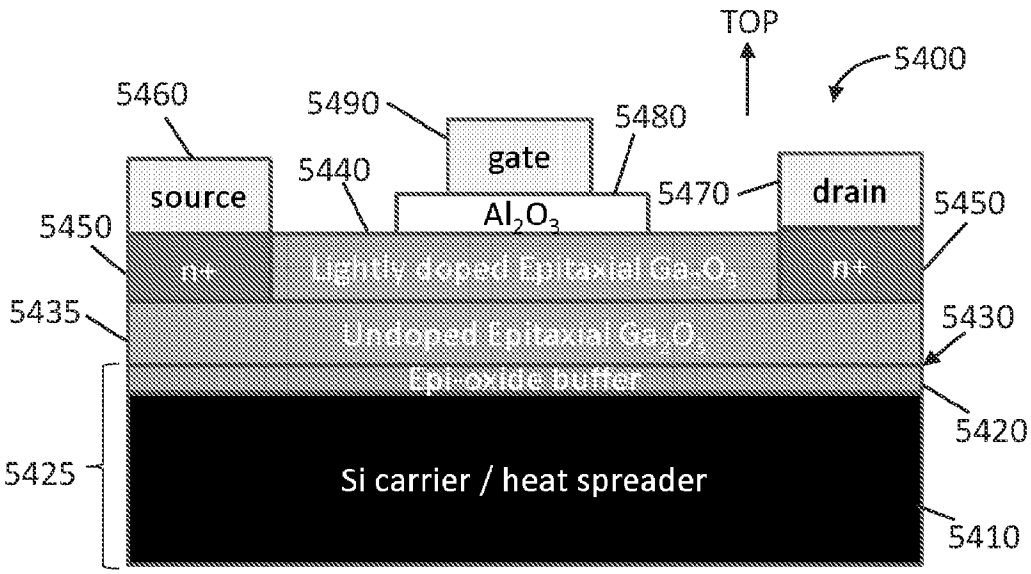
TOP
5400
5460
5490
5480
gate
5440
source
5470
drain
5450
5450
Al_2O_3
n+
Lightly doped Epitaxial Ga_2O_3
n+
5435
5430
Undoped Epitaxial Ga_2O_3
Epi-oxide buffer
5420
5425
Si carrier / heat spreader
5410

FIG. 54

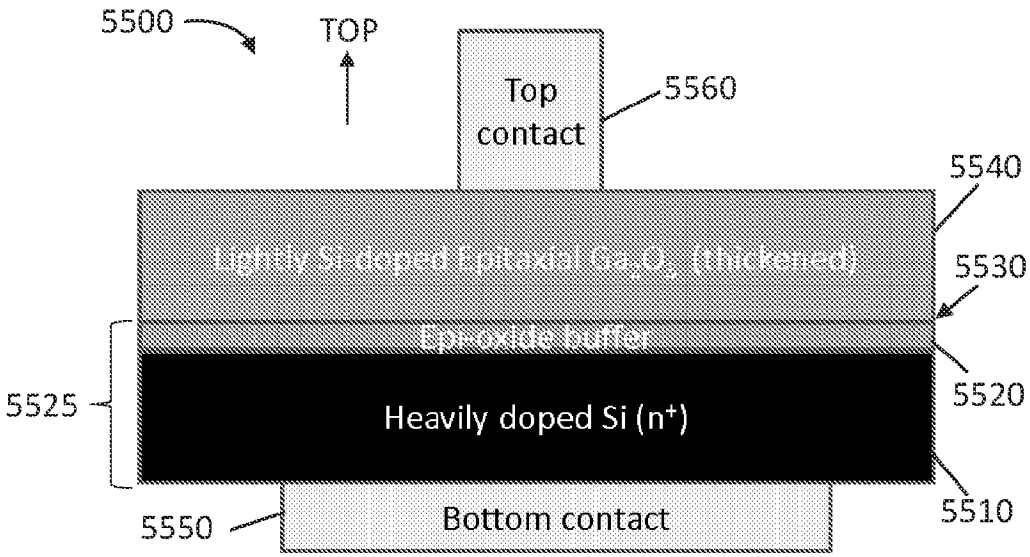
5500
TOP
Top contact
5560
5540
Lightly Si-doped Epitaxial Ga_2O_3 (thickened)
5530
Epi-oxide buffer
5520
5525
Heavily doped Si (n^+)
5510
5550
Bottom contact

FIG. 55

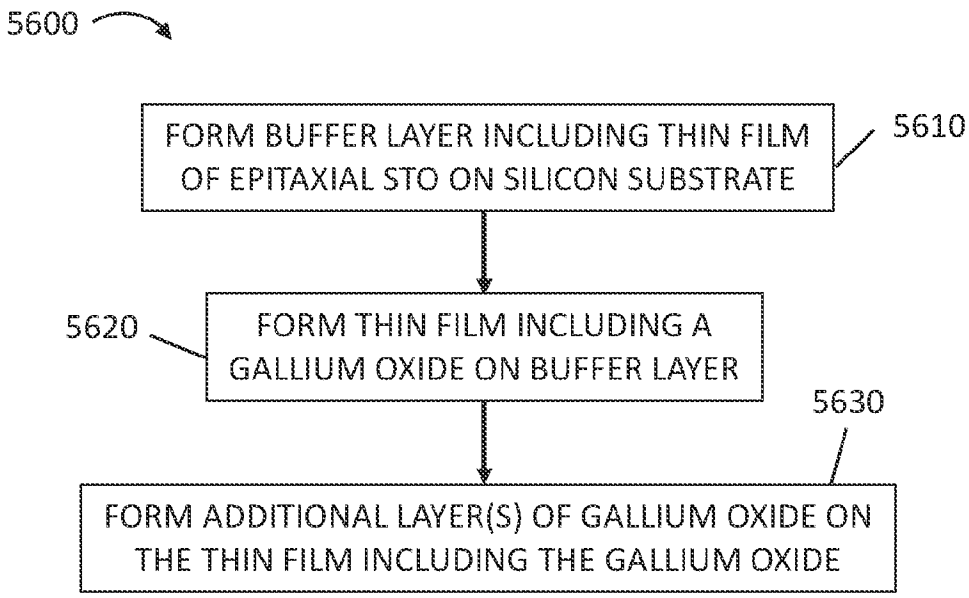
5600
FORM BUFFER LAYER INCLUDING THIN FILM OF EPITAXIAL STO ON SILICON SUBSTRATE
5610
5620
FORM THIN FILM INCLUDING A GALLIUM OXIDE ON BUFFER LAYER
5630
FORM ADDITIONAL LAYER(S) OF GALLIUM OXIDE ON THE THIN FILM INCLUDING THE GALLIUM OXIDE

FIG. 56

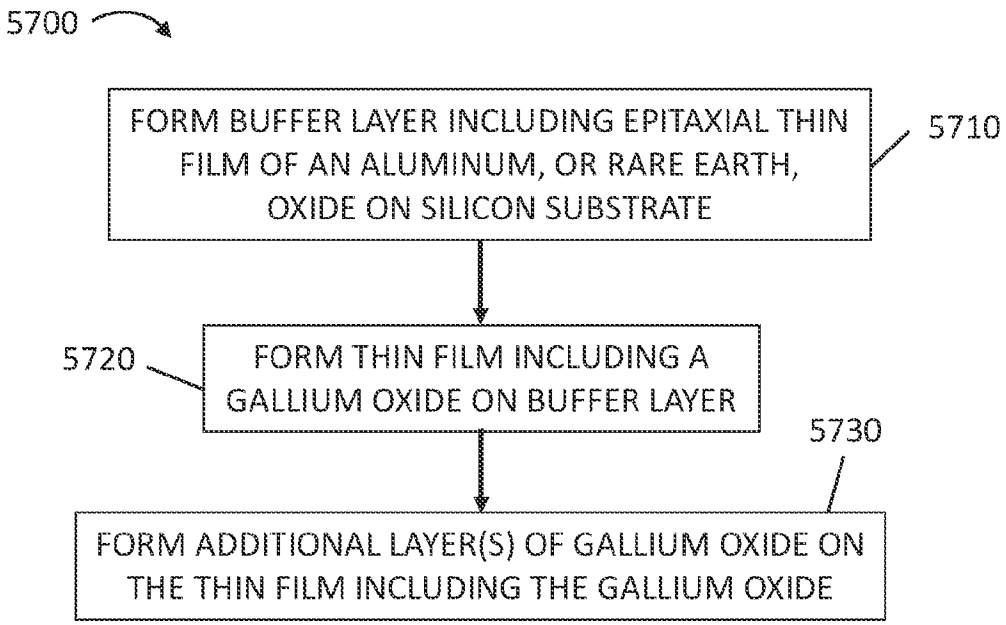
5700
FORM BUFFER LAYER INCLUDING EPITAXIAL THIN FILM OF AN ALUMINUM, OR RARE EARTH, OXIDE ON SILICON SUBSTRATE
5710
5720
FORM THIN FILM INCLUDING A GALLIUM OXIDE ON BUFFER LAYER
5730
FORM ADDITIONAL LAYER(S) OF GALLIUM OXIDE ON THE THIN FILM INCLUDING THE GALLIUM OXIDE

FIG. 57